Hydrogen storage materials with focus on main group I-II elements. Preparation and characterization

Andreasen, Anders

Publication date:
2005

Document Version
Publisher's PDF, also known as Version of record

RISØ

Risø-PhD-21(EN)

Hydrogen Storage Materials with Focus on Main Group I-II Elements

Anders Andreasen

Risø National Laboratory
Roskilde
Denmark
October 2005

Risø-PhD Thesis

Hydrogen storage materials with focus on main group I-II elements

Preparation and characterization

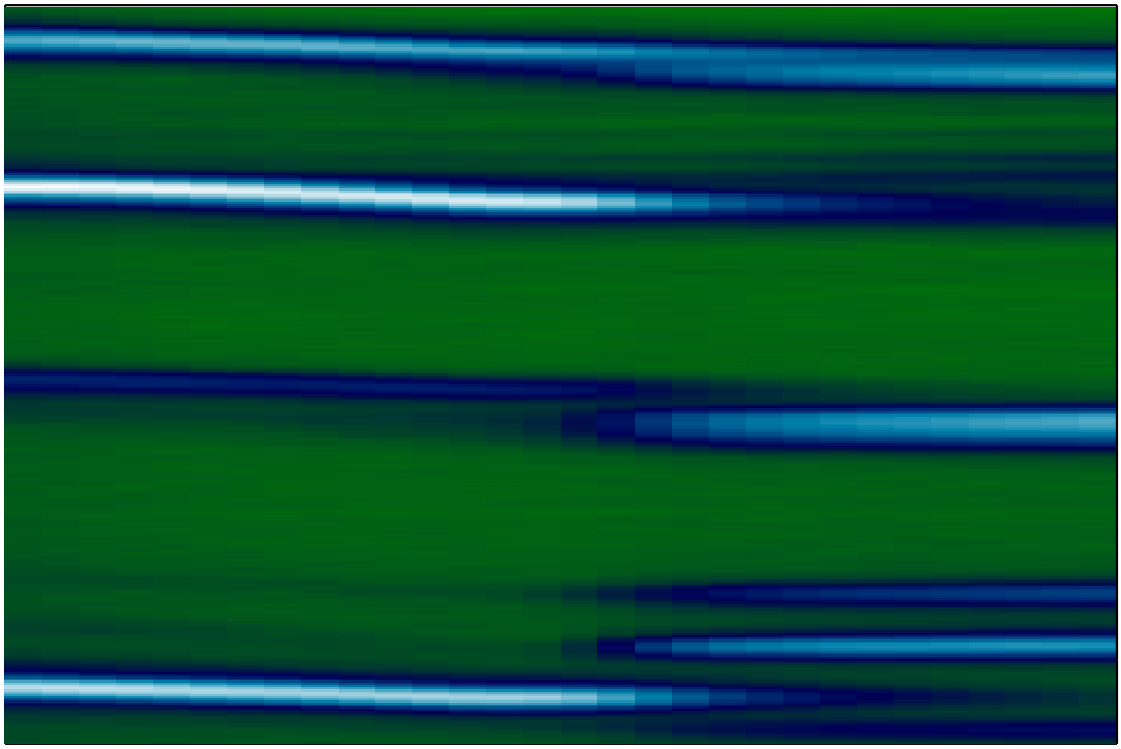

Ph.D. thesis by Anders Andreasen

Risø National Laboratory

Roskilde, 2005

RISØ

Author: Anders Andreasen
Title: Hydrogen Storage Materials with Focus on Main Group I-II Elements
Department: Materials Research Department

This thesis is submitted in partial fulfillment of the requirements for the Ph. D. degree at the
Department of Chemical Engineering, Technical University of Denmark

Abstract (max. 2000 char.):
A future *hydrogen based society*, viz. a society in which hydrogen is the primary energy carrier, is viewed by many as a solution to many of the energy related problems of the world { the ultimate problem being the eventual depletion of fossil fuels. Although, for the hydrogen based society to become realizable, several technical difficulties must be dealt with. Especially, the transport sector relies on a cheap, safe and reliable way of storing hydrogen with high storage capacity, fast kinetics and favourable thermodynamics. No potential hydrogen storage candidate has been found yet, which meets all the criteria just summarized.
The hydrogen storage solution showing the greatest potential in fulfilling the hydrogen storage criteria with respect to storage capacity, is solid state storage in light metal hydrides e.g. alkali metals and alkali earth metals. The remaining issues to be dealt with mainly concerns the kinetics of hydrogen uptake/release and the thermal stability of the formed hydride. In this thesis the hydrogen storage properties of some magnesium based hydrides and alkali metal tetrahydridoaluminates, a subclass of the so called *complex* hydrides, are explored in relation to hydrogen storage.
After briefly reviewing the major energy related problems of the world, including some basic concepts of solid state hydrogen storage the dehydrogenation kinetics of various magnesium based hydrides are investigated. By means of time resolved *in situ* X-ray powder diffraction, quantitative phase analysis is performed for air exposed samples of magnesium, magnesium-copper, and magnesium-aluminum based hydrides. From kinetic analysis of the different samples it is generally found that the dehydrogenation kinetics of magnesium hydride is severely hampered by the presence of oxide impurities whereas alloying with both Cu and Al creates compounds significantly less sensitive towards contamination. This leads to a phenomenological explanation of the large variations in the observed apparent activation energies of hydrogenation/ dehydrogenation of magnesium based systems, as generally found in the literature. Further, concurrent changes apparent prefactors i.e. a *compensation effect* (CE) is found. A detailed analysis leads to the general conclusion that any observed CE based on an Arrhenius analysis is false and a direct consequence of the data analysis. The effect of both particle/crystallite size reductions along with the effect of Ti-doping on the two-step dehydrogenation kinetics of lithium aluminum hydride is investigated. It is found
that only the kinetics the first reaction step is sensitive to a reduction in the crystallite size.
In order to achieve improved kinetics of the second reaction step as well, Ti-doping is found to be very effective. The main results of these investigations are; i) the first dehydrogenation step is subject to transport limitations probably diffusional limitations ii) the apparent activation energy of both dehydrogenation steps is insensitive to Ti-doping, suggesting that a prefactor effect is responsible for the kinetic improvements i.e. the number of reaction sites is probably increased e.g. by creation of lattice defects such as atomic vacancies.
Finally, the hydrogen mobility in sodium aluminum hydride, potentially limiting the overall kinetics of hydrogenation/dehydrogenation, is studies with neutron scattering experiments. Both the hydrogen jump frequency and the mean square atomic displacement of hydrogen atoms are estimated.

Risø-PhD-21(EN)
2005

ISBN 87-550-3498-5

Contract no.:

Group's own reg. no.:

Sponsorship:

Cover :
Cover graphic: Imaging the dehydrogenation of an Mg-Al based hydride by means of time resolved in situ X-ray powder diffraction.

Pages:
Tables:
References:

Risø National Laboratory
Information Service Department
P.O.Box 49
DK-4000 Roskilde
Denmark
Telephone +45 46774004
bibl@risoe.dk
Fax +45 46774013
www.risoe.dk

Andreasen, Anders
Hydrogen storage materials with focus on main group I-II elements –
Preparation and Characterization
Submitted Ph.D. thesis in Chemical Engineering.
Department of Chemical Engineering
Technical University of Denmark
DK-2800 Kgs. Lyngby, Denmark
October 2005

This thesis is typeset with Computer Modern using LaTeX

Pages: 196 including enclosed papers

Materials Research Department
Risø National Laboratory
Frederiksborgvej 399
DK-4000 Roskilde, Denmark
Phone: +45 46775700
Fax: +45 4677 5758
http://www.risoe.dk/afm

Cover graphic: Imaging the dehydrogenation of an Mg-Al based hydride by means of time resolved *in situ* X-ray powder diffraction.

Preface

This thesis is submitted in partial fulfilment of the requirements for the Ph. D. degree at the Department of Chemical Engineering, Technical University of Denmark. This thesis presents the results obtained during my work in the Hydrogen Storage Group, Materials Research Department, Risø National Laboratory[1] in the period October 2002 to October 2005. The work has been performed under supervision by Prof. Ib Chorkendorff, Interdisciplinary Research Center for Catalysis, Department of Physics and Department of Chemical Engineering, Technical University of Denmark, Dr. Allan Schrøder Pedersen, Materials Research Department, Risø National Laboratory, Dr. Søren Dahl, Haldor Topsøe A/S, and Prof. Flemming Besenbacher, *iNANO*, Department of Physics, University of Aarhus. This work has been financed through the Danish Technical Research Council project *Towards the Hydrogen Based Society*.

The motivation for the work presented in this thesis is the fact that our society in the future will inevitably face some serious challenges due to limited supply of fossil fuels and global warming issues. A possible solution to these problems is a gradual transition from the *hydrocarbon based society* to the *hydrogen society* i.e. a society in which hydrogen is the primary energy carrier (in opposition to e.g. oil, coal). Hydrogen can be produced by electrolysis using electricity from renewable energy sources and, ultimately, energy conversion can be performed with water being the only byproduct – thereby eliminating CO_2 emissions. The vision for the transport sector is that all cars utilize fuel cells instead of a traditional combustion engine and that they are powered by hydrogen. However one of the great *show stoppers* is the shortcomings of current hydrogen storage technologies especially concerning hydrogen capacity and operating temperature. One of the areas within the hydrogen storage technologies showing great potential, is solid state hydrogen storage in metals and complex hydrides. In this thesis the properties of some alkali and alkaline earth metal based hydrogen storage media (Mg, Mg-Al, Mg-Cu, $LiAlH_4$, and $NaAlH_4$) are investigated.

High priority has been given to presentation of the results obtained during my Ph.D. period. This has resulted in a number of peer-reviewed international publications (see List of papers). Papers 1-6 are the ones directly related to the subject of this thesis and they have served as the foundation of this thesis. This has evidently lead to some redundancy. Papers 7-9 are related to heterogeneous catalysis and kinetics. However, paper 7 was a direct inspiration for the writing of paper 1. Furthermore, some of the concepts introduced in paper 7 have been extended to also apply to the kinetics of solid state hydrogen storage materials. This work is in progress, but unfortunately the results are still of preliminary nature, and have therefore not found their way into this thesis. Paper 10 relates to the use of Small-Angle X-ray Scattering (SAXS) for studying size distributions. Papers 1-7 are included as appendices.

In addition results have been presented on a number of national and international meetings and symposia in the form of posters, proceedings papers etc. e.g. *International symposium on metal-hydrogen systems fundamentals and applications, Crakow (PL), 5-10 Sep 2004* and *Risø international energy conference*[2]*, Risø (DK), 23-25 May 2005.*

[1] http://www.risoe.dk/afm/hydrogen/hydrogen.htm

[2] Proceedings: http://www.risoe.dk/rispubl/SYS/ris-r-1517.htm

The results presented in this thesis heavily relies on a number of different experimental techniques. Although, only *in situ* X-ray powder diffraction (XRPD) and Quasielastic Neutron Scattering (QNENS) are described in some detail since these are judged as *state of the art*. Readers unfamiliar with the techniques *not* explained in detail, are encouraged to consult standard solid state chemistry and physics textbooks or similar.

I would like to thank the following colleagues at Risø for their kind help and assistance during this Ph.D. study: Mike Wichmann, Ove Rasmussen, Kim Lefmann, Jari í Hjøllum, Peter Kjær Willendrup, Nini Pryds, Allan Schrøder Pedersen. In particular I would like to thank Jens Wenzel Andreasen for helping out with *in situ* X-ray powder diffraction experiments and for numerous enlightening and exciting discussions about almost everything ranging from natural science to politics, football, Tour de France etc. Also special thanks to Tejs Vegge for general support and many stimulating and fruitful discussions regarding solid state hydrogen storage. From the Technical University of Denmark I would like to thank my fellow Ph.D. students associated with ICAT, in particular Jens Høegh, Søren Højgaard Jensen, Michael Andersen and Christopher Ostenfeld.

Large parts of the results presented in this thesis is a direct result of close collaboration with people from other research institutions. In this respect, I would like to acknowledge Torben R. Jensen from Department of Chemistry, Aarhus University, for valuable contributions to the *in situ* X-ray powder diffraction results presented in this thesis, Robin Christensen and Alfons M. Molenbroek from Haldor Topsøe A/S, for providing essential equipment and know-how to the *in situ* X-ray powder diffraction experiments, Christoph Niedermayer from the Paul Scherrer Institute, Switzerland, and Dennis Engberg from Department of Applied Physics, Chalmers University of Technology, Sweden, both for helping out with quasielastic neutron scattering experiments.

I would also like to thank my former fellow students Hasse H. Lynggaard and Carsten Stegelmann (present address Rambøll Oil & Gas, Esbjerg) as well as my former supervisor Prof. Per Stoltze all from the Microkinetic modelling and Catalysis group at Aalborg University Esbjerg for fruitful collaboration during this Ph.D. study. A direct result of this collaboration is the creation of papers 7, 8, and 9.

I am forever grateful to my lovely wife, Jette, for being supportive, enduring and forgiving during the last three years, and to my beautiful daughter, Tilde, for helping me remember that there are more important things to life than work. My deepest gratitude also goes to family and friends for being supportive and for showing interest in my work.

Roskilde, October 2005 Anders Andreasen

Abstract

A future *hydrogen based society*, viz. a society in which hydrogen is the primary energy carrier, is viewed by many as a solution to many of the energy related problems of the world – the ultimate problem being the eventual depletion of fossil fuels. Although, for the hydrogen based society to become realizable, several technical difficulties must be dealt with. Especially, the transport sector relies on a cheap, safe and reliable way of storing hydrogen with high storage capacity, fast kinetics and favourable thermodynamics. No potential hydrogen storage candidate has been found yet, which meets all the criteria just summarized.

The hydrogen storage solution showing the greatest potential in fulfilling the hydrogen storage criteria with respect to storage capacity, is solid state storage in light metal hydrides e.g. alkali metals and alkali earth metals. The remaining issues to be dealt with mainly concerns the kinetics of hydrogen uptake/release and the thermal stability of the formed hydride. In this thesis the hydrogen storage properties of some magnesium based hydrides and alkali metal tetrahydridoaluminates, a subclass of the so called *complex* hydrides, are explored in relation to hydrogen storage.

After briefly reviewing the major energy related problems of the world, including some basic concepts of solid state hydrogen storage the dehydrogenation kinetics of various magnesium based hydrides are investigated. By means of time resolved *in situ* X-ray powder diffraction, quantitative phase analysis is performed for air exposed samples of magnesium, magnesium-copper, and magnesium-aluminum based hydrides. From kinetic analysis of the different samples it is generally found that the dehydrogenation kinetics of magnesium hydride is severely hampered by the presence of oxide impurities whereas alloying with both Cu and Al creates compounds significantly less sensitive towards contamination. This leads to a phenomenological explanation of the large variations in the observed apparent activation energies of hydrogenation/dehydrogenation of magnesium based systems, as generally found in the literature. Further, concurrent changes apparent prefactors i.e. a *compensation effect* (CE) is found. A detailed analysis leads to the general conclusion that any observed CE based on an Arrhenius analysis is false and a direct consequence of the data analysis.

The effect of both particle/crystallite size reductions along with the effect of Ti-doping on the two-step dehydrogenation kinetics of lithium aluminum hydride is investigated. It is found that only the kinetics the first reaction step is sensitive to a reduction in the crystallite size. In order to achieve improved kinetics of the second reaction step as well, Ti-doping is found to be very effective. The main results of these investigations are; i) the first dehydrogenation step is subject to transport limitations probably diffusional limitations ii) the apparent activation energy of both dehydrogenation steps is insensitive to Ti-doping, suggesting that a prefactor effect is responsible for the kinetic improvements i.e. the number of reaction sites is probably increased e.g. by creation of lattice defects such as atomic vacancies.

Finally, the hydrogen mobility in sodium aluminum hydride, potentially limiting the overall kinetics of hydrogenation/dehydrogenation, is studies with neutron scattering experiments. Both the hydrogen jump frequency and the mean square atomic displacement of hydrogen atoms are estimated.

Resumé

Løsningen på mange af verdens energirelaterede problemer, hvoraf udtømningen af de fossile brændsler synes som det største, anses af mange for at være overgangen til et fremtidigt *brintsamfund*, dvs. et samfund, hvor brint er den primære energibærer. For at brintsamfundet kan realiseres er der dog adskillelige tekniske vanskeligheder, som skal løses. Ikke mindst i transportsektoren, som afhænger af en billig, sikker og pålidelig metode til lagring af brint med en høj lagringskapacitet, hurtig kinetik og favorabel termodynamik. Indtil videre er der ikke fundet nogen brintlagringskandidat, som opfylder disse krav.

Den mest lovende brintlagringsmetode med henblik på at opfylde kriteriet angående lagringskapacitet, er brintlagring i fast form i metalhydrider baseret på lette metaller f.eks. alkalimetaller og jordalkalimetaller. De resterende problemer som skal løses er hovedsageligt problemer relateret til hydrogenerings-/dehydrogeneringskinetikken og den termiske stabilitet af den den dannede hydrid. I denne afhandling behandles brintlagrinsegenskaberne af nogle magnesiumbaserede hydrider og nogle alkalimetal tetrahydridoaluminater, en undergruppe af de såkaldte *komplekse* hydrider.

Efter en kort gennemgang af de vigtigste energirelaterede problemer, forskellige metoder til lagring af brint samt basal baggrundsteori vedrørende faststofbrintlagring, bliver dehydrogeneringskinetikken af forskellige magensiumbaserede hydrider undersøgt. Ved brug af tidsopløst *in situ* røntgen pulverdiffraktion udføres kvantitativ fasebestemmelse for prøver af magnesium-, magnesium-aluminium og magnesium-kobberbaserede hydrider eksponeret til luft. Ud fra en kinetikanalyse for de forskellige prøver, fremstår det generelle billede, at dehydrogeneringskinetikken af magnesiumhydrid i svær grad inhiberes af oxidurenheder, hvorimod legering med både Cu og Al danner forbindelser, som er betydeligt mindre følsomme overfor forurening. Dette danner baggrund for en fænomenologisk forklaring af de store variationer i den tilsyneladende aktiveringsenergi for hydrogenering/dehydrogenering af magnesiumbaserede systemer, som rapporteres i litteraturen. Endvidere findes samhørende ændringer i tilsyneladende præfaktorer for hydrogenering/dehydrogenering dvs. en *kompensations effekt* (KE). En detaljeret analyse resulterer i den generelle konklusion, at enhver KE, som observeres i forbindelse med en Arrheniusanalyse, er falsk, og en direkte konsekvens af dataanalysen.

Deslige undersøges effekten på to-trins dehydrogeneringskinetikken af litium aluminiumhydrid, af både en reduktion af partikel-/krystallitstørrelse og dotering med titanium. Det vises, at kinetikken af det 1. reaktionstrin er følsom overfor en reduktion i krystallitstørrelse. For også at opnå forbedret kinetik for det 2. trin findes det, at dotering med Ti er meget effektiv. Hovedresultaterne af disse undersøgelser er at: i) det første dehydrogeneringstrin er underlagt transportbegrænsninger, sandsynligvis diffusionsbegrænsning ii) den tilsyneladende aktiveringsenergi af begge dehydrogenringstrin er ikke påvirket af Ti-dotering, hvilket tyder på, at en præfaktoreffekt er ansvarlig for den forbedrede kinetik f.eks. i kraft af dannelse af krystaldefekter såsom vakancer.

Til sidst undersøges brintmobiliteten i natrium aluminumhydrid vha. af neutronspredningseksperimenter. Både den atomere brinthoppefrekvens og den middelkvadrerede atomare flytning af brint i krystalgitteret er blevet estimeret.

List of papers

Paper 1

Compensation effect in the hydrogenation/dehydrogenation kinetics of metal hydrides
A. Andreasen, T. Vegge, A. S. Pedersen
J. Phys. Chem. B. **109** (2005) 3340-3344
DOI: 10.1021/jp0458755

Paper 2

Interaction of hydrogen with an Mg-Al alloy
A. Andreasen, M. B. Sørensen, R. Burkarl, B. Møller, A. M. Molenbroek, A. S. Pedersen, J. W. Andreasen, M. M. Nielsen, T. R. Jensen
J. Alloys Comps., In press
DOI: 10.1016/j.jallcom.2005.01.119

Paper 3

Dehydrogenation kinetics of air-exposed MgH_2/Mg_2Cu and $MgH_2/MgCu_2$ studied with in situ *X-ray powder diffraction*
A. Andreasen, M. B. Sørensen, R. Burkarl, B. Møller, A. M. Molenbroek, A. S. Pedersen, T. Vegge, T. R. Jensen
Appl. Phys. A, Accepted

Paper 4

Dehydrogenation kinetics of pure and nickel-doped magnesium hydride investigated by in situ *time resolved powder X-ray diffraction*
T. R. Jensen, A. Andreasen, T. Vegge, J. W. Andreasen, K. Ståhl, A. S. Pedersen, M. M. Nielsen, A. M. Molenbroek, F. Besenbacher
Int. J. Hydrogen Energy, Submitted

Paper 5

Dehydrogenation kinetics of as-received and ball milled $LiAlH_4$
A. Andreasen, T. Vegge, A. S. Pedersen
J. Solid State Chem., Accepted
DOI:10.1016/j.jssc.2005.09.027

Paper 6

Effect of Ti-doping on the dehydrogenation kinetic parameters of lithium aluminum hydride
A. Andreasen
J. Alloys Comps., Accepted

Paper 7

Analysis of simple kinetic models in heterogeneous catalysis
H. Lynggaard, A. Andreasen, C. Stegelmann, P. Stoltze
Prog. Surf. Sci. **77** (2004) 71-137
DOI: 10.1016/j.progsurf.2004.09.001

Paper 8

Simplified kinetic models of methanol oxidation on silver
A. Andreasen, H. Lynggaard, C. Stegelmann, P. Stoltze
Appl. Catal. A., **289** (2005) 267-273
DOI: 10.1016/j.apcata.2005.05.004

Paper 9

A microkinetic model of the methanol oxidation over silver
A. Andreasen, H. Lynggaard, C. Stegelmann, P. Stoltze
Surf. Sci., **544** (2003) 5-23
DOI: doi:10.1016/j.susc.2003.08.007

Paper 10

Dependence of magneto resistance on the size distribution of Co precipitates in phase-separated $Cu_{90}Co_{10}$ J. W. Andreasen, A. Andreasen, S. Jeppesen, M. Xu, N. Pryds
J. Appl. Cryst., Submitted

Contents

Chapter 1

Introduction

1.1 The beginning of the end

The world as we know it, and the industrialized countries in particular, relies heavily on fossil fuels. In fact 87% of the world energy consumption in year 2003 was from fossil fuels (cf. figure 1.1) – the rest mainly comes from nuclear power, hydro power, and burning of waste and wood. Although energy consumption from sustainable energy sources such as wind electricity are rapidly increaseing (increased by a factor of 5 from 1989-2003) the overall contribution is only 0.11%.

We consume fossil fuels for a wide variety of purposes from heating our houses, cooking of our food to transportation and manufacturing of consumer goods – the list could be continued and it is long and exhaustive. In fact almost every aspect of human life in the modern world is associated with the use of fossil fuels – the result is an ever increasing energy consumption caused by population growth and a general increase in living standard. The world population has been projected to increase from approx. 6.4 billion today to approx. 9 billion by year 2050 [1] and especially the explosive development in Asia, in particular in China, requires massive amounts of energy.

In order to support the growing demand for fossil fuels new reserves needs to be discovered. However, oil discovery already peaked in the 1962 with 40 billion barrels being found and have

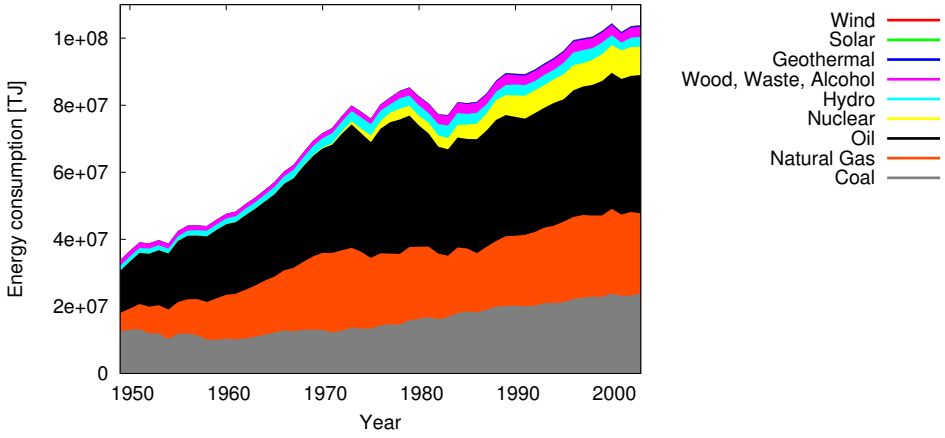

Figure 1.1: World energy consumption by source 1949-2003. Data are from the Energy Information Administration (EIA), U. S. Department of Energy, Annual Energy Review 2003 (http://www.eia.doe.gov/emeu/aer/txt/ptb0103.html).

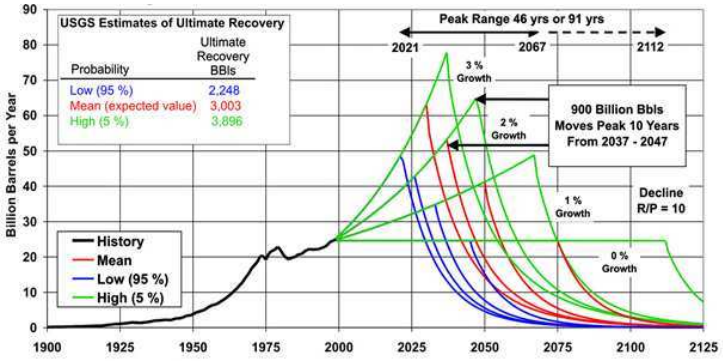

Figure 1.2: Peak oil. World conventional oil scenarios by the Energy Information Administration (EIA), U. S. Department of Energy based on ultimate oil recovery estimates by the U.S. Geological Survey. The figure has been adapted from ref. [2].

declined ever since. In 1997 only 6 billion barrels of oil was found in comparison with the production of 26 billion barrels [3, 4]. According to numbers from BP the total proven oil reserves of the world is approx. 1146 billion barrels of oil including the tar oil sands of Canada, gas condensate and natural gas liquids as well as crude oil [4]. With the current consumption of oil which is approx. 28 billion barrels a year, the proven reserves would last for only 40 years. However, a zero growth in energy demand is questionable and additional oil reserves will probably be discovered in the future including oil recovery from oil shale, complicating the exact estimate of when the oil production will peak and eventually start to decline. Figure 1.2 show different scenarios for different ultimate oil recoveries and energy consumption growth rates.

Someday, we will inevitably run out of fossil fuels, although due to relatively large reserves of natural gas and coal it may not happen in our lifetime. With the current consumption level the proven reserves should last for approx. 70 and 200 years, respectively [4]. Another issue which might become critical even before we run out of fossil fuels is the global warning issue (cf. figure 1.3) potentially threatening the life of many people due to rising sea levels and increasingly harsh weather conditions. Increasing levels of atmospheric CO_2 originating from the burning of fossil fuels correlate with the increasing global temperature [6], nevertheless, it is the subject of

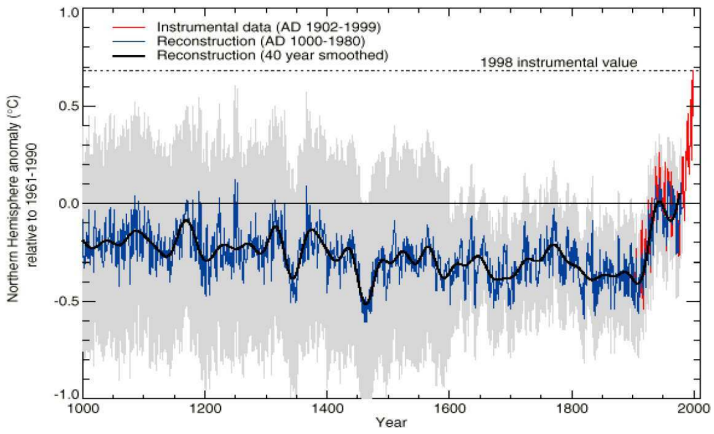

Figure 1.3: Northern hemisphere average temperature change for the past millenium relative to 1961–1990 mean. The figure has been adapted from ref. [5].

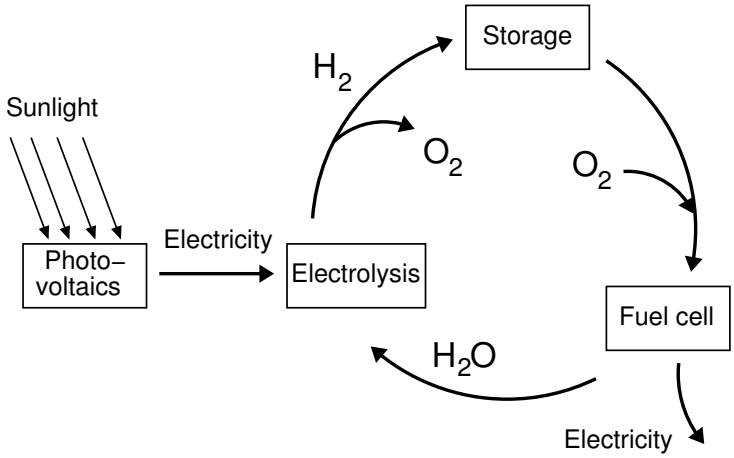

Figure 1.4: The hydrogen cycle based on photovoltaics and fuel cells. Photonic energy from the sunlight is converted into electricity by means of photovoltaic cells. The produced electricity is used in an electrolyzer to split water into hydrogen and oxygen. Oxygen is released to the atmosphere and hydrogen is intermediately stored, transported and distributed before being electrochemically compusted with oxygen (from the atmosphere) in a fuel cell whereby electricity is produced leaving water or steam into the atmosphere.

heavy debate to which extent this is the key relation or if other phenomena are equally or more important, e.g. solar activity [7], in determining the global temperature increase. Nevertheless, as long as a clear connection between CO_2 and other green house gas emissions related to human activities and the observed temperature increase has not been established (or disproven) it is, in my opinion, wise to limit the emissions of CO_2 as much as possible.

1.2 Towards the hydrogen based society

A possible way of addressing both the global warming issue and to keep a sustainable energy supply, also after the fossil fuels have been depleted, is a gradual transformation of our present *fossil fuel based society* to a *hydrogen based society* viz. a society in which hydrogen is the primary energy carrier. See also refs. [8, 9, 10, 11, 12].

Since hydrogen is not naturally present as H_2 it must be produced. Today most hydrogen is produced from steam reforming of natural gas or higher hydrocarbons [8], although in the future hydrogen society hydrogen is to be produced from water, utilizing electrolysis with electricity produced from sustainable energy sources e.g. solar, wind, hydro power or directly from photolysis [13]. However, since production of electricity (and thereby H_2) from sustainable sources are of intermittent nature and very seldom fits the energy demand, the need for an intermediate energy storage medium is obvious – especially for the transport sector which is responsible for alomost 60% of the world oil consumption equal to 25% of the world energy consumption [14] . In the hydrogen society energy conversion from stored H_2 into usable form can be realized either in a conventional internal combustion engine (ICE) or a fuel cell (FC). Due to Carnot cycle efficiency limitations of the ICE, a fuel cell (FC) is preferred [15], since it offers a potential efficiency of approx. twice that of an ICE [16]. In the FC H_2 recombines with O_2 producing electricity with water as the only byproduct (see ref. [17] for a review of different types of fuel cells). The hydrogen cycle is illustrated in figure 1.4.

1.3 The hydrogen storage problem

As seen from figure 1.4 the hydrogen society is ultimately completely free from CO_2 release as well as the dependence on fossil fuels. In fact, all steps of the cycle can be performed with present technology, although there are sizable barriers preventing the transition into the hydrogen society: *i)* Hydrogen production is very expensive compared to e.g. gasoline – the total cost including distribution of hydrogen from natural gas steam reforming is approx. twice that of gasoline/diesel pr. energy unit and hydrogen from photovoltaics is up to 5-8 times the price of gasoline [11, 18]. The high price of hydrogen from photovoltaics is mainly determined by the high production price of silicon solar cells. *ii)* PEM FCs are commercially available for the transport sector, but the production cost is high (the same price as a small sized car with danish tax policies) due to the use of expensive Nafion ® membrane material and expensive Pt/Ru electrode material [12]. *iii)* Although hydrogen has a high gravimetric energy density of approx. 3 times that of gasoline excluding tank weight [16] its volumetric energy density is low – even for liquefied hydrogen it is 3 times less than gasoline [19]. Especially hydrogen storage is being viewed as one of the major *s*howstoppers requiring an intense research effort [20, 21, 22, 23] in order for the hydrogen society to be realizable. The U. S. Department of Energy, through the FreedomCAR project, has developed targets for a hydrogen storage solution for transportation to meet market demands i.e. based on achieving similar performance and cost levels as current gasoline fuel storage systems c.f. table 1.1.

Several different methods of storing hydrogen are available. These can be generalized into three principal methods with each their different advantages and shortcomings as described below. A graphical representation of storage characteristics is shown in figure 1.5.

Gasseous Storage of hydrogen as a gas at high pressures in steel cylinders is a mature technology. Nevertheless, the volumetric energy density is low compared to gasoline – in fact 7 times lower even at 700 bar. Another drawback of steel cylinders is a relative large contribution from the cylinder material to the overall weight of the storage system reducing the gravimetric energy storage density Composite materials with higher tensile strength than steel are becoming available offering improved gravimetric hydrogen storage density.

Liquid Liquid hydrogen is usually stored around 20 K at ambient pressure in open systems

		DOE technical targets		
Storage parameter	Unit	2007	2010	2015
Gravimetric				
energy density	MJ/kg	5.4	7.2	10.8
hydrogen density	wt.% H_2	4.5	6	9
Volumetric				
energy density	MJ/L	4.32	5.4	9.72
hydrogen density	kg H_2/m^3	36	45	81
Cycle life	Cycles	500	1000	1500
Min/max delivery temperature	°C	-20/85	-30/85	-40/85
Min H_2 delivery pressure	atm	8	4	3
System fill time (5kg H_2)	min	10	3	2.5

Table 1.1: DOE technical hydrogen storage targets for on-board hydrogen storage [24].

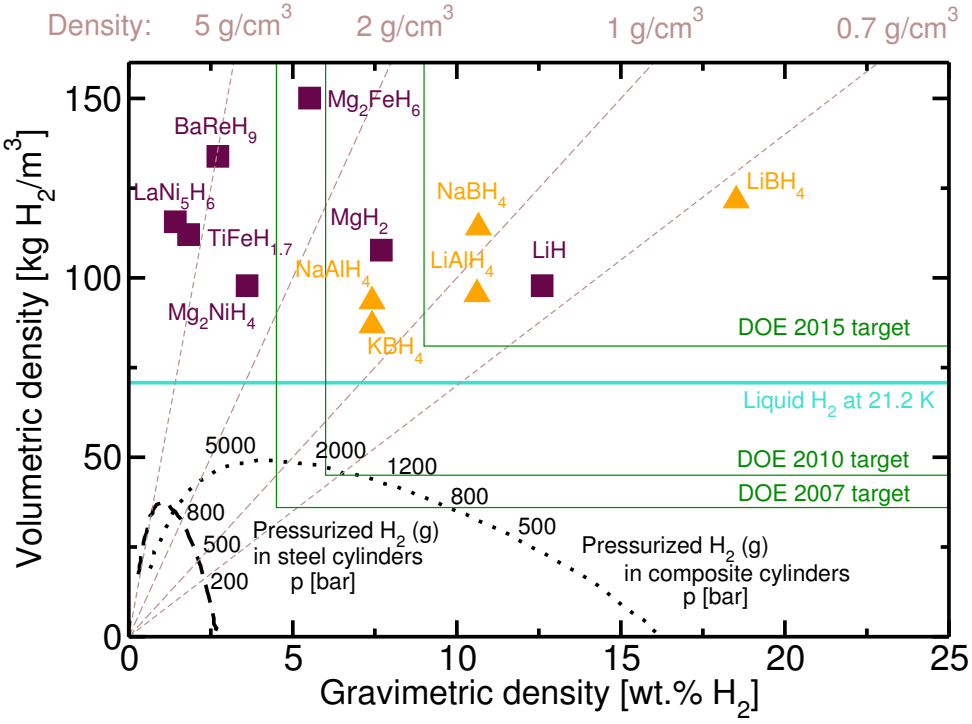

Figure 1.5: Volumetric and gravimetric hydrogen storage densities of different hydrogen storage methods. Metal hydrides are represented with squares and complex hydrides with triangles. $BaReH_9$ has the highest know hydrogen to metal ratio (4.5), Mg_2FeH_6 has the highest known volumetric H_2 density, $LiBH_4$ has the highest gravimetric density. Reported values for hydrides are excluding tank weight. DOE targets are including tank weight, thus the hydrogen storage characteristics of the shown hydrides may appear too optimistic.

to prevent pressure build-up. The advantage of liquid H_2 is, as already mentioned, its high gravimetric energy density, whereas the drawback is a low volumetric energy density. Another drawback is the energy demanding liquefying process which requires up to 40% of the energy content of H_2 [21].

Solid state Hydrogen storage in solid state materials is diverse. The method which historically have attracted most attention is storage in metal hydrides and hydrides of intermetallic compomunds which is based on the fact that many metallic elements reversibly absorbs large quantities of hydrogen. Hhydrogen storage in metal hydrides can roughly be grouped into *a)* low temperature hydrides which release H_2 at 1 bar around RT but with hydrogen capacity restricted to <2.5 wt.% H_2 e.g. $FeTiH_{1.8}$ and $LaNi_5H_6$, and *b)* High temperature hydrides which require heating to above 300 °C for hydrogen desorption but with hydrogen capacities up to 12.6 wt.% H_2 (LiH). The volumetric energy density is usually higher than for liquid hydrogen.

Another subclass of solid state hydrogen storage materials are the so-called complex hydrides (often classified as belonging to the metal hydrides) which are ionic compounds of AlH_4^- or BH_4^- anions and cations usually from the alkali or the the alkaline earth metals e.g. $NaAlH_4$ and $LiBH_4$. In contrast to conventional metal hydrides the complex hydrides combine large hydrogen storage capacities with a hydrogen release temperature down to approx. 100 °C. Thus, potentially meeting the DOE hydrogen storage criteria. The main issue with the complex hydrides so far, has been reversibility, which has remained unre-

solved until recently.

Especially, high capacity and highly stable hydrides i.e. hydrides which has to be heated to high temperatures in order to release hydrogen e.g. $NaBH_4$ and MgH_2 have been considered for irreversible on-board hydrogen storage with hydrogen being released through hydrolysis viz. chemical reaction with water. This method is sometimes referred to as chemical hydrides hydrogen storage. The oxide or hydroxide product can be subject to off-board regeneration.

A special case of liquid hydrogen storage is the physisorption (monolayer condensation) of hydrogen on high area materials such as carbon nanotubes, active carbon etc. although often grouped in the solid state storage category. The hydrogen storage capacity for carbon materials is limited to approx. 2 wt.% H_2 and reports of higher capacities is often explained by errorneous results [16, 25, 26]. Recently, microporous materials such as clathrate hydrates [27] and metal-organic frameworks (MOFs) [28] have received attention as hydrogen storage candidates with preliminary results demonstrating 4 wt.% H_2 and 4.5 wt.% H_2 at 270 and 78 K, respectively.

Apparently, no solid state hydrogen storage solution combines a high gravimetric hydrogen storage density with favourable thermodynamics. Thus, despite a tremendous research effort no potentially commercial candidate has been found which stores significantly more than 2 wt. % H_2 reversibly below 100 °C [29, 30]. For excellent reviews of hydrogen storage methods see ref. [16, 21, 25, 26].

1.4 Motivation and outline

The main focus of this thesis is hydrogen storage in alkali metal and alkaline earth metal based hydrides - to be more precise, hydrogen storage properties of magnesium based hydrides and complex hydrides based on Li and Na. The main motivation for studying magnesium based hydrides, despite the fact that they probably fail to meet the DOE hydrogen storage criteria regarding operating temperature, is that magnesium is both cheap and abundant. Magnesium is the 8. most abundant element in the earths crust and one cubic meter of seawater contains 1.3 kg Mg [31]. The price of Mg is approx. 3 $/kg in comparison with a price of 4-15 $/kg for Ni and Ti, and a price of 350 $/kg for La [32]. Thus, in terms of price pr. stored kg H_2, Mg is superior to most traditional hydrides. Therefore, magnesium based hydrides may found their way into hydrogen storage applications with less strict demands for the hydrogen delivery temperature e.g. stationary applications. The main motivation for studying complex hydrides is obviously their potential in storing large amounts of hydrogen at temperatures near 100 °C. Furthermore, the kinetics are generally not particularly well understood neither which processes limits the overall hydrogen uptake/release nor why and how doping with catalytic elements improve the kinetics.

The outline of this thesis is as follows:

- Chapter 2 gives a basic introduction to the concepts of solid state hydrogen storage. The main focus is on; *i)* the properties of the hydrides of the alkali metals and alkaline earth metals (and to some extent transition metals) *ii)* the hydrogen metal reaction *iii)* thermodynamic properties of metal hydrides in general.

- Chapter 3 is an introduction to the methodology of using *in situ* X-ray powder diffraction (XRPD) as a tool for studying metal hydrides. Main focus is on *in situ* XRPD as a tool for time-resolved quantitative analysis i.e. kinetic analysis. Included is also a condensed presentation of the results obtained on Mg-alloys using *in situ* XRPD. For a more detailed

representation of the results on Mg based materials papers 2, 3, and 4 are referred to. In addition the hydrogen storage properties of Mg-Al alloys are reviewed in a recently published report available for public download[1].

- Chapter 4 is an investigation of the existence of a *Compensation effect* i.e. concurrent changes in activation energies and prefactors in the hydrogenation/dehydrogenation of metal hydrides including a general explanation of the Compensation effect observed in a variety of sciences. A qualitative explanation is given in order to rationalize large variations in the apparent activation energy of hydrogenation/dehydrogenation of Mg/MgH_2. This chapter is more or less based on paper 1.

- Chapter 5 is a presentation of the results obtained on the complex hydrides, $LiAlH_4$ and $NaAlH_4$. The dehydrogenation of $LiAlH_4$ is studied and the effect of ball-milling and Ti-doping is investigated. Neutron scattering is applied in order to investigate the hydrogen mobility in $NaAlH_4$ – both the H-jump frequency as well as the mean-square displacement is investigated. The part related to $LiAlH_4$ is based on Papers 5 and 6.

- Chapter 6 is a summary including a highlight of the most important results obtained including suggestions for future work

[1] http://www.risoe.dk/rispubl/AFM/ris-r-1523.htm

Chapter 2

Basic concepts of solid state hydrogen storage

2.1 The metal-hydrogen reaction

The reaction between hydrogen and a metal can be expressed by the following reaction

$$\mathrm{Me(s)} + \mathrm{xH_2(g)} \rightleftharpoons \mathrm{MeH_x(s)} + Q \tag{2.1}$$

where Q is the released heat during reaction. Metal hydrides of practical interest are exothermic. While the above reaction can be sufficient for thermodynamical considerations, it is very misleading, from a kinetic point of view, to think of the formation of a metal hydride as a *single* reaction. In the following it will be illustrated, starting with a picture of the adsorption process and then turning to the overall processes involved in the formation of a bulk hydride, that the mechanism of hydride formation has a high degree of complexity.

2.1.1 The Lennard-Jones picture

The reaction between gas phase H_2 and a metal surface is schematically illustrated in figure 2.1 where the one-dimensional Lennard-Jones potential of atomic H (orange line) and molecular H_2 is shown (maroon line). Far from the surface the two lines are separated by the hydrogen dissociation energy which is 218 kJ/mol H. A H_2 molecule moving towards the surface will at some point feel a weak attractive force in the range of approx. 0-20 kJ/mol H (van der Waals forces) corresponding to molecular physisorption (point 1 in figure 2.1). If the molecule is moved closer to the surface the potential energy will increase due to repulsion. At some point the potential energy of the H_2 molecule will intersect with the potential energy of the H atom. After this point, it is energetically more favourable for the two H atoms to be separated and bonded to the metal surface rather than bonded to each other. Hence dissociation will occur. If this intersection is at a potential energy larger than zero relative to gas phase H_2 (point 2) dissociation is said to be *activated* and the height of point 2 determines the activation barrier. If the intersection is located at approx. zero potential energy dissociation is said to be *non-activated* (point 3). In the former case only the fraction of H_2 molecules with an energy larger than the activation barrier will be able to dissociate. After dissociation the H atoms find a potential energy minimum shown as point 4 (chemisorption) which corresponds to the H atoms being bonded to the metal surface. If the H-M bond is stronger than the H-H bond, chemisorption is said to be exothermic. Likewise if the H-H bond is the strongest, chemisorption is said to be endothermic. Beyond the point of chemisorption the H-atoms can penetrate the first metal atomic layer into the subsurface through an activated process from which it can diffuse into the bulk (as a solid solution) of the metal. If the potential energy of bulk H-atoms is

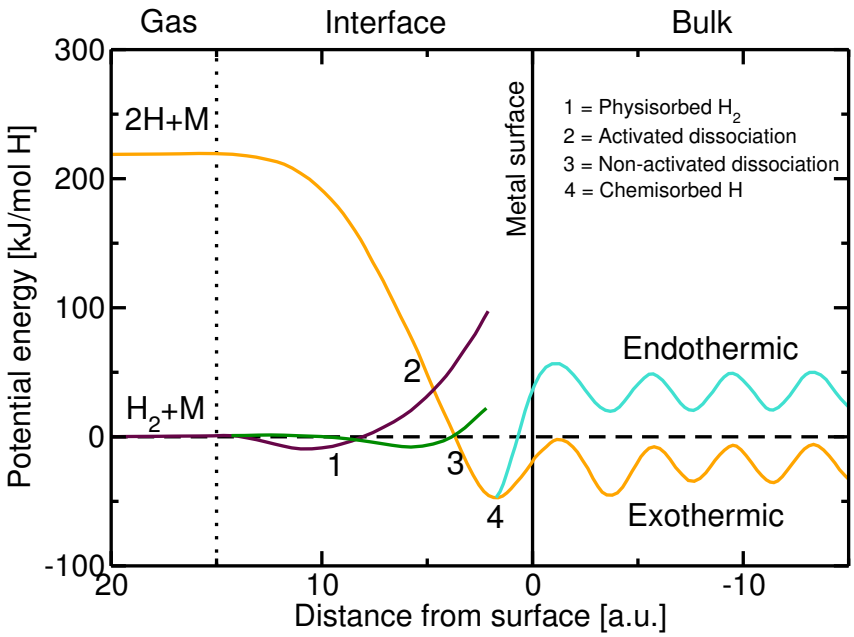

Figure 2.1: Simple schematic Lennard-Jones potential energy diagram of chemisorption of hydrogen on metals. The figure has been adapted from ref. [16, 25, 33].

below zero relative to gas phase H_2, hydrogen solid solution is said to exothermic, likewise if the potential energy of bulk H-atoms is above zero hydrogen solid solution is said to be endothermic.

2.1.2 Reaction mechanism and kinetics

A schematic visualization of the interaction of hydrogen with a metal is depicted in figure 2.2. In contrast to figure 2.1 which was an energy representation, figure 2.2 shows all the individual reaction steps including bulk processes. The formation of the metal hydride can be divided into the following "elementary" reactions [33, 34, 35, 36].

Dissociation/adsorption The first step is the dissociative adsorption of hydrogen on the metal/hydride surface. This is shown as point 1 in figure 2.2.

Surface penetration From the surface the hydrogen atoms can penetrate into the sub-surface (point 3).

Bulk diffusion From the sub-surface, the hydrogen atoms can diffuse into the bulk or from the bulk and further in (point 4).

Hydride formation Hydrogen atoms in the bulk (corresponding to a solid solution) can create a hydride nuclei which can grow to larger hydride grains by trapping of additional hydrogen atoms (point 6). The formation of a hydride phase complicates the picture somewhat since hydrogen diffusion can also take place through the hydride (point 5).

For dehydrogenation the process is the reverse i.e. the hydride phase decomposes and hydrogen atoms diffuses to the sub-surface and subsequently to the surface, where the hydrogen atoms recombine and desorbs as H_2 (point 2). A reaction mechanism can be proposed on the basis of the above reversible elementary reactions. For illustrative purposes only the first processes including dissociation, surface penetration and diffusion are written out in a simplified manner:

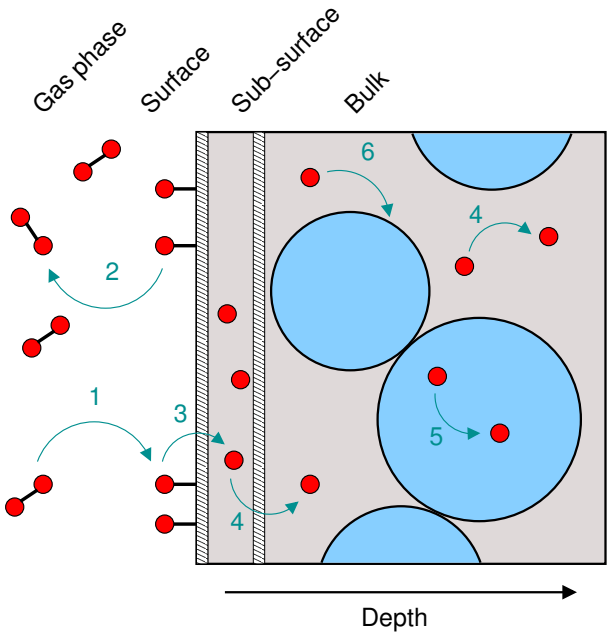

Figure 2.2: Schematic illustration of the different mechanisms involved in the formation of a metal hydride. Hydrogen atoms are shown in red, the metal host lattice is shown in grey, and the metal hydride is shown in blue.

.

$$H_2(g) + 2*_{surf} \rightleftharpoons 2H*_{surf} \tag{2.2}$$

$$H *_{surf} + *_{subsurf} \rightleftharpoons H *_{subsurf} + *_{surf} \tag{2.3}$$

$$H *_{subsurf} + *_{bulk} \rightleftharpoons H *_{bulk} + *_{subsurf} \tag{2.4}$$

where $*$ denotes a free site where one H-atom can sit. Each of the involved elementary reactions can be assigned a net rate

Writing up a material balance and applying a sensible choice of geometry along with appropriate initial and boundary condition one can solve for the hydrogen concentration both as a function of space and time without no *a priory* choice of a rate limiting step. However, this will turn out to be a numerical nightmare, which is why a rate limiting step is often assumed [34, 35, 36, 37, 38, 39] – effectively leading to a significant reduction of the complexity. When experimental kinetic data is fitted with a rate equation, limitations due to either hydride nucleation and growth or diffusion seems to be popular choices [40, 41, 33, 42, 43, 44, 45, 46, 47, 48].

When reviewing the shape of reported hydrogenation/dehydrogenation curves, i.e. macroscopic hydrogen uptake/release as a function of time, they can roughly be divided into two major classes; one with a monotonically decreasing uptake rate and one with a sigmoidal shape. The two classes are illustrated in figure 2.3 and the former corresponds to curve A and the latter corresponds to B. Curve A is usually rationalized in terms of either a surface process such as dissociation or bulk diffusion is rate limiting the overall kinetics. Curve B is usually rationalized in terms of a nucleation and growth mechanism limiting the overall kinetics. Nucleation and growth kinetics is usually explained by a Johnson-Mehl-Avrami (JMA) rate equation [49, 50, 51, 52, 53]

The JMA equation has the following form

$$\alpha(t) = 1 - \exp\left(-(kt)^n\right) \tag{2.5}$$

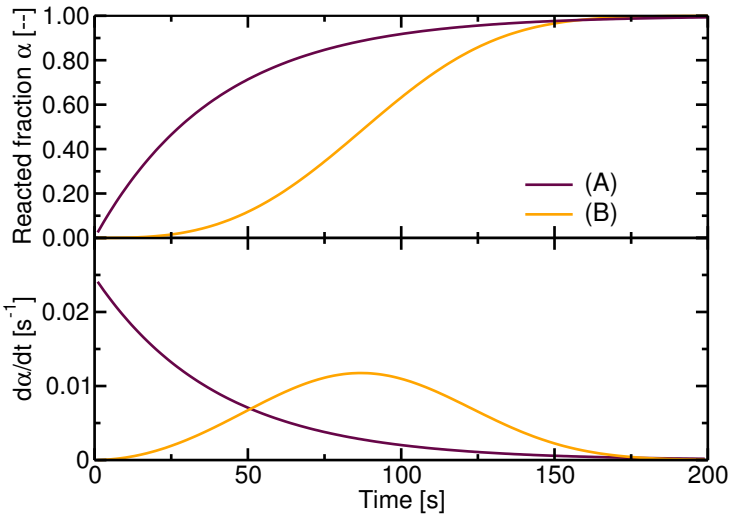

Figure 2.3: The two major classes of hydrogenation/dehydrogenation curves. The hydrogen uptake is shown in the upper part, the hydrogenation rate is shown in the lower part.

.

The parameters describing nucleation and growth rates are contained within an effective kinetic parameter, k. The exponent, n, is often referred to as the Avrami exponent [54]. The temperature dependency of the rate constant k is usually described by an Arrhenius relation.

$$k = A \exp\left(-\frac{E_A}{RT}\right) \tag{2.6}$$

where A is a pre-exponential factor, E_A is the apparent activation energy and R is the universal gas constant.

The most interesting property of the JMA equation is that it explains not only curves with a sigmoidal shape, but also curves of type A in figure 2.3 i.e. situations where e.g. diffusion may be rate limiting, when n is allowed to have values of 1 or less. This is probably why the JMA model is often successfully invoked when dealing with the kinetics of hydrogenation/dehydrogenation of metal hydrides – and its use sometimes result in conclusions about a diffusional process being rate limiting [41, 43]. It is also interesting to note that a sigmoidal uptake curve can be a result of a hydride with a protective surface oxide layer as observed for e.g. magnesium [55, 56, 57]. During the first hydrogenation, cracks are developed in the oxide layer due to the volume expansion of the hydride formed underneath. Even though the JMA equation may provide a good fit, any conclusions about nucleation and growth being rate limiting in such a process should of course be taken with care.

2.2 Thermodynamics

2.2.1 The Pressure Composition Isotherm

The Pressure Composition Isotherm from now on called PCI is the work horse when it comes to determination of several key properties of metal hydrides. A generic PCI is depicted in figure 2.4 (left). When initially increasing the hydrogen pressure at isothermal conditions the adsorbed amount of hydrogen (H/M is the hydrogen to metal stoichiometric ratio) will increase only slightly. This corresponds to the formation of a solid solution of hydrogen and this is denoted the α-phase. When the maximum solubility of hydrogen in the α-phase is reached the hydride

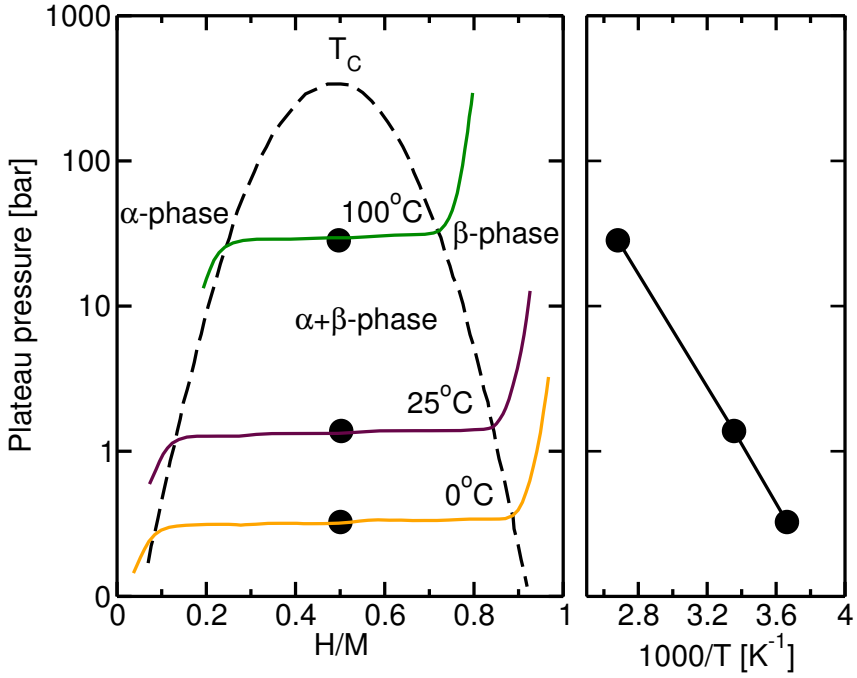

Figure 2.4: Left: Pressure-Composition-Isotherms (PCI) for a hypothetical metal hydride. Adapted from ref. [16]. Right: Van't Hoff plot for a hypothetical metal hydride derived from the measured pressures at plateau midpoints from the PCI's.

phase (β-phase) will start forming. Increasing the hydrogen pressure further will now result in a substantial increase in the absorbed amount of hydrogen. This phenomenon may be explained from the Gibbs phase rule [58]

$$F = 2 - \pi + N \tag{2.7}$$

where F is the degree of freedom, π is the number of phases and N is the number of chemical species. Thus, existanece of one additional phase leads to the loss of a degree of freedom. The pressure at which this transformation takes place is referred to as the plateau pressure and in this region the α-phase and β-phase co-exist. When the stoichiometric hydride have formed completely depleting the α-phase one additional degree of freedom is regained and the additional absorption of hydrogen will now require a large pressure increase. This corresponds to the solid solution of hydrogen in the β-phase. The plateau pressure gives valuable information about reversible storage capacity from the width of the plateau and the position of the plateau at a given temperature may give an idea of the stability of the hydride. Stable hydrides will require higher temperatures than less stable hydrides to reach a certain plateau pressure.

2.2.2 Thermodynamic properties from PCI

Assuming ideality the equilibrium relation for reaction Eq. 2.1 is

$$K^{-1} = \frac{p_{H_2}}{p^{\ominus}} \tag{2.8}$$

From the definition of the equilibrium constant we know that $-RT \ln K = \Delta G^{\ominus}$, where $\Delta G^{\ominus}$ is the change in standard Gibbs free energy upon hydrogenation. Further the definition of $\Delta G^{\ominus} = \Delta H^{\ominus} - T\Delta S^{\ominus}$ inserted into the equation above yields

$$\ln\left(\frac{p_{H_2}}{p^{\ominus}}\right) = \frac{\Delta H^{\ominus}}{RT} - \frac{\Delta S^{\ominus}}{R} \tag{2.9}$$

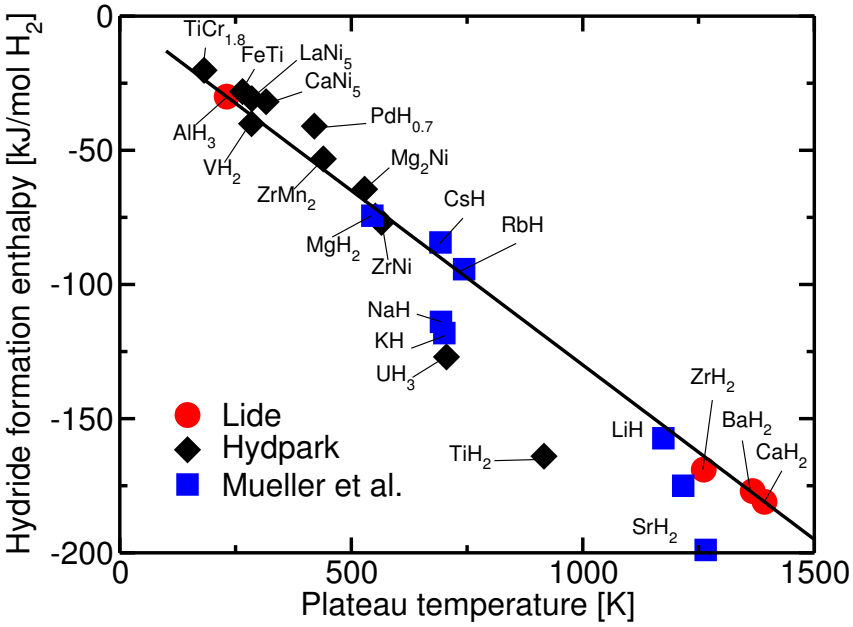

Figure 2.5: Hydride formation enthalpy, ΔH_f per mole H_2 as a function of the plateau temperature at 1 bar. The plateau temperature is calculated from reported thermodynamic parameters using the Van't Hoff equation. Data represented by circles is from ref. [59], data represented by squares is taken from ref. [60] and data represented by diamonds is taken from ref. [30, 29].

where $\Delta H^{\ominus}$ and $\Delta S^{\ominus}$ is the change in standard enthalpy and the change in standard entropy, respectively from now on denoted ΔH_f and ΔS_f. Eq. 2.9 is known as the Van't Hoff equation and it states that plateau pressure midpoints measured at different temperatures will lie on a straight line when plotted as $\ln(p_{H_2}/p^{\ominus})$ vs. reciprocal temperature with slope equal to ΔH_f and intercept ΔS_f cf. figure 2.4 (right). Hence, from a number of measurements of plateau pressures at different temperatures the Van't Hoff equation can by applied to determine ΔH_f and ΔS_f.

If ΔS_f is known *a priori* one single PCI is enough to determine ΔH_f. In fact, it turns out that it is possible to give a reasonable estimate of ΔS_f. In figure 2.5 the formation enthalpy of a number of different metal hydrides both binary and ternary compounds is plotted against the temperature required to give a plateau pressure of 1 bar H_2. Rearranging eq. 2.9 with $p_{H_2}/p^{\ominus} = 1$ gives

$$\Delta H_f = \Delta S_f T \tag{2.10}$$

Hence, if the entropy change upon hydrogenation is more or less the same regardless of the host metal a plot of the formation enthalpy vs. plateau temperature at 1 bar H_2 should lie on a straight line with slope ΔS_f . According to fig. 2.5 this is actually the case. The straight line depicted in the figure has slope $\Delta S_f = -130$ J/(mol K). The entropy loss of 130 J/(mol K) roughly corresponds to the loss of the translational degree of freedom when H_2 from the gas phase is absorbed in the metal.

As stated earlier the USDOE criterion regarding thermodynamics for a hydrogen storage material is desorption of hydrogen above 1 bar to be possible below 100 °C [61]. Eq. 2.10 can now be applied to reformulate this criterion in terms of ΔH_f. We find that in order for a metal hydride to meet the USDOE criterion ΔH_f should not be more exothermic than 48 kJ/mol.

2.3 Binary hydrides of the elements

2.3.1 Alkali metals

The alkali metals, group I of the periodic table of the elements, form hydrides with a high degree of ionic bonding character i.e. the electrons are localized around the atom nuclei, thus the bonding between hydrogen and metal is strong resulting in high decomposition temperatures. The alkaline metals are light elements (low density) which crystallizes in a body centered cubic (*bcc*) arrangement, however the density of the hydrides is even lower. This is partly due to the fact that the hydrides are arranged in a face centered cubic (*fcc*) lattice with a packing density of 0.74 compared to 0.68 for *bcc*. Due to their low melting points the hydrides of the alkali metals decompose into hydrogen and pure metal above the melting point of the metal. Selected properties of the alkali metal hydrides are compiled in table 2.1.

2.3.2 Alkaline earth metals

The alkaline earth metal hydrides ranges from BeH_2 which has a mostly covalent bonding character, due to a small difference in electronegativity between beryllium and hydrogen, to mainly ionic hydrides of CaH_2, SrH_2, and BaH_2 [62, 64, 65]. In between, is MgH_2 with a more complex bonding character. Generally the electronic density is located around the atoms with a net charge of Mg close to +2 and negatively charged H atoms with a charge of -0.94-(-0.26) [66, 67]. The remaining electron density is distributed evenly in the interstitial region [66], although recent experiments have revealed regions with increased electron density between Mg and H atoms clearly suggesting a partial covalent bonding character [67]. Both beryllium and magnesium crystallize in the hexagonal close packed (*hcp*) structure but transforms into a orthorhombic structure and a tetragonal structure, respectively, for the corresponding hydrides. Due to lower atomic packing density compared to the close packed hosts the density of the hydrides of Be and Mg are lower than the metals. Ca, Ba, and Sr all have *bcc* structures and Co_2Si orthorhombic structures for the corresponding hydrides [65, 64, 68, 69, 70]. The hydrides of the alkaline earth metals are insulators with band gaps in the range 3-6 eV for Be, Mg, and Ca [66, 65, 68]. The alkaline earth metal hydrides are quite stable and requires heating to elevated temperatures for decomposition into hydrogen and metal. Beryllium seems to deviate from the others with a remarkable low decomposition temperature which may rationalized in terms of a large cohesive energy of Be thereby reducing the stability of BeH_2. Selected properties of the alkali metal hydrides are compiled in table 2.2.

		Alkali metal hydride				
Property	Unit	LiH	NaH	KH	RbH	CsH
$\rho_m(H_2)$	wt.% H_2	12.7	4.2	2.5	1.2	0.8
$\rho(Me)$	g/cm^3	0.535	0.971	0.862	1.532	1.886
$\rho(MeH)$	g/cm^3	0.769	1.36	1.43	2.59	3.41
$T_{mp}(Me)$	°C	181	98	63	39	28
T_{dec}	°C	720	420	417	170	170

Table 2.1: Properties of the alkali metal hydrides. Data have been compiled from ref. [59, 62, 63].

		Alkaline earth metal hydride				
Property	Unit	BeH_2	MgH_2	CaH_2	SrH_2	BaH_2
$\rho_m(H_2)$	wt.% H_2	18.3	7.7	4.8	2.2	1.4
$\rho(Me)$	g/cm^3	1.85	1.74	1.54	2.64	3.62
$\rho(MeH)$	g/cm^3	0.65	1.45	1.7	3.26	4.18
$T_{mp}(Me)$	°C	1287	650	842	777	727
T_{dec}	°C	250	330	600	675	675

Table 2.2: Properties of the alkaline earth metal hydrides. Data have been compiled from ref. [59, 62, 63].

2.3.3 Transition metals

Compared to the hydrides of the main group I and II elements the transition metal hydrides have much more diverse physical properties. The hydrides formed by the early transition metals are generally very stable e.g. TiH_2 requires heating to above 450 °C for decomposition [59] and moving to right the hydrides become less stable. Around the middle of the of the transition metals (Mn, Fe) the stability goes through a local minimum. The late transition metals are unstable under ambient conditions [63, 64, 71, 72, 73, 74, 75, 76] e.g. CdH_2 decomposes at -20 °C [63]. In contrast to the group I and II metals most of the transition metals are excellent at dissociating hydrogen with the noble/late transition metals being an exception [72, 77, 78, 79, 80, 81, 82, 83, 84, 85]. Another major difference between transition metal hydrides and the hydrides of main group I and II is the fact that the bonding character in transition metals is metallic [64, 86, 87]. The ability to easily dissociate hydrogen has prompted many investigations of the effect on the kinetics of hydrogenation/dehydrogenation of Mg by addition of small amounts of transition metals see e.g. ref. [40, 88, 89, 90, 91, 92] for examples. Destabilization of MgH_2 by alloying with transition metals forming less less stable hydrides has also been the subject of many reported studies see e.g. [76, 93, 94, 95, 41, 96], although no magnesium based metal hydride which offers hydrogen desorption below 250 °C has been found.

2.4 Complex hydrides

From the previous section it is clear that hydrogen storage in binary metal hydrides of the alkali metal and alkaline earth metal hydrides does not succeed in fulfilling the hydrogen storage at temperatures near 100 °C. However, a way of taking advantage of their high hydrogen storage capacity in combination with potentially improved thermodynamics, is by combining them with e.g. Al into so-called complex hydrides.

Until recently complex hydrides such as $NaAlH_4$ and $LiAlH_4$, with a theoretical capacity of 7.3 and 10.6 wt. % H_2, respectively, have not been considered as potential hydrogen storage media due to their irreversible dehydrogenation and slow kinetics. However, this picture was changed in 1997 by the discovery of Ti-catalysed reversible hydrogen storage in $NaAlH_4$ by Bogdanović and Schwickardi [97]. Since then $NaAlH_4$ has received massive attention in order to improve the doping procedure including screening of other catalytic additives, maximizing the reversible capacity, and to get a comprehension of the catalyzing effect of Ti (see refs. [98, 99, 100, 101, 102, 103] and references therein). $LiAlH_4$ has not received the same attention as $NaAlH_4$ but several studies, both theoretical and experimental, have revealed important details about its thermal decomposition behaviour, thermodynamic stability, crystal structure,

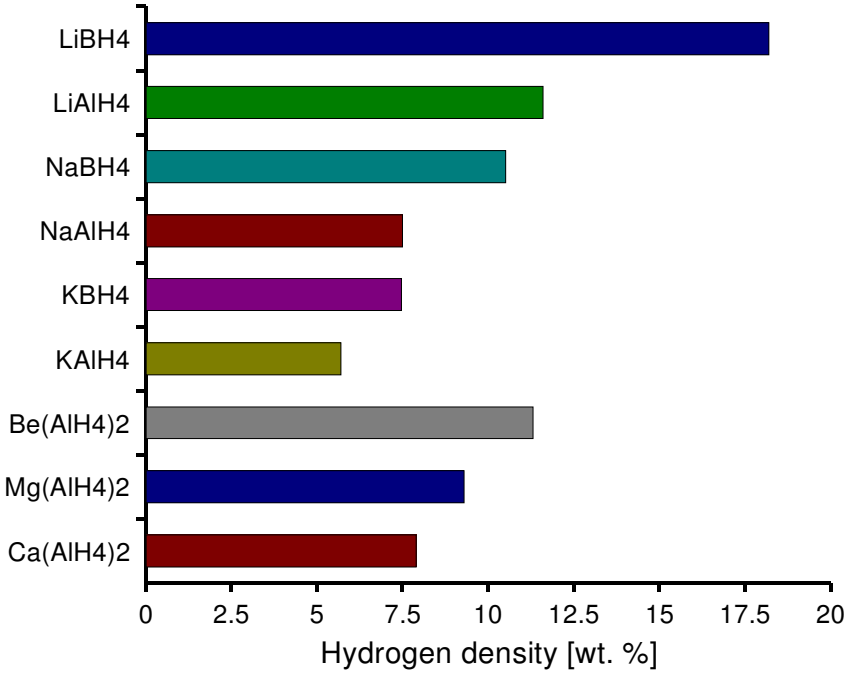

Figure 2.6: Theoretical hydrogen density of selected complex hydrides of the alkali and alkaline earth metals. The listed density assumes the release of all hydrogen i.e. only metal atoms are left after dehydrogenation.

and the effect of ball milling and catalytic doping on its decomposition behaviour. Furthermore, the thermodynamic stability of $LiAlH_4$ is lower that for $NaAlH_4$ in fact it has a potential of delivering hydrogen at 1 bar below 100 °C [104, 105, 106, 107, 108, 63, 109, 110, 111, 112, 113, 114, 115, 116, 62, 117, 118, 119, 120, 121, 122].

Figure 2.6 clearly illustrates the potential in gravimetric hydrogen density of various alkali and alkaline earth metal alanates ($MAlH_4$) and borohydrides (MBH_4). The thermal decomposition usually proceeds through a multi step process, which may be written in the following tentative form

$$MAlH_4 \rightarrow MH + Al + \frac{3}{2}H_2 \rightarrow M + \frac{1}{2}H_2 \tag{2.11}$$

If the stability of the intermediate binary hydride (MH) is high (which is the case for the alkali metal and alkaline earth metal hydrides) the theoretical hydrogen capacity is reduced due to requirements of high temperatures for a complete desorption of hydrogen. However, taking this into account $NaAlH_4$ and $LiAlH_4$ still has potential hydrogen storage densities of 5.5 and 7.9 wt.%, respectively.

In addition to the high hydrogen storage capacity the complex hydrides display a broad range of thermodynamic stabilities depending on the combination of metals making them suitable for a variety of applications. Generally, the borohydrides are more stable than the alanates and stability also increases though the series Li, Na, and K. As an example the thermodynamic properties of $NaAlH_4$ is presented in the form a Van't Hoff plot in figure 2.7. As seen from the figure the theoretical hydrogen capacity (exluding hydrogen bonded in NaH) is available at approx. 120 °C and reversible between 1-60 bar H_2. Althoug this temperature is too high for operation with a PEM fuel cell with a Nafion® membrane, this temperature can be met by improving the thermal stability of the PEM allowing to raise the operation temperature [123].

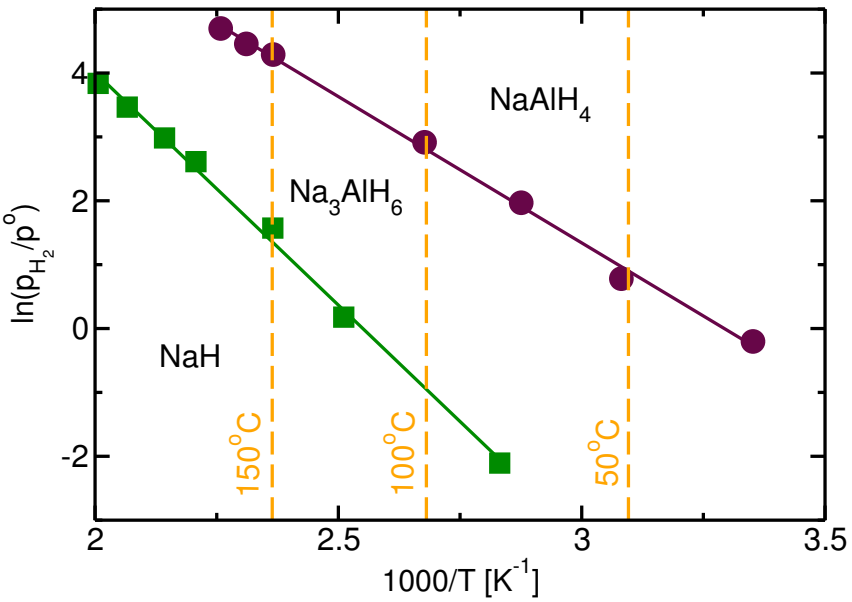

Figure 2.7: Van't Hoff plot for $NaAlH_4$. Data points have been extracted from ref. [124].

Chapter 3

Method of *in situ* X-ray powder diffraction

3.1 Basic X-ray diffraction theory

The purpose of this section is to give an introduction to X-ray diffraction theory. The level of detail in this section is by no means exhaustive, in fact just the basics are explained. For a more thorough description please refer to the relevant literature e.g. refs. [125, 126, 127].

3.1.1 Crystal structures

In order to describe the atomic arrangement in a given crystal lattice it is convenient to define a unit cell. The unit cell is the smallest unit still capable of reproducing the entire crystal purely by translation of the unit cell. Figure 3.1 illustrates the unit cell of a face centered cubic, *fcc*, solid.

A crystal contains different lattice planes where the atoms adopt different structures and with different separation distances. These planes are classified by using *Miller* indices, and these can by constructed from the unit cell cf. figure 3.2. A plane is assigned Miller indices from its reciprocal intersection with the three axes, a, b and c, of the unit cell given in multiplicity of the axis lengths and rounded up to integer values. Eg. if the plane intersects in $(1,\infty,\infty)$ corresponding to figure 3.2.A the Miller index becomes (1 0 0). Likewise intersection (1,2,2) corresponds to Miller indices (1 0.5 0.5) which corresponds to integer Miller indices (2 1 1). The three Miller indices are denoted h, k, and l. The distance between parallel lattice planes, denoted d, is a pivotal quantity in diffraction and it can be calculated from geometrical considerations.

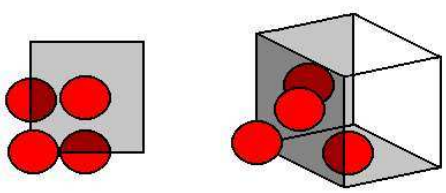

Figure 3.1: Unit cell of a *fcc* solid. The unit cell contains 4 atoms.

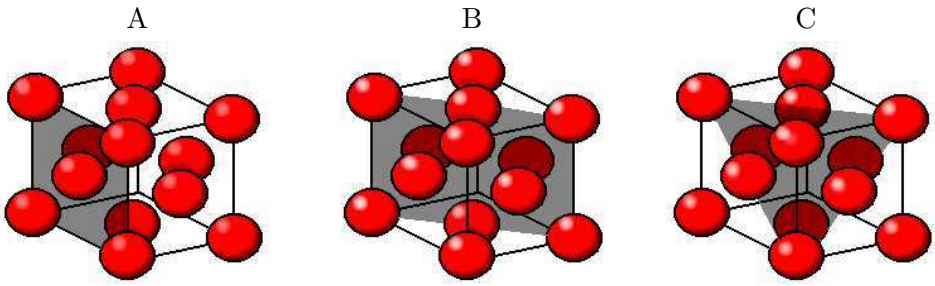

Figure 3.2: Low index lattice planes of a *fcc* solid.

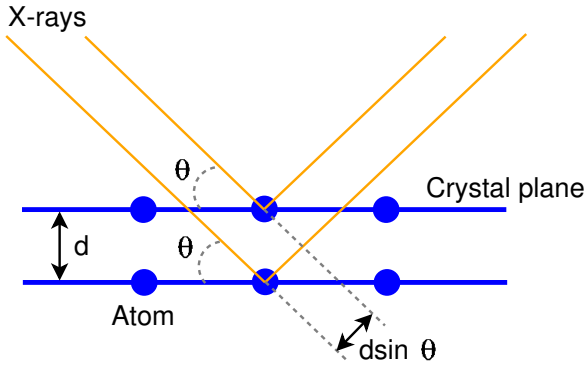

Figure 3.3: Illustration of diffraction of parallel X-rays with a wavelength of λ from atoms in a set of crystal planes separated by a distance of d. The diffraction angle is θ.

For a cubic crystal it can be calculated as

$$d = \frac{a}{\sqrt{h^2 + k^2 + l^2}} \tag{3.1}$$

where a is the lattice parameter (side length of the unit cell).

3.1.2 Diffraction from crystals

A simple way to conceive diffraction is to consider a lattice plane as a transparent mirror and modelling the crystal as an infinite stack of these reflecting lattice planes with an inter planar separation d. This model is shown in figure 3.3. The incoming X-rays are parallel and has a wavelength, λ, and the angle of incidence is θ. Constructive interference will occur *only* if the wave reflected from the lower plane travels a distance $2d \sin\theta$ longer than the wave reflected from the upper plane, where n is an integer number. This leads to the Bragg condition of diffraction

$$\lambda = 2d \sin\theta \tag{3.2}$$

The Bragg condition explains that if θ is varied and the intensity of the diffracted beam is recorded for each θ the recorded diffraction pattern will consist of sharp diffraction peaks when θ matches d according to Eq. 3.2.

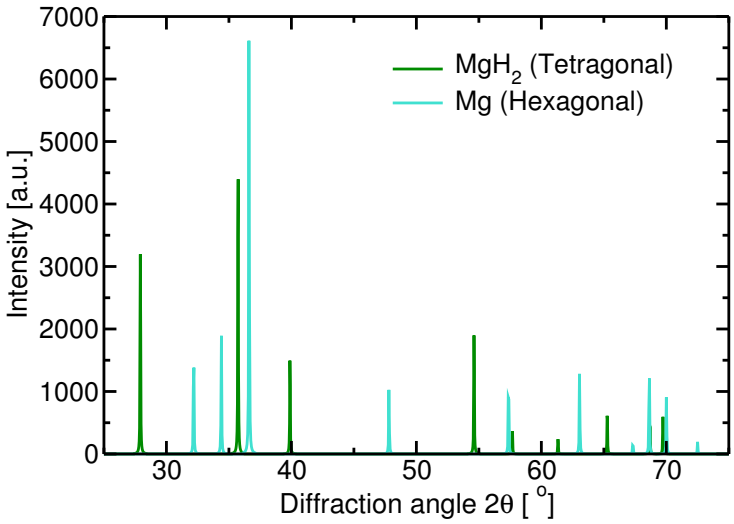

Figure 3.4: Calculated X-ray diffraction patters of Mg and MgH_2.

3.1.3 Intensity of the diffracted beam

While Bragg's law formulates the requirements for diffraction to occur i.e. the relationship between the diffraction angle and d, another important feature is the intensity of the diffracted beam. The intensity of the reflection hkl, I_{hkl} is related to the square amplitude of the structure factor F_{hkl} (ignoring polarization terms and multiplicity factors)

$$I_{hkl} \propto |F_{hkl}|^2 \tag{3.3}$$

The structure factor is given by the product of the atomic form factor, f_j, for atom j and the phase factor $\exp(i\delta_j)$ and summing over all atoms in the unit cell

$$F_{hkl} = \sum_j f_j \exp(i\delta_j) \tag{3.4}$$

where

$$\delta_j = 2\pi(hx + ky + lz) \tag{3.5}$$

with x, y, and z being the atomic coordinates of atom j.

The phase factor accounts for the fact that even when diffraction should occur according to the Bragg condition, a diffraction peak might be absent due to *systematic extinction*. The atomic form factor accounts for scattering from an atom surrounded by an electron cloud in which each electron absorbs and re-emits X-ray photons. For diffraction angles approaching 0 the atomic form factor becomes equal to the atomic number (equal to the number of electron) since scattering from all electrons are in phase. As the diffraction angle is increased the scattering intensity decrease due to partial destructive interference. The dependency of f on atomic number has a very important implication for the application to hydrogen storage materials; light atoms has a low scattering power i.e. it is very difficult to "see" hydrogen atoms with X-rays *ii)*. This makes it difficult to use X-ray diffraction to determine the hydrogen positions in the crystal lattice. However, a qualitative impression of the degree of hydrogenation is easily obtained when the crystal structure of the hydride is different from that of the host metal cf. figure 3.4 which shows calculated diffraction patterns of Mg and MgH_2. As seen from the figure it is easy to distinguish the metal from the hydride due to differences in crystal structure.

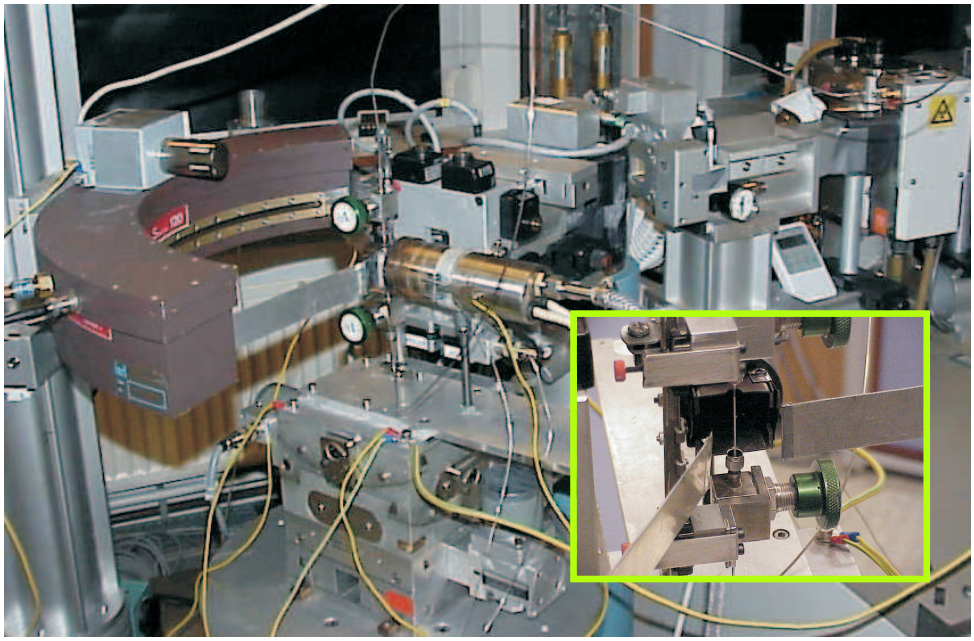

Figure 3.5: Experimental setup for the *in situ* time resolved XRPD investigations.

3.2 Experimental considerations and setup

In order to resolve dynamical structural changes in time, high quality data is required. In a usual XRPD experiment using a conventional laboratory diffractometer with an X-ray tube in so-called Bragg-Brentano geometry (reflection) the X-ray generator and the detector are moved simultaneously, whereby the diffraction angle 2θ is scanned. For each value of 2θ photons must be counted for some time, and a total time for the acquisition of a good quality powder pattern from say 0-120 ° of several hours is not unusual. The acquisition time, and hence the time resolution, can be reduced by increasing the intensity of the X-ray source and by more effective detection. By using a rotating anode X-ray source the X-ray intensity can be increased by a factor of, say 10, due to more effective cooling of the target. Furthermore, by using a Debye-Scherrer geometry (transmission) the sample can be placed in a capillary tube allowing a gas flow through the sample. In addition a curved position sensitive detector is used covering 120 ° in 2θ for improved time resolution.

The experimental setup used for *in situ* X-ray powder diffraction studies is shown in figure 3.5. The setup is built around a Rigaku rotating anode X-ray generator, as shown in the upper right corner of figure 3.5, in the Risø X-ray Basement. The generated X-ray radiation is conditioned by a monochromator and various slits before hitting the sample. The sample is placed in a vertically mounted 0.7 mm O.D. quartz glass capillary tube. The sample holder is shown in the middle of figure 3.5 and the small inset picture shows a close-up of the sample holder. The glass capillary is connected to stainless steel gas lines with Swagelok 1/16“ stainless steel fittings and carbon ferrules fitted to the capillary tube. The gas lines are connected to gas system whereby the gas environment including type of gas, gas flow and pressure can be controlled. Typically the sample is flushed with 10-20 ml/min Argon at atmospheric pressure. The temperature of the sample is controlled with an oven in which a stream of nitrogen gas is heated by a heating block, the stream of hot nitrogen gas heats the sample capillary. The INEL CPS-120 curved position sensitive detector is shown to the left in figure 3.5. The detector has 4096 channels covering 120 ° in 2θ resulting in a resolution of 0.03 °.

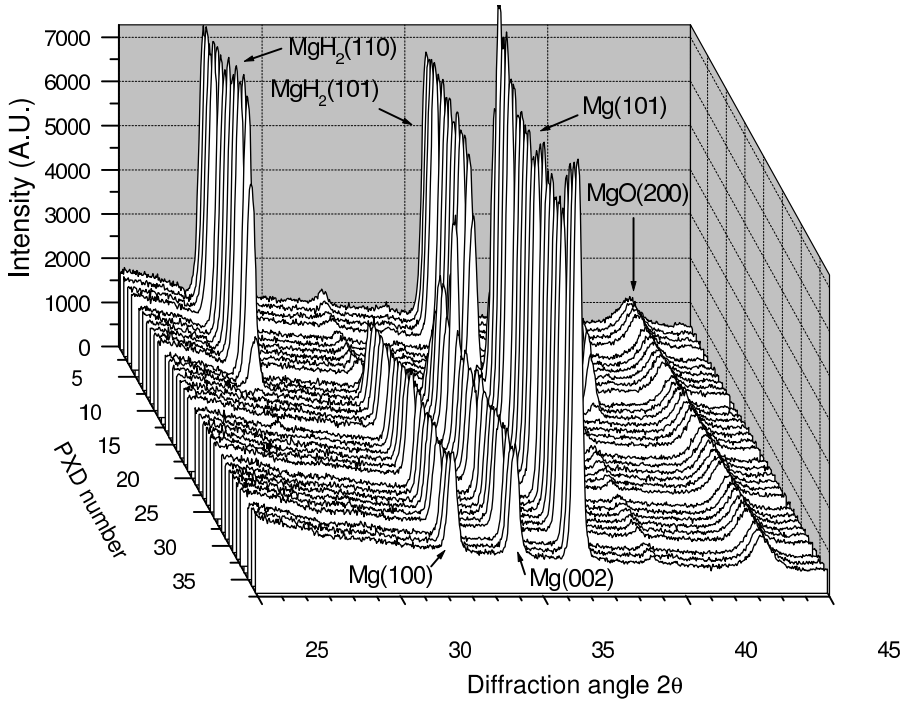

Figure 3.6: Time resolved *in situ* XRPD of hydrogenated magnesium doped with 2 wt. % nickel constituted of 40 consecutive diffraction patterns. The isothermal reaction temperature is T=390 °C and scan time t=170 s.

3.3 Time resolved structural changes from XRPD

The decomposition of air-exposed nickel doped (2. wt%) magnesium hydride is illustrated in figure 3.6 which shows 40 consecutive diffraction patterns. The showed stack of patterns were originally complete scans 2θ=0-120 ° but for clarity only the region from 2θ=25-45 ° is depicted. The recording time for each pattern were 170 s. The disappearance of the MgH_2(1 1 0) and (1 0 1) peaks around pattern no. 15 and the corresponding appearance of the Mg(1 0 0) and Mg(0 0 2) peaks clearly shows a transformation of the magnesium hydride phase into magnesium.

3.4 Quantitative analysis of XRPD data

A number of consecutive diffraction patterns recorded at a temperature of 370 °C during the decomposition of a sample of nickel doped MgH_2 have been analyzed with the Rietveld method (in which the complete diffraction pattern is simulated) in order to quantitatively determine the phase fractions of Mg, MgH_2 and MgO, respectively. The result of the refinement is shown in figure 3.7. For more detailed information about the Rietveld method see ref. [128, 129]. The Rietveld refinements presented here were performed with WINPOW[1].

The phase fractions of Mg and MgH_2 determined by Rietveld refinement have been compared with phase fractions determined by numerical integration of selected peaks form each phase. The (1 1 0) peak of MgH_2 and the (1 0 0) and (0 0 2) peaks of Mg have been numerically integrated.

[1]The WINPOW software can be downloaded from:
`http://struktur.kemi.dtu.dk/kenny/powprog.html`, The space group is fixed during refinement, but the unit cell parameters are allowed to vary. Diffraction peaks are modeled by Pseudo-Voigt profile functions, describing both Gaussian and Lorentzian nature in the peak. The background is fitted by a shifted Chebyshev polynomial with 15 coefficients.

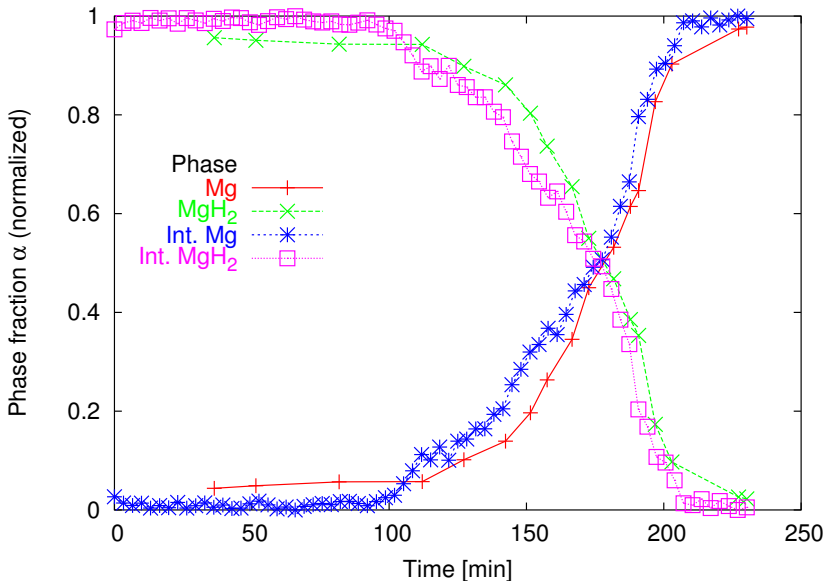

Figure 3.7: Normalized phase fractions of Mg and MgH_2. Comparison between phase fractions determined by Rietveld refinement and integrated intensities of selected peaks (denoted Int.), respectively.

MgO have been excluded from this analysis since the change in phase fraction is only moderate, and it has chosen to view this as an inert not participating in the reaction. The phase fraction of MgH_2 is calculated by the following equation

$$\alpha_{MgH_2}(t_i) = \frac{I_i - I_{bg}}{I_{max} - I_{bg}} \tag{3.6}$$

I_i is the integrated intensity of the (1 1 0) peak in diffraction pattern number i corresponding to time, t_i, in a series of diffraction patterns. I_{bg} is the observed intensity of background. I_{max} is the maximum observed intensity of the (1 1 0) peak. It is assumed that the sample is completely hydrogenated. The phase fraction of Mg is calculated in a similar manner as outlined in eq. 3.6. The phase fractions are normalized to make sure that they ad up to 1. From figure 3.7 it is evident that the more simple approach of peak integration yields results that compares very well to results obtained from Rietveld refinement (normalized phase fractions of Mg and MgH_2). However due to eq. 3.6 the phase fractions from peak integration are forced to show full hydrogenation and full dehydrogenation even though this is not necessary so.

3.5 Kinetics from time resolved *in situ* data

Dehydrogenation curves i.e. phase fraction of MgH_2 vs. time have been constructed by the above described method of integrated intensities. The results are shown in figures 3.8. All dehydrogenation curves show a sigmoidal shape like the dehydrogenation curve in figure 3.7. It is also evident that there is a trend showing faster dehydrogenation with higher temperatures as one would expect for a thermally activated process. A JMA type rate equation has been fitted to the dehydrogenation curves in figure 3.8. In order to describe decomposition instead of formation Eq. 2.5 is rearranged

$$\alpha(t) = \exp\left(-(kt)^n\right) \tag{3.7}$$

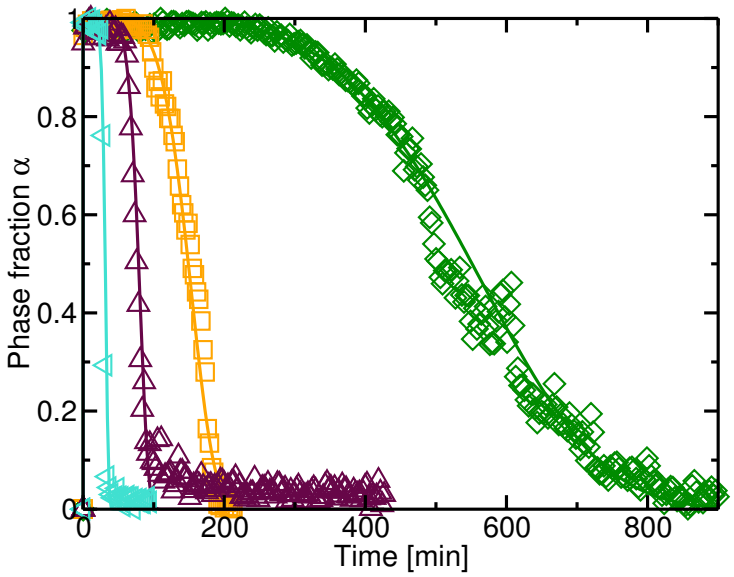

Figure 3.8: Experimental and theoretical dehydrogenation curves for nickel doped MgH_2. Experimental curves are determined by integrated intensity of the $MgH_2(110)$ peak and the theoretical curve is a JMA fit.

	Pure MgH_2		
Sample	T [°C]	k [s^{-1}]	n
1	360	3.93e-5	2.26
2	380	1.53e-4	6.99
3	390	4.53e-4	3.29
4	400	1.13e-3	4.41
E_A/R		36	

Table 3.1: Kinetic parameters obtained from fitting the JMA expression $\alpha(t) = \exp(-(kt)^n)$ to the dehydrogenation curves of pure air-exposed MgH_2.

The values of n and k determined by fitting the experimental data with equation 3.7 are presented in table 3.1.

Assuming an Arrhenius expression for the rate constant cf. eq. 2.6 the apparent activation energy can be extracted by plotting $\ln k$ vs. $1/T$ and E_A/R is found as the slope. The slope of the Arrhenius plot is also listed in table 3.1. This value correspond to an apparent activation energy of 298 kJ/mol for the dehydrogenation of pure MgH_2.

3.6 Selected results on magnesium based hydrides

Time resolved *in situ* XRPD has been used to study the dehydrogenation kinetics of various Mg-based hydrides: MgH_2, MgH_2 with 2 wt.% Ni, MgH_2 + Al (synthesized by hydrogenation of an Mg-Al alloy), MgH_2 + Mg_2Cu, and MgH_2 + $MgCu_2$ (synthesized by hydrogenation of an eutectic Mg-Cu alloy). The detailed studies of these hydrides are presented in Papers 2, 3, and 4. Here a brief exposition is given of some of the results.

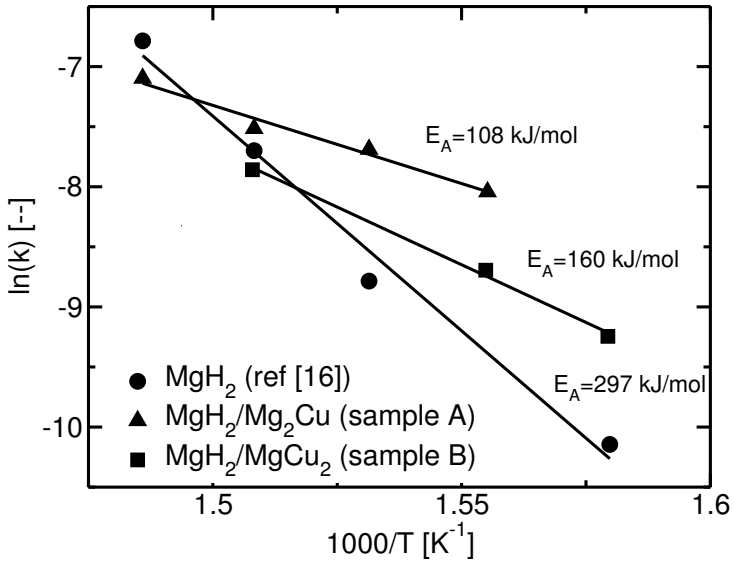

Figure 3.9: Arrhenius plot of the logarithmic rate constant (derived from the dehydrogenation data from time resolved *in situ* XRPD) vs. reciprocal temperature for the dehydrogenation of MgH_2 (from ref. [130]) MgH_2+Mg_2Cu and MgH_2+$MgCu_2$.

3.6.1 Determination of apparent activation energies

Using the methodology described in this chapter the dehydrogenation kinetics of air exposed samples of MgH_2 + Mg_2Cu, and MgH_2 + $MgCu_2$ have been investigated. Series of time resolved diffraction patterns have been acquired at different temperatures and subject to quantitative analysis. By fitting a JMA model rate constants are extracted for each temperature and the apparent activation energy is found from an Arrhenius analysis. The apparent activation energy for dehydrogenation of air-exposed MgH_2/Mg_2Cu (sample A) is found to be 108±12 kJ/mol, and for air exposed $MgH_2/MgCu_2$ we find 160±11 kJ/mol. For comparison results for dehydrogenation of pure air-exposed Mg is included in Fig. 3.9. An Arrhenius analysis reveals an apparent activation energy of 297±26 kJ/mol. These results clearly indicate that the presence of either Mg_2Cu or $MgCu_2$ in MgH_2 has a pronounced positive effect on the dehydrogenation kinetics of air-exposed samples. A similar effect is found for MgH_2 + Al.

We note that *(i)*: the apparent activation energy found for dehydrogenation of air-exposed MgH_2 [130] is significantly higher than the value of 120-160 kJ/mol often cited [44, 43, 131, 132, 133] *(ii)*: the apparent activation energy found for dehydrogenation of MgH_2 in MgH_2/Mg_2Cu (sample A) is in agreement with the value found by Karty [41] and *(iii)*: to the best of our knowledge apparent activation energies for the dehydrogenation of $MgH_2/MgCu_2$ (sample B) have not previously been reported. A more detailed discussion of the effect of air exposure on the kinetics of hydrogenation/dehydrogenation of Mg/MgH_2 is given in chapter 4.

3.6.2 Structural details of MgH_2 + Al dehydrogenation

The isothermal dehydrogenation kinetics of MgH_2 + Al (formed by hydrogenation of Mg-Al with approximate stoichiometric ratio of 50:50) has been studied at different temperatures applying *in situ* X-ray powder diffraction (XRPD). A typical result of such *in situ* XRPD studies is shown in figure 3.10.

From the diffraction pattern at $t = 0$ s it is observed that the host alloy has apparently undergone complete disproportionation during hydrogenation. Thus only diffraction peaks cor-

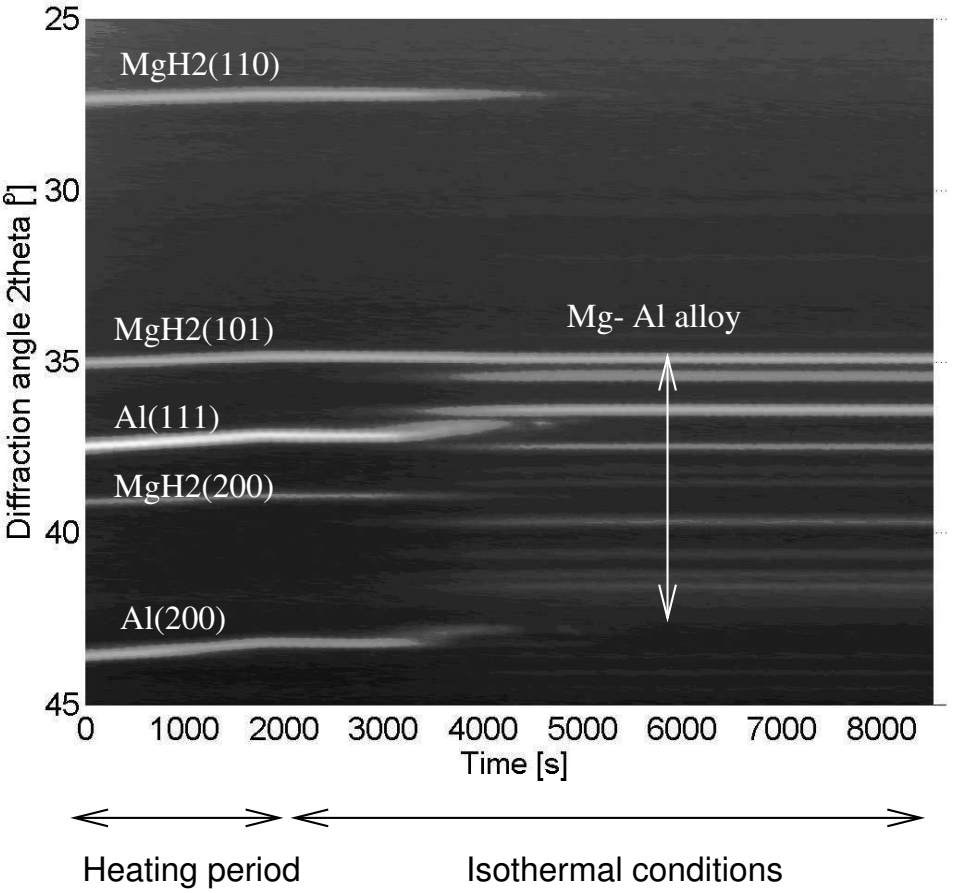

Figure 3.10: Series of consecutive *in situ* XRPD patterns stacked chronologically from left to right. High intensity corresponds to bright areas and low intensity correspond to dark areas. Figure is from ref. [134]. Isothermal temperature is 400 °C. See ref. [134] for experimental details etc.

responding to MgH_2 and Al are present. The dehydrogenation of MgH_2 + Al is visualized by the concurrent decrease in intensity of the MgH_2 and the Al peaks and the simultaneous occurrence of diffraction peaks corresponding to those of an Mg-Al alloy.

Diffraction peaks corresponding to pure Mg are not observed at any time during dehydrogenation. This strongly suggest that the dehydrogenation of MgH_2 as outlined below

$$MgH_2 \rightarrow Mg + H_2 \tag{3.8}$$

is slow compared to the subsequent removal of pure Mg, due to the formation of an Mg-Al alloy. From figure 3.10 it is evident that at least two types of Mg-Al phases are present during dehydrogenation. First, the formation of a β-phase Mg-Al alloy which remains throughout the dehydrogenation as visualized by the series of diffraction peaks in the range $2\theta = 35 - 45\,^{\circ}$. Second, the down shift in the diffraction angle of the Al peaks at $t = 3000 - 5000$ s, concurrent with the creation of the Mg-Al alloy, clearly suggests that a solid solution of Mg in Al is formed during dehydrogenation [135, 136]. The down shift in diffraction angle is caused by the lattice expansion due to replacement of Al atoms with larger Mg atoms. In contrast to the formed Mg-Al alloy, the solid solution phase is of intermediate nature, and only exists until MgH_2 has been completely dehydrogenated. Based on the above observations two additional reaction steps

α_{MgH_2}	$2\theta_{Al}$	a [Å]	$2\theta_{Al(Mg)}$	a [Å]	$I_{Al(Mg)}$ $/I_{Al}$
1.00	38.14	4.087	37.92	4.110	0.04
0.89	38.15	4.086	37.88	4.114	0.18
0.81	38.12	4.089	37.84	4.118	0.27
0.73	38.07	4.094	37.79	4.123	0.24

Table 3.2: Fitting parameters from the gaussian fits to the Al(1 1 1) reflection at different degrees of dehydrogenation. Included are also calculated lattice parameters. Corresponding diffraction peaks are shown in figure 3.11.

can be proposed

$$\mathrm{Mg} + \mathrm{Al} \rightarrow \mathrm{Al(Mg)} \tag{3.9}$$

$$\mathrm{Mg} + \mathrm{Al(Mg)} \rightarrow \mathrm{Mg_2Al_3}\ (\beta - \mathrm{phase}) \tag{3.10}$$

assuming that the Mg-Al alloy nucleates and grows from the solid solution, only, and not from pure Al. However, from figure 3.10 it is very difficult to distinguish if the initial alloy formation actually proceeds from the pure metals or from a solid solution with a low concentration of Mg.

In order to get a more detailed view of the initial formation of a solid solution from Al the Al(1 1 1) reflection is plotted for different degrees of dehydrogenation (phase fraction, α of MgH_2) in figure 3.11. In order to get a rough estimate, the Al(1 1 1) reflection is fitted with two gaussians. It is seen from 3.11 that even before dehydrogenation the Al(1 1 1) can be explained by a minor phase corresponding to a solid solution and a major phase corresponding to pure Al (or at least a lower concentration of Mg as compared with the minor phase). This suggests that some Mg is not hydrogenated which also, at least partially, explains the incomplete hydrogenation of Mg-Al alloys reported in the literature [137, 88, 134]. Table 3.2 summarizes the fitting parameters and it is noticed that during dehydrogenation the amount of solid solution compared to Al increases to a more or less constant level during the depletion of pure Al corresponding to phase fractions of MgH_2 from 1-0.73. From the peak positions shown in table 3.2, the concentration of Mg in the solid solution increases as evident from the down shift in 2θ while the position of the Al peak is more or less constant until a phase fraction <0.81 has been reached. From then also the pure Al phase is populated with Mg as evident from the continuous down shift in 2θ shown in both figure 3.10 and figure 3.12. Using the calculated lattice parameters from table 3.2 and the relation between Al lattice parameter and magnesium content given in ref. [135] it can be estimated that the Al phase prior to dehydrogenation contains approx. 5 at.% Mg. When the dehydrogenation has started including the formation β-phase, the concentration of Mg in Al(Mg) is approx. 7 at.%, which is quite interesting since the Mg-Al phase diagram suggests that formation of β-phase first takes place when the Mg concentration exceeds approx. 13 at.% [135]. This indicates that the formation of β-phase is somewhat inhomogenous and localized.

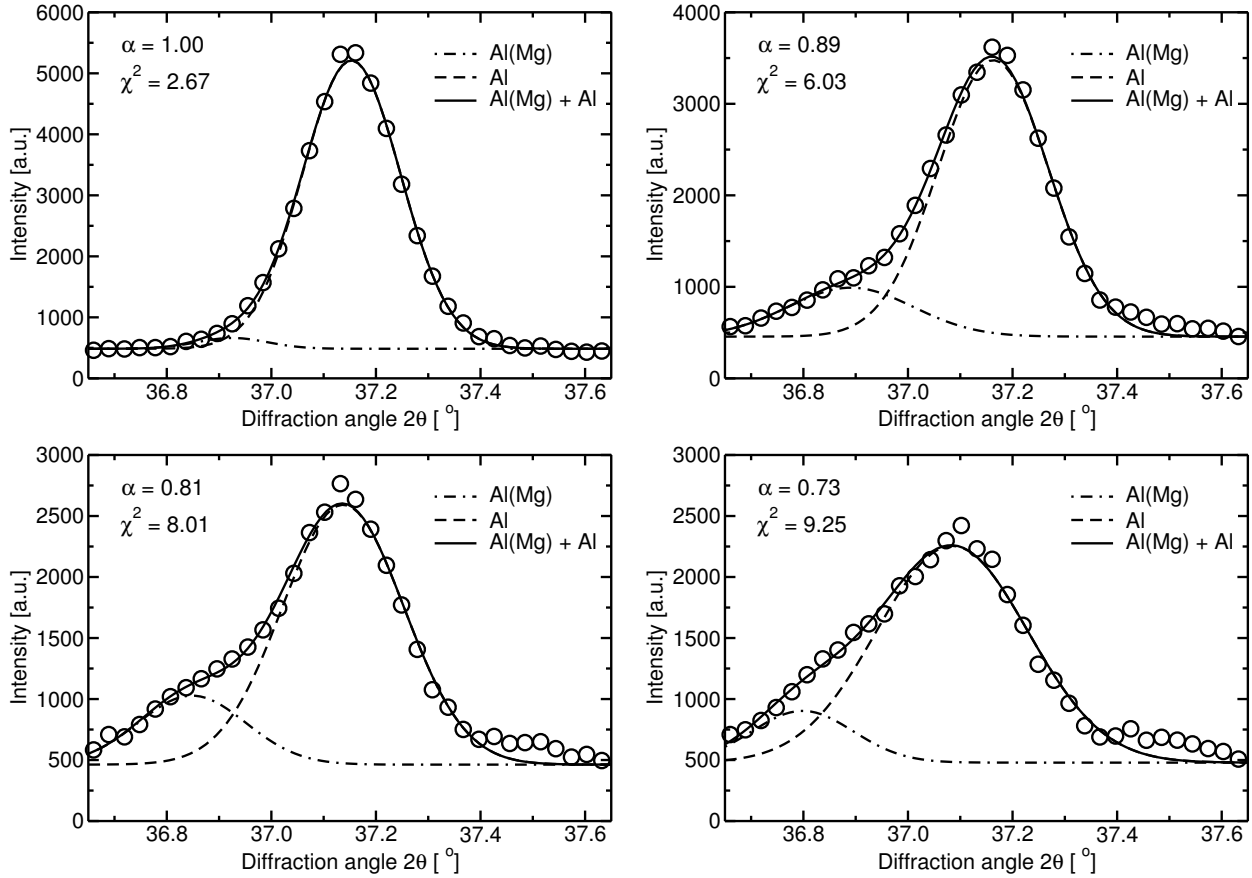

Figure 3.11: Decomposition of the Al(1 1 1) reflection corresponding to different phase fractions of MgH_2 into pure Al and a solid solution of Mg in Al. Isothermal temperature is 400 °C. See ref. [134] for experimental details etc.

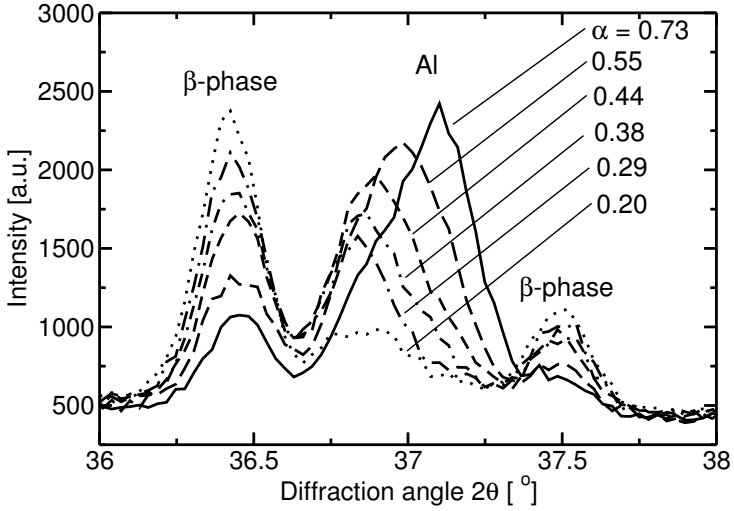

Figure 3.12: Corresponding diffraction peaks of the (1 1 1) reflection of the solid solution, reflections of β-phase, and phase fractions of MgH_2. Isothermal temperature is 400 °C. See ref. [134] for experimental details etc.

Chapter 4

The Compensation effect in metal hydrides

4.1 Background and motivation

The kinetics of metal hydrides have been investigated extensively in order to map the reaction mechanisms of hydrogen absorption and desorption, respectively, and to identify possible rate limiting steps to ultimately make steps towards improving the kinetics. Interestingly, obtained kinetic data are scattered extensively, even for similar systems. Thus reported apparent activation energies are often scattered and discrepancy among which steps are suggested as controlling the overall rate is often encountered [33, 132, 138].

In some reaction systems, it has been observed that the apparent activation energy varies under different measuring conditions. It is also found that the variation in apparent activation energy is accompanied by a change in A_{app}, i.e., a large apparent activation energy is accompanied by a large prefactor and vice versa [139, 140]; a phenomenon often referred to as the compensation effect (CE).

In some cases, the changes in prefactor and apparent activation enthalpy display a linear dependency according to the Cremer-Constable relation.[140]

$$\ln A_{app} = aE_A^{app} + b \tag{4.1}$$

The relation implies that values of the natural logarithm of the prefactor plotted against the apparent activation energy (denoted a Constable plot), fall on a straight line with slope a and intercept b.

Although the compensation effect has been known and studied for almost 100 years and been observed in a variety of different scientific fields, including electron emission [141], heterogeneous catalysis [142, 139, 143, 144, 140, 145, 146, 147], homogeneous catalysis [148], Temperature Programmed Desorption [149, 150], and diffusion [151, 152] , no consensus on the nature of CE has been reached. However, a number of different explanations for observed compensation effects have been suggested (most of them applicable to heterogeneous catalysis): *i)* Oversimplified data analysis [153, 154]. *ii)* Heterogeneity in activity and distribution of active sites [147]. *iii)* A correlation between applied reactant pressures and measured apparent activation energy due to coverage dependent terms [146, 140, 143, 144] *iv)* A change in anharmonicity in the adsorbate-surface bond changes the activation enthalpy of dissociation [155]. *v)* The enthalpy-entropy relationship [140, 139]. *vi)* The heat bath concept [156]. *vii)* The Brønsted-Evans-Polanyi relation [145].

The findings of large variations (approx. 200 kJ/mol) in the apparent activation energy for dehydrogenation of Mg-based hydrides [134, 157, 130] as shown in the previous chapter, has

Host	Method	$\ln(A_{app})$	E_a^{app} [kJ/mol]	Comment	Temp [K]	P [bar]	Sample	Ref.
Mg-Al	XRPD	20.65	160	d	643-673	$0^{\dagger}$	A	[134]
$Mg/MgCu_2$	XRPD	21.11	160	d	633-663	$0^{\dagger}$	B	[157]
Mg/Mg_2Cu	XRPD	17.40	137	d	643-673	$0^{\dagger}$	C	[157]
Mg	XRPD	46.04	296	d	633-673	$0^{\dagger}$	D	[130]
Mg(Ni)	XRPD	37.45	249	d	623-663	$0^{\dagger}$	E	[130]
Mg	TG	19.22	119	d	608-641	3.84	F	[44]
Mg	Sievert	23.67	167	d	613-643	0.25-6	G	[43]
Mg	TG	36.44	230	d	635-663	1.5	H	[158]
Mg(foil)	TG	49.23	284	h	650-700	10-30	I	[159]
Mg(foil)	TG	53.37	308	h	650-700	10-30	J	[159]
Mg(Ni)	PCI	9.53	66	h	543-616	1-13	K	[40]
Mg	Sievert	10.40	91	h	614-648	5-21	L	[43]

Table 4.1: Corresponding values of apparent prefactors and apparent activation energies for hydrogenation(h)/dehydrogenation(d) of magnesium based hydrides. If not otherwise stated the samples are on powder form. Mg(Ni): Nickel doped magnesium. TG: Thermogravimetry, PCI: Pressure-Composition-Isotherm apparatus, XRPD: Parameters determined from quantitative analysis of in-situ time resolved X-ray powder diffraction. †: Dehydrogenation in an Argon flow 10 ml/min with a pressure of 1 bar. The background pressure of hydrogen was not measured.

prompted an investigation of the possible existence of a compensation effect in metal hydride systems.

4.2 CE and metal hydrides

In order to investigate the potential existence of a CE in metal-hydrogen systems, the literature on kinetic studies for two of the most investigated systems, viz., Mg and $LaNi_5$ based hydrides is reviewed [29].

4.2.1 Mg-based hydrides

Corresponding values of $\ln(A_{app})$ and E_A^{app} along with information about the experimental method and reaction conditions (T,P) are presented in table 4.1. The values of A_{app} and E_A^{app} in table 4.1 are obtained by fitting the following equation

$$\ln(k) = \ln(A) - \frac{E_A}{RT} \tag{4.2}$$

to reported Arrhenius plots viz. $\ln(k)$ vs. $1/T$ data from the references also given in the table. In a single case (ref. [158]) no Arrhenius plot was reported, only raw kinetic data, i.e., reacted fraction vs. time. In order to extract the desired data, a JMA kinetic expression was fitted to the raw kinetic data. A_{app} and E_A^{app} were determined by an Arrhenius analysis of fitted values of k vs. $1/T$. This method of data analysis is analogous to the applied analysis in the previous chapter and in ref. [134, 157, 130]. Minor variations in the kinetic expressions used in the extraction of rate constants in the other references in table 4.1 is possible. However, it is generally found that the temperature dependence of the extracted rate constants is rather insensitive to the choice of kinetic expressions [130, 44, 41]. This allows for comparison of reported values of A_{app} and E_A^{app} between all the reported data, although the kinetic analysis may differ slightly.

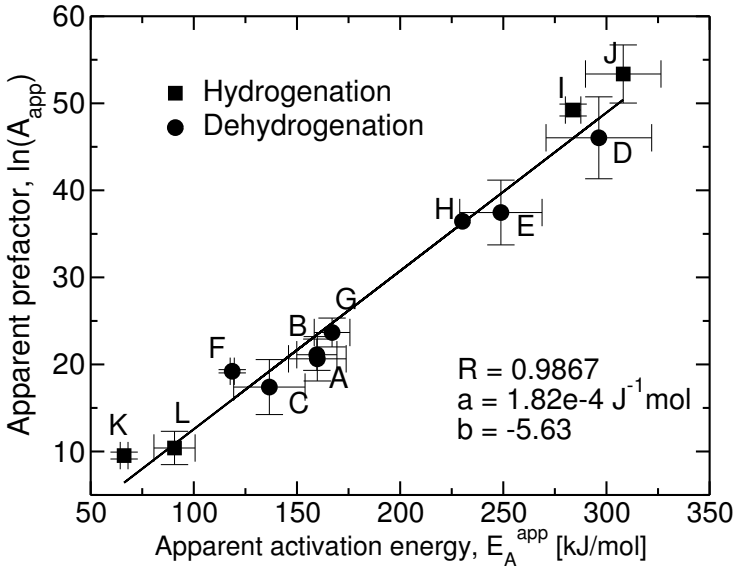

Figure 4.1: Constable plot of reported values of A_{app} vs. E_A^{app} from table 4.1 for magnesium based hydrides. Data points are assigned sample letters.

A Constable plot of the values of A_{app} and E_A^{app} in table 4.1 has been constructed in figure 4.1. It is clearly observed from the figure that the apparent prefactor is linearly correlated with the apparent activation energy, having a correlation coefficient of $R \approx 0.99$. Thus, in the case of hydrogenation/dehydrogenation of magnesium based hydrides a clear compensation effect according to the Cremer-Constable relation (eq. 4.1) is observed. From figure 4.1 and table 4.1 it also seen that the apparent activation energy cover a range of 66-308 kJ/mol for hydrogenation and 118-296 kJ/mol for dehydrogenation, respectively. The corresponding range in apparent prefactors is 18 orders of magnitude for hydrogenation and 11 orders of magnitude for dehydrogenation, respectively. Error bars for both apparent activation energies and apparent prefactors are based on standard deviations of fitted parameters from linear regression analysis. The error bars clearly indicate that observed scatter in apparent activation energies and apparent prefactors is *real* and not due to experimental uncertainties. A physical explanation for the possible existence of two - or more - kinetic regimes is therefore warranted, at least in the case of apparent activation energies.

4.2.2 $LaNi_5$ Hydrides

To investigate the possible existence of a compensation effect in other metal hydride systems, a number of reported kinetic studies on $LaNi_5$ based hydrides from the literature has been reviwed. This particular hydride was chosen, since it is not prone to oxide formation, and ample kinetic data is available.

Corresponding values of $\ln(A_{app})$ and E_A^{app} along with information about reaction temperature and the origin of the data are presented in table 4.2. As for the Mg-based samples the values of $\ln(A_{app})$ and E_A^{app} are obtained by fitting eq. 4.2 to reported values of $\ln(k)$ vs. $1/T$. In a single case (sample S) the values have been obtained by first fitting eq. 2.5 to raw kinetic data, extracting k at different temperatures, and thus finally performing an Arrhenius analysis.

Host	$\ln(A_{app})$	E_a^{app}	T	Sample	Ref.
$LaNi_5$	11.87	32	271-360	M	[160]
$LaNi_5$	9.35	33	289-352	N	[161]
$LaNi_5$	3.79	19	294-333	O	[138]
$LaNi_5$	17.37	53	267-333	P	[162]
$LaNi_xAl_y$	5.31	24	246-281	Q	[163]
$LaNi_5$	10.79	37	245-293	R	[164]
$LaNi_5$	11.26	38	245-293	S	[165]

Table 4.2: Corresponding values of apparent prefactors and apparent activation energies for hydrogenation of $LaNi_5$ based hydrides. For sample Q: $x = 4.75$ and $y = 0.25$. Sample P is for dehydrogenation. E_A^{app} is in kJ/mol and T is in Kelvin.

The data of $\ln(A_{app})$ and E_A^{app} is used to construct a Constable plot as shown in figure 4.2. Again, we observe a compensation effect in the reported data according to the Cremer-Constable relation. However, it is also noticed that the apparent activation energies for $LaNi_5$ span a much smaller interval (19-38 kJ/mol for hydrogenation) and cover only 3 orders of magnitude in apparent prefactor. Even with the uncertainty on the derived values of E_A^{app}, the compensation effect is found to be statistically significant.

4.3 Explanation of variations in apparent activation energy

4.3.1 Effect of activation of hydride particles

In order to explain the variation in apparent activation energies attention is directed to the pretreatment of the samples, also termed the *activation procedure*. The samples from table 4.1 are ordered as *activated* and *non-activated* samples in figure 4.3. The term *non-activated* imply that the kinetics are measured for the 1. hydrogenation or 1. dehydrogenation cycle. The term *activated* imply that the sample is hydrogenated/dehydrogenated for at least one and possibly several cycles prior to kinetic measurements. The activation process covers different phenomena and includes penetration of the natural oxide layer on as-prepared samples (if previously exposed to air), followed by complete hydride formation, which leads to cracking of the particles, due to the expansion associated with the hydrogenation process combined with the brittle nature of most metal hydrides [76, 33]. During the first hydrogenation/dehydrogenation cycles, the reaction rate increases due to the creation of fresh contamination-free surface and/or smaller particles (higher surface area and shorter diffusion paths) until a steady-state is reached. A potential physical explanation for the observed variations in $\ln A_{app}$ and E_A^{app}, are therefore likely to depend on sample treatment and cleanliness.

For the non-alloyed Mg samples (D-L) in figure 4.3 a trend of higher apparent activation energy for the *non-activated* samples than the *activated* samples for both hydrogenation and dehydrogenation is observed. The high apparent activation energy of the non-activated samples may be accounted for by the presence of an oxide shell/layer surrounding the bulk magnesium particles. For sample D and E the presence of MgO was confirmed by X-ray powder diffraction and Energy Dispersive X-ray Spectroscopy (EDX) [130]. Likewise, for the samples I and J, the production method and sample handling makes formation of a surface oxide with low defect density highly probable [166].

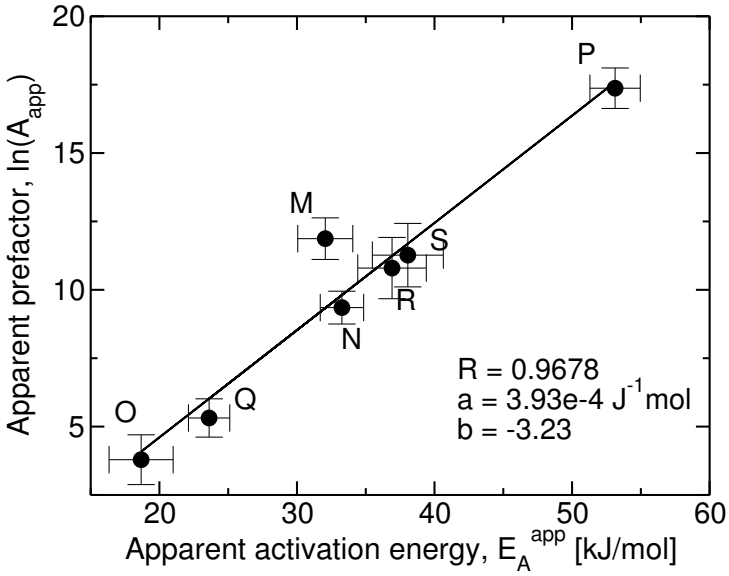

Figure 4.2: Constable plot of reported values of A_{app} vs. E_A^{app} from table 4.2 for $LaNi_5$ based hydrides. Data points are assigned sample letters.

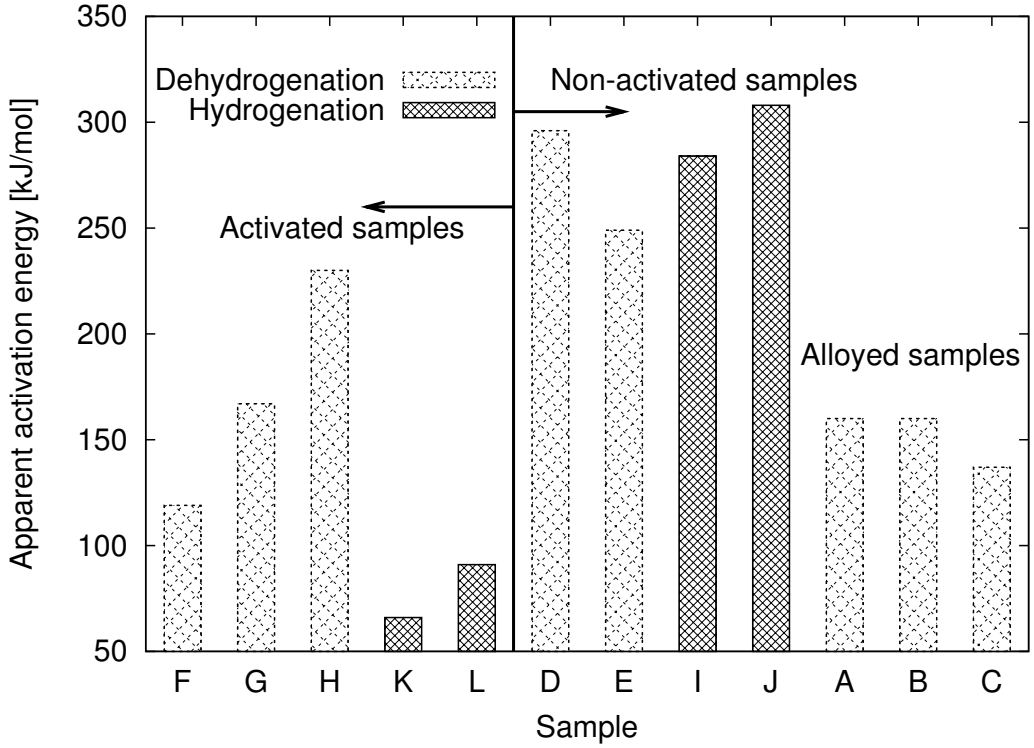

Figure 4.3: Apparent activation energy, E_A^{app}, from table 4.1 for magnesium based hydrides. Data points are assigned sample letters and grouped after pre-treatment procedure.

4.3.2 Influence of surface oxide on kinetics

The oxidation behavior of Mg is well investigated. A 1-2 nm thick oxide layer builds up within minutes when Mg is exposed to air. This MgO layer reaches approx. 3 nm after 2 hours and continues to grow slowly and the oxide thickness reaches approx. 4-5 nm within 10 months [167, 168, 166, 169, 170]. Both temperature and moisture can increase the speed of oxide growth [166].

It is known that hydrogen diffusion in the close packed MgO is extremely slow [171] and strongly thermally activated, when compared to diffusion of hydrogen in Mg [172] and MgH_2[173]. In fact Hjort *et al.* [174] have shown that the rate of hydrogen uptake at room temperature in Pd-coated Mg films decreased 2 orders of magnitude when exposed to oxygen. Further, exposing the sample to air at ambient conditions lead to a decrease in the uptake rate of 3 orders of magnitude. Pedersen *et al.* [175, 176] have investigated the effect of cycling magnesium powder in impure hydrogen. They found that introducing impure hydrogen containing approx. 5000 ppm O_2 lead to a decrease in hydrogen uptake capacity due to a decreased uptake rate compared to that in hydrogen with less than 1 ppm total impurities. Furthermore, activation of air exposed Mg by at least 1 cycle of hydrogenation/dehydrogenation is necessary in order to obtain steady-state kinetics [56, 57, 169].

The formation of MgO at the surface is therefore expected to contribute to a higher apparent activation energy. The observed lower activation energies for the activated samples are thus probably due to the creation of a fresh, oxide free surface from cracked particles. Quantifying the effect of *activation* on the apparent activation energy is, however, difficult due to the various procedures used on the samples.

Based on the above it is proposed that the vast difference in apparent activation energies is a consequence of the level of MgO formation, which strongly inhibits hydrogen diffusion. For non-activated samples hydrogen diffusion through MgO-rich surfaces limits the kinetics, whereas other processes such as hydrogen dissociation or diffusion in the hydride is expected to be rate-limiting for the activated samples. The smaller changes in apparent activation energy of $LaNi_5$ compared to Mg could be an indicator of the fact that $LaNi_5$ is more easily activated and less sensitive towards oxidation and contamination. In the following the effect of alloying will be discussed.

4.3.3 Improved resistance towards oxidation by alloying

The alloyed and non-activated Mg samples (A-C): MgH_2/Al, $MgH_2/MgCu_2$ and MgH_2/Mg_2Cu, respectively (corresponding to the ones already presented in the previous chapter), do not seem to fit the trend in applied activation procedure. The explanation probably relies on the fact that alloying with Cu and Al produces a compound less sensitive towards oxygen contamination. In fact Karty *et al.* [41] have suggested that Mg_2Cu adds an external oxide-free surface (in contrast to Mg which is easily oxidized as discussed above) on which hydrogen can dissociate with subsequent diffusion of H-atoms through bulk Mg_2Cu to the Mg/Mg_2Cu interface, where MgH_2 is formed. Similar conclusions have been reached by Au *et al.* [177] from the study of a multi component magnesium based alloy. Further, it has been suggested that upon exposure to air, Mg segregates to the surface induced by MgO formation, potentially forming particles of metallic Cu near the surface, catalyzing the dissociation of H_2 [177, 16, 178]. Effectively, the result of alloying with Al is the same as for $Mg_2Cu/MgCu_2$, although the physical explanation is likely different due to the stronger affinity of Al to oxygen.

Using XPS McIntyre and Chen [170] have investigated oxide formation on Mg alloys with Al content from 3-8.5 at.% exposed under ambient conditions. They showed that the Mg-Al alloys initially develop oxide films with a thickness of approx. 3.5 nm compared to pure Mg which develops a film with a thickness of 3 nm. However, the subsequent oxide film growth rate for the

Mg-Al alloys is much lower than for pure Mg. Scotto-Sheriff et al. [179] have investigated the composition and structure of the oxide film on Aluminum alloys with 4-5 at.% Mg. They found an oxide film thickness of approx. 4 nm consisting of MgO and Al_2O_3 in a 1:1 ratio due to Mg surface segregation. Electron diffraction suggests that both oxides are present in an amorphous state. Annealing at 360 °C leads to increased surface segregation of Mg (as MgO which remains amorpheous) and partly crystallization of Al_2O_3. It is also found that metallic Al is present in the outer most layer of the surface, propably due to reduction of Al_2O_3 by Mg [179, 180].

From the above we can summarize some general trends in the oxidation behaviour of Mg-Al alloys. Since both Mg and Al have a strong affinity towards oxide formation ($\Delta H_{MgO} = 1200$ kJ/mol O and $\Delta H_{Al_2O_3} = 1116$ kJ/mol O) alloying does obviously not prevent surface oxidation. The effect of oxidation of Mg-Al alloys in relation to e.g. hydrogen uptake is not exactly unambiguous, although there are some indications of somewhat improved properties compared to pure Mg: 1) The presence of both surface MgO, Al_2O_3 and possibly metallic Al, might enhance the formation of a less compact oxide layer as also proposed for surface segregated Mg_2Ni and Mg_2Cu [181, 41]. Furthermore a composite structure may contribute to additional grain boundaries favourable for diffusion. 2) A lower oxide growth rate for alloyed samples compared to pure Mg might suggest a higher resistance towards deactivation during continued cycling in the presence of impurities. 3) The presence of a partly amorphous oxide layer even at elevated temperatures may offer favorable hydrogen diffusion paths [33, 182].

4.4 Explanation of the CE

In the case of magnesium based hydrides, a probable physical explanation can be established for the large variation in apparent activation energy, whereas the pronounced changes in apparent prefactor seem unlikely to be explainable on the basis of, e.g., changes in vibrational frequencies [145]. Whether the observed compensation effect is an artifact of the derivation of $\ln(A_{app})$ from an Arrhenius plot, where $\ln(A_{app})$ is the intercept (the rate constant extrapolated to infinite temperature), is investigated in the following.

Recently, it has been shown [183] (Paper 7) for heterogeneous catalytic reactions that changes in apparent activation energies due to variations in reaction conditions or changing of the catalyst material always leads to a compensation effect when the corresponding apparent prefactors are determined from an Arrhenius analysis. Further, by tedious algebra it was shown that the slope in such a Constable plot is $a = (RT_m)^{-1}$, where T_m may be interpreted in terms of a mean experimental temperature. Thus it was concluded that the observed compensation effect could be explained by the method of data analysis rather than a physical effect.

The observation of $a = (RT_m)^{-1}$ calls for an investigation, whether the Constable plots presented here displays this correlation. The slope, a, in figure 4.1 and 4.2 and the derived T_m for Mg and $LaNi_5$ is shown in table 4.3. Also shown is the true experimental mean temperature $T_m(exp)$ for Mg and $LaNi_5$. From table 4.3 it is seen that there is good agreement between the calculated and experimental value of T_m for both Mg and $LaNi_5$. The larger slope in the Constable plot of $LaNi_5$ compared to Mg is thus simply accounted for by the lower temperature applied during experiments, i.e., the slopes are equal to $(RT)^{-1}$.

Having shown that the slopes in the Constable plots are equal to $(RT)^{-1}$ enables the data analysis to be taken one step further. From eq. (4.2), $\ln(A_{app})$ is given by

$$\ln(A_{app}) = \frac{E_A^{app}}{RT} + \ln(k) \tag{4.3}$$

To quantify the relative contributions to $\ln(A_{app})$, a modified Constable plot is constructed, where the data from table 4.1 is compared to $\frac{E_A^{app}}{RT_m}$ (figure 4.4, upper).

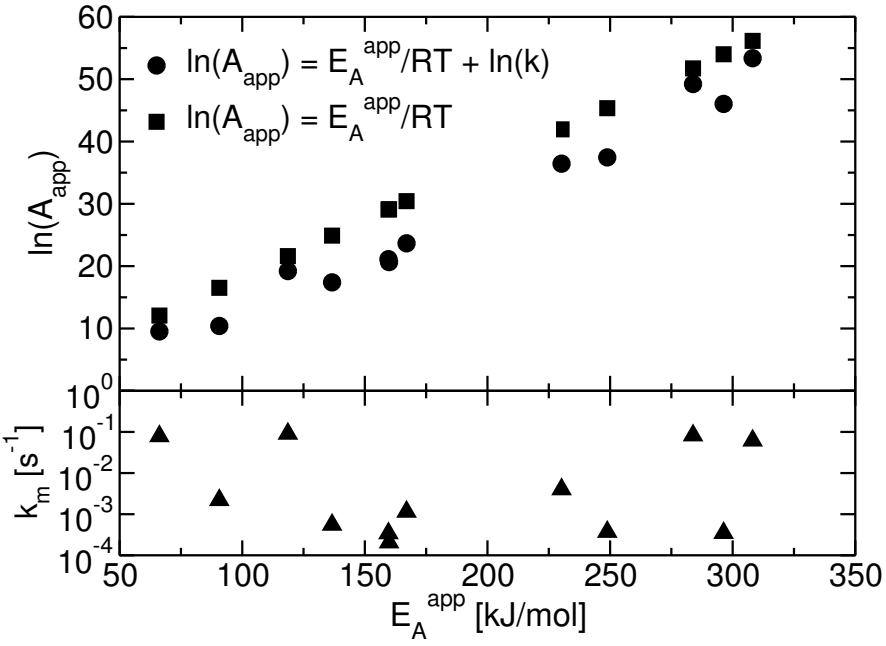

Figure 4.4: Constable plot of reported values of A_{app} vs. E_A^{app} from table 4.1 for Mg-based hydrides compared with $\frac{E_A^{app}}{RT_m}$ (upper).

From the figure it is noted that $\frac{E_A^{app}}{RT}$ is by far the most important contribution to $\ln(A_{app})$. Even though the rate constant, k_m, calculated for the different samples at T_m using the derived values of apparent activation energy and apparent prefactors varies by three orders of magnitude (cf. figure 4.4 lower) this is still only a minor contribution to $\ln(A_{app})$. This observation also explains why the slope in a Constable plot is simply $(RT)^{-1}$, since discarding $\ln(k)$ in eq. 4.3 introduces only minor errors in $\ln(A_{app})$.

The above decomposition of the apparent prefactor strongly indicates that the observed compensation effect, does not rely on any physical phenomena, but is simply a consequence of the simultaneous determination of E_A^{app} and $\ln(A_{app})$ from an Arrhenius analysis. In relation to this it is important to have in mind that unfortunately, an Arrhenius analysis is often the only method available of determining both the activation energy and the prefactor. Thus, extreme caution should be exercised when drawing conclusions based on such an analysis. Further, taking into account that the numerical value of rate constants reported often lie within a limited range (where the lower limit usually is determined by the instrumental time-resolution, end the upper

Metal hydride	a [J^{-1}mol]	T_m [K]	$T_m(exp)$ [K]
MgH_2	$1.82{\cdot}10^{-4}$	661	643
$LaNi_5$	$3.93{\cdot}10^{-4}$	306	293

Table 4.3: The Constable plot slope a and corresponding values of T_m and $T_m(exp)$ for Mg and $LaNi_5$ based hydrides.

limit is determined by the patience of the experimentalist) the use of an Arrhenius analysis will inevitably result in a Compensation effect.

4.5 Summary

In this chapter the kinetics in terms of apparent activation energies and apparent prefactors for hydrogenation/dehydrogenation has been reviewed for two of the most investigated metal-hydrogen systems: magnesium and $LaNi_5$ based hydrides. For both systems it is found that the values of the apparent activation energies are scattered. This is most pronounced for the magnesium based hydrides. This is taken as evidence for the fact that $LaNi_5$ is much more easily activated and less sensitive towards oxidation and contamination than Mg. In the case of Mg it is suggested that variations in reported apparent activation energies correlate with the presence of an MgO surface layer inhibiting diffusion of hydrogen. Thus oxidized samples show large apparent activation energies and well activated samples show smaller activation energies. Alloying of Mg with both Al and Cu leads to compounds less sensitive towards oxygen contamination and with dehydrogenation characteristics comparable to activated samples of pure Mg.

In the light of the above, it is very tempting to suggest that for magnesium based hydrides ultimate performance is achieved for samples being completely free from oxygen impurities. However, magnesium has a very high vapor pressure at the temperatures usually applied in hydrogenation/dehydrogenation experiments, which is reflected in its relatively low melting point of 660 °C. Recent investigations indicate that the presence of MgO acts as a stabilizer and that at least some oxide must be present, in order to prevent sintering of Mg-particles during continued cycling, thereby sustaining reversibility [184].

Further, the existence of a compensation effect in the hydrogenation/dehydrogenation of metal hydrides has been investigated. A clear compensation effect in the case of both magnesium and $LaNi_5$ based hydrides is found. The origin of this compensation effect is the simultaneous determination of the apparent prefactor and apparent activation energy from an Arrhenius analysis. Moreover, it is found that the slope in the Constable plots of both magnesium based hydrides and $LaNi_5$ based hydrides is equal to $(RT)^{-1}$. Whenever apparent activation energies and apparent prefactors are linked through an Arrhenius analysis the explanation of the compensation effect given here is of general applicability and not restricted to metal-hydrogen systems.

Chapter 5

Complex hydrides

5.1 Dehydrogenation of $LiAlH_4$

5.1.1 Literature review

In the following the literature on $LiAlH_4$ in relation to hydrogen storage will be briefly reviewed.

Hydrogen is generally suggested to desorb from $LiAlH_4$ in a three step decomposition, I-III [104, 105, 106], although some controversy about the details of the mechanism exists [107, 108, 63].

$$LiAlH_4 \rightarrow \frac{1}{3}Li_3AlH_6 + \frac{2}{3}Al + H_2 \tag{5.1}$$

$$\frac{1}{3}Li_3AlH_6 \rightarrow LiH + \frac{1}{3}Al + \frac{1}{2}H_2 \tag{5.2}$$

$$LiH \rightarrow Li + \frac{1}{2}H_2 \tag{5.3}$$

Reaction I, II, and III proceeds with a theoretical hydrogen release of 5.3 wt. %, 2.6 wt %, and 2.6 wt %, respectively. However, due to the thermodynamic stability of LiH, i.e. high decomposition temperature, only 7.9 wt. % H_2 is considered accessible for practical applications. Reaction I is endothermic by 3.5-10 kJ/mol H_2 and reaction II is endothermic by 27-40 kJ/mol H_2 [105, 109, 110, 111, 112]. Under ordinary reaction conditions, formation of $LiAlH_4$ from LiH + Al is not possible due to it's extremely high plateau pressure. Therefore, $LiAlH_4$ is usually not considered as a candidate for *on-board* reversible hydrogen storage, but the possibility of *off-board* regeneration still exists. On the other hand, Li_3AlH_6 which can be synthesized from LiH and $LiAlH_4$ by mechano-chemical treatment [111, 113, 114] with a theoretical hydrogen capacity of 5.6 wt. % H_2, shows reversibility at only 40 bar hydrogen [111].

In thermal analysis, reaction I occurs around 150-220 °C [111, 117] and is initiated by the melting of $LiAlH_4$ (endothermic), which is subsequently transformed into solid Li_3AlH_6 and Al during release of hydrogen gas (exothermic). Reaction II takes place around 190-260 °C (endothermic) [105, 106]. Reaction III (endothermic) proceeds at elevated temperatures around 350-400 °C [106, 115] and is probably followed by the formation of a Li-Al alloy from metallic Li and Al [106, 116, 62]. Experiments have demonstrated that reaction I may proceed spontaneous at room temperature directly from solid $LiAlH_4$ during prolonged storage [105]. ^{27}Al NMR has also demonstrated direct decomposition of solid $LiAlH_4$ into Li_3AlH_6 at 150 °C [107].

Doping with VCl_3 and $TiCl_3{\cdot}1/3AlCl_3$ results in a lowering of the decomposition temperature of both reaction I and II [106, 111]. Doping with $TiCl_3{\cdot}1/3AlCl_3$ has also been shown to facilitate isothermal dehydrogenation at temperatures in the range of 100-175 °C at a time scale of 50 min to a few hours [111]. Ball milling of pure $LiAlH_4$ results in a lowering of the decomposition

temperature of both reaction I and II [117, 115]. Pure $LiAlH_4$ does not decompose during ball milling at ambient temperatures [117], whereas $LiAlH_4$ doped with catalytic additives e.g. $TiCl_3$, $TiCl_4$, VCl_3, Fe etc. rapidly decomposes during milling [106, 113, 117, 118, 119].

5.1.2 Methods and outline

za

The kinetic parameters of reaction I and II have only been evaluated to a limited extent [185, 186]. These investigations suffer either from unclear separation of parameters from reaction I and II [185] or limitations to reaction I only [186]. This serves as a main motivation for studying the dehydrogenation kinetics of both step I and II for pure $LiAlH_4$. Furthermore, no systematic investigations of the influence of ball milling, application of different milling times, on kinetics have been reported. These investigations are essential in order to obtain a reliable reference for evaluation of the kinetic effects of doping with catalytic additives in combination with ball milling. Finally, only a few studies deal with the effect of Ti-doping on the dehydrogenation kinetic parameters and no solid conclusions about the influence of doping on the kinetic parameters can be drawn due to contradicting results [111, 186].

The dehydrogenation kinetics of $LiAlH_4$ is investigated using differential scanning calorimetry (DSC) in order to extract kinetic parameters of the reaction pathway going through melted $LiAlH_4$. Furthermore, the kinetics of direct dehydrogenation of solid $LiAlH_4$ is investigated by carrying out isothermal experiments below the melting point of $LiAlH_4$. In order to extract parameters for both reaction I and II a kinetic model is formulated, which takes both reactions into account, and kinetic parameters are found by fitting to experimental data. Moreover, the effect of different ball milling times on the dehydrogenation kinetics of both reaction I and II is investigated. Using X-ray powder diffraction it is possible to find corresponding crystallite sizes from line broadening and relate this to the observed kinetic effect. Finally, Ti-doped samples of $LiAlH_4$ are investigated by a combination of XRPD and DSC. For experimental details see paper 5 and 6.

5.1.3 Un-milled, as-received

The as-received $LiAlH_4$ powder has been investigated by DSC applying different heating rates cf. Figure 5.1. DSC traces shows the following features: an exothermic peak at 150 °C, an endothermic peak around 170 °C, an exothermic peak at 178-198 °C, and an endothermic peak around 227-247 °C.

The first exotherm have been previously been assigned to the interaction of $LiAlH_4$ with surface hydroxyl impurities [105], and the first endotherm corresponds to the melting of $LiAlH_4$ [104, 105]

$$LiAlH_4(s) \rightarrow LiAlH_4(l) \tag{5.4}$$

The melting of $LiAlH_4$ is immediately followed by the second exotherm corresponding to the decomposition of liquid $LiAlH_4$ [104, 105]

$$LiAlH_4(l) \rightarrow \frac{1}{3}Li_3AlH_6(s) + \frac{2}{3}Al(s) + H_2(g) \tag{5.5}$$

The second endotherm corresponds to the decomposition of Li_3AlH_6 as described by reaction III [104, 105, 114, 117]

By performing a Kissinger analysis [187], i.e. an analysis of the sensitivity of the peak positions to the applied heating rate, the apparent activation energy, E_A, can be obtained from

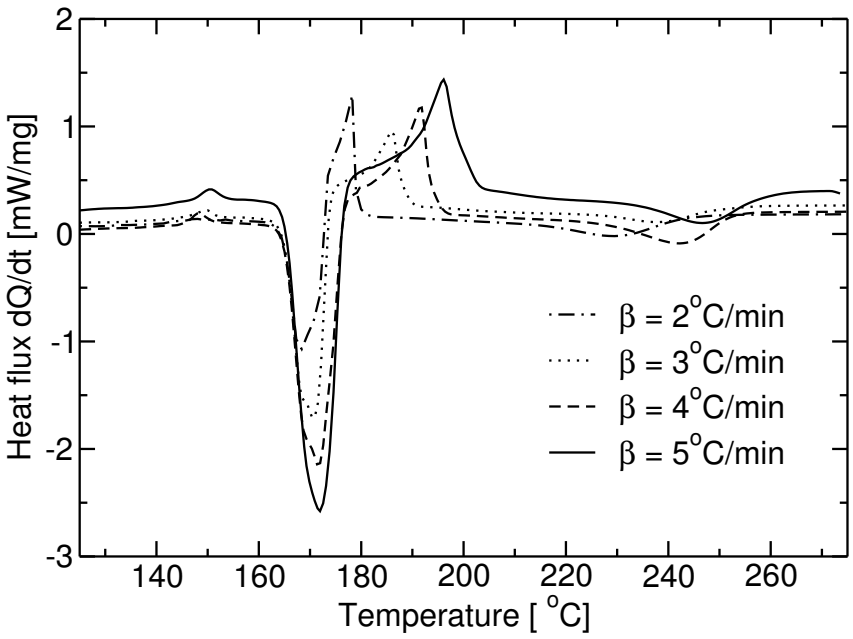

Figure 5.1: Dehydrogenation of as-received $LiAlH_4$ investigated by DSC.

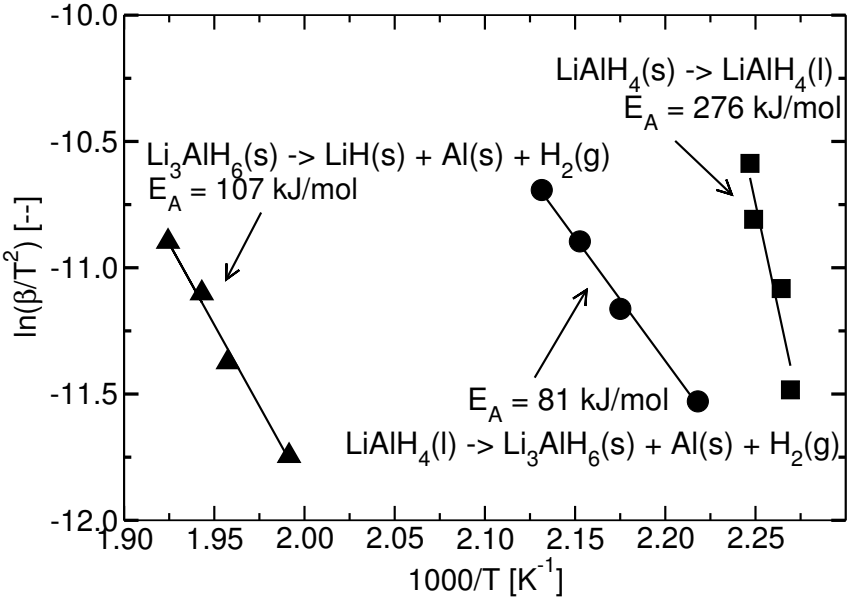

Figure 5.2: Kissinger plot for dehydrogenation of as-received $LiAlH_4$.

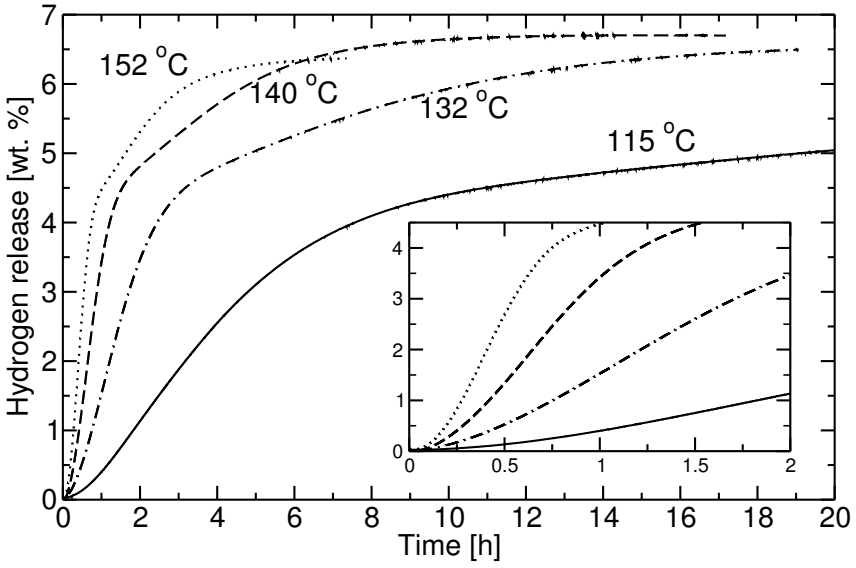

Figure 5.3: Isothermal dehydrogenation of as-received $LiAlH_4$ investigated in high pressure balance.

the following equation

$$\frac{d\ln\left(\frac{\beta}{T_m^2}\right)}{d\left(\frac{1}{T_m}\right)} = -\frac{E_A}{R} \tag{5.6}$$

where T_m is the temperature at peak maximum. Thus, E_A can be obtained as the slope in a plot of $\ln\left(\frac{\beta}{T_m^2}\right)$ vs. $\frac{1}{T_m}$. A Kissinger analysis is applied to the 1. endotherm corresponding to the melting of $LiAlH_4$, the 2. exotherm (reaction I), and the 2. endotherm (reaction II) cf. Figure 5.2. From the Kissinger analysis the apparent activation energy for decomposition of liquid $LiAlH_4$ into Li_3AlH_6, Al and H_2 is found to be 81±4 kJ/mol. The apparent activation energy for decomposition of Li_3AlH_6 into LiH, Al and H_2 is found to be 108±8 kJ/mol.

In order to also investigate the direct solid state decomposition of pure $LiAlH_4$ (without preceding melting) [105, 107], isothermal experiments at different temperatures have been carried out well below the melting point of $LiAlH_4$. The results are shown in Figure 5.3. As shown in the figure, the effect of increasing temperatures is an increase in the rate of hydrogen release as would be expected for a thermally activated process. The maximum observed hydrogen release of approx. 6.7 wt.% is slightly lower than the theoretical limit, even when correcting the observed hydrogen release with the purity of the sample. XRPD of the dehydrogenated samples (not shown) reveal that some Li_3AlH_6 is left after dehydrogenation in agreement with observations of Andrei et al. [188]. Thus incomplete dehydrogenation of Li_3AlH_6 offer, at least partially, an explanation for this difference.

Each dehydrogenation is initiated by a short acceleration period, i.e. an increase in reaction rate followed by a period of decelerating kinetics until a slight bend in the curves occur, corresponding to the termination of the 1. reaction step and the onset of the 2. reaction step. The net result is a sigmoidal dehydrogenation curve for decomposition of $LiAlH_4$ to Li_3AlH_6 (see inset in Figure 5.3). The apparent decomposition of Li_3AlH_6 is characterized by a decelerating reaction rate. In order to model the isothermal dehydrogenation curves in Figure 5.3 a model with the ability to account for both decomposition reactions should be chosen. A standard two-step kinetic expression of the following form provides a good fit to the experimental data

T [°C]	W_1 [wt.% H_2]	W_2 [wt.% H_2]	k_1 [h^{-1}]	k_2 [h^{-1}]	η_1 [–]	η_2 [–]	χ^2
115	4.28	1.56	0.229	0.040	1.53	1.95	0.0133
132	4.11	2.44	0.624	0.123	1.80	1.51	0.0030
140	4.25	2.44	1.191	0.235	1.99	1.71	0.0007
152	4.02	2.32	1.996	0.442	2.22	1.74	0.0302
A [h^{-1}]			$2.3{\cdot}10^{10}$	$4.9{\cdot}10^{10}$			
E_A [kJ/mol]			82±4	90±4			

Table 5.1: Kinetic parameters obtained from fitting isothermal measurements of the direct decomposition of $LiAlH_4$.

$$\begin{aligned} W_{tot}(t) &= W_1(1-\exp\left(-(k_1 t)^{\eta_1}\right)) \\ &\quad +W_2(1-\exp\left(-(k_2 t)^{\eta_2}\right)) \end{aligned} \tag{5.7}$$

where W_{tot} is the total hydrogen release at time t, W_1 and W_2 are the release of hydrogen from reaction I and II, respectively, k_1 and k_2, and η_1 and η_2 are exponents for reaction I and II, respectively, in analogy to the Avrami exponents used in JMA kinetics as previously discussed [50, 49, 54]. Except for the included exponents in Eq. 5.7 the model is similar to the one applied by Kiyobayashi *et al.* in order to model dehydrogenation of $NaAlH_4$ [189]. Since only dehydrogenation is considered and the fact that dehydrogenation is performed at constant pressure pressure dependent terms e.g. as proposed by Luo and Gross [190] are ignored. The kinetic expression is fitted to the isothermal experimental data using a Levenberg-Marquandt least squares algorithm [191]. As illustrated in paper 5 the model provides an excellent description of the dehydrogenation kinetics.

All extracted fitting parameters, and apparent activation energies and prefactors as determined from an Arrhenius analysis are summarized in table 5.1, including χ^2 goodness-of-fit values. As seen from the table, the apparent activation energies are in close agreement with those derived from the DSC experiments, although the activation energy E_A for dehydrogenation of Li_3AlH_6 determined from the isothermal data is slightly lower than the value obtained from the Kissinger analysis. The fact that the two different decomposition pathways for $LiAlH_4$, direct and from melt, have the same apparent activation energy suggests they share atomic scale similarities.

5.1.4 Ball milling

In order to investigate the effect of ball milling $LiAlH_4$ on the dehydrogenation kinetics, the as-received powder has been ball milled for different periods of time and milling intensities. Three batches were prepared: The first was ball milled for 1h@150rpm. The second was ball milled for 1h@400rpm. The third was balled milled for 2h@400rpm, then approx. 0.6 g powder was taken out from the ball mill for subsequent analysis, then the ball milling process was continued for 4 hours (a total of 6 h of ball milling) and a new sample was taken out from the ball milling vial, and finally the milling process was continued for another 4 hours, giving a total of 10 hours of ball milling. By this procedure a total of 5 different samples were prepared. These samples have been subject to both XRPD analysis and isothermal measurements of the dehydrogenation process. A few samples has been analysed by DSC.

XRPD patterns of all the ball milled samples are shown in Figure 5.4. Generally, the reflections become broader as a function of milling time/intensity suggesting that the average

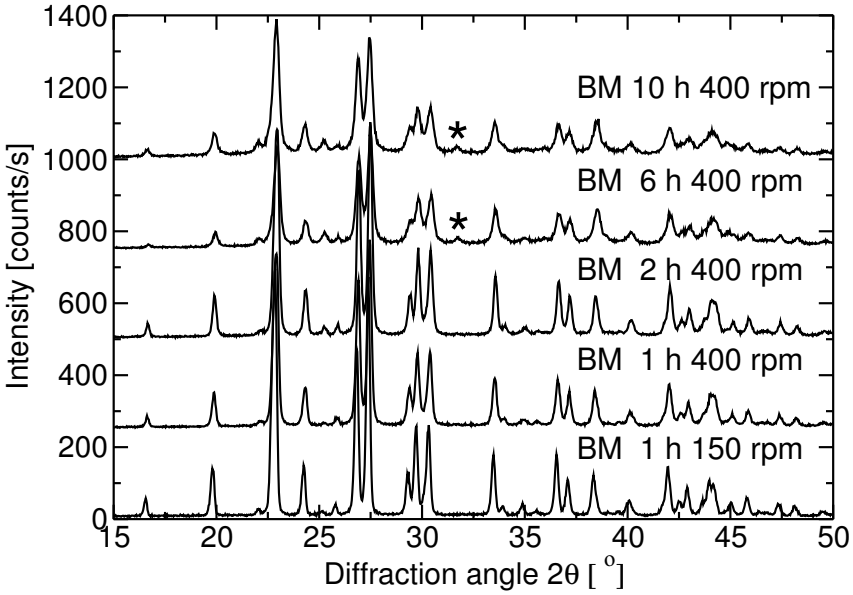

Figure 5.4: XRPD of as-received $LiAlH_4$, $LiAlH_4$ ball milled for 1 h at 150 rpm, and $LiAlH_4$ ball milled for 1 h at 400 rpm.

coherence length (crystallite size) is reduced upon milling. After 6 hours of milling an additional reflection (marked with an asterisk) appears around $2\theta = 31.7\,^{\circ}$. This feature could originate from either the (2 2 0) reflection of monoclinic [192] Li_3AlH_6 or the (2 0 -1) reflection of rhombohedral Li_3AlH_6 [110], suggesting a partial decomposition of $LiAlH_4$. In fact, after 2 hours of milling the sample changed colour from white/grayish to light gray indicating that a solid state reaction had taken place. On the other hand, apparently no crystalline metallic aluminum is formed suggesting that if any formation of Li_3AlH_6 has taken place the resulting aluminum is in an X-ray amorphous phase. Although the ball milling vial used in this work was carefully cleaned, the presence of small amounts of impurities that may act as a catalyst cannot be completely ruled out. However, this is considered as unlikely. On the other hand, is was noticed that the vial heated up slightly during milling, most pronounced for the longer milling times. Thus, the potential decomposition of $LiAlH_4$ may be thermally mediated.

The effect of ball milling on the dehydrogenation kinetics is visualized by isothermal dehydrogenation curves for all ball milled samples in Figure 5.5. It was intended to apply the same isothermal temperature to all dehydrogenation experiments for the ball milled samples. Though, in practice, an inter-sample temperature variance of a few degrees around 130 °C was observed, which is expected to be within experimental uncertainty. The dehydrogenation curve for as-received $LiAlH_4$ at 132 °C is included in Figure 5.5 as a reference.

From the dehydrogenation curves in Figure 5.5 it is observed that ball-milling effectively leads to faster kinetics for reaction I (first and steepest part of the curves up to 3-4.5 wt %), while reaction II seems to be more insensitive to the ball milling. Although the exact dependence of the kinetics of reaction II on ball milling cannot be determined visually. Further, it is observed that longer ball milling times leads to faster kinetics than for short periods of ball milling. Applying longer ball milling times, the smooth transition between reaction I and II as observed in the un-milled sample become more abrupt. The initial rate of dehydrogenation for the sample ball milled for 10 h seems to deviate somewhat from the others. This is due to the fact that dehydrogenation initiated during the heating period. It is also observed from Figure 5.5 that longer ball-milling times results in reduced hydrogen release mainly from $LiAlH_4$.

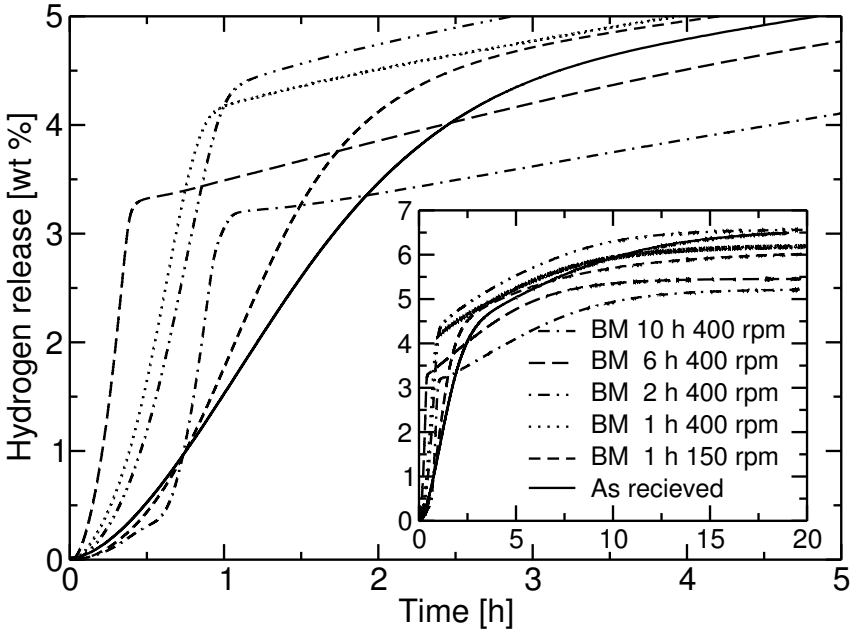

Figure 5.5: Isothermal dehydrogenation curves for ball milled samples. The isothermal temperature is approx. 130 °C. Dehydrogenation curve for un-milled as-received $LiAlH_4$ at 132 °C is included for comparison.

Time [h]	Intensity [rpm]	W_1 [wt.% H_2]	W_2 [wt.% H_2]	k_1 [h^{-1}]	k_2 [h^{-1}]	η_1 [–]	η_2 [–]	χ^2
1	150	3.85	2.17	0.751	0.180	2.48	1.18	0.0002
1	400	4.12	2.07	1.567	0.168	2.78	1.41	0.0047
2	400	3.57	3.26	1.305	0.190	3.66	0.80	0.0020
6	400	3.39	2.04	3.272	0.216	2.95	1.60	0.0095
10	400	2.81	1.97	3.817	0.163	2.26	1.63	0.0113

Table 5.2: Kinetic parameters obtained from fitting isothermal measurements of the direct decomposition of $LiAlH_4$.

In order to quantify the effect of ball milling on the dehydrogenation kinetics of $LiAlH_4$, kinetic parameters are extracted from the dehydrogenation curves by fitting Eq. 5.7 to the experimental dehydrogenation curves of the ball milled samples; the results are summarized in Table 5.2. In order to fit the dehydrogenation curve of the sample ball milled for 10 h it was necessary to exclude the first part of the curve corresponding to the non-isothermal hydrogen release from the fitting procedure. By inspection of the fitted parameters in Table 5.2 the faster kinetics of reaction I seen in Figure 5.5 is confirmed quantitatively. In fact, the rate constant of reaction I is increased by a factor of 6 by ball milling for 10 h. The only sample that does not follow the overall trend in rate constants as a function milling time is the 2h@400rpm. It is interesting to see that ball milling has virtually no effect on the rate constant of reaction II.

In the fitting procedure both η_1 and η_2 were allowed to vary freely and their values are somewhat higher and lower, respectively, than η_1 and η_2 for the as-received samples in Table 5.1. Rate constants for both reaction I and II for the ball milled samples were also obtained by fitting Eq. 5.7 with the constraints that η_1 and η_2 should retain values corresponding to $\bar{\eta_1}$ and $\bar{\eta_2}$ for the as-received samples. This did not change the trend in rate constants in Table 5.2 significantly.

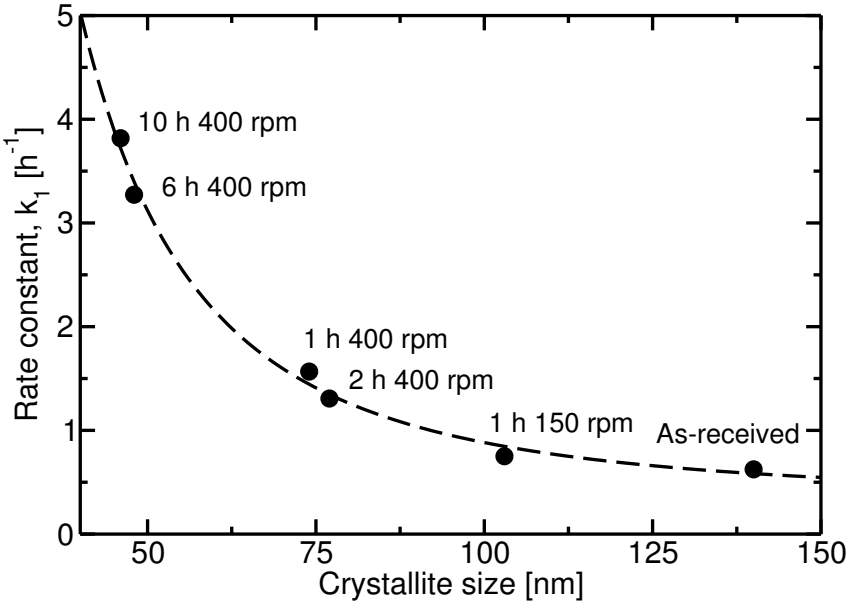

Figure 5.6: Rate constants for reaction I as a function of crystallite size obtained from XRPD line broadening.

5.1.5 Diffusion limited kinetics?

As previously mentioned, the diffraction patterns of the ball milled samples 5.4 showed wider reflection with longer ball milling times. In order to investigate a possible correlation between crystallite size and rate constants we have extracted crystallite sizes of the ball milled samples before dehydrogenation including the as-received sample applying the Scherrer equation 5.8.

$$\beta = \frac{\lambda}{B \cos\theta} \tag{5.8}$$

where β is the crystallite size, λ is the X-ray wavelength and B is the FWHM (corrected for instrumental broadening, which is assumed to be 0.10 °). In order to get a reliable picture of the average crystallite size instead of an average coherence lengths in certain crystallographic directions the average line broadening of several reflections up to 35 ° in 2θ have been used.

Figure 5.6 shows the rate constants as a function of crystallite size. Fitting the data to a power-law yields an excellent fit (dashed line) with an $1/\beta^{2.3}$ dependence. The strong dependence of k_1 on crystallite size may suggest a mass transfer process to be limiting the kinetics e.g. long range atomic diffusion of Al as proposed by Kiyobayashi *et al.* [189] and Sandrock *et al.* [100]. The exact order of the exponent can be used to obtain detailed physical information about the underlying rate limiting process(es).

According to Nabarro-Herring [193, 194], a $1/\beta^2$ relation corresponds to a process controlled by lattice diffusion (through grains) as observed for e.g. hydrogen diffusion in $Co_{90}Zr_{10}$ [195], whereas a process controlled by grain boundary diffusion displays a $1/\beta^3$ relation according to Coble [196]; as observed for e.g. hydrogen enhanced diffusional creep in Pd [197]. The apparent activation energy for diffusion in grain boundaries is usually lower than the value corresponding to lattice diffusion [194, 198]. Thus, diffusion in grain boundaries is generally favored at low temperatures, whereas for higher temperatures lattice diffusion is favored. Hydrogen diffusion in grain boundaries is found to be faster than lattice diffusion [199, 200], though for grain boundary hydrogen diffusion to become important the grain size should be reduced significantly (corresponding to an increase in ratio of grain boundary volume to bulk grain volume) [201, 202].

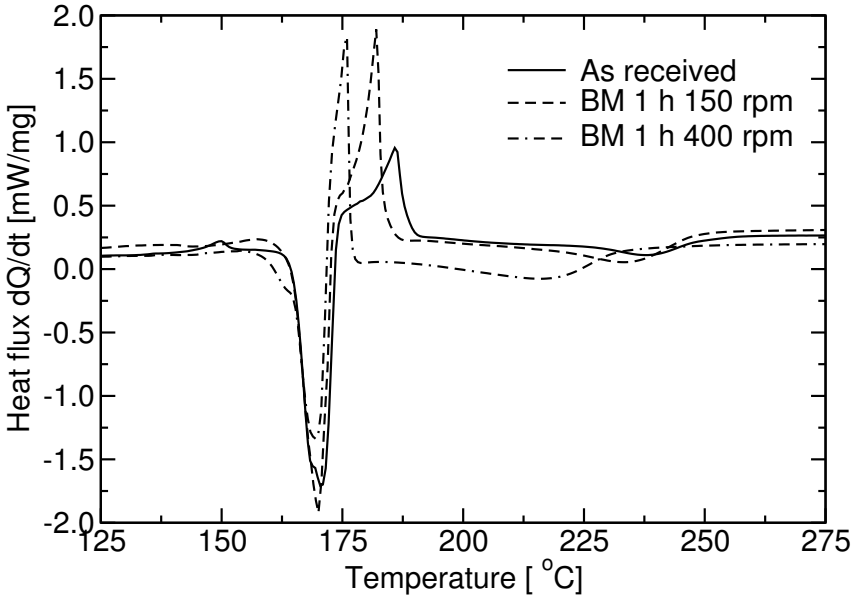

Figure 5.7: DSC of as received $LiAlH_4$, $LiAlH_4$ ball milled for 1h@150rpm, and $LiAlH_4$ ball milled for 1h@400rpm. The applied heating rate is 3 °C/min.

Considering Figure 5.6 displays a $1/\beta^{\sim 2}$ relation, reaction I is likely to be limited by a lattice diffusional process. Compared to typically observed grain boundary widths on the order of a few nanometers [201] the grain size of $LiAlH_4$ is, even for the longest milling times, more than an order of magnitude larger. Hence, a $1/\beta^2$ relation due to diffusion in grain boundaries with widths comparable to the grain size can be ruled out.

The fact that k_2 is more or less insensitive to the large variations in crystallite size indicates that reaction II, in contrast to reaction I, is not limited by mass transfer. Instead the intrinsic kinetics, such as bond breaking, seems to be limiting the kinetics at the relatively low temperature applied. In order to investigate the effect of ball milling on reaction II at higher temperatures DSC is performed cf. Figure 5.7. As shown in the figure, the kinetics of reaction II at elevated temperatures is indeed improved by ball milling. The decomposition temperature of Li_3AlH_6 is lowered from 237 °C for the as-received powder to 233 °C and 215 °C for the samples ball milled 1 h at 150 and 400 rpm, respectively. Although, this result is somewhat surprising considering the melting of $LiAlH_4$ as evident from the endotherm at 170 °C. It may, however, suggest that this melting is somewhat localized and that the melted particles are stabilized, likely by the presence of oxide in the outer parts, whereby agglomeration is prevented. This suggests that at the elevated temperatures in the DSC experiment the intrinsic kinetics is improved sufficiently in order *not* to be limiting the overall kinetics. Instead, the crystallite size seems to become important. However, for practical applications the temperature can not be increased above 200 °C in order to obtain improved kinetics. Thus, ball milling alone is not sufficient to improve the kinetics of reaction II. This example very clearly illustrates the need for a suitable catalytic additive, not only to the make reaction I+II reversible but also to improve the kinetics – especially of reaction II.

5.1.6 Catalysis and stability of $LiAlH_4$

To complement the work of Chen *et al.* [111] and Blanchard *et al.* [106] on dehydrogenation kinetics of $LiAlH_4$ doped with catalytic additives $LiAlH_4$ samples doped with 2 mole % $TiCl_3 \cdot 1/3AlCl_3$ have been prepared by ball milling.

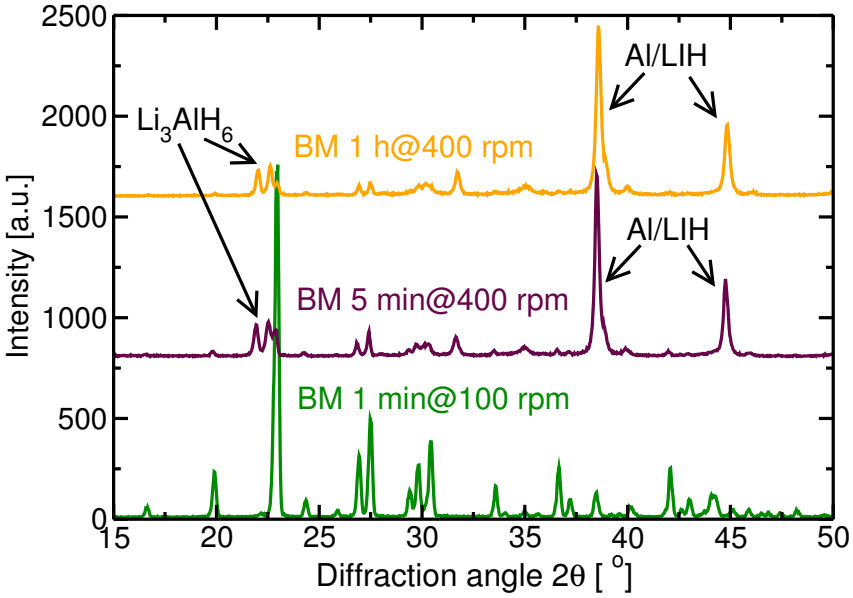

Figure 5.8: XRPD of $LiAlH_4$ doped with 2 mole % $TiCl_3 \cdot 1/3AlCl_3$ ball milled for 1 min at 100 rpm, 5 min at 400 rpm, and 1 hour at 400 rpm, respectively.

Figure 5.8 shows XRPD patterns of doped samples ball milled for 1 min at 100 rpm, 5 min at 400 rpm and 1 hour at 400 rpm. The sample ball milled for the shortest time and lowest speed shows no indication of any decomposition during the doping procedure. The diffraction pattern closely resembles that of the pure $LiAlH_4$ shown in figure 5.4 on page 46 with no significant signs of metallic Al in the diffraction pattern.

Before ball milling the the red/purple $TiCl_3 \cdot 1/3AlCl_3$ was gentle mixed with $LiAlH_4$ in the milling vial resulting in a powder with a touch of magenta. The colour remained after ball milling for 1 min at 100 rpm, however, the next day the magenta colour had disappeared and the powder appeared very much like the un-doped starting $LiAlH_4$ indicating that a reduction of Ti^{3+} in $TiCl_3$ had taken place. A possible reduction mechanism is outlined below [106]

$$3LiAlH_4 + TiCl_3 \cdot 1/3AlCl_3 \rightarrow Ti + 3Al + 3LiCl + 1/3AlCl_3 \tag{5.9}$$

The reduced Ti species may possibly be distributed as metallic Ti across the surface of the powdered particles [122] or present as a Ti_xAl_y alloy as proposed by Balema *et al.* for $TiCl_4$ doped $LiAlH_4$ [118] and as also proposed for $NaAlH_4$ [103, 203, 204]. The fact that the color of the sample ball milled for 1 min at 100 rpm did not change i.e. no darkening due to finely dispersed Ti and Al particles, may indicate that Ti is incorporated into the $LiAlH_4$ as suggested by Fichtner *et al.* [205]. However, this work is not conclusive about the chemical state of Ti in $LiAlH_4$.

The two samples ball milled for longer times show distinct diffraction peaks from Li_3AlH_6 Al (and possibly also LiH) clearly indicating that decomposition of $LiAlH_4$ has taken place. Further, it is also observed that the strongest reflections from $LiAlH_4$ have vanished almost completely, even after ball milling for only 5 min at 400 rpm. The found instability of $LiAlH_4$ towards mechano-chemical treatment with catalytic additives is in agreement with previous findings [106, 117, 118] although in disagreement with the work of Chen *et al.* [111].

Figure 5.9 shows DSC experiments performed with the samples ball milled for 1 min at 100 rpm and the sample ball milled for 1 h at 400 rpm. The DSC trace of the sample ball milled for 1 min at 100 rpm mainly consists of two endotherms, one with maximum around

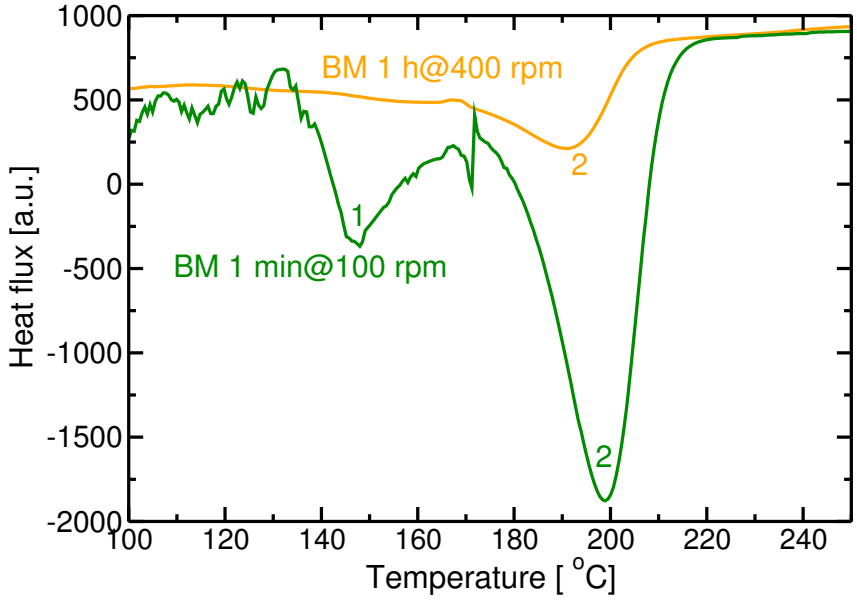

Figure 5.9: DSC trace of $LiAlH_4$ doped with 2 mole % $TiCl_3 \cdot 1/3AlCl_3$ ball milled for 1 min at 100 rpm, and 1 hour at 400 rpm, respectively. Applied linear heating rate: 3 °C/min.

150 °C and the other with maximum at approx. 200 °C. The first endotherm can be assigned to the dehydrogenation of solid $LiAlH_4$ into Li_3AlH_6 according to reaction I. Clearly the catalytic doping procedure has lowered the decomposition temperature of $LiAlH_4$ below its melting point in agreement with the findings reported in ref. [111, 106]. The small feature between the two dominating endothermic peaks, consisting of an endothermic and an exothermic peak, can be attributed to the melting of unreacted $LiAlH_4$ and subsequent decomposition into Li_3AlH_6. The second of the two dominating endothermic peaks corresponds to the decomposition of Li_3AlH_6 into LiH according to reaction II. The decomposition temperature of Li_3AlH_6 has also been lowered significantly compared to the pure $LiAlH_4$ cf. figure 5.7 on page 49. This exercise clearly demonstrates the effectiveness of $TiCl_3 \cdot 1/3AlCl_3$ in enhancing of the dehydrogenation kinetics of $LiAlH_4$. In the DSC trace of the sample ball milled for 1 h at 400 rpm the first endothermic peak at approx. 150 °C has almost completely vanished in agreement with the diffraction pattern of the sample. The maximum of the second endothermic peak have been lowered further by approx. 8-10 °C either due to a reduction of the crystallite size due to longer and more intensive ball milling treatment or due to a more favorable distribution of the catalyst or a combination of the two.

To further investigate the effect of Ti-doping on the dehydrogenation kinetics of $LiAlH_4$, a series of DSC experiments have been performed with the sample ball milled for 1 min at 100 rpm, in order to perform a Kissinger analysis as outlined in section 5.1.3. Figure 5.10 shows DSC experiments performed with heating rates of 3, 4, and 5 °C/min. As seen from the figure the maximum dehydrogenation rates shift upwards in temperature when the heating rate is increased. Figure 5.11 shows a Kissinger analysis of the DSC peaks in figure 5.10. The Kissinger analysis reveals apparent activation energies of 89±9 kJ/mol and 103±1 kJ/mol for reaction I and II, respectively. The found apparent activation energies are very close to those for the un-doped sample (81±4 kJ/mol and 108±8 kJ/mol). Reported values of apparent activation energies for dehydrogenation of Ti-doped $NaAlH_4$ and Na_3AlH_6 are found to be in the range of 73-100 and 97-100 kJ/mol, respectively [100, 190, 206, 189], which is similar to the reported values for reaction I and II of the un-doped samples of $LiAlH_4$ in this study. The

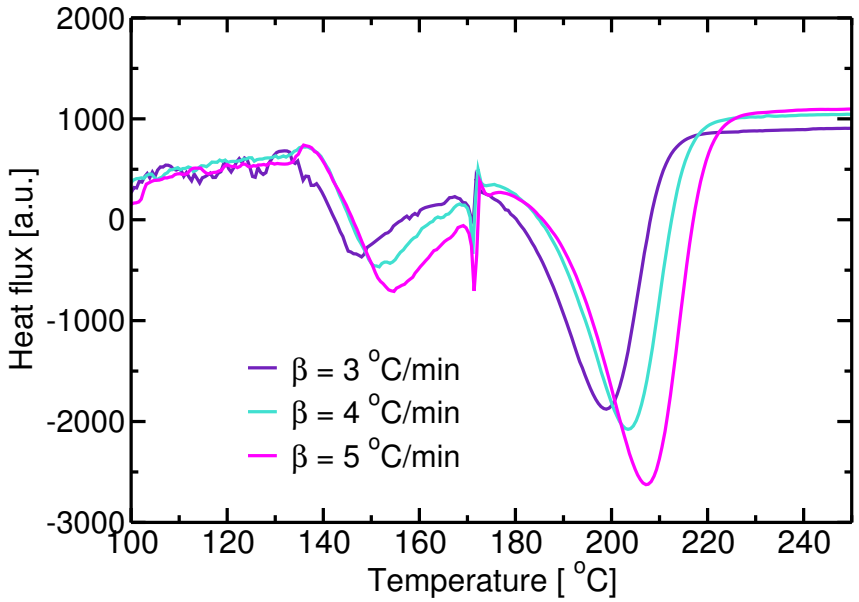

Figure 5.10: DSC for $LiAlH_4$ doped with 2 mole % $TiCl_3 \cdot 1/3AlCl_3$ ball milled for 1 min at 100 rpm at different apllied heating rates.

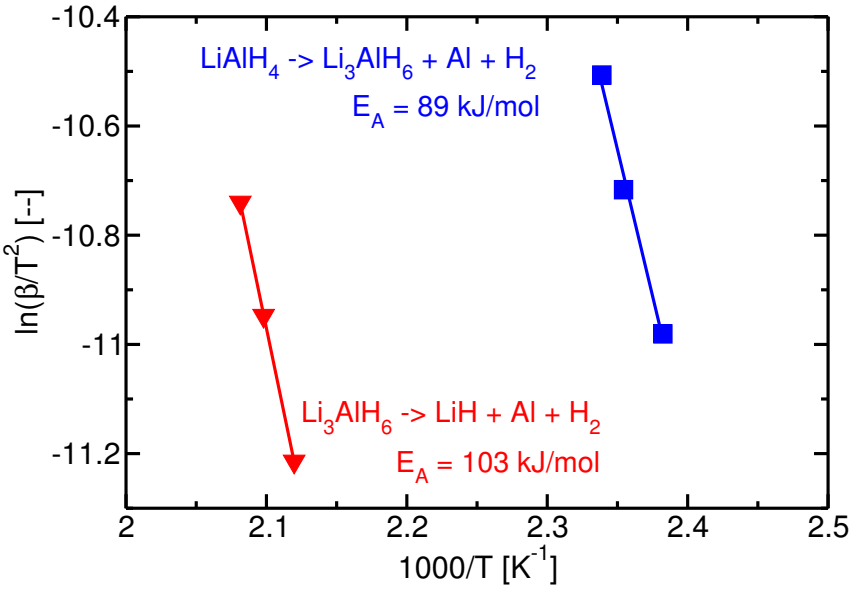

Figure 5.11: Kisinger analysis for $LiAlH_4$ doped with 2 mole % $TiCl_3 \cdot 1/3AlCl_3$ ball milled for 1 min at 100 rpm.

apparent activation energies for dehydrogenation of un-doped $NaAlH_4$ and Na_3AlH_6 is approx. 120 kJ/mol for both reactions [206]. Thus, apparently a lowering of the apparent activation energies of reaction I and II in $NaAlH_4$ is a consequence of Ti-doping.

Blanchard *et al.* [186] have studied the influence of doping with catalytic additives on the apparent activation energy of reaction I. They found a reduction of approx. 5-10 kJ/mol upon doping with either $TiCl_3{\cdot}1/3AlCl_3$ or VCl_3. Chen *et al.* [111] have investigated the dehydrogenation kinetics of $TiCl_3 \cdot 1/3AlCl_3$ doped $LiAlH_4$ and they found apparent activation energies of 43 kJ/mol and 55 kJ/mol for reaction I and II, respectively. The low values of apparent activation energies reported by Chen *et al.* are in contradiction to the ones reported in this study for Ti-doped $LiAlH_4$ and also in contradiction to the results of Blanchard *et al.* [186]. In this study no significant effect on the apparent activation energies are observed as a consequence of Ti-doping. This suggests that *a)* The effect of Ti-doping is different in $LiAlH_4$ compared to $NaAlH_4$, and *b)* since the dehydrogenation temperatures shift downwards in the DSC experiments upon doping this must be accounted for in terms of an increase in the prefactor since the activation energies are unaffected by the doping.

5.2 Hydrogen mobility in $NaAlH_4$

5.2.1 Theory of Quasielastic Neutron Scattering

In contrast to X-rays the scattering power of neutrons does not vary systematically with the atomic number as illustrated in figure 5.12 (A). This feature allows information about e.g. the positions of lighter elements to be more reliably determined from neutron diffraction experiments in contrast to X-ray diffraction experiments. Furthermore, due to the fact that the neutron beam interacts with the atomic nuclei, random distributions of nuclear spin (if present) also causes incoherent scattering. The total neutron scattering power expressed in terms of scattering cross sections (as a function of energy transfer, ω, and scattering vector, Q, in analogy to scattering angle in XRPD) is a sum of coherent and incoherent scattering

$$S^{tot}(Q,\omega) = S_{coh}(Q,\omega) + S_{inc}(Q,\omega) \tag{5.10}$$

Simply speaking the coherent scattering carry structural information e.g. information about the atomic arrangement and the incoherent scattering carry information about the individual atoms i.e. information about the dynamics e.g. vibrations, rotations, and translational motion. In this respect, neutron scattering is particularly well suited for the study of hydrogen dynamics due to the outstanding incoherent scattering cross section[1].

Since the focus of this section is on hydrogen dynamics, coherent scattering will be excluded from the following formalism. The incoherent scattering cross section can be further decomposed into an elastic, *el*, and an inelastic term, *in*

$$S^{tot}_{inc}(Q,\omega) = S^{el}_{inc}(Q,\omega) + S^{in}_{inc}(Q,\omega) \tag{5.11}$$

where the elastic contribution comes from static (H-)atoms and the inelastic contribution comes from atoms in some sort of motion. If the energy transfer is small, say below 1-2 meV the inelastic part is referred to as *quasielastic* or S^{qe}_{inc}. Energy transfers in this range usually corresponds to diffusional motion of hydrogen. In a quasielastic neutron scattering (QENS) experiment $S^{tot}_{inc}(Q,\omega)$ is measured around zero energy transfer.

It has been shown [208, 209] that asserting certain assumptions like e.g. diffusing particles move from one site to a nearest neighbour site by random instantaneous jumps etc. S^{qe}_{inc} will

[1] In contrast to H, D does not have a nuclear spin. For this reason H is substituted with D in order to reduce/remove the large background contribution from incoherent scattering in neutron diffraction experiments.

have a Lorentzian shape with linewidth $\Gamma(Q)$

$$S_{inc}^{qe}(Q,\omega) = \frac{1}{\pi}\frac{\Gamma(Q)}{\Gamma(Q)^2+\omega^2} \tag{5.12}$$

In a *perfect* experiment $S_{inc}^{tot}(Q,\omega)$ will be a sum of a delta function arising from elastically scattered neutrons and a Lorentzian peak due originating from hydrogen motion

$$S_{inc}^{tot}(Q,\omega) = A_0\delta(\omega) + A_1 L(\omega,\Gamma) \tag{5.13}$$

where $\delta(\omega)$ is the elastic delta function, $A_0(Q)$ is the elastic incoherent structure factor, $L(\omega,\Gamma)$ is the quasielastic Lorentzian , with halfwidth Γ proportional to the H hopping rate [210]. The ratio of the amplitudes A_1/A_0 determine the fraction of mobile hydrogen atoms.

The hydrogen jump frequency is given as

$$\nu = \frac{1}{\tau} = \frac{\Gamma}{h} \tag{5.14}$$

where h is Planck's constant.

Nevertheless, in a *real* experiment $S_{inc}^{tot}(Q,\omega)$ is subject to instrumental broadening, which means that the measured total incoherent neutron scattering is actually a convolution of the left hand side of the above equation with the instrumental resolution function $R(Q,\omega)$.

$$S_{inc}^{tot}(Q,\omega) = R(Q,\omega) \otimes (A_0\delta(\omega) + A_1 L(\omega,\Gamma)) \tag{5.15}$$

For further introductory reading on QENS and inelastic neutron scattering refs. [33, 209, 211, 212] are referred to. For application of QENS to metal hydride systems see e.g. ref. [33, 213, 214, 215, 210, 216].

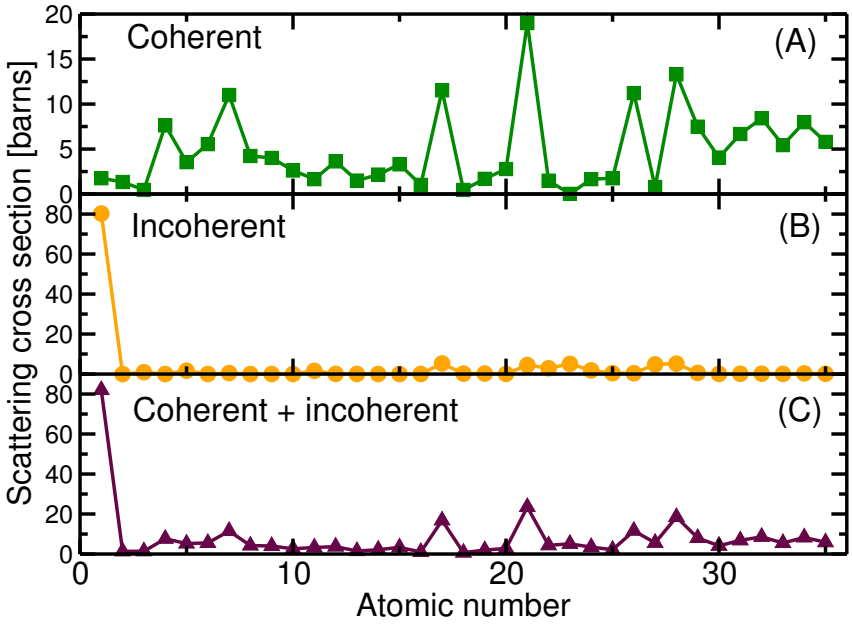

Figure 5.12: Neutron scattering cross sections for atomic numbers 1(H)-35(Br). (A) Coherent scattering cross section, (B) Incoherent scattering cross section, (C) Total scattering cross section. Data are taken from ref. [207].

Figure 5.13: The RITA-II triple-axis spectrometer at PSI

5.2.2 Experimental methods

The experiments described in this section have been conducted on the Paul Scherrer Institute (PSI)/Risø joint collaboration instrument RITA-II (Re-Invented Triple Axis Spectrometer) located at SINQ, PSI, CH-Villigen. The instrument has been described in detail elsewhere [217, 218, 219, 220], although a brief description of the instrument will be given in the following.

The RITA-II instrument is depicted in figure 5.13. The neutron beam is lead through the monochromator which is located in the green cylinder shaped structure to the left. The monochromatized beam passes through a collimator, a ^{3}He monitor, diaphragms before it hits the sample mounted on the sample table (shown in the middle of the picture). After the sample the scattered beam passes through another set of diaphragms and enters the detector tank (yellow to the right). In the detector tank the beam is focused by a multiple-bladed analyzator on a position sensitive detector (PSD).

Approx. 1 g $NaAlH_4$ powder (90 wt. % purity from Sigma-Aldrich) was loaded in a 10/12 mm cylindrical hollow core aluminum sample can in an argon filled glove box. The sample can was sealed using a lead o-ring. The sample was mounted in a CTI4 cryostat/furnace on the RITA-II sample table. Spectrometer setup: 40' collimator, ^{3}He monitor, diaphragm, sample, radially collimating BeO filter, diaphragm, 5-bladed focusing PG analyser, PSD detector. The purpose of the BeO filter is to cut off elastically scattered neutrons from the sample in order to improve the resolution function of the instrument.

The sample was cooled to 60 K in order to determine the spectrometer resolution function. The resolution function was determined be energy scans at 4 different Q-values: 2.15, 1.6, 1.0, and 0.4 Å. An energy scan was performed by changing the energy of the incoming neutron beam while measuring the scattered neutrons at a fixed energy . The sample was subsequently heated to 423 K where a new Q-scan was performed and the 4 energy scans were repeated. After cooling to room temperature another Q-scan was performed.

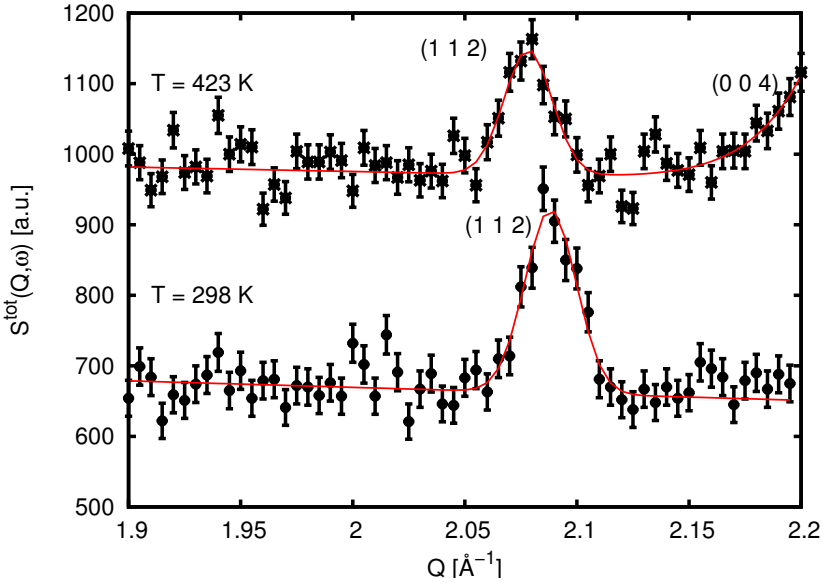

Figure 5.14: Q-scan of $NaAlH_4$ at 423 K and 298 K. The Q-scan at 423 K been scaled for illustrational purpose.

5.2.3 Results

In figure 5.14 Q-scans are shown of the sample at 423 K and after subsequent cooling to room temperature. As seen from the figure the diffraction peak at around Q=2.07 Å shifts upward after cooling due to lattice contraction. The peak corresponds to the (1 1 2) reflection. The fact that the reflection is present even after being kept at 423 K for several hours indicating that the sample have not transformed into Na_3AlH_6.

The total scattering function $S^{tot}(Q,\omega)$ was measured at 4 different Q-values at 60 K and the resolution function, $R(Q,\omega)$, was determined for each value of Q by fitting the measured QENS-spectra by the following function obtained by performing the convolution in Eq. 5.15 assuming that $R(Q,\omega)$ is described by the sum of a Gaussian (monochromator,analyser) and a Lorentzian (analyzer), with half widths σ and γ, respectively.

$$S^{tot}_{inc}(Q,\omega) = [G(\omega,\sigma) + T(\omega)A_R L(\omega,\gamma)] \otimes [A_0\delta(\omega) + A_1 L(\omega,\Gamma)] + B \quad (5.16)$$

$$= A_0 G(\omega,\sigma) + T(\omega)A_R A_0 L(\omega,\gamma) + T(\omega)A_R A_1 L(\omega,\gamma+\Gamma) + A_1 Voigt(\sigma,\Gamma) + B \quad (5.17)$$

As seen from the above equation a constant background term, B, have been included. Also a $T(\omega)$ term have been included in the Lorentzian part of the resolution function. This term represents the measured neutron transmission through the sample as a function of energy and is included in order to model the effect of the BeO filter on the tails of the resolution function. This accounts for elastically scattered neutrons reaching the detector due to the thermal diffuse scattering of the PG analysers.

In fitting the low temperature measurements the H-atoms are assumed to be frozen, thus the quasielastic line width (Γ) is set to zero when determining the resolution function. All other parameters are allowed to vary although in some cases it was necessary to fix the background in order to improve the fit. Having determined the instrumental resolution function at 60 K for all 4 values of Q, the QENS-spectra of corresponding Q-values at 423 K are fitted with the same model. However, this time σ and γ are fixed and Γ (the quasielastic line width) is allowed to

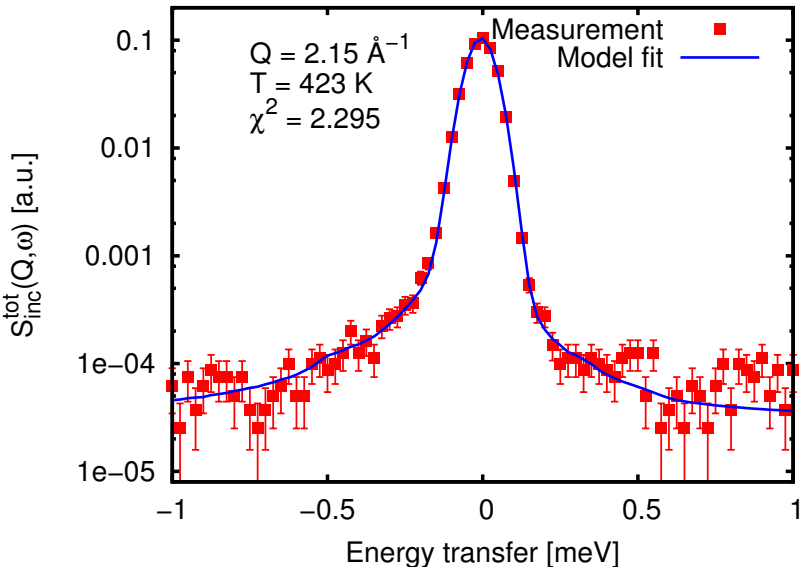

Figure 5.15: QENS spectrum of $NaAlH_4$ recorded at 423 K including a model fit.

vary. All QENS-spectra have been modelled using the **M***fit*[2] package for MATLAB®.

Figure 5.15 shows experimental data and model fit at 423 K and Q = 2.15 Å^{-1} using the resolution function determined at 60 K. As shown the model gives a reasonable fit to the experimental data. Although at energies below an energy transfer of -0.5 meV and above 0.5 meV there are some unexplained features. Figure 5.16 shows a decomposition of the model fit into its various components. As seen from the figure the major contribution is from the instrumental broadening of the elastically scattered neutrons. The contribution from inelastically scattered neutrons due to hydrogen motion contributes both to the 2. and 3. term of the model. Compared to the instrumental broadening the QENS-peak broadening is relatively small clearly illustrating the limitations of the RITA-II instrument.

Table 5.3 summarizes fitted values of the quasielastic Lorentzian halfwidths, Γ, as a function of scattering vector. Also listed are calculated hopping rates and A_1/A_0. Γ seems to be independent of Q. However, due to the uncertainty at low Q this work is not conclusive about the influence of Q on Γ. According to the Chudley-Elliott model [208] for long range diffusion of H-atoms the Q-dependency of Γ at large values of Q is given by

$$\Gamma(Q) = \frac{6hD}{l^2}\left(1 - \frac{\sin Ql}{Ql}\right) \tag{5.18}$$

where l is the hydrogen jump length and D is the hydrogen diffusion coefficient. This type of behaviour is observed for several types of intermetallic hydrides [33, 210, 221, 222, 223]. The lack of a Q-dependency on Γ for $NaAlH_4$ might suggest localized H-motion [210]. However, multiple scattering and the high hydrogen content [33] may also be important as well as trapping [224]. Only a small fraction (<10 %) of the H-atoms are able to move (A_1/A_0).

In addition to the QENS experiments, the Q-dependency of the total scattering function $S^{tot}(Q)$ was determined from Q=0-4 Å in order to find the mean square displacement of hydrogen, $< u^2 >$ at room temperature. Neglecting coherent scattering the total scattering function is given as [215, 216, 222]

[2]Available from `http://www.ill.fr/tas/matlab/doc/mfit4/mfit.html`

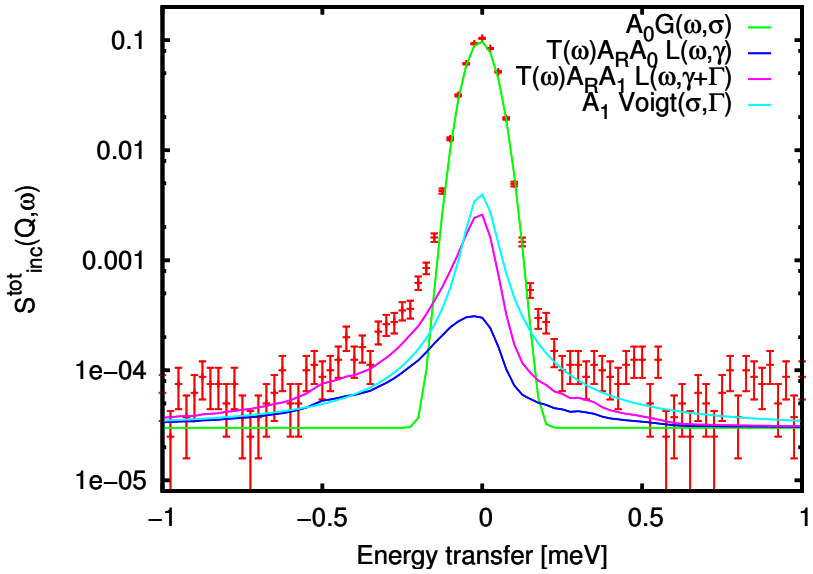

Figure 5.16: QENS spectrum of $NaAlH_4$ recorded at 423 K with a model fit decomposed into the four separate model contributions.

	Q [Å^{-1}]			
	0.4	1.0	1.6	2.15
Γ [μeV]	76±79	73±50	71±60	61±19
$1/\tau$ [s^{-1}]	1.9·10^{10}	1.8·10^{10}	1.8·10^{10}	1.4·10^{10}
A_1/A_0	0.04	0.06	0.04	0.10

Table 5.3: Measured quasielastic halfwidths Γ as a function of Q and corresponding H-hopping rates.

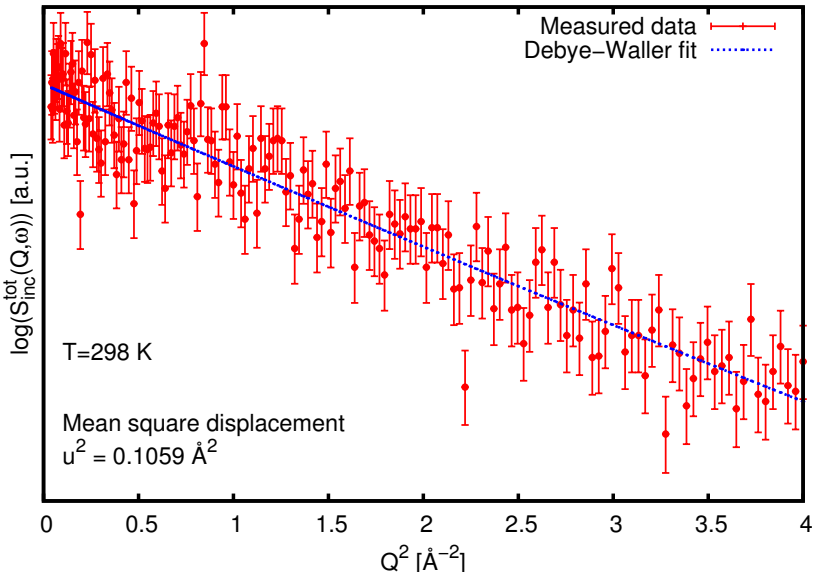

Figure 5.17: Experimentally determined influence of Q on the total scattering function of $NaAlH_4$ including a Debye-Waller fit.

$$S^{tot}(Q) = \exp\left(-\frac{1}{3} < u^2 > Q^2\right) S_{inc}(Q) \tag{5.19}$$

where the exponential term is the so called isotropic Debye-Waller factor [33, 225]. Thus plotting $\ln\left(S^{tot}(Q)\right)$ as a function of Q^2 should yield a straight line with the following formula

$$\ln\left(S^{tot}(Q)\right) = \ln\left(S_{inc}(Q)\right) - \frac{1}{3} < u^2 > Q^2 \tag{5.20}$$

where the mean square displacement is found as the slope. A plot of $\ln\left(S^{tot}(Q)\right)$ as a function of Q^2 including a model fit according to Eq. 5.20 is shown in figure 5.17. As seen from the figure the model gives an excellent description of the measurements within experimental uncertainty. The slope is 0.1059 Å^2 $= \frac{1}{3} < u^2 >$ giving a mean square displacement of $< u^2 >= 0.0353$ Å^2.

In structure determination using X-ray or neutron scattering usually an isotropic temperature factor, B_{iso} is reported, which is related to the mean square displacement in the following manner

$$B_{iso} = 8\pi^2 < u^2 > \tag{5.21}$$

Table 5.4 summarizes a comparison of the experimentally determined mean square displacement of hydrogen in $NaAlH_4$ with mean square displacement of deuterium in $NaAlH_4$ and $LiAlH_4$ from neutron structure determination and with DFT calculations of H in $NaAlH_4$. It is evident from the table that the determined mean square displacement of hydrogen using incoherent neutron scattering is in excellent agreement with both the theoretically determined value and temperature factors from structure determination at room temperature. The mean square displacement of hydrogen in $LiAlH_4$ is similar to $NaAlH_4$.

5.3 Summary

The effect of ball milling and Ti-doping on the apparent activation energy of the two-step dehydrogenation of $LiAlH_4$ has been investigated. Ball milling leads to a reduction in the crystallite

Hydride	$< u^2 >$ [Å^2]	T [K]	Ref.
$NaAlH_4$	0.0353	298	This work
$NaAlH_4$	0.0317	298	[226]
$NaAlH_4$	0.0197	≈0	[226]
$NaAlD_4$	0.0332	298	[227]
$NaAlD_4$	0.0310	295	[228]
$NaAlD_4$	0.0161	8	[228]
$LiAlD_4$	0.0355	295	[121]
$LiAlD_4$	0.0171	8	[121]

Table 5.4: Mean square displacement of hydrogen and deuterium in $NaAlH_4$ and $LiAlH_4$. The listed mean square displacement for $LiAlH_4$ are an average over all 4 different hydrogen positions.

size, which has a strong positive effect on the rate of the first dehydrogenation step, indicating transport limitations, probably diffusion. The second step is insensitive to the reduction in diffusion path indicating an intrinsic process, e.g. bond breaking, to be rate limiting. The determined apparent activation energies for both reaction steps shows no effect from Ti-doping, suggesting that a prefactor effect is responsible for the improved kinetics. The hydrogen mobility in $NaAlH_4$ has been studied with QENS at the RITA-II spectrometer. Due to instrumental limitations, no solid conclusions can be made regarding hydrogen diffusion in $NaAlH_4$. Nevertheless, indications of a H-jump process with a rate of 10^{10} jumps/s are found, and the fact that less than 10% of the hydrogen atoms are mobile at 150 °C. The mean square displacement of hydrogen has been established more reliably to approx. 0.04 Å^2.

Chapter 6

Conclusions and outlook

6.1 Magnesium based hydrides

6.1.1 Alloying effects

The dehydrogenation kinetics of air-exposed magnesium hydride along with Mg-Cu and Mg-Al based hydrides have been investigated by means of time resolved *in situ* X-ray powder diffraction. It has been shown that X-ray powder diffraction is indeed a powerful tool for studying the dynamics of structural changes in hydride systems – even with the X-rays being generated by a rotating anode the intensity is sufficient to obtain an adequate time resolution allowing kinetic parameters to be extracted from a quantitative analysis of consecutive diffraction patterns. The main result obtained from the investigated magnesium based hydrides is the fact that the resistance towards contamination by oxygen i.e. due to the formation of a dense surface oxide shell retarding the transport of hydrogen atoms, can be improved significantly by alloying with both Al and Cu. In addition the dehydrogenation mechanism of MgH_2/Al is elucidated and it is found that during dehydrogenation the formed Mg (from dehydrogenation of MgH_2) rapidly diffuses into the Al-matrix, thereby forming a solid solution of Mg in Al, from where an Mg-Al alloy is formed.

6.1.2 The compensation effect

From a literature survey on magnesium based hydrides in combination with the results obtained in this thesis it is generally found that the determined apparent activation energies of the hydrogenation/dehydrogenation depends strongly on the sample pretreatment. Unless magnesium is alloyed as discussed above, the lack of *activation* generally leads to a high apparent activation energy. This effect is rationalized in terms of a closed oxide shell retarding the kinetics. On the other hand, activated samples and alloyed samples display a low apparent activation energy due to either a break up of the oxide layer of a more hydrogen permeable oxide. The large variations in apparent activation energies are accompanied by proportionally large variations in the apparent prefactors as determined from an Arrhenius analysis, corresponding to a clear *compensation effect* (CE). A detailed analysis of the CE leads to the conclusion, that whenever an Arrhenius analysis is used to link apparent activation energies and apparent prefactors a CE is forced, hence it is not a physical effect. This conclusion is not restricted to hydride systems, in fact it has also been shown to be applicable to heterogeneous catalysis. It might very well be the primary explanation to the fact that CE is observed in so many different sciences.

6.2 Complex hydrides

6.2.1 Lithium aluminum hydride

The dehydrogenation kinetics of both as-received, ball milled, and Ti-doped $LiAlH_4$ has been investigated. For the as-received samples it is found that, although melting of $LiAlH_4$ occurs before dehydrogenation in linear heating rate experiments, the kinetics of dehydrogenation is sufficiently fast to allow the study of the direct decomposition at isothermal conditions below the melting point of $LiAlH_3$. Applying different periods of ball milling both the particle size and the crystallite size is reduced. A strong correlation between the crystallite size of $LiAlH_4$ and the dehydrogenation kinetics of the first dehydrogenation step (formation of Li_3AlH_6) is found, suggesting mass transfer e.g. diffusion to be limiting the kinetics. Interestingly, the second dehydrogenation step (formation of LiH) is insensitive to crystallite size reductions, suggesting that this reaction step is *not* subject to diffusional limitations but probably the intrinsic kinetics instead. This clearly illustrates the need of a suitable catalyst/doping-agent, not only to make hydrogen storage in $LiAlH_4$ reversible, but indeed also in order to speed up the hydrogenation/dehydrogenation of Li_3AlH_6, which is not possible solely by mechanical treatment. Investigations involving Ti-doping reveal that the apparent activation energy of both dehydrogenation steps is unaffected by the presence of Ti. However, the decomposition temperatures of both steps shifts approx. 50 °C downwards upon doping, clearly suggesting a prefactor effect, e.g. an increased number of reaction sites, to be responsible for the improved kinetics. This also indicates, that the effect of Ti-doping of $LiAlH_4$ is likely different on the microscopic scale than Ti-doping of $NaAlH_4$.

6.2.2 Sodium aluminum hydride

The hydrogen atomic mobility in $NaAlH_4$ has been studied by means of Quasielastic Neutron Scattering (QENS). To the best of my knowledge the experiments constitutes the first application of neutron spectroscopy in order to study hydrogen dynamics in complex hydrides. The results are of preliminary nature and suffer from poor instrumental resolution. The results indicate the following about the hydrogen dynamics in $NaAlH_4$: i) only a small fraction (<10%) of the available hydrogen atoms are able to move ii) hydrogen jumps are localized and proceed with a rate of approx. 10^{10} s^{-1}@150 °C. In addition to the QENS experiments elastic scattering experiments allow the estimation of the room temperature mean square displacement of H-atoms in the $NaAlH_4$ lattice. The result is in perfect agreement with both previous estimates based on neutron diffraction experiments on $NaAlD_4$ and theoretical predictions on $NaAlH_4$.

6.3 Suggestions for future work

6.3.1 Synthesis, catalysis, and reversibility of Li_3AlH_6

$NaAlH_4$ which is the prototype complex hydride hydrogen storage candidate is limited by a theoretical hydrogen capacity of 5.6 wt.% (assuming NaH as the final product), and it is too stable for operation with a conventional PEMFC. Interestingly, Li_3AlH_6, which can be sythezied by ball milling LiH and $LiAlH_4$ in a 2:1 stoichiometry [111, 114], also stores 5.6 wt.% assuming LiH as the final product. The apparent advantage of Li_3AlH_6 is that only one reaction step is involved and that thermodynamics allow hydrogen to be delivered at a lower temperature compared to $NaAlH_4$ [111, 105, 112, 116]. It seems as a mystery why this material has not been investigated in more detail with respect to hydrogen storage. Indications of a reversible reaction after doping with Ti has been reported in only a single paper [111]. It is my opinion that it could be highly interesting to explore the cyclic reversibility including the cyclic hydrogen capacity of

this material. Also the plateau pressure at various temperatures also needs to be established more precisely.

6.3.2 Neutron scattering experiments

Working with neutron scattering as a probe for hydrogen dynamics in $NaAlH_4$ has really been an eyeopener for me. While a few studies on the hydrogen dynamics in $NaAlH_4$ using NMR and mechanical relaxation have been reported [229, 230, 231], it is, in my opinion, difficult to extract unidirectional information from these findings. I think QENS is superior to these techniques, and conducting QENS experiments on a high resolution instrument could be very helpful in mapping the hydrogen dynamics in $NaAlH_4$ both for the un-doped material but much more importantly also for $NaAlH_4$ under the influence of Ti.

Bibliography

[1] United Nations Populations Division, World population prospects: The 2004 revision population database (June 2005).
URL http://esa.un.org/unpp/

[2] J. H. Wood, G. R. Long, D. F. Morehouse, Long-Term World Oil Supply Scenarios, Energy Information Administration (August 2004).
URL http://www.eia.doe.gov/pub/oil_gas/petroleum/feature_articles/2004/-worldoilsupply/oilsupply04.html

[3] B. J. Fleay, Climaxing oil: How will transport adapt?, Institute for Science and Technology Policy Murdoch University, Western Australia (November 1998).
URL http://wwwistp.murdoch.edu.au/teaching/N212/n212content/topics/-topic5/00content.html

[4] BP Distribution Services, BP Statistical Review of World Energy 2004 (June 2004).
URL http://www.bp.com/statisticalreview2004

[5] M. E. Mann, R. S. Bradley, M. K. Hughes, Geophys. Res. Lett. 26 (1999) 759–762.

[6] M. E. Mann, R. S. Bradley, M. K. Hughes, Nature 392 (1998) 779–787.

[7] E. Friis-Christensen, K. Lassen, Science 254 (1991) 698–700.

[8] J. A. Turner, Science 305 (2004) 972–.

[9] J. A. Turner, Science 285 (1999) 687–689.

[10] M. Schrope, Nature 414 (2001) 682–684.

[11] R. F. Service, Science 305 (2004) 958–961.

[12] G. W. Crabtree, M. S. Dresselhaus, M. V. Buchanan, Physics Today December (2004) 39–45.

[13] M. Grätzel, Nature 414 (2001) 338–344.

[14] International Energy Agency, Key world energy statistics (June 2004).
URL http://www.iea.org/dbtw-wpd/Textbase/nppdf/free/2004/keyworld2004.pdf

[15] I. Chorkendorff, J. W. Niemantsverdriet, Concepts of modern catalysis and kinetics, Wiley-VCH, 2003.

[16] L. Schlapbach, A. Züttel, Nature 414 (2001) 353–358.

[17] B. C. H. Steele, A. Heinzel, Nature 414 (2001) 345–352.

[18] G. Simbolotti, Is hydrogen an energy product?, International Energy Agency, Energy Statistics Working Group Meeting (presentation) (November 2004).
URL http://www.iea.org/Textbase/work/2004/eswg/-06_Hydrogen_G_Simbolotti.pdf

[19] A. S. Pedersen, Hydrogen storage with special emphasis on metal hydrides, in: L. S. Petersen, H. Larsen (Eds.), Proceedings Risø International Energy Conference, 2003, pp. 236–243.

[20] M. Dresselhaus, G. Crabtree, M. Buchanan (Eds.), Basic research needs for the hydrogen economy, Argonne National Laboratory, Argonne, IL 60439, USA, 2003.

[21] H. Larsen, R. Feidenhans'l, L. Sønderberg Petersen (Eds.), Risø Energy Report 3: Hydrogen and its competitors, Risø-R-1469(en), Risø National Laboratory, Roskilde, Denmark, 2004.

[22] Key Tasks for future European Energy R&D, EUR 21352, European Commision, Directorate-General for Research Sustanable Energy Systems, Brussels, Belgium, 2005.

[23] Towards the European Energy Research Area, EUR 21353, European Commision, Directorate-General for Research Sustanable Energy Systems, Brussels, Belgium, 2005.

[24] U. S. Department of Energy, Energy Efficiency and Renewable Energy, Targets for on-board hydrogen storage systems (2005).
URL http://www.eere.energy.gov/hydrogenandfuelcells/pdfs/-freedomcar_targets_explanations.pdf

[25] A. Züttel, Materials Today 9 (2003) 24–33.

[26] A. Züttel, Naturwissenschaften 91 (2004) 157–172.

[27] H. Lee, J. w. Lee, D. Y. Kim, J. Park, Y. T. Seo, H. Zeng, I. L. Moudrakowski, C. I. Ratcliffe, J. A. Ripmeester, Nature 434 (2005) 743–746.

[28] N. L. Rosi, J. Eckert, M. Eddaoudi, D. T. Vodak, J. Kim, M. O'Keeffe, O. M. Yaghi, Science 300 (2003) 1127–1129.

[29] G. Sandrock, G. Thomas, Appl. Phys. A. 72 (2001) 153–155.

[30] Hydride information center, sandia national laboratories.
URL http://hydpark.ca.sandia.gov

[31] Webelemets^{TM} periodic table.
URL http://www.webelements.com/

[32] J. Sachs (Ed.), Metal Prices in the United States through 1998, U.S. Department of the Interior and U.S. Geological Survey Minerals Information, 2005.
URL http://minerals.usgs.gov/minerals/pubs/metal_prices/

[33] L. Schlapbach (Ed.), Hydrogen in Intermetallic Compounds II, Vol. 67 of Topics in Applied Physics, Springer-Verlag, 1992.

[34] J. Bloch, J. Alloys Comps. 312 (2000) 135–153.

[35] C. S. Wang, X.-. H. Wang, Q. Lei, P. Chen, Q. D. Wang, Int. J. Hydrogen Energy 21 (1996) 471–478.

[36] M. Martin, G. Gommel, C. Borkhardt, E. Fromm, J. Alloys Comps. 238 (1996) 193–201.

[37] G. E. Fernández, D. Rodríguez, G. Meyer, Int. J. Hydrogen Energy 23 (1998) 1193–1196.

[38] C. N. Park, J. Y. Lee, J. Less-Common Met. 83 (1982) 39–48.

[39] J.-. Y. Lee, H. H. Park, J. S. Han, J. Mater. Sci. 21 (1986) 3952–3956.

[40] G. Friedlmeier, M. Groll, J. Alloys Comps. 253-254 (1997) 550–555.

[41] A. Karty, J. Grunzweig-Genossar, P. Rudman, J. Appl. Phys. 50 (11) (1979) 7200–7209.

[42] A. Inomata, H. Aoki, T. Miura, J. Alloys Comps. 278 (1998) 103–109.

[43] J. F. Fernandez, C. R. Sanchez, J. Alloys Comps. 340 (2002) 189–198.

[44] C. Stander, J. Inorg. Nucl. Chem. 39 (1977) 221–223.

[45] K.-C. Chou, Q. Li, Q. Lin, L.-J. Jiang, K.-D. Xu, Int. J. Hydrogen Energy 30 (2005) 301–309.

[46] Q. Li, K.-C. Chou, K.-D. Xu, Q. Lin, L.-J. Jiang, F. Zhan, J. Alloys Comps. 387 (2005) 86–89.

[47] L. Belkbir, E. Joly, N. Gerard, J. C. Achard, A. Percheron-Guegan, J. Less-Common Met. 73 (1980) 69–77.

[48] A. Yoshida, T. Naka, Y. Ohkita, Trans. JSME B 56 (522) (1990) 536–540.

[49] W. A. Johnson, R. F. Mehl, Trans. A.I.M.E. 135 (1939) 416–458.

[50] M. Avrami, J. Chem. Phys. 7 (1939) 1103–1112.

[51] M. Avrami, J. Chem. Phys. 8 (1940) 212–224.

[52] M. Avrami, J. Chem. Phys. 9 (1941) 177–184.

[53] C. H. Bamford, C. F. H. Tipper (Eds.), Reactions in the solid state, Vol. 22 of Comprehensive chemical kinetics, Elsevier, 1980.

[54] K. Kelton, Mater. Sci. Eng. A226-228 (1997) 142–150.

[55] K. B. Gerasimov, E. L. Goldberg, E. Y. Ivanov, J. Less-Common Met. 131 (1987) 99–107.

[56] A. Léon, E. J. Knystautas, J. Huot, R. Schulz, J. Alloys Comps. 345 (2002) 158–166.

[57] A. Léon, E. J. Knystautas, J. Huot, R. Schulz, Thin Solid Films xxx (2005) xxx–xxx.

[58] J. Smith, H. Van Ness, M. Abbott, Introduction to Chemical Engineering Termodynamics, fifh Edition, McGraw-Hill, 1996.

[59] D. R. Lide (Ed.), Handbook of Chemistry and Physics, 78th Edition, CRC Press LLC, 1997.

[60] W. M. Mueller, J. P. Blackledge, G. G. Libowitz (Eds.), Metal Hydrides, Academic Press, Inc., 1968.

[61] U. S. Department of Energy, Last checked april 2004.
URL `http://www.eere.energy.gov/hydrogenandfuelcells/hydrogen/storage.html`

[62] E. Wiberg, E. Amberger, Hydrides of the elements of main groups I-IV, Elsevier publishing company, Amsterdam, 1971.

[63] W. Grochala, P. P. Edwards, Chem. Rev. 104 (2004) 1283–1315.

[64] H. Smithson, C. A. Marianetti, D. Morgan, A. Van der Ven, A. Predith, G. Ceder, Phys. Rev. B 66 (2002) 144107–1.

[65] C. Y. Xiao, J. L. Yang, K. M. Deng, Z. H. Bian, K. L. Wang, J. Phys.: Condens. Matter 6 (1994) 8539–8547.

[66] R. Yu, P. K. Lam, Phys. Rev. B 37 (1988) 8730–8737.

[67] T. Norikate, M. Aoki, S. Towata, Y. Seno, Y. Hirose, E. Nishibori, M. Takata, M. Sakata, Appl. Phys. Lett. 81 (2002) 2008–2010.

[68] P. Vajeeston, P. Ravindran, A. Kjekhus, H. Fjellvåg, Appl. Phys. Lett. 84 (2004) 34–36.

[69] P. Villars (Ed.), Pearson's Handbook Desk Edition, Vol. 1, ASM International, 1997.

[70] P. Villars (Ed.), Pearson's Handbook Desk Edition, Vol. 2, ASM International, 1997.

[71] P. Nordlander, J. K. Nørskov, F. Besenbacher, J. Phys. F: Met. Phys. 16 (1986) 1161–1171.

[72] J. K. Nørskov, F. Besenbacher, J. Less-Common Met. 130 (1987) 475–490.

[73] O. B. Christensen, P. Stoltze, K. W. Jacobsen, J. K. Nørskov, Phys. Rev. B 41 (18) (1990) 12413–12423.

[74] K. Miwa, A. Fukumoto, Phys. Rev. B 64 (2002) 155114–1.

[75] C. Wolwerton, V. Ozoliņš, M. Asta, Phys. Rev. B 69 (2004) 144109–1.

[76] G. Alefeld, J. Völkl (Eds.), Hydrogen in metals II, Vol. 29 of Topics in Applied Physics, Springer-Verlag, 1978.

[77] J. K. Nørskov, A. Houmøller, P. K. Johansson, B. I. Lundquist, Phys. Rev. Lett. 46 (4) (1981) 257–260.

[78] B. Hammer, J. K. Nørskov, Nature 376 (1995) 238–240.

[79] J. Harris, S. Andersson, Phys. Rev. Lett. 55 (1985) 1583–1586.

[80] J. Harris, S. Andersson, Appl. Phys. A. 47 (1988) 63–71.

[81] P. T. Sprunger, E. W. Plummer, Surf. Sci. 307-309 (1994) 118–123.

[82] P. T. Sprunger, E. W. Plummer, Chem. Phys. Lett. 187 (1991) 559–564.

[83] P. B. Rasmussen, P. M. Holmblad, H. Christoffersen, P. A. Taylor, I. Chorkendorff, Surf. Sci. 287-288 (1993) 79–.

[84] H. J. Robota, W. Vielhaber, M. C. Lin, J. Segner, G. Ertl, Surf. Sci. 155 (1985) 101–120.

[85] K.-H. Ernst, E. Schwartz, K. Christmann, J. Chem. Phys. 101 (1994) 5388–5401.

[86] W. Wolf, P. Herzig, Journal of Physics: Condensed Matter 12 (21) (2000) 4535–4551.

[87] M. Gupta, Phys. Rev. B. 25 (1982) 1027–1038.

[88] A. Zaluska, L. Zaluski, J. Ström-Olsen, Appl. Phys. A 72 (2001) 157–165.

[89] A. Zaluska, Z. L., J. Ström-Olsen, J. Alloys Comps. 288 (1999) 217–225.

[90] J. Pelletier, J. Huot, M. Sutton, R. Schulz, A. Sandy, L. Lurio, S. Mochrie, Phys. Rev. B 63 (2001) 052103.

[91] C. X. Shang, M. Bououdina, Y. Song, Z. X. Guo, Int. J. Hydrogen Energy 29 (2004) 73–80.

[92] W. Oelerich, T. Klassen, R. Bormann, J. Alloys Comps. 322 (2001) L5–L9.

[93] T. Vegge, L. S. Hedegaard-Jensen, J. Bonde, T. R. Munter, J. K. Nørskov, J. Alloys Comps. 386 (2004) 1–7.

[94] J. J. Reilly, R. H. Wiswall, Inorg. Chem. 6 (1967) 2220–2223.

[95] J. J. Reilly, R. H. Wiswall, Inorg. Chem. 7 (1968) 2254–2256.

[96] A. Reiser, B. Bogdanović, K. Schlichte, Int. J. Hydrogen Energy 25 (2000) 425–430.

[97] B. Bogdanović, M. Schwickardi, J. Alloys Comps. 253-254 (1997) 1–9.

[98] D. L. Anton, J. Alloys Comps. 356 (2003) 400–404.

[99] K. J. Gross, E. H. Majzoub, S. W. Spangler, J. Alloys and Comps. 356-357 (2003) 423–428.

[100] G. Sandrock, K. Gross, G. Thomas, C. Jensen, D. Meeker, S. Takara, J. Alloys Comps. 330-332 (2002) 686–701.

[101] A. Leon, O. Kirchner, J. Rothe, M. Fichtner, J. Phys. Chem. B. 108 (42) (2004) 16372–16376.

[102] M. Felderhoff, K. Klementiev, W. Grunert, B. Spliethoff, B. Tesche, J. M. B. von Colbe, B. Bogdanović, M. Hartel, A. Pommerin, F. Schuth, C. Weidenthaler, Phys. Chem. Chem. Phys. 6 (17) (2004) 4369–4374.

[103] H. W. Brinks, C. M. Jensen, S. S. Srinivasan, B. C. Hauback, D. Blanchard, K. Murphy, J. Alloys Comps. 376 (2004) 215–221.

[104] J. A. Dilts, E. C. Ashby, Inorg. Chem. 11(6) (1972) 1230–1236.

[105] T. N. Dymova, D. P. Aleksandrov, V. N. Konoplev, T. A. Silina, A. S. Sizareva, Russ. J. Coord. Chem. 20 (4) (1994) 279–285.

[106] D. Blanchard, H. W. Brinks, B. C. Hauback, P. Norby, Mater. Sci. Eng. B. 108 (2004) 54–59.

[107] J. W. Wiench, V. P. Balema, V. K. Pecharsky, M. Pruski, J. Solid State Chem. 177 (2004) 648–653.

[108] V. P. Balema, L. Balema, Phys. Chem. Chem. Phys. 7 (6) (2005) 1310–1314.

[109] M. B. Smith, G. E. Bass Jr., J. Chem. Eng. Data 8(3) (1963) 342–346.

[110] O. M. Løvvik, S. M. Opalka, H. W. Brinks, B. C. Hauback, Phys. Rev. B 69 (2004) 134117.

[111] J. Chen, N. Kuriyama, Q. Xu, H. T. Takeshita, T. Sakai, J. Phys. Chem. B. 105 (2001) 11214–11220.

[112] S. C. Chung, H. Morioka, J. Alloys Comps. 372 (2004) 92–96.

[113] V. P. Balema, K. W. Dennis, V. K. Pecharsky, Chem. Comm. (17) (2000) 1665–1666.

[114] L. Zaluski, A. Zaluska, J. O. Ström-Olsen, J. Alloys Comps. 290 (1999) 71–78.

[115] M. D. Resan, M. Hampton, J. K. Lomness, D. K. Slattery, Int. J. Hydrogen Energy In pres.

[116] J. K. Kang, J. Y. Lee, R. P. Muller, W. A. Goddard III, J. Chem. Phys. 121 (21) (2004) 10623–10633.

[117] V. P. Balema, V. K. Pecharsky, K. W. Dennis, J. Alloys Comps. 313 (2000) 69–74.

[118] V. P. Balema, J. W. Wiench, K. W. Dennis, M. Pruski, V. K. Pecharsky, J. Alloys Comps. 329 (2001) 108–114.

[119] D. K. Slattery, M. D. Hampton, C. Read, FY 2003 Progress report for Hydrogen, Fuel Cells, and Infrastructure Technologies program, U.S. Department of Energy, 2003, Ch. III: Complex hydrides for hydrogen storage.

[120] N. Sklar, B. Post, Inorg. Chem. 6 (1967) 669–.

[121] B. C. Hauback, H. Brinks, H. W. Fjellvåg, J. Alloys. Comps. 346 (2002) 184–189.

[122] C. M. Andrei, J. C. Walmsley, H. W. Brinks, R. Holmestad, B. C. Blanchard, D. Hauback, G. A. Botton, J. Phys. Chem. B. In press.

[123] J. O. Jensen, Q. Li, R. He, C. Pan, N. J. Bjerrum, J. Alloys Comps. xxx (In press 2005) xx–xx.

[124] K. J. Gross, J. C. Thomas, G., J. Alloys Comps. 330-332 (2002) 683–690.

[125] A. R. West, Solid State Chemistry and its Applications, John Wiley & Sons Ltd., 1984.

[126] S. Elliott, Physics and Chemistry of Solids, John Wiley & Sons Ltd., 1998.

[127] M. M. Woolfson, An Introduction to X-ray crystallography, 2nd Edition, Cambrigde University Press, 1997.

[128] R. A. Young (Ed.), The Rietveld Method, Oxford University Press, 1993.

[129] L. McCusker, R. Von Dreele, D. Cox, D. Louër, P. Scardi, J. Appl. Cryst. 32 (1999) 36–50.

[130] T. R. Jensen, A. Andreasen, T. Vegge, J. W. Andreasen, K. Ståhl, F. Besenbacher, A. Molenbroek, M. M. Nielsen, A. S. Pedersen, Int. J. Hydrogen Energy Submitted.

[131] J. F. Fernandez, C. R. Sanchez, J. Alloys Comps. 356-357 (2003) 348–352.

[132] J. Han, M. Pezat, J.-Y. Lee, J. Less-Common Met. 130 (1987) 395–402.

[133] M. Martin, G. Gommel, C. Borkhardt, E. Fromm, J. Alloys Comps. 238 (1996) 193–.

[134] A. Andreasen, M. B. Sørensen, R. Burkarl, B. Møller, A. M. Molenbroek, A. S. Pedersen, J. W. Andreasen, M. M. Nielsen, T. R. Jensen, J. Alloys Comps. Accepted.

[135] J. L. Murray, Bull. Alloy Phase Diagrams 3 (1982) 60–74.

[136] J. Gubicza, M. Kassem, G. Ribáric, T. Ungár, Mater. Sci. Eng. A. 372 (2004) 115–122.

[137] M. H. Mintz, Z. Gavra, G. Kimmel, J. Less-Common Met. 74 (1980) 263–270.

[138] K. S. Nahm, W. Y. Kim, S. P. Hong, W. Y. Lee, Int. J. Hydrogen Energy 17 (5) (1992) 333–338.

[139] A. K. Galwey, Adv. Catal 26 (1977) 247–322.

[140] G. C. Bond, M. A. Keane, H. Kral, J. A. Lercher, Catal. Rev. -Sci. Eng. 42(3) (2000) 319–327.

[141] H. A. Wilson, Philos. Trans. A. 208 (1908) 247.

[142] F. H. Constable, Proc. Roy. Soc. London A. 108 (1925) 355.

[143] G. C. Bond, Catal. Today 49 (1999) 41–48.

[144] G. C. Bond, A. D. Hooper, J. C. Slaa, A. O. Taylor, J. Catal. 163 (1996) 319–327.

[145] T. Bligaard, K. Honkala, A. Logadottir, J. K. Nørskov, S. Dahl, C. J. H. Jacobsen, J. Phys. Chem. B. 107 (2003) 9325–9331.

[146] A. Wootsch, Z. Páal, J. Catal. 205 (2002) 86–96.

[147] G. A. Somorjai, Introduction to Surface Chemistry and Catalysis, John Wiley & Sons, 1994.

[148] G. V. Loukova, A. I. Mikhailov, A. E. Shilov, Kinet. Catal. 43(5) (2002) 746–747.

[149] J. B. Miller, H. R. Siddiqui, S. M. Gates, J. N. Russell Jr., J. T. Yates Jr., J. C. Tully, M. J. Cardillo, J. Chem. Phys. 87(11) (1987) 6725–6732.

[150] D. L. S. Nieskens, A. P. van Bravel, J. W. Niemantsverdriet, Surf. Sci. 546 (2003) 159–169.

[151] R. W. Keyes, J. Chem. Phys 29(3) (1958) 467–475.

[152] J. Barth, H. Brune, B. Fischer, J. Weckesser, K. Kern, Phys. Rev. Lett. 84(8) (2000) 1732–1735.

[153] C. Ratsch, M. Scheffler, Phys. Rev. B. 58(19) (2001) 13163–13166.

[154] S. Ovesson, A. Bogicevic, G. Wahnström, B. I. Lundqvist, Phys. Rev. B. 64 (2001) 125423.

[155] B. J. McCoy, J. Chem. Phys. 80(8) (1984) 3629–3631.

[156] E. Peacock-Lopéz, H. Suhl, Phys. Rev. B. 26(7) (1982) 3774–3782.

[157] A. Andreasen, M. B. Sørensen, R. Burkarl, B. Møller, A. M. Molenbroek, A. S. Pedersen, T. R. Jensen, Appl. Phys. A Accepted.

[158] B. Vigeholm, Chemical energy storage based on metal hydrides, Tech. Rep. Risø-M-2608, Risoe National Laboratory, DK-4000 Roskilde, Denmark, (In Danish) (1989).

[159] A. Pedersen, K. Jensen, B. Larsen, B. Vigeholm, J. Less-Common Met. 131 (1987) 31–40.

[160] O. Boser, J. Less-Common Met. 46 (1976) 91–99.

[161] M. Miyamoto, K. Yamaji, Y. Nakata, J. Less-Common Met. 89 (1983) 111–116.

[162] M. Ron, J. Alloys Comps. 283 (1999) 178–191.

[163] Z. Haberman, J. Bloch, M. H. Mintz, I. Jakob, J. Alloys Comps. 253-254 (1997) 556–559.

[164] A. Osovizky, J. Bloch, M. H. Mintz, I. Jakob, J. Alloys Comps. 245 (1996) 168–178.

[165] J. Bloch, J. Alloys Comps. 270 (1998) 194–202.

[166] V. Fournier, P. Marcus, I. Olejord, Surf. Interface Anal. 34 (2002) 494–497.

[167] C. Chen, S. J. Splinter, T. Do, N. S. McIntyre, Surf. Sci. 382 (1997) L652–L657.

[168] T. Do, S. J. Splinter, C. Chen, N. S. McIntyre, Surf. Sci. 387 (1997) 192–198.

[169] B. Vigeholm, J. Kjøller, B. Larsen, A. S. Pedersen, Int. J. Hydrogen Energy 8(10) (1983) 809–817.

[170] C. Chen, N. S. McIntyre, Corrosion Science 40 (1998) 1697–1709.

[171] R. Gonzalez, Y. Chen, K. L. Tang, Phys. Rev. B. 26 (8) (1982) 4637–4645.

[172] T. Vegge, Phys. Rev. B. 70 (2004) 035412.

[173] J. Töpler, H. Buchner, H. Säufferer, K. Knorr, W. Prandl, J. Less-Common Met. 88 (1982) 397.

[174] P. Hjort, A. Krozer, B. Kasemo, J. Alloys Comps. 237 (1996) 74–80.

[175] A. S. Pedersen, B. Vigeholm, J. Kjøller, B. Larsen, Int. J. Hydrogen Energy 12 (1987) 765–771.

[176] A. S. Pedersen, B. Larsen, Int. J. Hydrogen Energy 18 (1993) 297–300.

[177] M. Au, J. Wu, Q. Wang, Int. J. Hydrogen Energy 20 (1995) 141–150.

[178] P. Selvam, B. Viswanathan, C. S. Swamy, V. Srinizasan, Int. J. Hydrogen Energy 13 (1988) 87–94.

[179] S. Scotto-Sheriff, E. Darque-Ceretti, G. Plassart, M. Aucouturier, J. Mater. Sci. 34 (1999) 5081–5088.

[180] N. Shamir, M. H. Mintz, J. Bloch, U. Atzmony, J. Less-Common Met. 92 (1983) 253–263.

[181] A. Seiler, L. Schlapbach, T. von Waldkirch, D. Shaltiel, F. Stucki, J. Less-Common Met. 73 (1980) 193–199.

[182] A. B. Belonoshko, A. Rosengren, Q. Dong, G. H. C. Leygraf, Phys. Rev. B. 69 (2004) 024302.

[183] H. Lynggaard, A. Andreasen, C. Stegelmann, P. Stoltze, Prog. Surf. Sci. 77 (3-4) (2004) 71–137.

[184] C. W. Ostenfeld, I. Chorkendorff, To be submitted .

[185] M. M. Jr., J. N. Maycook, V. R. P. Verneker, J. Phys. Chem. 72 4009–4014.

[186] D. Blanchard, H. W. Brinks, B. C. Hauback, P. Norby, J. Muller, J. Alloys Comps. . URL DOI:10.1016/j.jallcom.2005.01.126

[187] H. Kissinger, Anal. Chem. 29 (11) (1957) 1702–1706.

[188] C. M. Andrei, J. Walmsley, D. Blanchard, H. W. Brinks, R. Holmestad, B. C. Hauback, J. Alloys. Comps. In press.

[189] T. Kiyobayashi, S. S. Srinivasan, D. Sun, C. M. Jensen, J. Phys. Chem. A. 107 (39) (2003) 7671 –7674.

[190] W. Luo, K. J. Gross, J. Alloys Comps. 385 (2004) 224–231.

[191] J. J. Moré, B. S. Garbow, K. E. Hillstrom, User guide for MINPACK-1, Tech. Rep. ANL-80-74, Argonne National Laboratory, Argonne, IL, USA (Aug 1980).

[192] J. Mayet, J. Tranchan, Bull. Soc. Chim. Fr. (2) (1973) 510–510.

[193] C. Herring, J. Appl. Phys. 21 (1950) 437–445.

[194] F. R. N. Nabarro, H. L. de Villiers, The physics of creep, Taylor & Francis, 1995.

[195] M. Hirsher, J. Mössinger, H. Kronmüller, NanoStructured Materials 6 (1995) 635–638.

[196] R. L. Coble, J. Appl. Phys. 34 (1963) 1679–1682.

[197] Z. R. Xu, R. B. McLellan, Acta. Mater. 46 (1998) 4543–4547.

[198] K. Yamakawa, B. Hohler, H. Kronmüller, J. Phys.: Condens. Matter. 1 (1989) 2031–2040.

[199] U. Stuhr, T. Striffler, H. Wipf, H. Natter, B. Wettermann, S. Janssen, R. Hempelmann, H. Hahn, J. Alloys Comps. 253-254 (1997) 393–396.

[200] D. S. Sibirtsev, A. V. Skripov, N. Natter, R. Hempelmann, Solid State Comm. 108 (1998) 583–586.

[201] S.-i. Orimo, F. Kimmerle, G. Majer, Phys. Rev. B. 63 (2001) 094307.

[202] S. Heinze, B. Vuillemin, J.-. C. Colsen, P. Giroux, D. Laterq, Solid State Ionics 122 (1999) 51–57.

[203] B. Bogdanović, M. Felderhoff, M. Germann, M. Härtel, A. Pommerin, F. Schüth, C. Weidenthaler, B. Zibrowius, J. Alloys and Comps. 350 (2003) 246–255.

[204] E. H. Majzoub, K. J. Gross, J. Alloys and Comps. 356-357 (2003) 363–367.

[205] M. Fichtner, P. Canton, O. Kircher, A. Léon, J. Alloys Comps. .
URL DOI:10.1016/j.jallcom.2004.12.178

[206] G. Sandrock, K. J. Gross, G. Thomas, J. Alloys Comps. 339 (2002) 299–308.

[207] V. F. Sears, Neutron News 3 (1992) 29–37.

[208] C. T. Chudley, R. J. Elliott, Proc. Phys. Soc. 77 (1961) 353–361.

[209] G. Alefeld, J. Völkl (Eds.), Hydrogen in metals I, Vol. 28 of Topics in Applied Physics, Springer-Verlag, 1978.

[210] A. V. Skripov, J. Combet, H. Grimm, R. Hempelmann, V. N. Kozhanov, J. Phys.: Condens. Matter 12 (2000) 3313–3324.

[211] D. L. Price, Curr. Opin. Solid State & Mater. Sci. 2 (1997) 477–482.

[212] M. T. Dove, Eur. J. Mineral 14 (2002) 203–224.

[213] T. J. Udovic, Q. Huang, C. Karmonik, J. J. Rush, J. Alloys Comps. 293–295 (1999) 113–117.

[214] A. V. Skripov, J. C. Cook, T. J. Udovic, V. N. Kozhanov, Phys. Rev. B. 62 (2000) 14099–14104.

[215] A. V. Skripov, A. V. Soloninin, D. S. Sibirtsev, A. L. Buzlukov, A. P. Stepanov, J. J. Balbach, M. S. Conradi, R. G. Barnes, R. Hempelmann, Phys. Rev. B. 66 (2002) 054306.

[216] D. Richter, R. Hempelmann, L. A. Vinhas, J. Less-Common Met. 88 (1982) 353–360.

[217] S. N. Klausen, Manual for the RITA2 spectrometer, Risø National Laboratory, ver. 0 (August 2001).
URL `http://rita2.psi.ch/misc/rita2_usermanual.ps`

[218] K. Lefmann, D. F. McMorrow, H. Rønnow, K. Nielsen, K. N. Clausen, B. Lake, G. Aeppli, Physica B 283 (2000) 343–354.

[219] K. Clausen, D. F. McMorrow, K. Lefmann, G. Aeppli, T. Mason, A. Schröder, M. Issikii, H. Nohara, M.and Takagi, Physica B 241 (1997) 50–55.

[220] S. Klausen, K. Lefmann, D. McMorrow, F. Altorfer, S. Janssen, M. Luthy, Appl. Phys. A. 74 (2002) S1508–S1510.

[221] A. V. Skripov, J. Töpler, D. Noréus, R. Hempelmann, D. Richter, Int. J. Hydrogen Energy 14 (1989) 187–200.

[222] R. Hempelmann, D. Richter, R. Pugliesi, L. A. Vinhas, J. Phys. F.: Met. Phys. 13 (1983) 59–68.

[223] A. V. Skripov, J. C. Cook, T. J. Udovic, M. A. Gonzalez, R. Hempelmann, V. N. Kozhanov, J. Phys.: Condens. Matter 15 (2003) 3555–3566.

[224] D. Richter, T. Springer, Phys. Rew. B. 18 (1978) 126–140.

[225] E. Burkel, J. Phys.: Condens. Matter 13 (2001) 7477–7498.

[226] A. Peles, To be submitted .

[227] V. Ozolins, E. H. Majzoub, T. J. Udovic, J. Alloys Comps. 375 (2004) 1–10.

[228] B. C. Hauback, H. W. Brinks, C. M. Jensen, K. Murphy, A. J. Maeland, J. Alloys Comps. 358 (2003) 142–145.

[229] C. M. Jensen, D. Sun, B. Lewandowski, K. K. Kumashiro, W. P. Niemczura, D. Morales-Morales, Z. Wang, Catalytically enhanced systems for hydrogen storage, in: Proceedings of the 2001 DOE Hydrogen Program Review, 2002.

[230] G. Majer, E. Stani, L. E. Valiente Banuet, F. Grinberg, O. Kirchner, M. Fichtner, J. Alloys Comps. xxx (2005) xxx–xxx.

[231] O. Palumbo, A. Cantelli, R. amd Paolone, C. M. Jensen, S. S. Srinivasan, J. Phys. Chem. B 109 (3) (2005) 1168–1173.

Appendix A

Paper 1

Compensation Effect in the Hydrogenation/Dehydrogenation Kinetics of Metal Hydrides

Anders Andreasen,*,†,‡ Tejs Vegge,§,|| and Allan S. Pedersen†

Materials Research Department, Risø National Laboratory, DK-4000 Roskilde, Denmark, Interdisciplinary Research Center for Catalysis, Department of Chemical Engineering, Technical University of Denmark, DK-2800 Lyngby, Denmark, and Center for Atomic-scale Materials Physics, Department of Physics, Technical University of Denmark, DK-2800 Lyngby, Denmark

Received: September 13, 2004; In Final Form: December 9, 2004

The possible existence of a compensation effect, i.e. concurrent changes in activation energy and prefactor, is investigated for the hydrogenation and dehydrogenation kinetics of metal hydrides, by analyzing a series of reported kinetic studies on Mg and $LaNi_5$ based hydrides. For these systems, we find a clear linear relation between apparent prefactors and apparent activation energies, as obtained from an Arrhenius analysis, indicating the existence of a compensation effect. Large changes in apparent activation energies in the case of Mg based hydrides are rationalized in terms of a dependency of observed apparent activation energy on the degree of surface oxidation, i.e., a physical effect. On the other hand, we find the large concurrent changes in apparent prefactors to be a direct result of the Arrhenius analysis. Thus, we find the observed compensation effect to be an artifact of the data analysis rather than a physical phenomenon. In the case of $LaNi_5$ based hydrides, observed scatter in reported apparent activation energies is less pronounced supporting the general experience that $LaNi_5$ is less sensitive toward surface contamination.

1. Introduction

Soaring oil-prices—driven by limited supply, terrorist threats, and growing energy demands in Asia—has sparked intense research efforts in alternative energy carriers for the future. In particular, hydrogen stored in complex or metal hydrides has been the subject of multiple research projects. To be of practical interest for storage purposes these materials must willingly take up hydrogen and subsequently release it again at a sufficiently high rate. Thus, the kinetics of metal hydrides have been investigated extensively in order to map the reaction mechanisms of hydrogen absorption and desorption, respectively, and to identify possible rate limiting steps to ultimately take steps toward improving the kinetics. Interestingly, obtained kinetic data are scattered extensively, even for similar systems. Thus, reported apparent activation energies are often scattered, and discrepancies among which steps are suggested as controlling the overall rate are often encountered.[1−3]

In this paper we investigate the possible existence of a compensation effect in the kinetics of the metal−hydrogen reaction viz. hydrogenation of metals and dehydrogenation of metal hydrides (see for instance refs 1 and 4−9 for detailed information).

In a simplified manner, the reaction rate, r, is usually expressed as the product of a rate constant, k, some functional, f, dependent on temperature, T, and concentration, θ, and an approach to equilibrium, β:

$$r = kf(\theta, T)\beta \tag{1}$$

Depending on the nature of the reaction, f can be a functional of gas-phase pressures of the reactants and products, and surface coverages of reaction intermediates (heterogeneous catalysis) or the bulk concentration of adsorbed atoms (gas−solid reactions). The approach to equilibrium accounts for the rate decrease near equilibrium and secures that the equilibrium limit is not crossed.

The rate constant of most thermally activated processes is usually described well by an Arrhenius relationship

$$k = A\exp\left(\frac{-E_A}{RT}\right) \tag{2}$$

where A is denoted the prefactor and E_A is the activation energy. The prefactor may be interpreted as the potential reaction rate if the temperature is significantly higher than E_A. By taking the natural logarithm of eq 2:

$$\ln(k) = \ln(A) - \frac{E_A}{RT} \tag{3}$$

the Arrhenius relationship implies that a plot of the measured rate constants as a function of the reciprocal temperature will result in a straight line with slope E_A/R and intercept $\ln(A)$. Henceforth we will use the terms "apparent activation energy", E_A^{app}, and "apparent prefactor", A_{app}, since k values obtained from kinetic studies can potentially be a sum of several reaction steps.

In some reaction systems, it has been observed that the apparent activation energy varies under different measuring conditions. It is also found that the variation in apparent activation energy is accompanied by a change in A_{app}, i.e., a large apparent activation energy is accompanied by a large prefactor and vice versa;[10,11] a phenomenon often referred to as the compensation effect (CE).

In some cases, the changes in prefactor and apparent activation enthalpy display a linear dependency according to the Cremer−Constable relation.[11]

$$\ln A_{app} = aE_A^{app} + b \tag{4}$$

* Corresponding author. E-mail: anders.andreasen@risoe.dk. Telephone: +45 46 77 57 76 (office). Fax: +45 46 77 57 58 (department).
† Materials Research Department, Risø National Laboratory.
‡ Department of Chemical Engineering, Technical University of Denmark.
§ Department of Physics, Technical University of Denmark.
|| Present address: Materials Research Department, Risø National Laboratory, DK-4000 Roskilde, Denmark.

10.1021/jp0458755 CCC: $30.25
Published on Web 02/04/2005

TABLE 1: Corresponding Values of Apparent Prefactors and Apparent Activation Energies for Hydrogenation (h)/Dehydrogenation (d) of Magnesium Based Hydrides[a]

host	method	ln (A_{app})	E_a^{app} [kJ/mol]	com-ment	temp [K]	P [bar]	sample	ref
Mg−Al	XRPD	20.65	160	d	643-673	0[b]	A	28
Mg/$MgCu_2$	XRPD	21.11	160	d	633-663	0[b]	B	29
Mg/Mg_2Cu	XRPD	12.20	108	d	643-673	0[b]	C	29
Mg	XRPD	46.04	296	d	633-673	0[b]	D	30
Mg(Ni)	XRPD	37.45	249	d	623-663	0[b]	E	30
Mg	TG	19.22	119	d	608-641	3.84	F	32
Mg	Sievert	23.67	167	d	613-643	0.25-6	G	33
Mg	TG	36.44	230	d	635-663	1.5	H	34
Mg(foil)	TG	49.23	284	h	650-700	10-30	I	35
Mg(foil)	TG	53.37	308	h	650-700	10-30	J	35
Mg(Ni)	PCI	9.53	66	h	543-616	1-13	K	36
Mg	Sievert	10.40	91	h	614-648	5-21	L	33

[a] If not otherwise stated, the samples are in powder form. Mg(Ni): Nickel doped magnesium. TG: Thermogravimetry. PCI: pressure−composition isotherm apparatus. XRPD: Parameters determined from quantitative analysis of in situ time resolved X-ray powder diffraction. [b] Dehydrogenation in an argon flow 10 mL/min with a pressure of 1 bar. The background pressure of hydrogen was not measured.

The relation implies that values of the natural logarithm of the prefactor plotted against the apparent activation energy (denoted a Constable plot), as obtained from an Arrhenius plot, fall on a straight line with slope a and intercept b.

Although the compensation effect has been known and studied for almost 100 years and been observed in a variety of different fields of science, including electron emission,[12] heterogeneous catalysis,[10,11,13−18] homogeneous catalysis,[19] temperature-programmed desorption,[20,21] and diffusion,[22,23] no consensus on the nature of CE has been reached. However, a number of different explanations for observed compensation effects have been suggested (most of them applicable to heterogeneous catalysis): (i) oversimplified data analysis;[24,25] (ii) heterogeneity in activity and distribution of active sites;[18] (iii) a correlation between applied reactant pressures and measured apparent activation energy due to coverage dependent terms;[11,14,15,17] (iv) a change in anharmonicity in the adsorbate−surface bond changes the activation enthalpy of dissociation;[26] (v) the enthalpy−entropy relationship;[10,11] (vi) the heat bath concept;[27] (vii) the Brønsted−Evans−Polanyi relation.[16]

Our recent findings of large variations (approximately 200 kJ/mol) in the apparent activation energy for dehydrogenation of Mg-based hydrides,[28−30] prompted us to investigate the possible existence of a compensation effect in metal hydride systems.

2. Results and Discussion

To investigate the potential existence of a CE in metal−hydrogen systems, we review the literature on kinetics studies for two of the most investigated systems, viz., Mg and $LaNi_5$ based hydrides; in particular the kinetics of the magnesium based hydrides has been investigated thoroughly in the past.[31]

2.1. Mg-Based Hydrides. Corresponding values of ln(A_{app}) and E_A^{app} along with information about the experimental method and reaction conditions (T,P) are presented in Table 1. The values of A_{app} and E_A^{app} in Table 1 are obtained by fitting eq. 3 to reported Arrhenius plots viz. ln(k) vs 1/T data from the references also given in the table. In a single case,[34] no Arrhenius plot was reported, only raw kinetic data, i.e., reacted fraction vs time. To extract the desired data, a kinetic expression was fitted to the raw kinetic data. For this purpose we have chosen a conventional Johnson−Mehl−Avrami[37−40] nucleation and growth kinetic expression (also referred to as the Johnson−Mehl−Avrami−Kohlmogorov equation[41]) of the form

$$\alpha(t) = 1 - \exp(-(kt)^n) \quad (5)$$

where $\alpha(t)$ is the time-dependent phase fraction of magnesium hydride. The parameters describing nucleation and growth rates are contained within an effective kinetic parameter, k, and an exponent, n, often referred to as the Avrami exponent.[41] Although the Avrami exponent is sometimes ascribed physical nature in terms of nucleation and growth,[42] the derived k values are quite insensitive to the value of n, hence both k and n were fitted. A_{app} and E_A^{app} were determined by an Arrhenius analysis of fitted values of k vs 1/T. This method of data analysis is analogous to the applied analysis in refs 28−30. Minor variations in the kinetic expressions used in the extraction of rate constants in the other references in Table 1 is possible. However, it is generally found that the temperature dependence of the extracted rate constants is rather insensitive to the choice of kinetic expressions.[30,32,43] This allows for comparison of reported values of A_{app} and E_A^{app} between all the reported data, although the kinetic analysis may differ slightly.

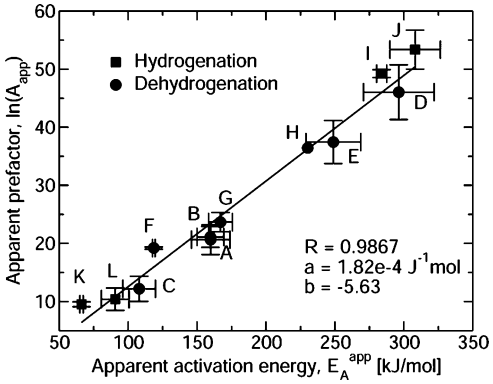

Figure 1. Constable plot of reported values of A_{app} vs E_A^{app} from Table 1 for magnesium based hydrides. Data points are assigned sample letters.

A Constable plot of the values of A_{app} and E_A^{app} in Table 1 has been constructed in Figure 1. It is clearly observed from the figure that the apparent prefactor is linearly correlated with the apparent activation energy, having a correlation coefficient of $R \approx 0.99$.

Thus, in the case of hydrogenation/dehydrogenation of magnesium based hydrides a clear compensation effect according to the Cremer−Constable relation (eq. 4) is observed. From Figure 1 and Table 1 it also seen that the apparent activation energy covers a range of 66−308 kJ/mol for hydrogenation and 118−296 kJ/mol for dehydrogenation, respectively. The corresponding range in apparent prefactors is 19 orders of magnitude for hydrogenation and 12 orders of magnitude for dehydrogenation, respectively. Error bars for both apparent activation energies and apparent prefactors are based on standard deviations of fitted parameters from linear regression analysis. The error bars clearly indicate that observed scatter in apparent activation energies and apparent prefactors is *real* and not due to experimental uncertainties.

A physical explanation for the possible existence of two—or more—kinetic regimes is therefore warranted, at least in the case of apparent activation energies.

To explain the variation in apparent activation energies we will focus on the pretreatment of the samples also termed the *activation procedure*. The samples from Table 1 are ordered as *activated* and *nonactivated* samples in Figure 2. The term

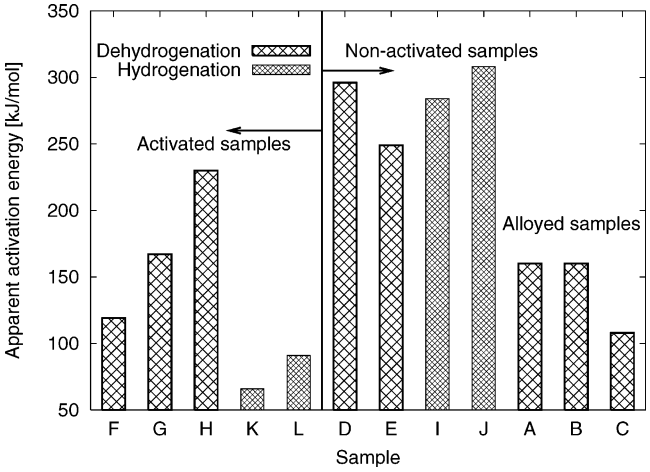

Figure 2. Apparent activation energy, E_A^{app}, from Table 1 for magnesium based hydrides. Data points are assigned sample letters and grouped after pretreatment procedure.

nonactivated implies that the kinetics are measured for the first hydrogenation or first dehydrogenation cycle. The term *activated* implies that the sample is hydrogenated/dehydrogenated for several cycles prior to kinetic measurements. The activation process covers different phenomena and includes penetration of the natural oxide layer on as-prepared samples (if previously exposed to air), followed by complete hydride formation, which leads to cracking of the particles, due to the expansion associated with the hydrogenation process combined with the brittle nature of most metal hydrides.[1,6] During the first hydrogenation/dehydrogenation cycles, the reaction rate increases due to the creation of a fresh contamination-free surface and/or smaller particles (higher surface area and shorter diffusion paths) until a steady-state is reached. A potential physical explanation for the observed variations in ln A_{app} and E_A^{app}, are therefore likely to depend on sample treatment and cleanliness.

For the nonalloyed Mg samples (D−L) in Figure 2, a trend of higher apparent activation energy for the *nonactivated* samples than the *activated* samples for both hydrogenation and dehydrogenation is observed. The high apparent activation energy of the nonactivated samples may be accounted for by the presence of an oxide shell/layer surrounding the bulk magnesium particles. For sample D and E the presence of MgO was confirmed by X-ray powder diffraction and energy dispersive X-ray spectroscopy (EDX).[30] Likewise, for samples I and J, the production method and sample handing makes formation of a surface oxide with low defect density highly probable.[44]

It is known that hydrogen diffusion in the close packed MgO is extremely slow[45] and strongly thermally activated, when compared to diffusion of hydrogen in Mg[46] and MgH_2.[47] The formation of MgO at the surface is therefore expected to contribute to a higher apparent activation energy. The observed lower activation energies for the activated samples are thus probably due to the creation of a fresh, oxide free surface from cracked particles, and new hydrogen diffusion channels in the interface regions. Quantifying the effect of *activation* on the apparent activation energy is, however, difficult due to the various procedures used on the samples. Other effects may also be important, such as particle morphology, presence of other impurities both in bulk samples and in the surrounding gas phase of H_2/inert, etc.

The alloyed and nonactivated Mg samples (A−C), MgH_2/Al, $MgH_2/MgCu_2$, and MgH_2/Mg_2Cu, respectively, do not seem to fit the trend in applied activation procedure. The explanation probably relies on the fact that alloying with Cu and Al produces a compound less sensitive toward oxygen contamination; no crystalline MgO was found in the air-exposed samples by X-ray powder diffraction.[28,29] Furthermore, it has also been suggested by Karty et al.[43] that the presence of Mg_2Cu provides an oxide free surface and favorable hydrogen diffusion paths. Effectively, the result of alloying with Al is the same as for $Mg_2Cu/MgCu_2$, although the physical explanation is likely different, since the marginal stability of the Mg−Al alloys does not block oxide formation.[28] With both Al and Mg present in the surface layers, the formation of amorphous or hydrogen porous alumina, Al_2O_3, and $MgAl_2O_4$ spinel is possible;[48a] both structures and their interface regions with MgO have improved hydrogen diffusion channels.[48b]

TABLE 2: Corresponding Values of Apparent Prefactors and Apparent Activation Energies for Hydrogenation of $LaNi_5$ Based Hydrides[a]

host	ln(A_{app})		E_a^{app}T	sample	ref
$LaNi_5$	11.87	32	271−360	M	49
$LaNi_5$	9.35	33	289−352	N	50
$LaNi_5$	3.79	19	294−333	O	3
$LaNi_5$	17.37	53	267−333	P	51
$LaNi_xAl_y$	5.31	24	246−281	Q	52
$LaNi_5$	10.79	37	245−293	R	53
$LaNi_5$	11.26	38	245−293	S	54

[a] For sample Q: $x = 4.75$ and $y = 0.25$. Sample P is for dehydrogenation. $E_A{}^{app}$ is in kJ/mol and T is in Kelvin.

We therefore propose that the vast difference in apparent activation energies is a consequence of the level of MgO formation, which strongly inhibits hydrogen diffusion. For the activated or and alloyed samples, hydrogen dissociation is expected to be rate-limiting, whereas hydrogen diffusion through MgO-rich surfaces limits the kinetics for the nonactivated samples.

2.2. $LaNi_5$ Hydrides. To investigate the possible existence of a compensation effect in other metal hydride systems, we have reviewed a number of reported kinetic studies on $LaNi_5$ based hydrides from the literature. This particular hydride was chosen since it is not prone to oxide formation, and ample kinetic data are available.

Corresponding values of ln(A_{app}) and E_A^{app} along with information about reaction temperature and the origin of the data are presented in Table 2. As for the Mg-based samples the values of ln(A_{app}) and E_A^{app} are obtained by fitting eq 3 to reported values of ln(k) vs $1/T$. In a single case (sample S) the values have been obtained by first fitting eq 5 to raw kinetic data, extracting k at different temperatures, and thus finally performing an Arrhenius analysis.

The data of ln(A_{app}) and E_A^{app} is used to construct a Constable plot as shown in Figure 3. Again, we observe a compensation effect in the reported data according to the Cremer−Constable relation. However, it is also noticed that the apparent activation energies for $LaNi_5$ span a much smaller interval (19−38 kJ/mol for hydrogenation) and cover only 4 orders of magnitude in apparent prefactor. Even with the uncertainty on the derived values of E_A^{app}, the compensation effect is found to be statistically significant. Thus, the smaller changes in apparent activation energy of the $LaNi_5$ compared to Mg could be an indicator of the fact that $LaNi_5$ is more easily activated and less sensitive toward oxidation and contamination.

2.3. Discussion. In the case of magnesium based hydrides, a probable physical explanation can be established for the large variation in apparent activation energy, whereas the pronounced changes in apparent prefactor seem unlikely to be explainable on the basis of, e.g., changes in vibrational frequencies.[16]

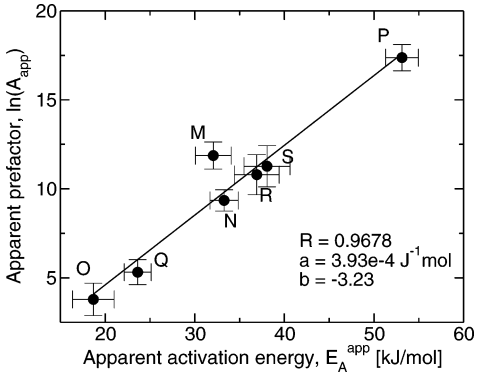

Figure 3. Constable plot of reported values of A_{app} vs E_A^{app} from Table 2 for $LaNi_5$ based hydrides. Data points are assigned sample letters.

TABLE 3: Constable Plot Slope *a* and Corresponding Values of T_m and $T_m(exp)$ for Mg and $LaNi_5$ Based Hydrides

metal hydride	a [J^{-1} mol]	T_m [K]	$T_m(exp)$ [K]
MgH_2	1.82×10^{-4}	661	643
$LaNi_5$	3.93×10^{-4}	306	293

Whether the observed compensation effect is an artifact of the derivation of $\ln(A_{app})$ from an Arrhenius plot, where $\ln(A_{app})$ is the intercept (the natural logarithm to the rate constant extrapolated to infinite temperature), is investigated in the following.

Recently, it have been shown[55] for heterogeneous catalytic reactions that changes in apparent activation energies due to variations in reaction conditions or changing the catalyst material always leads to a compensation effect when the corresponding apparent prefactors are determined from an Arrhenius analysis. Further, it was shown by algebraic derivation that the slope in such a Constable plot is $a = (RT_m)^{-1}$, where T_m may be interpreted in terms of a mean experimental temperature. Thus, it was concluded that the observed compensation effect could be explained by the method of data analysis rather than a physical effect.

The theoretical observation of $a = (RT_m)^{-1}$ prompted us to investigate whether the Constable plots presented in this paper displayed this correlation. The slope, a, in Figures 1 and 3 and the derived T_m for both Mg and $LaNi_5$ are shown in Table 3. Also shown is the true experimental mean temperature $T_m(exp)$ for Mg and $LaNi_5$. From Table 3 we notice that there is good agreement between the calculated and experimental value of T_m for both Mg and $LaNi_5$. The larger slope in the Constable plot of $LaNi_5$ compared to Mg is thus simply accounted for by the lower temperature applied during experiments; i.e., the slopes are equal to $(RT)^{-1}$.

Having shown that the slopes in the Constable plot are in fact equal to $(RT)^{-1}$ enables us to take the data analysis a step further. From eq 3, $\ln(A_{app})$ is given by

$$\ln(A_{app}) = \frac{E_A^{app}}{RT} + \ln(k) \qquad (6)$$

To quantify the relative contributions to $\ln(A_{app})$, a modified Constable plot is constructed, where the data from Table 1 is compared to E_A^{app}/RT_m (Figure 4, upper).

From the figure we note that E_A^{app}/RT is by far the most important contribution to $\ln(A_{app})$. Even though the rate constant, k_m, calculated for the different samples at T_m using the derived values of apparent activation energy and apparent prefactors varies by 3 orders of magnitude (cf. Figure 4 lower) this is still only a minor contribution to $\ln(A_{app})$. This observation can

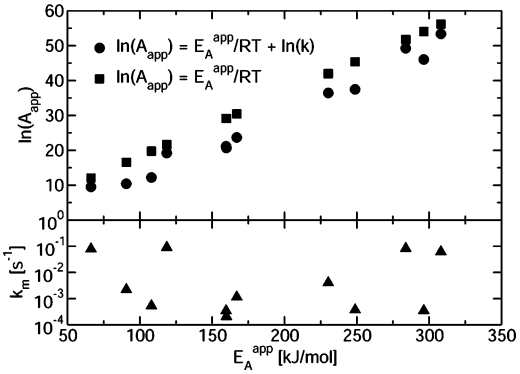

Figure 4. Constable plot of reported values of A_{app} vs E_A^{app} from Table 1 for Mg based hydrides compared with (E_A^{app}/RT_m) (upper).

explain why the slope in a Constable plot is simply $(RT)^{-1}$, since discarding $\ln(k)$ in eq. 6 introduces only minor errors in $\ln(A_{app})$.

The described decomposition of the apparent prefactor strongly indicates that the observed compensation effect, does not rely on a physical phenomenon, but is simply a consequence of the simultaneous determination of E_A^{app} and $\ln(A_{app})$ from an Arrhenius analysis. In this context it is important to note that an Arrhenius analysis is often the only method available to determine both the activation energy and the prefactor. Thus, caution should be exercised when drawing conclusions based on such an analysis. Taking into account that numerical values of reported rate constants often lay within a limited range (where the lower limit is determined by the instrumental time-resolution and the upper limit is determined by the patience of the experimentalist), the use of an Arrhenius analysis will often result in an apparent compensation effect.

3. Conclusion

In this paper, we have reviewed the kinetics in terms of apparent activation energies and apparent prefactors of two of the most investigated metal−hydrogen systems: magnesium and $LaNi_5$ based hydrides. For both systems we find that the values of the apparent activation energies are scattered. In the case of Mg we suggest that variations in reported apparent activation energies correlate with the presence of a MgO surface layer inhibiting diffusion of hydrogen. Thus, oxidized samples show large apparent activation energies and well activated samples show smaller activation energies. The observed scatter is most pronounced for the magnesium based hydrides. We take this as evidence for the fact that $LaNi_5$ is much more easily activated and less sensitive toward oxidation and contamination than Mg.

Further, we have investigated the existence of a compensation effect in the formation/decomposition of metal hydrides. We find a clear compensation effect in the case of both magnesium and $LaNi_5$ based hydrides. The origin of this compensation effect is the simultaneous determination of the apparent prefactor and apparent activation energy from an Arrhenius analysis. It is found that the slope in the Constable plots of both magnesium based hydrides and $LaNi_5$ based hydrides is equal to $(RT)^{-1}$. Whenever apparent activation energies and apparent prefactors are linked directly through an Arrhenius analysis, the observation of a potential compensation effect should be examined for a $(RT)^{-1}$ correlation.

Acknowledgment. This work has received financial support from the The Danish Technical Research Council, through the Center of Excellence *Toward a hydrogen based society*, and

the Danish Research Agency and Danfoss Corporate Ventures A/S through Grant No. 2013-01-0043.

References and Notes

(1) Schlapbach, L., Ed. *Hydrogen in Intermetallic Compounds II*; Topics in Applied Physics 67; Springer-Verlag: Berlin, 1992.
(2) Han, J. I.; Lee, J.-Y. *Int. J. Hydrogen Energy* **1989**, *14*, 181−186.
(3) Nahm, K. S.; Kim, W. Y.; Hong, S. P.; Lee, W. Y. *Int. J. Hydrogen Energy* **1992**, *17*, 333−338.
(4) Mueller, W. M.; Blackledge, J. P.; Libowitz, G. G., Eds.; *Metal Hydrides;* Academic Press: San Diego, CA, 1968.
(5) Alefeld, G., Völkl, J., Eds. *Hydrogen in metals I*; Topics in Applied Physics 28; Springer-Verlag: Berlin, 1978.
(6) Alefeld, G., Völkl, J., Eds. *Hydrogen in metals II*; Topics in Applied Physics 29; Springer-Verlag: Berlin, 1978.
(7) Schlapbach, L., Ed. *Hydrogen in Intermetallic Compounds I*; Topics in Applied Physics 63; Springer-Verlag: Berlin, 1988.
(8) Schlapbach, L.; Züttel, A. *Nature (London)* **2001**, *414*, 353−358.
(9) Züttel, A. *Mater. Today* **2003**, *9*, 24−33.
(10) Galwey, A. K. *Adv. Catal.* **1977**, *26*, 247−322.
(11) Bond, G. C.; Keane, M. A.; Kral, H.; Lercher, J. A. *Catal. Rev. −Sci. Eng.* **2000**, *42* (3), 319−327.
(12) Wilson, H. A. *Philos. Trans. A.* **1908**, *208*, 247.
(13) Constable, F. H. *Proc. R. Soc. London, A.* **1925**, *108*, 355.
(14) Bond, G. C. *Catal. Today* **1999**, *49*, 41−48.
(15) Bond, G. C.; Hooper, A. D.; Slaa, J. C.; Taylor, A. O. *J. Catal.* **1996**, *163*, 319−327.
(16) Bligaard, T.; Honkala, K.; Logadottir, A.; Nørskov, J. K.; Dahl, S.; Jacobsen, C. J. H. *J. Phys. Chem. B.* **2003**, *107*, 9325−9331.
(17) Wootsch, A.; Páal, Z. *J. Catal.* **2002**, *205*, 86−96.
(18) Somorjai, G. A. *Introduction to Surface Chemistry and Catalysis;* John Wiley & Sons: New York, 1994.
(19) Loukova, G. V.; Mikhailov, A. I.; Shilov, A. E. *Kinet. Catal.* **2002**, *43*, 746−747.
(20) Miller, J. B.; Siddiqui, H. R.; Gates, S. M.; Russell, J. N., Jr.; Yates, J. T., Jr.; Tully, J. C.; Cardillo, M. J. *J. Chem. Phys.* **1987**, *87*, 6725−6732.
(21) Nieskens, D. L. S.; van Bravel, A. P.; Niemantsverdriet, J. W. *Surf. Sci.* **2003**, *546*, 159−169.
(22) Keyes, R. W. *J. Chem. Phys.* **1958**, *29*, 467−475.
(23) Barth, J.; Brune, H.; Fischer, B.; Weckesser, J.; Kern, K. *Phys. Rev. Lett.* **2000**, *84*, 1732−1735.
(24) Ratsch, C.; Scheffler, M. *Phys. Rev. B.* **2001**, *58*, 13163−13166.
(25) Ovesson, S.; Bogicevic, A.; Wahnström, G.; Lundqvist, B. I. *Phys. Rev. B.* **2001**, *64*, 125423.
(26) McCoy, B. J. *J. Chem. Phys.* **1984**, *80*, 3629−3631.
(27) Peacock-Lopéz, E.; Suhl, H. *Phys. Rev. B.* **1982**, *26*, 3774−3782.
(28) Andreasen, A.; Sørensen, M. B.; Burkarl, R.; Møller, B.; Molenbroek, A. M.; Pedersen, A. S.; Andreasen, J. W.; Nielsen, M. M.; Jensen, T. R. *J. Alloys Compd.* **2004**, submitted for publication.
(29) Andreasen, A.; Vegge, T.; Sørensen, M. B.; Burkarl, R.; Møller, B.; Molenbroek, A. M.; Pedersen, A. S.; Jensen, T. R. Manuscript in preparation, 2004.
(30) Jensen, T. R.; Andreasen, A.; Andreasen, J. W.; Vegge, T.; Ståhl, K.; Besenbacher, F.; Molenbroek, A.; Nielsen, M. M.; Pedersen, A. S. **2004**, manuscript in preperation.
(31) Sandrock, G.; Thomas, G. *Appl. Phys. A: Mater. Sci. Process.* **2001**, *72*, 153−155.
(32) Stander, C. *J. Inorg. Nucl. Chem.* **1977**, *39*, 221−223.
(33) Fernandez, J. F.; Sanchez, C. R. *J. Alloys Compd.* **2002**, *340*, 189−198.
(34) Vigeholm, B. Chemical Energy Storage Based on Metal Hydrides; Technical Report Risø-M-2608, Risoe National Laboratory, DK-4000 Roskilde, Denmark, 1989 (In Danish).
(35) Pedersen, A.; Jensen, K.; Larsen, B.; Vigeholm, B. *J. Less-Common Met.* **1987**, *131*, 31−40.
(36) Friedlmeier, G.; Groll, M. *J. Alloys Compd.* **1997**, *253−254*, 550−555.
(37) Avrami, M. *J. Chem. Phys.* **1939**, *7*, 1103−1112.
(38) Avrami, M. *J. Chem. Phys.* **1940**, *8*, 212−224.
(39) Avrami, M. *J. Chem. Phys.* **1941**, *9*, 177−184.
(40) Johnson, W. A.; Mehl, R. F. *Trans. A.I.M.E.* **1939**, *135*, 416−458.
(41) Kelton, K. *Mater. Sci. Eng.* **1997**, *A226−228*, 142−150.
(42) Bamford, C. H., Tipper, C. F. H., Eds.; *Reactions in the solid state;* Comprehensive chemical kinetics 22; Elsevier: Amsterdam, 1980.
(43) Karty, A.; Grunzweig-Genossar, J.; Rudman, P. *J. Appl. Phys.* **1979**, *50*, 7200−7209.
(44) Fournier, V.; Marcus, P.; Olejord, I. *Surf. Interface Anal.* **2002**, *34*, 494−497.
(45) Gonzalez, R.; Chen, Y.; Tang, K. L. *Phys. Rev. B.* **1982**, *26*, 4637−4645.
(46) Vegge, T. *Phys. Rev. B.* **2004**, *70*, 035412.
(47) Töpler, J.; Buchner, H.; Säufferer, H.; Knorr, K.; Prandl, W. *J. Less-Common Met.* **1982**, *88*, 397.
(48) (a) Scotto-Sheriff, S.; Sarque-Ceretti, E.; Plassart, G.; Aucouturier, M. *J. Mater. Sci.* **1999**, *34*, 5081−5088. (b) Belonoshko, A. B.; Rosengren, A.; Dong, Q.; Hultquist, G.; Leygraf, C. *Phys. Rev. B* **2004**, *69*, 024302.
(49) Boser, O. *J. Less-Common Met.* **1976**, *46*, 91−99.
(50) Miyamoto, M.; Yamaji, K.; Nakata, Y. *J. Less-Common Met.* **1983**, *89*, 111−116.
(51) Ron, M. *J. Alloys Compd.* **1999**, *283*, 178−191.
(52) Haberman, Z.; Bloch, J.; Mintz, M. H.; Jakob, I. *J. Alloys Compd.* **1997**, *253−254*, 556−559.
(53) Osovizky, A.; Bloch, J.; Mintz, M. H.; Jakob, I. *J. Alloys Compd.* **1996**, *245*, 168−178.
(54) Bloch, J. *J. Alloys Compd.* **1998**, *270*, 194−202.
(55) Lynggaard, H.; Andreasen, A.; Stegelmann, C.; Stoltze, P. *Prog. Surf. Sci.* **2004**, *77*, 71−137.

Appendix B

Paper 2

ELSEVIER

Journal of Alloys and Compounds xxx (2005) xxx–xxx

Journal of ALLOYS AND COMPOUNDS

www.elsevier.com/locate/jallcom

Interaction of hydrogen with an Mg–Al alloy

A. Andreasen[a,b,*], M.B. Sørensen[c], R. Burkarl[c], B. Møller[c], A.M. Molenbroek[d], A.S. Pedersen[a], J.W. Andreasen[a,e], M.M. Nielsen[e], T.R. Jensen[c,**]

[a] *Materials Research Department, Risø National Laboratory, DK-4000 Roskilde, Denmark*
[b] *Interdisciplinary Research Center for Catalysis, Department of Chemical Engineering, Technical University of Denmark, DK-2800 Lyngby, Denmark*
[c] *iNano, Department of Chemistry, Aarh(s University, DK-8000 Aarh(s C, Denmark*
[d] *) aldor Topsøe A/S, DK-2800 Kgs. Lyngby, Denmark*
[e] *Danish Polymer Centre, Risø National Laboratory, DK-4000 Roskilde, Denmark*

Received 31 May 2004; received in revised form 25 January 2005; accepted 31 January 2005

Abstract

The interaction of hydrogen with an Mg–Al alloy pre-exposed to air have been studied with in situ time resolved X-ray powder diffraction. Phase fractions as a function of time are derived from series of consecutive diffraction patterns allowing kinetic analysis. The apparent activation energy for dehydrogenation of the Mg–Al alloy is found to be 160 kJ/mol. This is not significantly higher than for pure and fully activated Mg. It is suggested that the addition of Al improves the resistance towards oxygen contamination.

PACS: 61.10.Nz; 81.05.Bx; 82.20.Pm

Keywords: Intermetallics; Hydrogen storage materials; Gas–solid reactions; X-ray diffraction

1. Introduction

Magnesium hydride has a high theoretical gravimetric hydrogen density (7.6 wt.%) but, suffers from several drawbacks e.g.: (i) thermodynamics dictate heating to above 280–300 °C for desorption of hydrogen from MgH_2, making it unsuitable for low-temperature applications, (ii) kinetics of hydrogenation/dehydrogenation may be regarded as slow and (iii) magnesium is very sensitive to gaseous impurities such as oxygen, creating an oxide shell retarding the kinetics. Thermodynamics and kinetics may be improved to some degree by alloying. The price being a reduced hydrogen capacity.

Alloying with Al have been reported to improve both thermodynamics [1,2] and kinetics [3]. From X-ray powder diffraction studies of the hydrogenated Mg–Al compound disproportionation into MgH_2 and Al could be concluded [1]. Desorption of hydrogen leads to complete reaction forming an Mg–Al compound, suggesting reversibility upon hydrogenation/dehydrogenation. These findings are in agreement with those of Bouaricha et al. [3]. Moreover, the addition of aluminum may add improved heat transfer properties to the hydride bed. This has prompted us to study the interaction of hydrogen with an Mg–Al alloy.

2. Experimental

The Mg–Al alloy subject to our investigations was prepared by arc melting approximately 5 g of a mixture of magnesium and aluminum according to the stoichiometry $Mg_{17}Al_{12}$ (γ-phase [4]) in an Edmund Buhler Arc Melting system. The magnesium (7.9 mm rod from Goodfellow) and aluminum (5–15 mm ingots from Sigma–Aldrich) used were 99.9% purity. The Mg–Al sample was melted repeatedly in an Argon atmosphere until the sample appeared homogeneous. Subsequently, the Mg–Al sample was ball milled for 10 min using WC balls.

* Corresponding author. Tel.: +45 4677 5776; fax: +45 4677 5758.
** Co-corresponding author. Tel.: +45 8942 3894; fax: +45 8619 6199.
E-mail addresses: anders.andreasen@risoe.dk (A. Andreasen); trj@chem.au.dk (T.R. Jensen).

0925-8388/$ – see front matter © 2005 Elsevier B.V. All rights reserved.
doi:10.1016/j.jallcom.2005.01.119

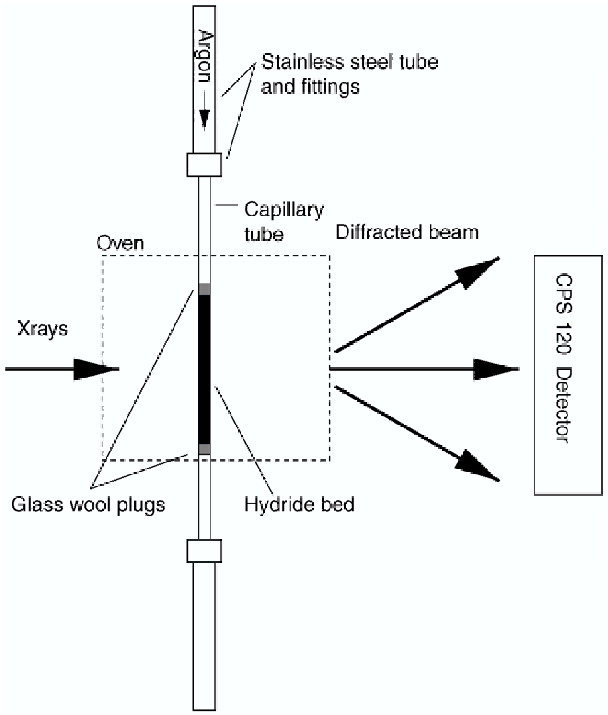

Fig. 1. Schematic drawing illustrating the experimental setup.

The ball milled sample of Mg–Al alloy was initially hydrogenated in a Sartorius high pressure balancing unit described in detail elsewhere [5]. The sample was hydrogenated by applying a hydrogen pressure (99.9997% purity from Air Liquide) of approximately 30 bar and a temperature of approximately 350 °C.

The X-ray instrument used for time resolved in situ X-ray powder diffraction (XRPD) was built around a Rigaku rotating anode (Cu $K\alpha_{12}$ radiation, $\bar{\lambda}$ = 1.5418 Å, 50 kV and 300 mA). The intensity of the diffracted beam was recorded with a curved position sensitive detector, INEL CPS 120, covering 120° in 2θ with a resolution of ca. 0.03°. The acquisition time per powder pattern was chosen to be 150 s. The in situ reactor cell is described in detail elsewhere [6]. The powder sample was loaded between plugs of quartz glass wool in a quartz capillary tube (0.7 mm o.d.) in order to fix the bed and allow a gas flow (Ar, 10 mL/min) through the sample during data acquisition as shown in Fig. 1. The samples were heated by a stream of hot nitrogen gas (20 °C/min) to a constant temperature in the range 350–400 °C and the dehydrogenation was followed under isothermal conditions.

3. Results and discussion

The XRPD of the as prepared ball milled sample is shown in Fig. 2. No metallic magnesium or aluminum was observed. The powder pattern shows relatively wide reflections and the peak positions correspond well with those observed for the

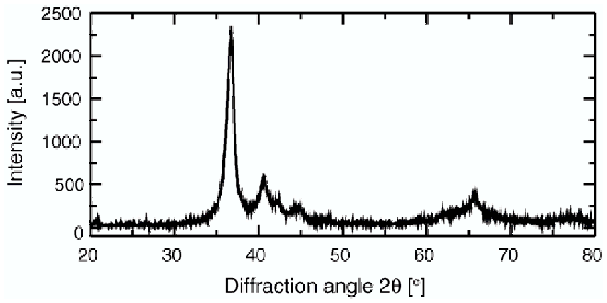

Fig. 2. XRPD of the as-prepared ball milled sample.

γ-phase ($Mg_{17}Al_{12}$). However, content of the ϵ ($Mg_{42}Al_{58}$ [4]) and β-phase (Mg_2Al_3 [4]) can not be ruled out. Using the Scherrer equation the crystallite size is approximated to be 10 nm.

The initial hydrogenation of the ball milled Mg–Al alloy showed almost complete hydrogenation within approximately 17 h. The total hydrogen uptake was approximately 3.1 wt.% corresponding to an approximate stoichiometry of $Mg_{0.41}Al_{0.59}$ assuming hydrogenation of Mg only. This stoichiometry is close to both that of the β and the ϵ-phase. The hydrogen uptake is somewhat lower than expected from the initial stoichiometry. The Mg–Al alloy is transformed completely into MgH_2 and metallic Al cf. Fig. 3 at $t = 0$. The peak width is reduced probably due to sintering at the elevated temperature during hydrogenation and corresponds to a crystallite size of approximately 70 nm.

The decomposition of MgH_2 + Al studied with in situ time resolved XRPD is illustrated by 72 consecutive XRPD patterns in Fig. 3 showing the disappearance of the MgH_2 (1 1 0), (1 0 1), (2 2 0) and the Al (1 1 1) and (2 0 0) reflections and the corresponding appearance of several reflections in the range 2θ = 35–43 °C of an Mg–Al alloy. During the heating of the sample the MgH_2 and Al reflections shift towards lower 2θ values due to the thermal expansion of the crystal lattices.

The phase fraction of MgH_2 have been calculated from the in situ XRPD data by numerically integrating the (1 1 0) reflection of MgH_2. Dehydrogenation curves i.e. phase fraction of MgH_2 versus time have been constructed for all experiments using normalized integrated intensities. The results are shown in Fig. 4. All dehydrogenation curves show a sigmoidal shape and faster dehydrogenation with higher temperatures, although, the shape of the dehydrogenation curve at 390 °C seems to deviate slightly from the others.

A Johnson–Mehl–Avrami (JMA) type nucleation and growth rate equation has been fitted to the dehydrogenation curves in Fig. 4

$$\alpha(t) = \exp(-(kt)^n) \quad (1)$$

where $\alpha(t)$ is the time-dependent phase fraction. Assuming an Arrhenius expression for the rate constant k cf. Eq. (2)

$$k = A \exp\left(-\frac{E_A}{RT}\right) \quad (2)$$

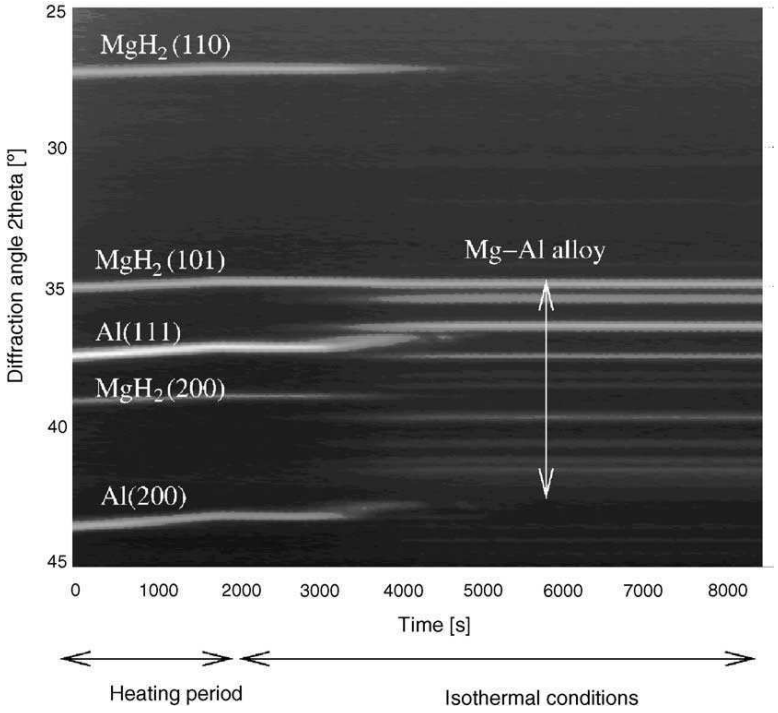

Fig. 3. Time resolved in situ XRPD of the dehydrogenation of MgH_2 + Al. The graphic consists of 72 consecutive diffraction patterns stacked chronologically from left to right. Bright areas correspond to a high detector count rate (reflections), whereas dark areas correspond to low detector count rates (background). The isothermal reaction temperature is $T = 400\,^{\circ}C$ and acquisition time is $t = 150$ s.

where A is a pre-exponential factor, E_A the apparent activation energy and R is the universal gas constant, we can extract the apparent activation energy by plotting $\ln k$ versus $1/T$ cf. Fig. 5 and find E_A/R as the slope. As shown in the figure the data points fit the Arrhenius expression Eq. (2) fairly well. The apparent activation energy is found to be 160 kJ/mol H_2. This value is very close to the activation barrier of 160–166 kJ/mol H_2 for the dehydrogenation of pure magnesium hydride recently found by Fernandez and Sanchez [7,8]. The sample in this investigation differs from the one investigated by Fernandez and Sanchez not only in composition but also in pretreatment. Special precautions were taken not to oxidize the sample in Ref. [7,8] prior to kinetic measurements and the sample was also fully activated by several adsorption/desorption cycles before measurements. In this investigation the sample has been exposed to air both before the initial hydrogenation and before the time resolved XRPD study. Recently, we investigated the dehydrogenation of pure magnesium [9] with the same setup used here and with the same pretreatment procedure. We found a substantial increase in the apparent activation enthalpy of dehydrogenation to approximately 250–300 kJ/mol (probably due to oxygen contamination/magnesium oxide formation). This comparison suggests that alloying with Al creates a compound less sensitive towards oxygen contamination which requires little if any pretreatment in order to activate the sample. No crystalline magnesium oxide is observed neither in the as-prepared ball milled sample nor in the hydrogenated/dehydrogenated sample. However, oxygen was detected using Energy Dispersive X-ray Spectroscopy suggesting the presence of an X-ray amorphous oxide. This is consistent with the observations of Scotto-Sheriff et al. [10]. Compared to a crystalline oxide layer, the presence of an amorphous oxide layer is likely to offer improved hydrogen diffusion [11,12].

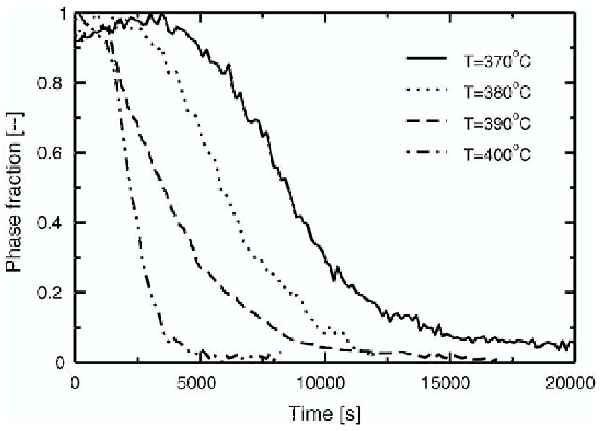

Fig. 4. Experimental dehydrogenation curves for pure MgH_2 in MgH_2 + Al determined by integrated intensity of the MgH_2 (1 1 0) reflection from time resolved in situ XRPD data.

There may be other kinetic improvements associated with alloying Mg with Al. The grain boundaries between MgH_2/Al/Mg–Al may provide favorable diffusion paths as proposed for Mg/Mg_2Cu [13].

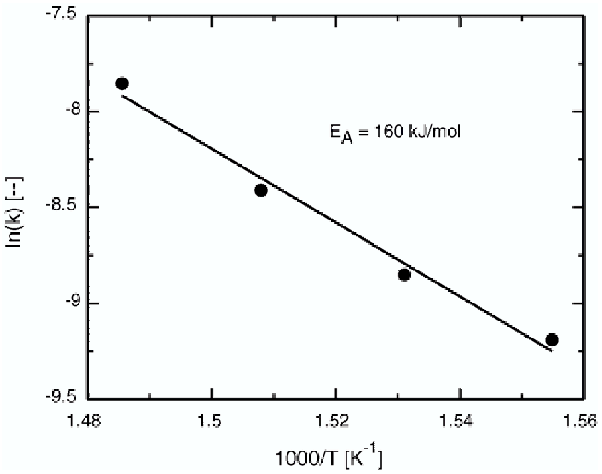

Fig. 5. Arrhenius plot of the logarithmic rate constant (derived from fitting the dehydrogenation data from time resolved in situ XRPD) vs. reciprocal temperature for the dehydrogenation of $MgH_2 + Al$.

4. Conclusion

The interaction of hydrogen with an Mg–Al alloy has been studied by in situ time resolved X-ray powder diffraction. The activation energy of dehydrogenation is found to be 160 kJ/mol. Further, we suggest that Mg–Al is less sensitive than Mg to oxygen contamination.

Acknowledgments

This work has received financial support from The Danish Technical Research Council through the Center of Excellence *Towards a hydrogen based society*. TRJ thanks The Danish National Research Council for a Steno stipend. R. Christensen (Haldor Topsøe A/S) is greatly acknowledged for assisting with in situ XRPD experiments.

References

[1] A. Zaluska, L. Zaluski, J. Ström-Olsen, Appl. Phys. A 72 (2001) 157–165.
[2] M. Bououdina, Z.X. Guo, J. Alloys Compd. 336 (2002) 222–231.
[3] S. Bouaricha, J.P. Dodelet, D. Guay, J. Huot, S. Boily, R. Schulz, J. Alloys Compd. 297 (2000) 282–293.
[4] H.L. Su, M. Harmelin, P. Donnadieu, C. Baetzner, H.J. Seifert, H.L. Lukas, G. Effenberg, F. Aldinger, J. Alloys Compd. 247 (1997) 57–65.
[5] A. Pedersen, J. Kjøller, B. Larsen, B. Vigeholm, Int. J. Hydrogen Energy 8 (3) (1983) 205–211.
[6] B. Clausen, G. Steffensen, B. Fabius, J. Villadsen, R. Feidenhans'l, H. Topsøe, J. Catal. 132 (1991) 524–535.
[7] J.F. Fernandez, C.R. Sanchez, J. Alloys Compd. 340 (2002) 189–198.
[8] J.F. Fernandez, C.R. Sanchez, J. Alloys Compd. 356–357 (2003) 348–352.
[9] T.R. Jensen, A. Andreasen, J.W. Andreasen, T. Vegge, K. Ståhl, F. Besenbacher, A. Molenbroek, M.M. Nielsen, A.S. Pedersen, Int. J. Hydrogen Energy, submitted for publication.
[10] S. Scotto-Sheriff, E. Darque-Ceretti, G. Plassart, M. Aucouturier, J. Mater. Sci. 34 (1999) 5081–5088.
[11] L. Schlapbach (Ed.), Hydrogen in intermetallic compounds II. Surface and dynamic properties, applications, Vol. 67 of Topics in Applied Physics, Springer-Verlag, 1992.
[12] A.B. Belonoshko, A. Rosengren, Q. Dong, G. Hultquist, C. Leygraf, Phys. Rev. B. 69 (2004) 024302.
[13] M. Au, J. Wu, Q. Wang, Int. J. Hydrogen Energy 20 (1995) 141–150.

Appendix C

Paper 3

Applied Physics A manuscript No.
(will be inserted by the editor)

Dehydrogenation kinetics of air-exposed MgH_2/Mg_2Cu and $MgH_2/MgCu_2$ studied with *in situ* X-ray powder diffraction

A. Andreasen[1,2], M. B. Sørensen[3], R. Burkarl[3], B. Møller[3], A. M. Molenbroek[4], A. S. Pedersen[1], T. Vegge[5,6⋆], T. R. Jensen[3]

[1] Materials Research Department, Risø National Laboratory, DK-4000 Roskilde, Denmark
[2] Interdisciplinary Research Center for Catalysis, Department of Chemical Engineering, Technical University of Denmark, DK-2800 Lyngby, Denmark
[3] Department of Chemistry, iNANO, Aarhus University, DK-8000 Aarhus C, Denmark
[4] Haldor Topsøe A/S, DK-2800 Kgs. Lyngby, Denmark
[5] CAMP and Department of Physics, Technical University of Denmark, DK-2800 Kgs. Lyngby, Denmark
[6] Danfoss Corporate Ventures A/S, DK-6430 Nordborg, Denmark

Received: date / Revised version: date

Abstract The dehydrogenation kinetics of air exposed samples of MgH_2/Mg_2Cu and $MgH_2/MgCu_2$ have been studied with *in situ* time resolved X-ray powder diffraction. The X-ray setup enabled the recording of full diffraction patterns within 150 s, thereby allowing the study of structural changes combined with simultaneous extraction of kinetic parameters. Phase fractions as a function of time and temperature were derived from series of consecutive diffraction patterns by numerical integration of selected diffraction peaks. The apparent activation energy for the dehydrogenation of the MgH_2/Mg_2Cu, and $MgH_2/MgCu_2$ sample was found to be 108 kJ/mol and 160 kJ/mol, respectively. Furthermore, substantially improved dehydrogenation kinetics of MgH_2 and resistance towards oxidation of Mg due to the presence of $Mg_2Cu/MgCu_2$ are discussed in relation to previous work.

PACS 61.10.Nz; 81.65.Mq; 82.20.Pm;

1 Introduction

Magnesium hydride, MgH_2, has a high theoretical gravimetric hydrogen density of $\rho_{H_2}(m)$ = 7.6 wt. % and is the binary metal hydride that comes closest to fulfilling the year 2010 target proposed by the U. S. Department of Energy for hydrogen storage materials regarding hydrogen density and stabillity viz. $\rho_{H_2}(m) > 6$ wt.% and desorption of hydrogen at 1 bar below 85 °C, corresponding to a formation enthalpy of $\Delta H_f \approx -47$ kJ/mol H_2 [1]. However, magnesium hydride requires approx. 280 °C for dehydrogenation at 1 bar ($\Delta H_f = -75$ kJ/mol H_2) and suffers from slow kinetics. Still, magnesium has been the subject of extensive research during the past decades, especially regarding possible improvements of kinetics and thermodynamic properties. Both kinetics and thermodynamic properties are affected by alloying with transition metals e.g. Ni, Cu, Fe, Co [2–4]; the price being a reduced hydrogen capacity.

Magnesium reacts with hydrogen forming magnesium hydride

$$Mg + H_2 \rightleftharpoons MgH_2 \quad (1)$$

and it has been shown that Mg_2Cu disproportionates during hydrogenation [5,6]

$$2Mg_2Cu + 3H_2 \rightleftharpoons 3MgH_2 + MgCu_2 \quad (2)$$

According to reaction Eq. 2, Mg_2Cu has a calculated hydrogen capacity of 2.62 wt. %, and ΔH_f for reaction eq. 2 is approx. 5 kJ/mol H_2 lower than for reaction Eq. 1 ($\Delta H_f \approx$ -70 kJ/mol H_2) [2,5]. The difference in ΔH_f for reactions 1 and 2 leads to a difference in the plateau pressure, p_{pl}. Thus, by proper selection of the hydrogen pressure during hydrogenation, the eutectic alloy can react with hydrogen forming either MgH_2/Mg_2Cu (low pressure, reaction 1) or $MgH_2/MgCu_2$ (high pressure, reaction 1+2). $MgCu_2$ does not hydrogenate under conventional hydrogenation conditions [5,7]. According to calculations this can be explained by a large positive formation enthalpy of Mg-Cu hydrides [8,9].

The presence of Mg_2Cu in Mg has been suggested to have several positive effects. Karty *et al.* [2] have suggested that Mg_2Cu adds an external oxide-free surface (in contrast to Mg which is easily oxidized) on which hydrogen can dissociate with subsequent diffusion of H-atoms through bulk Mg_2Cu to the Mg/Mg_2Cu interface, where MgH_2 is formed. Similar conclusions have been reached by Au *et al.* [10] from the study of a multi component magnesium based alloy. However, in contrast to Karty *et al.*, Au *et al.* propose that atomic

Send offprint requests to: A. Andreasen
⋆ *Present address: Materials Research Department, Risø National Laboratory, DK-4000 Roskilde, Denmark*
Correspondence to: trj@chem.au.dk

hydrogen diffusion takes place mainly at the Mg-Mg_2Cu interface rather than in bulk Mg_2Cu. Studies of MgH_2 formation in composites containing Mg/Mg_2Cu suggest that the hydrogenation properties are improved due to improved diffusion of H-atoms in bulk Mg_2Cu or along the Mg-Mg_2Cu interface, and the addition of stable nucleation sites along the Mg-Mg_2Cu interface [11–13]. Further, it has been suggested that upon exposure to air, Mg segregates to the surface induced by MgO formation, potentially forming particles of metallic Cu near the surface, catalyzing the dissociation of H_2 [10,14,15].

In this paper we investigate the improved dehydrogenation kinetics of MgH_2/Mg_2Cu, as compared to MgH_2, due to improved resistance towards oxygen contamination. We compare the dehydrogenation kinetics of air exposed MgH_2/Mg_2Cu to air exposed pure MgH_2 from previous work [16]. In addition, we study the dehydrogenation of $MgH_2/MgCu_2$. Applying *in situ* time-resolved X-ray powder diffraction (XRPD) both structural information and phase fractions vs. time can be extracted. Time dependent phase fractions are subject to kinetic analysis. The results are compared to literature data on dehydrogenation kinetics. We proceed with a discussion of the role of Cu on hydrogenation/dehydrogenation kinetics of MgH_2.

2 Experimental

The Mg-Cu sample investigated is the Mg/Mg_2Cu eutectic alloy similar in composition to the one investigated by Karty *et al.* [2]. According to the phase diagram this alloy has a composition of 85.5 % Mg and 14.5 % Cu (atomic). The Mg/Mg_2Cu alloy was prepared by arc melting a mixture of magnesium and copper according to the stoichiometry of the eutectic alloy in a Edmund Buhler Arc Melting system. The Mg-Cu sample was melted repeatedly in an Argon atmosphere until the sample appeared homogeneous. Subsequently, the Mg/Mg_2Cu sample was ball milled for 10 min using Tungsten carbide balls.

The ball milled sample of Mg/Mg_2Cu was divided into two portions and hydrogenated by two different methods (method **A** and **B**). Method **A**: A hydrogen pressure of 6 bar and a temperature of 325 °C was applied to the sample until the hydrogen uptake had saturated. The low hydrogen pressure should facilitate the formation of MgH_2 + Mg_2Cu. Method **B**: like method **A**, but instead a hydrogen pressure of 30 bar was applied in order to facilitate the formation of MgH_2 + $MgCu_2$. For both samples, hydrogenation was carried out in a Sartorius high pressure balancing unit (see ref. [17] for equipment details) using 99.9997 % H_2 from Air Liquide. The hydrogen uptake was followed by measuring the weight gain of the sample.

The X-ray instrument used for *in situ* time resolved XRPD was built using a Rigaku rotating anode (Cu $K_{\alpha_{12}}$ radiation, $\bar{\lambda}$ = 1.5418 Å, 50 kV and 300 mA). The intensity of the diffracted beam was recorded with a curved position sensitive detector, INEL CPS 120, covering 120 ° in 2θ with a resolution of approx. 0.03 °. The acquisition time per powder pattern was chosen to be in the range 50-190 s as a compromise between time resolution and count rate.

The *in situ* reactor cell was developed to study gas-solid reactions [18]. The powder sample was loaded between plugs of quartz glass wool in a quartz capillary tube (0.7 mm O.D.) in order to fix the bed and allow a gas flow (Ar, 10 mL/min) through the sample during data acquisition as shown in Fig. 1. The samples were heated by a stream of hot nitrogen gas (20 °C/min) to a constant temperature in the range 360-400 °C and the dehydrogenation was followed under isothermal conditions. In order to promote isothermal conditions the glass capillary is capped with a 180 ° graphite window.

All samples were exposed to air under ambient conditions both during loading in high pressure balance, and during transport of the hydrogenated samples from high pressure balance to the quartz capillary tube in the XRPD reaction cell.

3 Results and Discussion

3.1 Hydrogenation

The hydrogenation of the Mg/Mg_2Cu eutectic alloy by methods **A** and **B** are shown in Fig. 2. Both methods result in complete hydrogenation within approx. 15 hours. Method **B** seems to provide faster kinetics, possibly due to the larger driving force (p_{H_2}-p_{pl}) towards formation of MgH_2 through reaction eq. 1. The total hydrogen uptake in method **A** is 3.26 wt. %, which is close to the theoretical uptake of 3.51 wt. % assuming that only Mg hydrogenates, while Mg_2Cu remains stable at the low pressure applied. The total observed hydrogen uptake in method **B** is 4.50 wt.%, which also is close to the calculated uptake of 4.86 wt. % assuming disproportionation of Mg_2Cu according to reaction 2 accompanying reaction 1. The difference between theoretical and experimental values may be due to loss of magnesium during arc melting (The boiling point of Magnesium is close to the melting point of Cu [19]) or the loss of magnesium due to irreversible oxide formation.

Figure 3 shows XRPD patterns of samples A and B. Diffraction peaks up to $2\theta = 60$ ° is assigned to MgH_2, Mg_2Cu and $MgCu_2$ using the crystallographic information shown in Table 1. It is observed that only MgH_2 and Mg_2Cu are formed in sample A, and in sample B only MgH_2 and $MgCu_2$ is observed, which confirms the picture from the gravimetric measurements and reactions eq. 1 and eq. 2. A small feature around 2θ = 42-43 ° could be due to the presence of small amounts of crystalline MgO in samples A and B.

3.2 Dehydrogenation studied with in situ *XRPD*

The decomposition of MgH_2+Mg_2Cu (A) and MgH_2 + $MgCu_2$ (B) investigated by *in situ* time resolved XRPD is illustrated by series of consecutive diffraction patterns in Fig. 4. For the dehydrogenation of MgH_2 + Mg_2Cu (A), figure 4A shows the disappearance of all MgH_2 reflections and the corresponding

appearance of reflections from pure Mg, while the Mg_2Cu reflections are unaffected. The dehydrogenation of MgH_2 + $MgCu_2$ (B), 4B, shows the simultaneous reaction of MgH_2 to Mg and $MgCu_2$ to Mg_2Cu, which is clearly observed by inspection of integrated intensities for all four constituent phases in Fig. 5. During heating of the samples the MgH_2, Mg_2Cu and $MgCu_2$, reflections shift towards lower 2θ values due to thermal expansion of the crystal lattices.

The peak position of the MgH_2 (110) and the Mg (100) reflections are determined from consecutive XRPD patterns for the dehydrogenation of MgH_2/Mg_2Cu (A) at 380 °C. These parameters are compared to the reaction cell temperature and the degree of transformation (phase fractions) in Fig. 6. We notice that the position of the MgH_2 (110) reflection shifts downwards in 2θ during the heating period, corresponding to a thermal expansion of the MgH_2 crystal lattice. The time when the peak position reaches a constant value coincides with the end of the temperature ramp of the reaction cell. This indicates that there is negligible heat resistance between the hot nitrogen gas in the oven (position of the thermocouple) and the interior of the hydride bed in the quartz capillary tube.

From t = 3500 s to t = 5800 s the phase fraction of MgH_2 changes from α = 0.9 to 0.1. In this region no significant changes in peak position takes place, indicating that the crystal lattices are unaffected by the dehydrogenation. It should, however, be noted that no reliable data could be extracted from neither the MgH_2 (110) peak in the limit of complete transformation nor the Mg (110) peak at the start of the reaction. No significant changes are observed in neither the FWHM of MgH_2 (110) nor the FWHM of Mg (110). The crystallite size of MgH_2 and Mg have been estimated to 45-50 nm using the Scherrer equation:

$$\beta = \frac{\lambda}{B\cos\theta} \tag{3}$$

where β is the crystallite size, λ is the X-ray wavelength and B is the FWHM (corrected for instrumental broadening, which is estimated to 0.05 °).

3.3 Kinetics from in situ *XRPD*

The phase fraction of MgH_2 has been calculated from the *in situ* XRPD data of both samples by numerical integration of the MgH_2 (110) reflection. Dehydrogenation curves i.e. phase fraction of MgH_2 vs. time ($\alpha(t)$) have been constructed for all experiments using normalized integrated intensities. The results are shown in Fig. 7. All dehydrogenation curves show a sigmodal shape and faster dehydrogenation with higher temperatures.

A conventional Johnson-Mehl-Avrami (JMA) type nucleation and growth rate equation (4) has been fitted to the dehydrogenation curves in Fig. 7 [23–26]

$$\alpha(t) = \exp\left(-(kt)^n\right) \tag{4}$$

The parameters describing nucleation and growth rates are contained within an effective kinetic parameter, k, and an exponent, n. We note that the value of the rate constant, k, is often insensitive to the specific choice of rate expression [2, 27, 16]. Therefore, the derived rate constants are not restricted to the use of a JMA type of rate equation.

A conventional Arrhenius expression ,cf. eq. 5, is assumed for the rate constant, k

$$k = A\exp\left(-\frac{E_A}{RT}\right) \tag{5}$$

where A is a pre-exponential factor, E_A is the apparent activation energy and R is the universal gas constant. A plot of $\ln k$ vs. $1/T$ can provide E_A from the slope as seen in Fig. 8. According to the figure the data points fit the Arrhenius relation eq. 5 quite well. The term *apparent* implies that extracted activation energies may contain contributions from several processes and not only the activation barrier for a single elementary reaction.

The apparent activation energy for dehydrogenation of MgH_2 in MgH_2/Mg_2Cu (sample A) is found to be 108 $\pm$ 12 kJ/mol, and for MgH_2 in $MgH_2/MgCu_2$ we find 160 $\pm$ 11 kJ/mol. For comparison we have included results in Fig. 8 for dehydrogenation of pure air-exposed MgH_2 [16] obtained using an identical experimental procedure and data analysis, E_a = 297$\pm$26. These results clearly indicate that the presence of either Mg_2Cu or $MgCu_2$ in MgH_2 has a pronounced positive effect on the dehydrogenation kinetics of air-exposed samples. Similar values for the apparent activation energies were found when the rate constant was fitted to phase fractions derived from other phases e.g. the formation of Mg or the consumption of $MgCu_2$ (sample B).

Before we proceed with a more detailed discussion of our results in relation to the literature we note that *(i)*: the apparent activation energy found for dehydrogenation of air-exposed MgH_2 [16] is significantly higher than the value of 120-160 often cited [27–31] *(ii)*: the apparent activation energy found for dehydrogenation of MgH_2 in MgH_2/Mg_2Cu (sample A) is in agreement with the value found by Karty [2] and *(iii)*: to the best of our knowledge apparent activation energies for the dehydrogenation of $MgH_2/MgCu_2$ (sample B) have not previously been reported.

3.4 Cu catalyzed dissociation/recombination of H_2

It is generally agreed that magnesium does not promote dissociation of hydrogen molecules, H_2 [32] . Both experiments and recent DFT-GGA calculations suggest that the activation energy for dissociation of hydrogen on Mg is indeed an activated process with a barrier of approx. 100 kJ/mol [33, 34]. From both experiments and calculations the dissociation barrier for H_2 on a Cu(111) surface is found to be approx. 50 kJ/mol [35–38].

As already mentioned in the introduction, due to oxidation induced surface segregation of Mg in Mg_2Cu, globules of metallic Cu is likely to form near the surface. Thus the

presence of metallic Cu could indeed be possible in the samples of investigation leading to improved kinetics due to Cu assisted dissociation/association of H_2.

Karty *et al.* [2] reported apparent activation energies of E_A= 132 and 106 kJ/mol for dehydrogenation of vapor deposited MgH_2 and bulk MgH_2/Mg_2Cu, respectively, thus, indicating improved kinetics by addition of Mg_2Cu to Mg. They proposed that Mg_2Cu provides a clean contamination free (reduced) external surface in contrast to Mg, which is easily oxidized. According to their proposed mechanism, hydrogen diffuses from MgH_2 upon dehydrogenation through the freshly produced Mg phase, across the grain boundary to neighboring Mg_2Cu through the Mg_2Cu phase to the oxide free surface, where it recombines to H_2.

Further, the catalytic effect of some metals has renewed the interest in the possible use of magnesium as a hydrogen storage media during the past decade [39–41]. Composite materials can have very fast kinetics for hydrogen absorption and release, e.g. ball milled, La_2Mg_{17} + 40 wt.% $LaNi_5$, which absorbed 95% of its full hydrogen capacity (3.7 wt.% H2) in 27 s at 250 °C and desorped the same quantity of hydrogen in 4 min. [42]. Other composite materials prepared by ball milling of MgH_2 with $LaNi_5$, Pd have also shown improved kinetics compared to pure MgH2, possibly due to the catalytic effect of the additives [43,44].

Although applicable to the experiments of Karty *et al.* the theory of Cu induced hydrogen dissociation/recombination does not (or at least only partially) seem to offer an explanation of the relatively large difference in apparent activation energy of dehydrogenation between pure and Cu containing samples of MgH_2 in this study. Furthermore, metallic Cu is not observed in the samples investigated here.

3.5 Effect of surface oxide on kinetics

The oxidation behavior of Mg is well investigated. A 1-2 nm thick oxide layer builds up within minutes when Mg is exposed to air. This MgO layer reaches approx. 3 nm after 2 hours and continues to grow slowly and the oxide thickness reaches approx. 4-5 nm within 10 months [45–49]. Both temperature and moisture can increase the speed of oxide growth [47].

It is known that hydrogen diffusion in the close packed MgO is extremely poor [50] and strongly thermally activated compared to diffusion of hydrogen in Mg [34] and MgH_2[51]. The presence of an oxide layer/shell on magnesium particles therefore lowers the rate of MgH_2 formation/decomposition [52]. In fact Hjort *et al.* [53] have shown that the rate of hydrogen uptake at room temperature in Pd-coated Mg films decreased 2 orders of magnitude when exposed to oxygen. Further, exposing the sample to air at ambient conditions lead to a decrease in the uptake rate of 3 orders of magnitude. Pedersen *et al.* [54,55] have investigated the effect of cycling magnesium powder in impure hydrogen. They found that introducing impure hydrogen containing approx. 5000 ppm O_2 lead to a decrease in hydrogen uptake capacity due to a decreased uptake rate compared to that in hydrogen with less than 1 ppm total impurities. Furthermore, activation of air exposed Mg by at least 1 cycle of hydrogenation/dehydrogenation is necessary in order to obtain steady-state kinetics [48]. The applied activation procedure covers different phenomena including penetration of the surface oxide film, followed by hydrogenation leading to cracking of particles (including oxide film), due to the crystal lattice expansion associated with the hydride formation and the brittle nature of the hydride [6,14,56,57].

We have previously compiled representative values of the apparent activation energy for dehydrogenation of magnesium hydride samples with different compositions, investigated with different methods and subject to different activation procedures [52]. The general picture found was, that E_A for dehydrogenation of activated non-alloyed samples lies in the range 100-170 kJ/mol. Second, E_A for non-alloyed and non-activated samples is significantly higher and close to 300 kJ/mol. This may be rationalized in terms of creation of an MgO film on Mg particles. Third, the alloyed and non-activated samples have an apparent activation energy comparable to the activated and non-alloyed samples. This suggests that reduction in E_A due to the presence of $Mg_2Cu/MgCu_2$ observed in this study is mainly due to the creation of an external surface free of oxide or only being partially oxidized. A similar effect was recently shown for dehydrogenation of MgH_2/Al [60].

What remains unexplained is the fact that E_A for dehydrogenation of $MgH_2/MgCu_2$ is higher than for MgH_2/Mg_2Cu. A preliminary hypothesis is that this is due to a slow solid state transition of $MgCu_2$ + Mg to form Mg_2Cu [59] combined with slow hydrogen diffusion from MgH_2 through $MgCu_2$ to the external surface.

4 Conclusion

The dehydrogenation of air exposed MgH_2/Mg_2Cu, and $MgH_2/MgCu_2$ was studied by time resolved *in situ* powder X-ray diffraction. The apparent activation energy is found to be 108 kJ/mol and 160 kJ/mol, respectively. The range of apparent activation energies found lie within the range usually reported for well activated samples of pure Mg. In comparison the apparent activation energy for air exposed Mg is approx. 300 kJ/mol, suggesting that alloying Mg with Cu creates a hydrogen storage compound less sensitive towards surface oxidation.

Acknowledgements This work has received financial support from the The Danish Technical Research Council through the Center of Excellence *Towards a hydrogen based society* and from the Danish Research Agency and Danfoss Corporate Ventures A/S through Grant No. 2013-01-0043. The Center for Atomic-scale Materials Physics (CAMP) is sponsored by the Danish National Research Foundation. TRJ is grateful to SNF for a Steno stipend and to Carlsbergfondet for a research stipend. M. M. Nielsen (Risø), J. W. Andreasen (Risø), R. Christensen (Haldor Topsøe A/S) are greatly acknowledged for assisting with *in situ* XRPD experiments. Nini Pryds (Risø) is acknowledged for kindly prepared the Mg/Mg_2Cu eutectic alloy by Arc Melting.

References

1. U. S. Department of Energy, URL http://www.eere.energy.gov/-hydrogenandfuelcells/hydrogen/storage.html.
2. A. Karty, J. Grunzweig-Genossar, P. Rudman, J. Appl. Phys. **50 (11)**, 7200 (1979)
3. A. Reiser, B. Bogdanović, K. Schlichte, Int. J. Hydrogen Energy **25**, 425 (2000)
4. G. Sandrock, G. M. Thomas, Appl. Phys. A. **72**, 153 (2001)
5. J. J. Reilly, R. H. Wiswall, Inorg. Chem. **6**, 2220 (1967)
6. L. Schlapbach (Ed.), Hydrogen in Intermetallic Compounds II. Surface and dynamic Properties, Applications, Vol. 67 of Topics in Applied Physics (Springer-Verlag 1992)
7. Y. Tsushio, E. Akiba, J. Alloys Comps. **269**, 219 (1998)
8. T. Vegge, L. S. Hedegaard-Jensen, J. Bonde, T. R. Munter, J. K. Nørskov, J. Alloys Comps. **386**, 1 (2005)
9. Y. Song, Z. X. Guo, R. Yang, Phys. Rev. B **69**, 094205 (2004)
10. M. Au, J. Wu, Q. Wang, Int. J. Hydrogen Energy **20**, 141 (1995)
11. S. Orimo, H. Fujii, S. Horie, J. Alloys Comps. **231**, 766 (1995)
12. K. Yamamoto, Y. Tsushio, S. Tanioka, T. Shimizu, T. Morishita, S. Orimo, H. Fujii, J. Alloys Comps. **231**, 689 (1995)
13. K. Yamamoto, S. Tanioka, Y. Tsushio, T. Shimizu, T. Morishita, S. Orimo, H. Fujii, J. Alloys Comps. **243**, 144 (1996)
14. A. Seiler, L. Schlapbach, Th. Von Waldkirch, D. Shaltiel, F. Stucki, J. Less-Common Met. **73**, 193 (1980)
15. P. Selvam, B. Viswanathan, C. S. Swamy, V. Srinivasan, Int. J. Hydrogen Energy **13**, 87 (1988)
16. T. R. Jensen, A. Andreasen, T. Vegge, J. W. Andreasen, K. Ståhl, A. M. Molenbroek, M. M. Nielsen, A. S. Pedersen, F. Besenbacher, *S*ubmitted (2005).
17. A. Pedersen, J. Kjøller, B. Larsen, B. Vigeholm, Int. J. Hydrogen Energy **8 (3)**, 205 (1983)
18. B. Clausen, G. Steffensen, B. Fabius, J. Villadsen, R. Feidenhans'l, H. Topsøe, J. Catal. **132**, 524 (1991)
19. D. R. Lide (Ed.), Handbook of Chemistry and Physics, 78th Edition (CRC Press 1997)
20. F. Ellinger, C. Holley jr., B. McInteer, D. Pavone, R. Potter, E. Staritzky, W. Zachariasen, J. Am. Chem. Soc. **77**, 2647 (1955)
21. P. Villars, Pearson's Handbook - Desk Edition, Vol. 2, (ASM International 1997)
22. J. Pelletier, J. Huot, M. Sutton, R. Schulz, A. Sandy, L. Lurio, S. Mochrie, Phys. Rev. B **63**, 052103 (2001)
23. M. Avrami, J. Chem. Phys. **7**, 1103 (1939)
24. M. Avrami, J. Chem. Phys. **8**, 212 (1940)
25. M. Avrami, J. Chem. Phys. **9**, 177 (1941)
26. W. A. Johnson, R. F. Mehl, Trans. A.I.M.E. **135**, 416 (1939)
27. C. Stander, J. Inorg. Nucl. Chem. **39**, 221 (1977)
28. J. F. Fernandez, C. R. Sanchez, J. Alloys Comps. **340**, 189 (2002)
29. J. F. Fernandez, C. R. Sanchez, J. Alloys Comps. **356-357**, 348 (2003)
30. J. Han, M. Pezat, J.-Y. Lee, J. Less-Common Met. **130**, 395 (1987)
31. M. Martin, G. Gommel, C. Borkhardt, E. Fromm, J. Alloys Comps. **238**, 193 (1996)
32. P. T. Sprunger, E. W. Plummer, Surf. Sci. **307-309**, 118 (1994)
33. P. T. Sprunger, E. W. Plummer, Chem. Phys. Lett. **187**, 559 (1991)
34. T. Vegge, Phys. Rev. B, **70**, 035412 (2004)
35. P. B. Rasmussen, P. M. Holmblad, H. Christoffersen, P. A. Taylor, I. Chorkendorff, Surf. Sci. **287-288**, 79 (1993)
36. J. K. Nørskov, B. Hammer, Nature **376**, 238 (1995)
37. B. Hammer, M. Scheffler, K. W. Jacobsen, J. K. Nørskov, Phys. Rev. Lett. **73**, 1400 (1994)
38. S. Sakong, A. Groß, Surf. Sci. **525**, 107 (2003)
39. P. Mandal, K. Dutta, K. Ramakrishna, J. Alloys Comp. **184**, 1 (1992)
40. K. J. Gross, P. Spatz, A. Züttel, L. Schlapbach, J. Alloys Comps. **240**, 206 (1996)
41. K. J. Gross, P. Spatz, A. Züttel, L. Schlapbach, J. Alloys Comps. **261**, 276 (1997)
42. K. J. Gross, D. Chartouni, E. Leroy, A. Züttel, L. Schlapbach, J. Alloys Comps. **269**, 259 (1998)
43. H. Reule, M. Hirscher, A. Weisshardt, H. Kronmüller, J. Alloys Comps. **305**, 246 (2000)
44. F. von Zeppelin, H. Reule, M. Hirscher, J. Alloys Comps. **330–332**, 723 (2002)
45. C. Chen, S. J. Splinter, T. Do, N. S. McIntyre, Surf. Sci. **382**, L652 (1997)
46. T. Do, S. J. Splinter, C. Chen, N. S. McIntyre, Surf. Sci. **387**, 192 (1997)
47. V. Fournier, P. Marcus, I. Olejord, Surf. Interface Anal. **34**, 493 (2002)
48. B. Vigeholm, J. Kjøller, B. Larsen, J. Less-Common Met. **74**, 341 (1980)
49. C. Chen, N. S. McIntyre, Corrosion Science **40**, 1697 (1998)
50. R. Gonzalez, Y. Chen, K. L. Tang, Phys. Rev. B. **26(8)**, 4637 (1982)
51. J. Töpler, H. Buchner, H. Säufferer, K. Knorr, W. Prandl, J. Less-Common Met. **88**, 397 (1982)
52. A. Andreasen, T. Vegge, A. S. Pedersen, J. Phys. Chem. B., **109**, 3340-3344 (2005)
53. P. Hjort, A. Krozer, B. Kasemo, J. Alloys Comps. **237**, 74 (1996)
54. A. S. Pedersen, B. Vigeholm, J. Kjøller, B. Larsen, Int. J. Hydrogen Energy **12**, 765 (1987)
55. A. S. Pedersen, B. Larsen, Int. J. Hydrogen Energy **18**, 297 (1993)
56. B. Vigeholm, K. Jensen, B. Larsen, A. S. Pedersen, J. Less-Common Met. **131**, 133 (1987)
57. G. Alefeld, J. Völkl, (Eds.), Hydrogen in metals II, Vol. 29 of Topics in Applied Physics (Springer-Verlag 1978)
58. A. S. Pedersen, K. Jensen, B. Larsen, B. Vigeholm, J. Less-Common Met. **131**, 31 (1987)
59. K. Nonaka, T. Sakazawa, H. Nakajima, Mater. T. JIM **36**, 1463 (1995)
60. A. Andreasen, M. B. Sørensen, R. Burkarl, B. Møller, A. M. Molenbroek, A. S. Pedersen, J. W. Andreasen, M. M. Nielsen, T. R. Jensen, J. Alloys Comps. *In press:* DOI: 10.1016/j.jallcom.2005.01.119

Figure and table captions

Figure 1: Schematic drawing illustrating the experimental setup for *in situ* X-ray powder diffraction.

Figure 2: Hydrogen uptake of the Mg/Mg_2Cu eutectic alloy of composition 85.5 atomic % magnesium by method **A** and **B**. The dashed lines show theoretical hydrogen uptakes according to reaction 1 and 2, of 3.51 and 4.86 wt.%, respectively.

Figure 3: XRPD acquired at room temperature of sample A, MgH_2/Mg_2Cu (upper) and B, $MgH_2/MgCu_2$ (lower). **#**: MgH_2, **+**: Mg_2Cu and **o**: $MgCu_2$.

Figure 4: Time resolved *in situ* XRPD of the dehydrogenation of sample A, MgH_2/Mg_2Cu (upper) and sample B, $MgH_2/MgCu_2$ (lower). Heating from RT to an isothermal reaction temperature of T = 400 °C and T = 390 °C, respectively, and the acquisition time is t = 150 s pr. powder pattern.

Figure 5: Crystalline phase fractions of MgH_2, $MgCu_2$, Mg_2Cu, and Mg vs. time for $MgH_2/MgCu_2$ from numerical integration of selected reflections. For illustrative purpose the phase fractions have been scaled to reflect the initial stoichiometry of the eutectic alloy. T = 360 °C and the acquisition time is 150 s.

Figure 6: Peak position (upper) of the MgH_2 (110) and the Mg (100) reflection and recorded reaction cell temperature (lower). The limits of 10 % and 90 % transformation of MgH_2 into Mg are marked with vertical dashed lines. Data points are for dehydrogenation of MgH_2/Mg_2Cu (A) at 380 °C.

Figure 7: Experimental dehydrogenation curves for MgH_2/Mg_2Cu (A), and $MgH_2/MgCu_2$ (B), respectively, determined by integrated intensity of the MgH_2(110) reflection from time resolved *in situ* XRPD data. Full lines represent the best fit of Eq. 4 to the data.

Figure 8: Arrhenius plot of the logarithmic rate constant (derived from the dehydrogenation data from time resolved *in situ* XRPD) vs. reciprocal temperature for the dehydrogenation of MgH_2 (from ref. [16]) MgH_2/Mg_2Cu (A) and $MgH_2/MgCu_2$ (B).

Table 1: Space group and lattice parameters for the observed phases in the hydrogenated samples. From ref. [20,21].

	MgH_2	Mg_2Cu	$MgCu_2$
s.g.	$P4_2/mnm$	$Fddd$	$Fd\bar{3}m$
a [Å]	4.5168	5.2840	7.034
b [Å]	4.5168	9.070	7.034
c [Å]	3.0205	18.25	7.034

Table 1

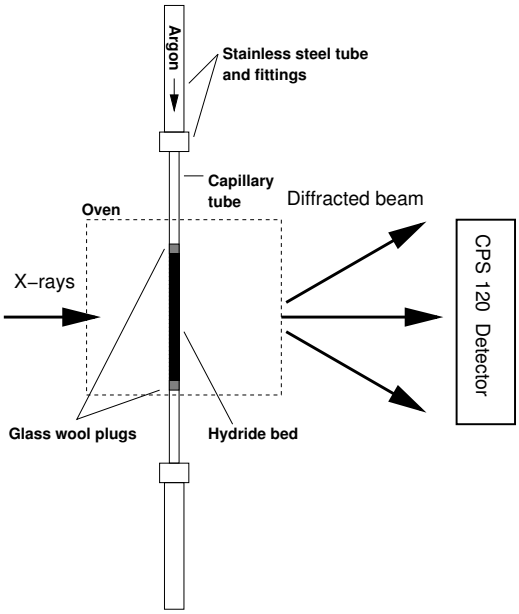

Fig. 1

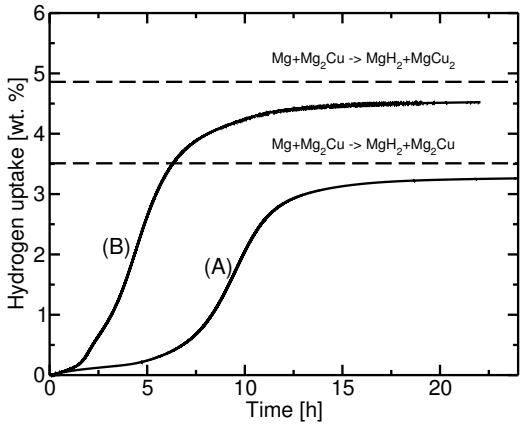

Fig. 2

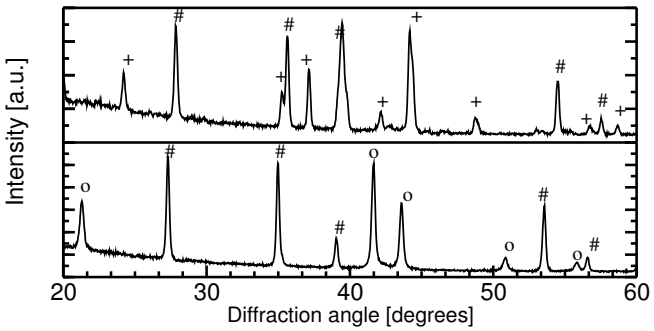

Fig. 3

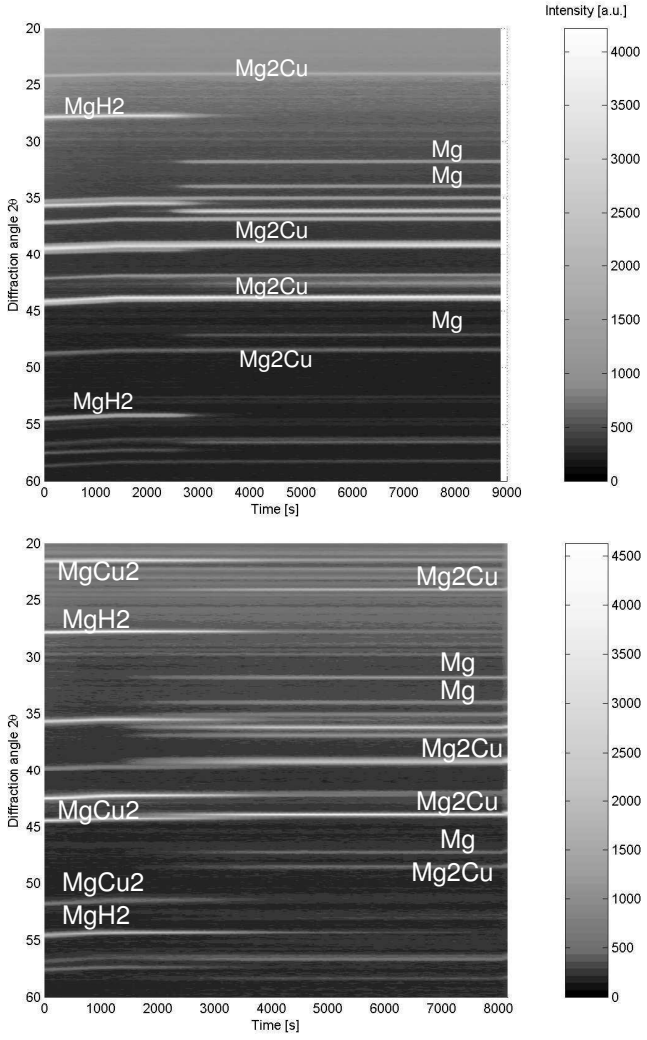

Fig. 4

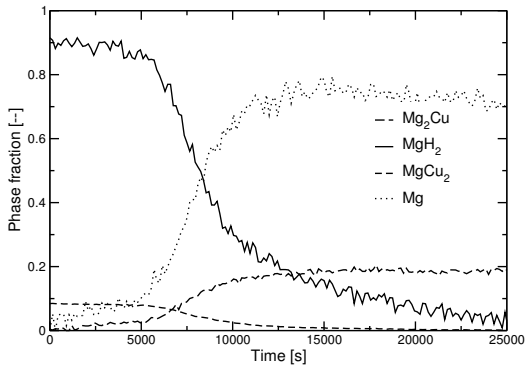

Fig. 5

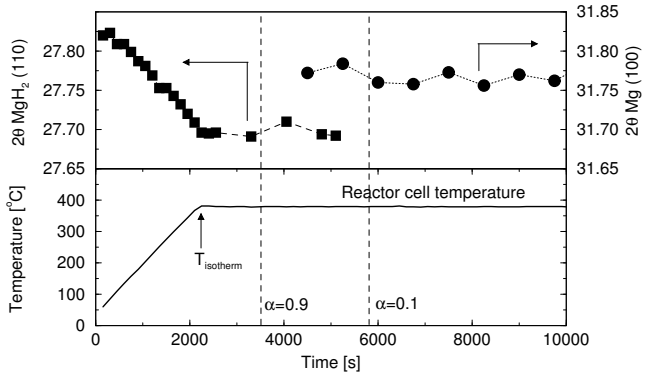

Fig. 6

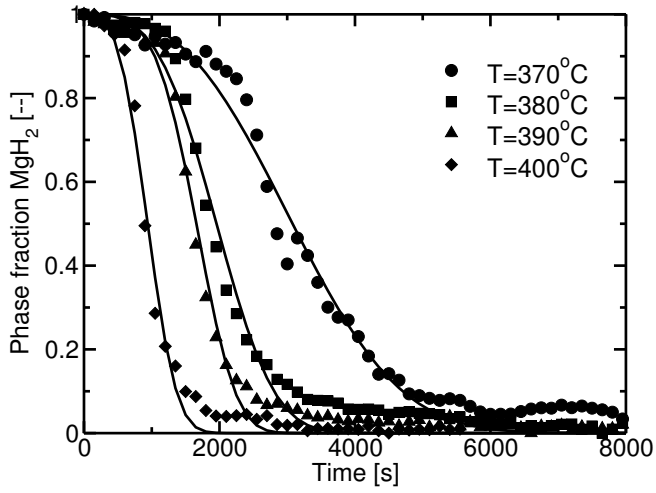

(A)

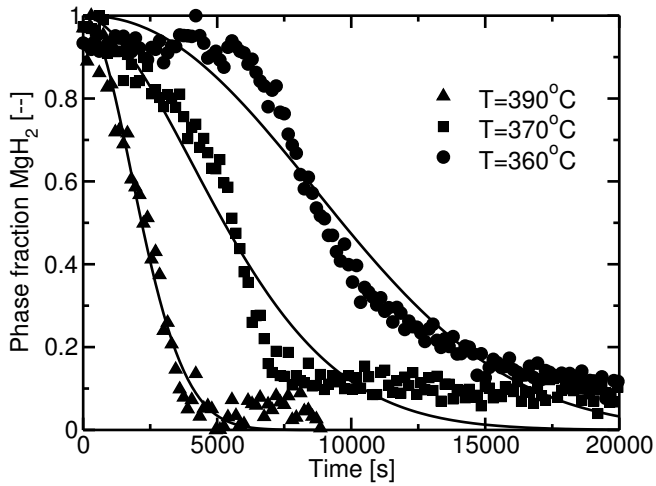

(B)

Fig. 7

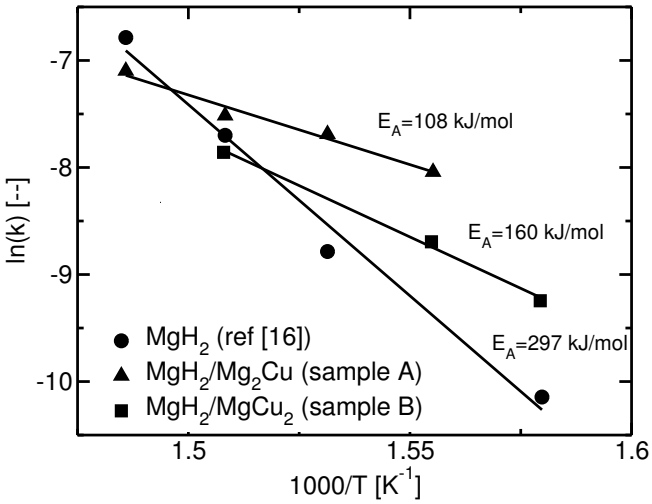

Fig. 8

Appendix D

Paper 4

Dehydrogenation kinetics of pure and nickel-doped magnesium hydride investigated by *in situ* time resolved powder X-ray diffraction

Torben R. Jensen,[a,*] Anders Andreasen,[b,c] Tejs Vegge,[b,d] Jens W. Andreasen,[b,e,f] Kenny Ståhl,[e] Allan S. Pedersen,[b] Martin M. Nielsen,[f] Alfons M. Molenbroek,[g] Flemming Besenbacher,[h]

[a]*Interdisciplinary Nanoscience Center (iNANO), Department of Chemistry, University of Aarhus, DK-8000 Aarhus C, Denmark*
[b]*Materials Research Department, Risø National Laboratory, DK-4000 Roskilde, Denmark*
[c]*Interdisciplinary Research Center for Catalysis, Department of Chemical Engineering, Technical University of Denmark, DK-2800 Lyngby, Denmark*
[d]*Department of Physics and Center for Atomic scale Materials Physics, Technical University of Denmark, DK-2800 Lyngby, Denmark,*
[e]*Department of Chemistry, Technical University of Denmark, DK-2800 Lyngby, Denmark*
[f]*Danish Polymer Centre, Risø National Laboratory, DK-4000 Roskilde, Denmark*
[g]*Haldor Topsøe A/S, DK-2800 Kgs. Lyngby, Denmark*
[h]*Interdisciplinary Nanoscience Center (iNANO), Department of Physics and Astronomy, University of Aarhus, DK-8000 Aarhus C, Denmark*

* Corresponding author. Fax: +45 8619 6199
E-mail address: trj@chem.au.dk (T. R. Jensen)

Dr. Torben R. Jensen,
Interdisciplinary Nanoscience Center (*i*NANO)
Department of Chemistry
University of Aarhus
Langelandsgade 140
DK-8000 Aarhus C, Denmark
Phone: +45 8942 3894, *Fax*: +45 8619 6199, *e-mail*: trj@chem.au.dk

Abstract

The dehydrogenation kinetics of pure and nickel doped (2 w/w %) magnesium hydride have been investigated by *in situ* time resolved powder X-ray diffraction (PXD). Deactivated samples, *i.e.* air exposed, are investigated in order to focus on the effect of oxidised MgO surface layers, which might be unavoidable for magnesium based storage media for mobile applications. A quartz capillary cell allowed the study of gas/solid reactions. A curved position sensitive detector covering 120° in 2θ and a rotating anode X-ray source provide a time resolution of 45 s and up to 90 powder patterns collected during an experiment under isothermal conditions. Three phases were identified, Mg, MgH_2 and MgO, and their phase fractions were extracted by Rietveld refinement or integration of selected reflections from each phase. Dehydrogenation curves were constructed and analyzed by the Johnson- Mehl-Avrami formalism in order to derive rate constants at different temperatures. The apparent activation energies for dehydrogenation of pure and nickel doped magnesium hydride were $E_A \approx 300$ and 250 kJ/mol, respectively. Differential scanning calorimetry gave, E_A = 270 kJ/mol for dehydrogenation of the Ni doped sample. The relatively high activation energies are due to magnesium oxide surface layers, which retards the diffusion of hydrogen out of MgH_2/Mg. The observed difference in E_A of *ca.* 50 kJ/mol is likely due to the catalytic effect of Ni on the recombination of H atoms to hydrogen molecules verified by theoretical considerations.

Keywords: *Magnesium hydride, Nickel doped magnesium hydride, Hydrogen storage materials, Gas- solid reactions, in situ powder X-ray diffraction, Dehydrogenation kinetic, Differential scanning calorimetry.*

1. Introduction

Future utilisation of renewable energy can be realised by implementing a 'hydrogen society' with hydrogen as the energy carrier. One of the remaining problems is the development of a safe and economic hydrogen storage system [1, 2]. Magnesium and magnesium based alloys have been explored intensively due to the high theoretical gravimetric hydrogen density in MgH_2, ρ_m = 7.6 w/w % and the high volumetric hydrogen density, ρ_v = 110 g/L (*i.e.* 153 % relative to the density of liquid hydrogen, $\rho_{H2(l)}$ = 71 g/L). The hydrogen storage capacity in MgH_2 exceeds the requirements stated by the International Energy Association (IEA), $\rho_m > 5.0$ w/w % [3]. In addition, the light metal Mg is cheap and virtually limitless, *i.e.* occur to an extent of 0.13% in sea water and 2.76% by weight in the earth crust. One of the problems however, is that magnesium has unfavourable thermodynamics and slow kinetics for hydrogen uptake and release. Thermodynamics dictate that relatively high temperatures (T > 280 °C) must be applied to desorb hydrogen from pure magnesium hydride, MgH_2, *i.e.* the formation enthalpy of magnesium hydride is, ΔH_f = - 75 kJ/mol [4]. Furthermore, investigations have shown that kinetics can be improved remarkably either by reduction of the particle size by ball milling, by mechanical alloying or sputter deposition of other elements or by doping with carbon [5- 13]. In this way, the kinetics can be improved by reducing the diffusion path of hydrogen atoms in Mg and MgH_2, facilitating the diffusion process or by adding catalysts on the metal surface for the dissociation or formation of H_2 molecules.

The detailed kinetics of both hydrogenation and dehydrogenation of magnesium and its alloys have been investigated by a variety of different techniques and this is possibly the group of hydrogen storage materials that has attracted most interest during the past decades. A wide range of apparent activation energies have been

reported suggesting a complex sorption mechanism sensitive to the pretreatment and experimental conditions. This has prompted us to investigate dehydrogenation of MgH_2 and Ni doped MgH_2 using *in situ* time resolved powder X-ray diffraction (PXD) and determine phase fractions of the involved phases, Mg, MgO and MgH_2. *In situ* PXD has proved to be a powerful tool for the investigation of metal hydrides, for example Mg_2Ni and $LaNi_5$ [14, 15]. Phase separation during hydrogenation was observed for the alloys $LaMg_{12}$ and La_2Mg_{17}, which decompose to LaH_3 and MgH_2 upon heating in a hydrogen atmosphere [16]. Hydrogen desorption from MgH_2/Nb nanocomposite revealed an intermediate niobium hydride phase suggested to act as a gateway for hydrogen flowing out of the magnesium reservoir, and the diffusion coefficient for hydrogen was found to reach a maximum at an H/Nb ratio corresponding to the intermediate phase, $NbH_{0.6}$ [17-19]. *In situ* PXD is an invaluable technique for studies of complex hydrides such as $NaAlH_4$, which currently are considered as very promising candidates for H_2 storage materials and interact with hydrogen via a complex reaction mechanism with several steps [20-22].

In this study, we will explore the use of *in situ* PXD as a tool for kinetic investigations of new potential hydrogen storage materials. We will demonstrate that the low scattering power of hydrogen towards photons is compensated by a significant symmetry or volume change during hydrogenation and dehydrogenation of most materials. Therefore, hydrogen-metal interactions are often clearly detectable by X-ray scattering. A kinetic study of the dehydrogenation of MgH_2 and nickel doped MgH_2 is presented, and the results are discussed in relation to previous experimental work and theoretical calculations. This work is the first part of our on-going investigation of deactivated, *i.e.* air exposed, magnesium and magnesium based alloys. The aim is to gain further insight into the mechanism for hydrogenation and dehydrogenation. For possible applications of Mg-based storage media surface oxidation, *i.e.* creation of a few nm thick MgO surface layer, can be unavoidable either due to oxygen impurities in the hydrogen gas or due to air exposure.

2. Experimental

2.1 Materials and initial characterisation

The materials used in this investigation are magnesium (99%) and nickel-doped (2 w/w%) magnesium commercially available from Sigma-Aldrich. For both materials, *ex situ* powder X-ray diffraction analysis showed diffraction peaks from magnesium only. Elemental analysis for the nickel doped sample, denoted Mg(Ni) in the following, was performed with Energy Dispersive X-ray Spectroscopy (EDX) giving 87 ± 4, 11 ± 5 and 2 ± 2 w/w % for Mg, O and Ni, respectively. The particle size distributions of the starting materials were determined by laser diffraction using a Bechman Coulter LS 13 320 Multi-Wavelength particle size analyzer. The nickel doped powder has a slightly higher mean particle diameter, 76 ± 28 μm compared to 60 ± 22 μm for the Mg sample.

Pure and nickel doped magnesium hydride were prepared from the starting materials in a Sartorius high pressure balance unit [23] at $p(H_2)$ = 30 bar and T = 400 °C, using 99.9997 % H_2 from Air Liquide. The hydrogen uptake was measured from the weight gain of the sample and verified by powder X-ray diffraction showing a nearly 100 % transformation of Mg into MgH_2.

The materials were investigated with a scanning electron microscope (SEM) JEOL JSM-5310LV operated at 15 kV. Typical images are shown in Figure 1. The morphology of the hydrogenated samples appear more homogeneous with a reduced number of deeper cracks possibly due to the structural expansion of metal to hydride. The white areas in the images of the hydrogenated samples may suggest

local electric charging due to a lower electrical conductivity of the insulating salt-like hydride, having a calculated band gap of 3.4 eV [24].

2.2 Calorimetry

Differential scanning calorimetry (DSC) data were measured for the dehydrogenation of $Mg(Ni)H_2$ from R*T* to 490 °C at heating rates, β, of 2, 3.5, 5 and 10 °C/min in a flow of He (200 mL/min) using a Seiko DSC 120 U. The hydride (*ca*. 10 mg) and the reference (α-Al_2O_3, *ca*. 10 mg) were loaded in open aluminium crucibles. The heat flux is proportional to the rate of reaction and goes through a maximum, T_P. Apparent activation energy can be extracted from these data using the Kissinger equation [25].

$$d\,(\ln(\beta/T_P^2))\,/\,d\,(T_P^{-1}) = -\,E_A\,/\,R \qquad (1)$$

2.3 *In situ* powder X-ray diffraction

The X-ray instrument was built with a Rigaku rotating anode X-ray source operated at 50 kV and 300 mA with a curved graphite monochromator producing Cu *K*α radiation, λ = 1.542 Å (~10^7 photons/s). The intensity of the diffracted beam was recorded with a curved position sensitive detector, INEL CPS 120, covering 120° in 2θ with a resolution of *ca*. 0.03°. The samples were exposed to X-rays 30 to 120 s corresponding to acquisition time per powder pattern between 48 to 192 s including read-out and overhead time.

The Haldor Topsøe A/S *in situ* reactor cell described in detail by Clausen *et al*. was used to study gas-solid reactions at elevated temperature and pressure [26]. The reactor was connected to a gas control system allowing control of both gas flow and pressure, respectively. The powder sample was loaded between plugs of quartz glass wool in a quartz capillary tube (0.7 mm O.D.) in order to fix the hydride bed and allow a gas flow (Ar, 10 mL/min) through the sample during data acquisition as shown in Figure 2. The magnesium hydride was exposed to air during this procedure. The samples were heated by an external stream of hot nitrogen gas (20 °C/min) to a constant temperature in the range 350-400 °C and the dehydrogenation was studied at isothermal conditions. The experimental details for the PXD experiments are described in Table 1. In each experiment a new load of sample was dehydrogenated. It was not possible to re-hydrogenate the samples under the present experimental conditions.

Full profile Rietveld refinement of the *in situ* PXD data was performed in order to determine the phase fractions as a function of time during dehydrogenation of MgH_2 and $Mg(Ni)H_2$ [27, 28]. Three phases are observed in the powder patterns, Mg, MgH_2 and MgO and the crystallographic information for these phases are listed in Table 2. The Rietveld refinements are performed with the *winpow* software [29] using Pseudo-Voigt profile functions, a shifted Chebyshev polynomial (15 coefficients) for the background and the constraint that the sum of phase fractions of Mg, MgH_2 and MgO is equal to one. The X-ray data is also analysed by numerical peak integration of the MgH_2 (110) reflection and the (100) and (002) from Mg. MgO was excluded from this analysis since the change in phase fraction is small and it do not quantify the desorption of hydrogen from MgH_2. The phase fractions are calculated by

$$\alpha(t) = [I_i(t) - I_{min}]\,/\,[I_{max} - I_{min}] \qquad (2)$$

$I(t)$ is the integrated intensity for reflection i at time t, and I_{min} and I_{max} are the minimum and maximum observed intensity, respectively. The background intensity is estimated by, I_{min}. Phase fractions typically in the range 0.2 to 0.8 are used for the kinetic investigation using an empirical rate law for isothermal phase formation

$$\alpha(t) = \exp(-(k\,t)^n) \qquad (3)$$

The parameters describing growth rates and nucleation are contained in a rate constant, k, and the Avrami exponent, n [30]. Equation 3 is often denoted the Johnson- Mehl- Avrami (JMA) model. To eliminate the temperature variations of the Avrami exponent a fixed value can be chosen, *e.g.* $n = 4$. In some cases a delay time, t_o, can be observed prior to the reaction, which can be related to a nucleation time as shown in *eq.* 4

$$\alpha(t) = \exp(- (k(t - t_o))^n) \quad (4)$$

Fitting equation (3) and (4) to the experimental data provide the rate constant, the Avrami exponents and the apparent nucleation time. An apparent activation energy, E_A, and a pre- factor, A, for the overall reaction can be calculated using Arrhenius law

$$k = A \exp(- E_A/R T) \quad (5)$$

where R is the gas constant and T the absolute temperature. The delay, t_o, can be interpreted as a nucleation time and an Arrhenius plot ($-\ln(t_o)$ *vs.* $1/T$) gives an apparent activation energy for the nucleation process, E_{A0} [31].

3. Results

The decomposition of nickel doped magnesium hydride, $Mg(Ni)H_2$, is illustrated by 40 consecutive powder X-ray diffraction patterns in Figure 3 showing the dehydrogenation of MgH_2 by the disappearance of the (110) and (101) reflections and the corresponding appearance of Mg(100) and Mg(002) reflections. Rietveld refinement of a selected pattern of Mg(Ni) reveal the existence of three phases during dehydrogenation of the sample as shown in the Figure 4. The unit cell parameters derived from Rietveld refinement of both Mg and MgH_2 are plotted as a function of the degree of dehydrogenation in Figure 5 with literature values for Mg measured at 370 °C [34].

Phase fractions derived by Rietveld refinement, Figure 6, for Mg and MgH_2 *vs.* time have a sigmoidal shape, whereas the fraction of MgO is only slightly increasing. Dehydrogenation curves *i.e.* phase fractions of MgH_2 *vs.* time have been constructed for all experiments as shown in Figures 7 and 8 for pure and nickel doped MgH_2, respectively. The phase fractions determined by Rietveld refinement and those by integration of Bragg reflection intensities were identical within the experimental accuracy. Integration of reflections with different Miller indices gave similar formation curves and there were no signs of preferred crystallite orientation in the samples. An empirical rate law (JMA type), *eq.* 3 and 4, can describe the data as shown in Figures 7 and 8 (curves). Avrami exponents, n, and rate constants, k, are presented in Table 3 using *eq.* 3 and in Table 4 rate constants, k', are given for a fixed value of, $n = 4$. Rate constants, k'', and delay time, t_o, extracted with *eq.* 4 and a fixed exponent $n = 2$ are also given in Table 4. An Arrhenius plot to provide activation energies for PXD data is shown in Figure 9.

In Figure 10 is depicted the DSC data, which shows increasing peak temperature, T_p, with increasing heating rate, β. From observations of the heating rate and the corresponding peak temperature the apparent activation energy can be extracted using the Kissinger equation [25], see Figure 11.

4. Discussion

The unit cell parameters derived from Rietveld refinement for both Mg and MgH_2 are shown in Figure 5 as a function of the degree of dehydrogenation and compared to literature values for Mg measured at 370 °C [34]. One unit cell parameter, a, for both Mg and MgH_2 remains almost constant while the c- axis of Mg contracts initially, indicating the presence of interstitial hydrogen.

Faster dehydrogenation kinetics with higher temperatures are clearly visible along with the sigmoidal shape of all curves, see Figures 7 and 8, in accordance with previous investigations [35, 36]. The observed data seem to indicate a nucleation time, t_o, prior to the onset of dehydrogenation, *e.g.* by visual inspection of Figure 3. A fixed Avrami exponent, $n = 2$, was chosen in order to extract t_o. The Avrami exponent was shown to increase from $n = 2$ to 4 for hydrogen desorption from MgH_2 due a temperature increase [37, 38]. However, it is generally agreed that the temperature dependency of the rate constant is not sensitive to the choice of function describing the time dependence [39, 40]. The X-ray data was also analysed using a fixed value of $n = 4$. The apparent activation energy of both pure and nickel-doped samples are listed in Tables 3 and 4 showing values of *ca.* 300 and *ca.* 250 kJ/mol, respectively, for the dehydrogenation. The estimated apparent activation energy for the nucleation process, E_{AO}, is less than E_A for the overall reaction as expected and in accordance with previous work [31].
From a Kissinger plot of the DSC data (Figure 11) the apparent activation energy for the dehydrogenation of $Mg(Ni)H_2$ is found to be 270 kJ/mol in agreement with the activation energy of *ca.* 250 kJ/mol found from the *in situ* PXD experiments. Note, that the two experimental techniques are different in nature: the former operated with continuous heating and the latter at isothermal conditions.

4.1 Comparison with related work

In the present work the focus is on the apparent activation energy for the overall dehydrogenation process. This reaction, metals with hydrogen, consists of several steps: (*i*) nucleation and growth of Mg (*ii*) diffusion of hydrogen in bulk Mg/MgH_2, (*iii*) surface penetration, *i.e.* through MgO for oxidised samples, (*iv*) 2D surface diffusion of H, (*v*) recombination of 2H to H_2 a catalysed process. Furthermore, (*vi*) for alloys cation migration can also be of importance during phase formation/phase separation induced by hydrogenation or dehydrogenation. The rate-determining step (the slowest) has the largest contribution to the apparent activation energy.
An overview of experimentally determined apparent activation energies for formation and decomposition of magnesium hydride and selected hydrides of magnesium based alloys is presented in Table 5. This table covers a range of different materials and experimental techniques and reveals a significant variation between the apparent activation energies measured. There is a clear difference in E_A for activated samples measured after several cycles of hydrogenation/dehydrogenation and deactivated samples exposed to air and measured after the first cycle.

4.2 The effect of surface oxidation

The diffracted intensity indicates an increasing amount of crystalline magnesium oxide (see Figure 6) possibly due to crystallisation of amorphous MgO, reaction of Mg with the quartz capillary (SiO_2) or with gas impurities. Magnesium powders with different particle size were previously characterized by both neutron activation and wet-chemical analysis in order to measure the amount of MgO [51]. These results suggest that *ca.* 4 w/w % oxygen might be expected for the particle size used in this investigation assuming all oxygen being present in a surface oxide layer.
MgO is expected to act as a barrier between bulk MgH_2, gas phase and Ni, due to its dense rock-salt structure limiting the diffusion of hydrogen atoms [52, 53]. For both samples investigated diffusion of atomic hydrogen through Mg/MgH_2 and MgO is contributing to the overall rate, whereas two dimensional surface diffusion of H on MgO is assumed to have negligible activation energy and thus a high rate. The apparent activation energies reported in this work are somewhat higher, possibly due to exposure of the samples to the atmosphere prior to PXD measurements that has created an oxidised surface layer of MgO on the particles of MgH_2. This work

serves as an estimate of the maximal apparent activation energy and the influence of MgO surface layers.
A freshly hydrogenated material can be considered as *activated* with defects in the surface oxide layer. Diffusion of hydrogen atoms to the gas/solid interface is thereby facilitated. When the activated sample is exposed to air it is deactivated by oxidation of Mg forming a more perfect surface oxide layer. The results from the materials characterization by EDX indicate that additional contamination by oxygen was introduced after hydrogenation.

4.3 The catalytic effect of Nickel

It is generally agreed that magnesium does not promote dissociation of hydrogen molecules, H_2, to atoms on the metal surface [54, 55]. Nørskov *et al*. calculated the potential energy surface (PES) of hydrogen adsorption and dissociation on the Mg (0001) close packed surface, which is the most thermodynamically stable [56]. These calculations showed an activation barrier for H_2 dissociation of *ca*. 0.5 eV (~50 kJ/mol) in qualitative agreement with experiments [57]. The bridge site (*i.e*. position between two identical atoms) has the lowest dissociation barrier, 0.4 eV determined by LDA-calculations [58]. Recent theoretical work determine the activation energy for H_2 dissociation on a Mg(0001) surface in the bridge site to be $E_A \approx 100$ kJ/mol, without the presence of a molecular chemisorbed state acting as a precursor to dissociation [59]. In contrast, calculations and experimental work show that the dissociation of H_2 on nickel has a negligible activation barrier around 0-10 kJ/mol, *i.e*. the addition of nickel is expected to lower the dissociation barrier significantly [60-62]. Furthermore, assuming microscopic reversibility the same effect would apply for recombination of atomic hydrogen into H_2 molecules.
The experimentally observed difference in E_A for the dehydrogenation of MgH_2 and $Mg(Ni)H_2$ (300 and 250 kJ/mol, respectively) is indeed 50 kJ/mol. Furthermore, the two samples of MgH_2 and $Mg(Ni)H_2$ have similar particle sizes and oxygen content suggesting that the overall bulk diffusion of atomic H through $Mg/MgH_2/MgO$ are comparable for the samples.
This might indicate that the dissociation of H_2 and recombination of H to H_2 mainly occur on nickel sites on the surface due to its lower barrier compared to pure magnesium even with as little as 2 w/w % Ni present. This may suggest that Ni mainly catalyzes the dissociation/recombination reaction barrier for H_2 and has minor influence on other processes as mentioned earlier. Nickel, like magnesium, is oxidised in air to the oxide, NiO. In contrast to MgO, NiO is readily reduced by hydrogen gas [63].

4.4 Comparison with magnesium alloys

Table 5 reveals a large span in E_A values for magnesium and its alloys, supporting the hypothesis that the overall reaction consists of several individual steps [64]. Alloying magnesium or including additives can lead to more complex reaction schemes for the metal-hydrogen interaction. Extremely fast kinetics was observed for the additives Nb_2O_5 and V where up to 6 w/w% hydrogen was absorbed or desorbed within a few minutes [11, 46, 47]. The very fast kinetics is due to the catalytic effect of the additive as well as ball-milling of the samples prior to the measurements. In this work the catalytic effect of Ni was clearly detectable by *in situ* PXD. In some cases alloying magnesium can influence thermodynamics, *e.g*. for $Mg_{0.87}Al_{0.07}Ni_{0.03}Mn_{0.03}H_2$, and the enthalpy for hydrogen desorption was $\Delta H = 55$ kJ/mol [48].

In a parallel study we investigated the alloy $Mg_{0.85}Cu_{0.15}$. Hydrogenation at low and high hydrogen pressure provided samples of (A) $MgH_2 + Mg_2Cu$ and (B) $MgH_2 +$

$MgCu_2$, respectively, and *in situ* PXD reveal E_A for the dehydrogenation of deactivated samples to be 108 and 160 kJ/mol, respectively [49]. The difference is possibly due to the phase formation reaction during dehydrogenation, $3Mg + MgCu_2 \rightarrow 2Mg_2Cu$ for (B). The same experimental setup was utilised for investigation of a magnesium aluminium alloy, $Mg_{17}Al_{12}$, which phase separated to MgH_2 + Al during hydrogenation [50]. Dehydrogenation of this air-exposed (deactivated) sample was followed by phase formation by cation migration to form an MgAl-alloy, with E_A = 160 kJ/mol.
Despite three decades of intensive research the complexity of magnesium and its alloys reaction with hydrogen is still not fully understood. Deeper knowledge of all the individual steps in the overall reaction might reveal new ideas for possible applications. Magnesium is still considered as having potential applications as hydrogen storage material in future.

5. Conclusion

The present results demonstrates that in situ powder X-ray diffraction is a useful technique for kinetic investigation of dehydrogenation of magnesium and magnesium doped alloys, in this case with only 2 w/w %Ni ($Mg(Ni)H_2$). The method gives information on the phase composition of the sample as a function of time and temperature. Furthermore, phase fractions can be extracted as a function of time as demonstrated in this work and utilised for kinetic analysis providing apparent activation energies. The method is sensitive and can clearly probe the difference in dehydrogenation kinetics of MgH_2 and $Mg(Ni)H_2$, *i.e.* $E_A \approx 300$ and 250 kJ/mol, respectively. The values are relatively high compared to previous work possibly because the samples were exposed to air prior to the investigations. The lower activation energy for the Ni-doped sample suggests that Ni catalyzes the recombination of H to H_2. The observed difference of 50 kJ/mol in apparent activation energy is in quantitative agreement with both calculated and experimentally determined values.

Acknowledgements

The Danish Technical Research Council is acknowledged for funding the center of excellence *Towards the hydrogen based society.* TRJ is greatful to the Danish Natural Research Council for at *Steno* stipend, and T. Vegge to the Danish Research Agency and Danfoss Corporate Ventures A/S (grant # 2013-01-0043).

References

[1] L. Schlapbach, A. Züttel, *Nature* 414 (2001) 353-358.
[2] J. A. Ritter, A. D. Ebner, J. Wang, and R. Zidan, *Materials Today*, 2003, sept., 18-23.
[3] http://www.ieahia.org/tasks/task17.html
[4] U. S. Department of Energy,
http://www.eere.energy.gov/hydrogenandfuelcells/hydrogen/-storage.html.
[5] A. Zaluska, L. Zaluski, J. Ström-Olsen, *Appl. Phys. A 72* (2001) 157-165.
[6] K. J. Gross, P. Spatz, A. Züttel, L. Schlapbach, *J. Alloys Comp*. 261 (1997) 276-280.
[7] F. von Zeppelin, H. Reule, M. Hirscher, *J. Alloys Comp*. 330-332 (2002) 723-726.
[8] N. E. Tran, M. A. Imam, C. R. Feng, *J. Alloys Comp*. 259 (2003) 225-229.
[9] S. Rivoirard, P. de Rango, D. Fruchart, J. Charbonnier, D. Vempaire, *J. Alloys Comp*. 356-357 (2003) 622-625.
[10] J. Wang, F. Wu, Zh. Q. Shan, *J. Alloys Comp*. 359 (2003) 315-319.
[11] G. Liang, J. Huot, S. Boily, A. van Neste, R. Schulz, *J. Alloys Comp*. 292 (1999) 247-252.
[12] A. Reiser, B. Bogdanović and K. Schlichte, *Int. J. Hydrogen Energy 25* (2000) 425-430.

[13] L. Schlapbach (Ed.), *Hydrogen in Intermetallic Compounds II. Surface and dynamic Properties, Applications*, Vol. 67 of Topics in Applied Physics, Springer- Verlag, 1992.
[14] T. Hirata, T. Matsumoto, M. Amano and Y. Sasaki, *J. Phys. F. Metal Phys. 11* (1981) 521-529.
[15] P.H.L. Notten, J.L.C. Daams, A.E.M. De Veirman and A.A. Staals, *J. Alloys Comp. 209* (1994) 85- 91.
[16] D. Sun, F. Gingle, Y. Nakamura, H. Enoki, M. Bououdina, E. Akiba, *J. Alloys Comp*. 333 (2002) 103.
[17] J. Pelletier, J. Huot, M. Sutton, R. Schulz, A. Sandy, L. Lurio and S. Mochrie, *Phys. Rev. B 63* (2001) 052103.
[18] J. Hout, J. F. Pelletier, G. Liang, M. Sutton, R. Schulz, *J. Alloys Comp*. 330- 332 (2002) 727.
[19] J. Hout, J. F. Pelletier, L. B. Lurio, M. Sutton, R. Schulz, *J. Alloys Comp*. 348 (2003) 319.
[20] H. W. Brinks, B. C. Hauback, P. Norby, H. Fjellvåg, *J. Alloys Comp*. 351 (2003) 222- 227.
[21] K. J. Gross, G. Sandrock, G. J. Thomas, *J. Alloys Comp*. 330 322 (2002) 691- 695.
[22] M. P. Balogh, G. G. Tibbetts, F. E. Pinkerton, G. P. Meisner, C. H. Olk, *J. Alloys Comp*. 350 (2003) 136- 144.
[23] A. Pedersen, J. Kjøller, B. Larsen, and B. Vigeholm, *Int. J. Hydrogen Energy 8 (3)* (1983) 205- 211.
[24] The DFT calculations are performed with the Dacapo pseudopotential code (www.fysik.dtu.dk/campos), using a 45 Ry plane wave cut- off, a 3D *k*- point density of ~0.04 $Å^{-1}$, and the PW91 exchange- correlation functional.
[25] H. E. Kissinger, *Anal. Chem*. 29 (1957) 1702- 1706.
[26] B. S. Clausen, G. Steffensen, B. Fabius, J. Villadsen, R. Feidenhans'l and H. Topsøe, *J. Catal. 132* (1991) 524- 535.
[27] R. A. Young (Ed.), *The Rietveld Method*, Oxford University Press, 1993.
[28] L. McCusker, R. Von Dreele, D. Cox, D. Louër and P. Scardi, *J. Appl. Crystallogr. 32* (1999) 36- 50.
[29] *WINPOW*, a Rietveld refinement program written by Kenny Ståhl, Department of Chemistry, Technical University of Denmark, can be downloaded from http://struktur.kemi.dtu.dk/kenny/powder_program.html.
[30] K. Kelton, *Mater. Sci. Eng. A226- 228* (1997) 142- 150.
[31] A. N. Christensen, T. R. Jensen, P. Norby and J. C. Hanson, *Chem. Mater.*, 10 (1998) 1688-1693.
[32] M. Straumanis, *J. Appl. Phys. 20* (1949) 726- 734.
[33] F. Ellinger, C. Holley jr., B. McInteer, D. Pavone, R. Potter, E. Staritzky, W. Zachariasen, *J. Am. Chem. Soc. 77* (1955) 2647- 2648.
[34] P. Karen, A. Kjekshus, Q. Huang and V. Karen, *J. Alloys and Comp. 282* (1999) 72- 75.
[35] A. Pedersen, K. Jensen, B. Larsen and B. Vigeholm, *J. Less- Common Met. 131* (1987) 31-40.
[36] J. Han, M. Pezat and J.- Y. Lee, *J. Less- Common Met. 130* (1987) 395- 402.
[37] J.F. Fernandez, C.R. Sanchez, *J. Alloys and Comp*. 340 (2002) 189- 198.
[38] J.F. Fernandez, C.R. Sanchez, *J. Alloys and Comp*. 356- 357 (2003) 348- 352.
[39] B. Vigeholm, J. Kjøller, B. Larsen, and A. Pedersen, *J. Less- Common Met. 89* (1983) 135-144.
[40] C. Stander, *J. Inorg. Nucl. Chem. 39* (1977) 221- 223.
[41] A. Karty, J. Grunzweig- Genossar and P. Rudman, *J. Appl. Phys. 50 (11)* (1979) 7200-7209.
[42] J. Huot, G. Liang, S. Boily, A. Van Neste, R. Schulz, *J. Alloys Comp. 293- 295* (1999) 495-500.
[43] G. Friedlmeier and M. Groll, *J. Alloys Comp. 253- 254* (1997) 550- 555.
[44] M. Martin, G. Gommel, C. Borkhardt and E. Fromm, *J. Alloys Comp. 238* (1996) 193- 201.
[45] G. Liang, J. Huot, S. Boily, R. Schulz, *J. Alloys Comp. 305* (2000) 495- 500.
[46] G. Liang, J. Huot, S. Boily, A. Van Neste, R. Schulz, *J. Alloys Comp.* 291 (1999) 295- 299.
[47] G. Barkhordarian, T. Klassen, R. Bormann, *J. Alloys Comp. 364* (2004) 242- 246.
[48] P. Delchev, P. Solsona, B. Drenchev, N. Drenchev, T. Spassov, M. D. Baro, *J. Alloys Comp. 388* (2005) 98- 103.
[49] A. Andreasen, M. B. Sørensen, R. Burkarl, B. Møller, A. M. Molenbroek, A. S. Pedersen, T. Vegge, T. R. Jensen, *Appl. Phys. A*, 2005, to be submitted
[50] A. Andreasen, M. B. Sørensen, R. Burkarl, B. Møller, A. M. Molenbroek, A. S. Pedersen, J.W. Andreasen, M.N. Nielsen and T. R. Jensen, *J. Alloys and Comp*., 2005, accepted.

[51] B. Vigeholm, *Chemical energy storage based on metal hydrides*, Tech. Rep. Risø-M-2608, Risoe National Laboratory, DK-4000 Roskilde, Denmark, (In Danish) (1989).
[52] P. Hjort, A. Krozer, B. Kasemo; J. Alloys and Comp. 237 (1996) 74-80.
[53] R. Gonzalez, Y. Chen, K.L. Tsang; Phys. Rev. B 26 (1982) 4637-4645.
[54] P.T. Sprunger, E.W. Plummer; *Surf. Sci.* 307-309 (1994) 118-123
[55] J. K. Nørskov, F. Besenbacher, J. Less Common Metals 130 (1987) 475.
[56] J.K. Nørskov, A. Houmøller, P.K. Johansson, B.I. Lundquist; *Phys. Rev. Lett.* 46(4) (1981) 257-260.
[57] P.T. Sprunger, E.W. Plummer; *Chem. Phys. Lett.* 187 (1991) 559-564.
[58] D.M. Bird, L.J Clarke, M.C. Payne, I. Stich; Chem. Phys. Lett. 212 (1993) 518-524.
[59] T. Vegge, Phys. Rev. B 70 (2004) 035412.
[60] J.K. Nørskov, B. Hammer, *Nature* 376 (1995) 238 – 240.
[61] J. Harris, S. Anderson; *Phys. Rev. Lett.* 55 (1985) 1583-1586
[62] H.J. Robota, W. Vielhaber, M.C. Lin, J. Segner, G. Ertl; *Surf. Sci.* 155 (1985) 101-120.
[63] J.A. Rodriguez, J.C. Hanson, A.I. Frenkel, J.Y. Kim, M. Pérez, *J. Am. Chem. Soc.,* 124(2) (2002) 346-354.
[64] A. Andreasen, T. Vegge, A.S. Pedersen, *J. Phys. Chem. B* 109 (2005) 3340-3344.
[65] R. Busk, *J. Metals* 4 (1952) 207-209.

Table 1 Experimental details for the *in situ* time resolved powder X-ray diffraction investigations.

	MgH_2				$Mg(Ni)H_2$		
No.	*T* / °C	Acquisition *t* / s	Exposure *t* / s	*No.*	*T* / °C	Acquisition *t* / s	Exposure *t* / s
1	360	182	120	5	350	182	120
2	380	182	120	6	370	182	120
3	390	48	30	7	380	182	120
4	400	48	30	8	390	182	120

Table 2 Unit cell parameters and crystallographic information for magnesium, magnesium hydride and magnesium oxide, the three phases included in the Rietveld refinement.

	Substance		
Property	**Mg**	**MgH_2**	**MgO**
a / Å	3.2093	4.5168	4.2198
c / Å	5.2103	3.0205	-
V / Å^3	46.47	61.62	75.14
Space group	$P6_3/mmc$	$P4_2/mnm$	$Fm3m$
Crystal System	Hexagonal	Tetragonal	Cubic
Ref.	[32]	[33]	[34]

Table 3 Kinetic parameters for the dehydrogenation of both pure and nickel doped MgH_2 obtained using *eq*. 3.

	MgH_2				**$Mg(Ni)H_2$**		
No.	*T* / °C	*k* / s^{-1}	*n*	*No.*	*T* / °C	*k* / s^{-1}	*n*
1	360	$3.93 \cdot 10^{-5}$	2.26	5	350	$2.72 \cdot 10^{-5}$	4.20
2	380	$1.53 \cdot 10^{-4}$	6.99	6	370	$1.00 \cdot 10^{-4}$	6.29
3	390	$4.53 \cdot 10^{-4}$	3.29	7	380	$2.00 \cdot 10^{-4}$	6.47
4	400	$1.13 \cdot 10^{-3}$	4.41	8	390	$5.30 \cdot 10^{-4}$	14.9
E_A/kJ/mol		**299**				**249**	

Table 4 Kinetic parameters for the dehydrogenation of pure and nickel doped MgH_2 obtained using *eq*. 3, with a fixed value of the exponent, $n = 4$ (the rate constant, k'), and *eq*. 4, with $n = 2$ (the rate constant, k'' and apparent nucleation time, t_o). The standard deviation for the apparent activation energies is less than ±20 kJ/mol.

	MgH_2					**$Mg(Ni)H_2$**			
No.	*T* / °C	*k'* / s^{-1}	*k''* / s^{-1}	t_0 / s	*No.*	*T* / °C	*k'* / s^{-1}	*k''* / s^{-1}	t_0 / s
1	360	$4.12 \cdot 10^{-5}$	$4.73 \cdot 10^{-5}$	$3.99 \cdot 10^{3}$	5	350	$2.71 \cdot 10^{-5}$	$3.88 \cdot 10^{-5}$	$1.13 \cdot 10^{4}$
2	380	$1.50 \cdot 10^{-4}$	$2.20 \cdot 10^{-4}$	$2.22 \cdot 10^{3}$	6	370	$9.99 \cdot 10^{-5}$	$1.43 \cdot 10^{-4}$	$3.27 \cdot 10^{3}$
3	390	$4.57 \cdot 10^{-4}$	$6.19 \cdot 10^{-4}$	577	7	380	$1.92 \cdot 10^{-4}$	$2.75 \cdot 10^{-4}$	$1.68 \cdot 10^{3}$
4	400	$1.13 \cdot 10^{-3}$	$1.58 \cdot 10^{-3}$	258	8	390	$4.99 \cdot 10^{-4}$	$7.35 \cdot 10^{-4}$	66
E_A / kJ/mol		**291**					**241**		**216**
E_{AO} / kJ/mol			**308**	**241**				**249**	

Table 5 Apparent activation energy for hydrogenation and dehydrogenation of magnesium and some selected alloys measured by different techniques. Activated samples, **A**, and deactivated, **D**. *Technique*: 1) Sievert type apparatus, 2) High pressure micro balance, 3) Pressure sweep method, 4) Thermal desorption spectroscopy, 5) Time resolved in situ X-ray diffraction, 6) TG/DSC.

Sample	*Technique*	E_A /(kJ/mol)		*Ref.*
Hydrogenation - magnesium				
Mg (powder)	1	100	A	[37]
Mg (vapor deposit)	3	138		[41]
Mg (foil)	2	270- 314	D	[35]
Dehydrogenation				
MgH_2 (powder)	1	120	A	[42]
MgH_2 (powder)	2	120- 126	A	[40]
MgH_2 (vapor deposit)	3	132	A	[41]
MgH_2 (powder)	4	142	A	[36]
MgH_2 (powder)	1	156	A	[42]
Mg (powder)	1	160	A	[37]
MgH_2 (powder)	2	233 [e]	D	[23]
MgH_2 (powder)	5	299	D	*This work*
Hydrogenation - alloys of magnesium				
$Mg_{0.98}Ni_{0.02}$ (powder)	1	66	A	[43]
Mg/Mg_2Cu (powder)	3	100		[41]
$Mg_xNi_yH_z$ (powder) [f]	1	120	A	[44]
Dehydrogenation				
$Mg_{0.95}V_{0.05}H_2$	1	52- 99	A	[45]
$Mg_{0.95}V_{0.05}H_2$	1	62	A	[46]
$0.99MgH_2 \cdot 0.01Nb_2O_3$	1	62	A	[47]
$Mg_{0.95}Nb_{0.05}H_2$	1	62- 77	A	[19]
Mg/Mg_2CuH_z (powder)	3	106		[41]
$Mg_{0.87}Al_{0.07}Ni_{0.03}Mn_{0.03}H_2$	6	100- 115	A	[48]
MgH_2/Mg_2Cu	5	108	D	[49]
$MgH_2/MgCu_2$	5	160	D	[49]
$MgAlH_x$	5	160	D	[50]
$Mg(Ni)H_2$ (powder)	5	249	D	*This work*
$Mg(Ni)H_2$ (powder)	6	270	D	*This work*

Footnotes: e) E_A was extracted by reanalyzing the data in Ref. [23], f) The exact composition is not given in Ref. [44].

Figure 1 SEM images of (**A**) nickel doped magnesium powder and (**B**) nickel doped magnesium hydride.

Figure 2 Schematic illustration of the experimental setup illustrating the gas/solid reactor for in situ investigations allowing a controlled gas flow, analysis of the exhaust gas, simultaneous heating and exposure to X-ray radiation.

Figure 3 Time resolved *in situ* powder X-ray diffraction of dehydrogenation of $Mg(Ni)H_2$. A stack of 40 consecutive diffraction patterns measured at T = 390 °C and with acquisition time t = 182 s.

Figure 4 Experimental and calculated powder X-ray diffraction patterns for a partly dehydrogenated sample of $Mg(Ni)H_2$ (T = 370 °C). The difference between observed and calculated intensities is also included. The **X**, # and **O** markers correspond to MgH_2, Mg and MgO, respectively (R_p = 6.37 %, R_{wp} = 9.41 %).

Figure 5 Unit cell parameters of Mg (upper graphs) and MgH_2 (lower graphs) during dehydrogenation of $Mg(Ni)H_2$ at 370 °C determined by Rietveld refinement. Unit cell parameters for pure Mg measured at 370 °C are shown for comparison [65].

Figure 6 Phase fractions determined by Rietveld refinement of MgH_2, Mg and MgO as a function of time for $Mg(Ni)H_2$ dehydrogenated at 370 °C.

Figure 7 Dehydrogenation curves for pure MgH_2 extracted from the *in situ* PXD data (points) the theoretical curves are a fit using *eq*. 3 and with the results given in Table 3.

Figure 8 Dehydrogenation curves for pure $Mg(Ni)H_2$ extracted from the *in situ* PXD data (points) the theoretical curves are a fit using *eq*. 3 and with the results given in Table 3.

Figure 9 Arrhenius plot of the kinetic data given in Table 3 for the dehydrogenation of both pure MgH_2 and $Mg(Ni)H_2$.

Figure 10 Differential scanning calorimetry for the dehydrogenation of Mg $(Ni)H_2$ showing the heat flux as a function of temperature at different heating rates. Each spectrum has been scaled for illustrative reasons.

Figure 11 The DSC data (Figure 10) displayed as a Kissinger plot providing an apparent activation energy for the dehydrogenation of $Mg(Ni)H_2$.

Figure 1

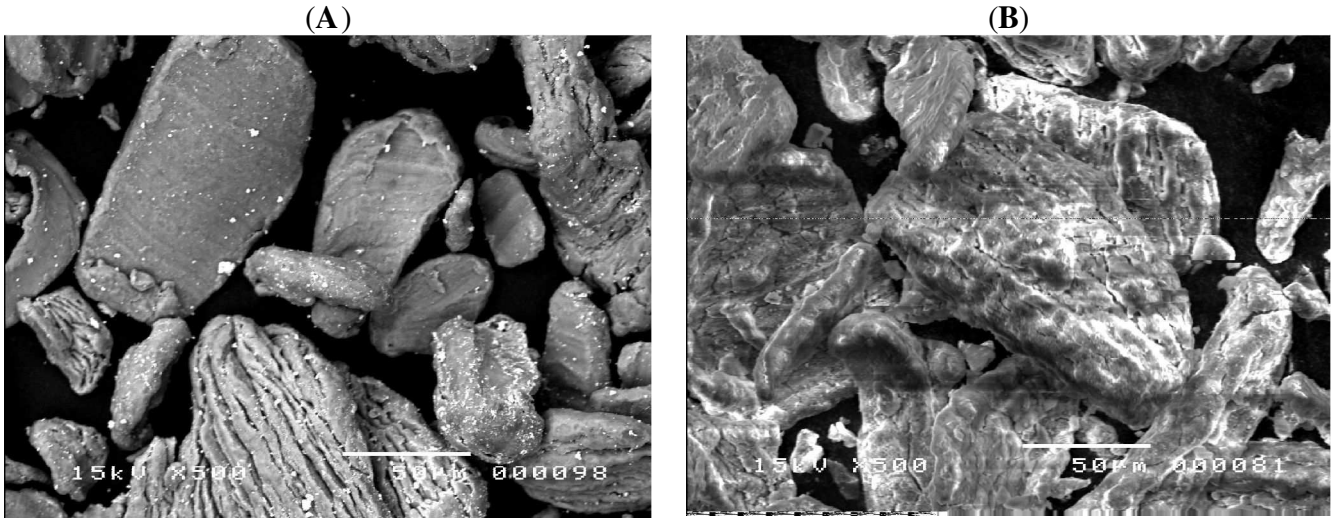

Figure 2

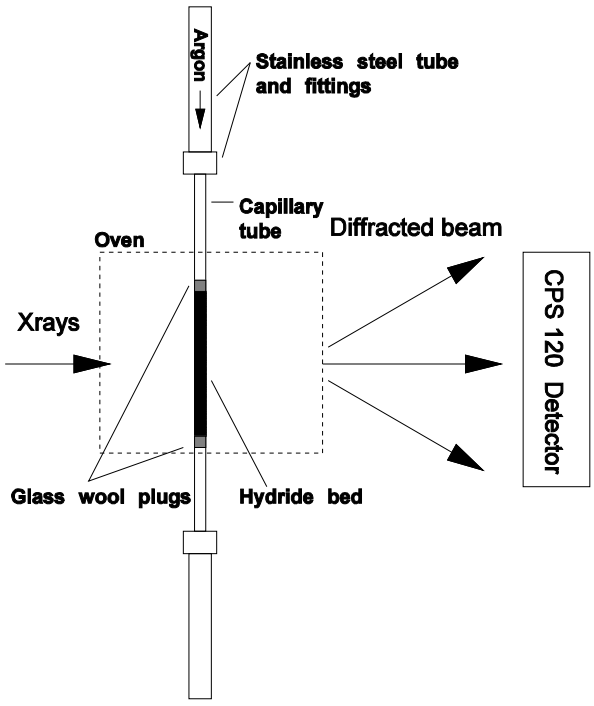

Figure 3

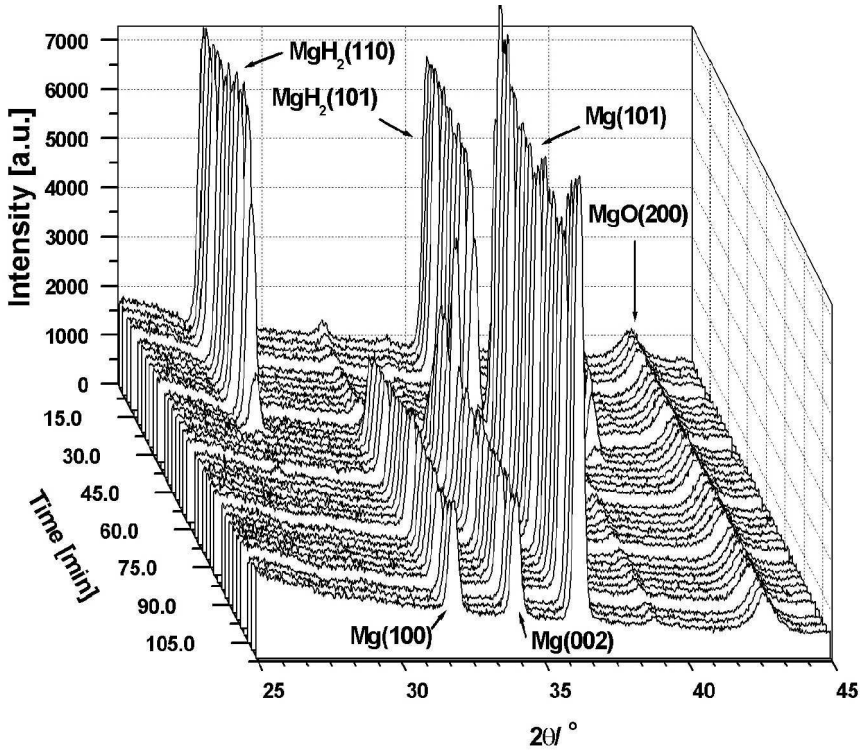

Figure 4

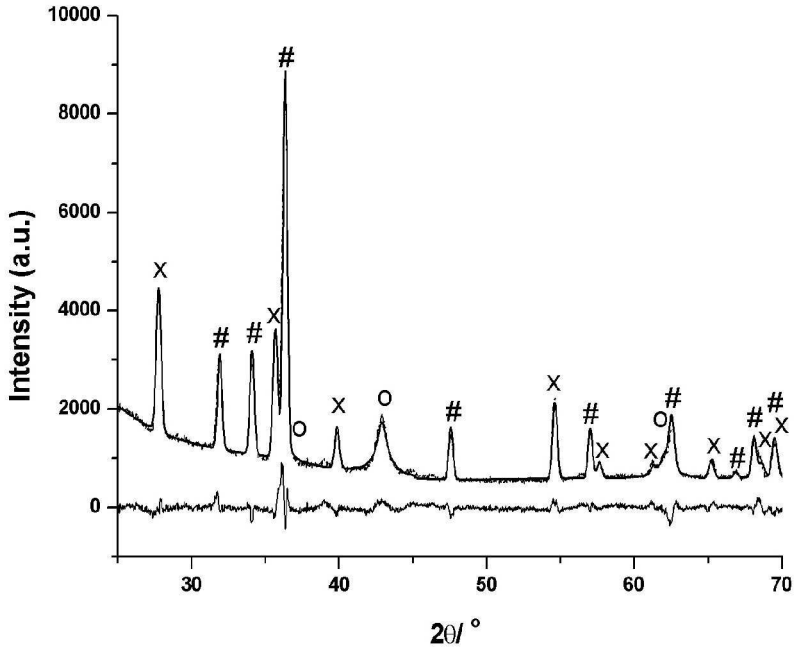

Figure 5

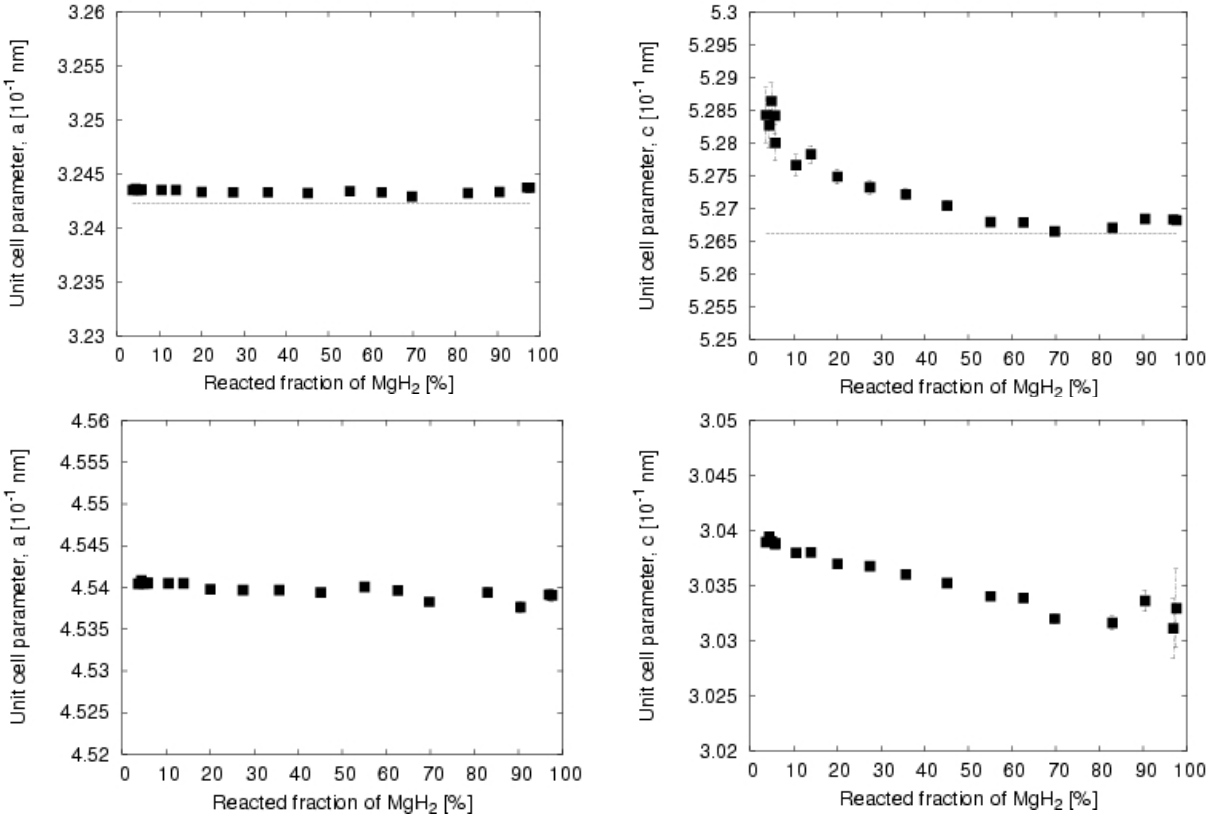

Figure 6

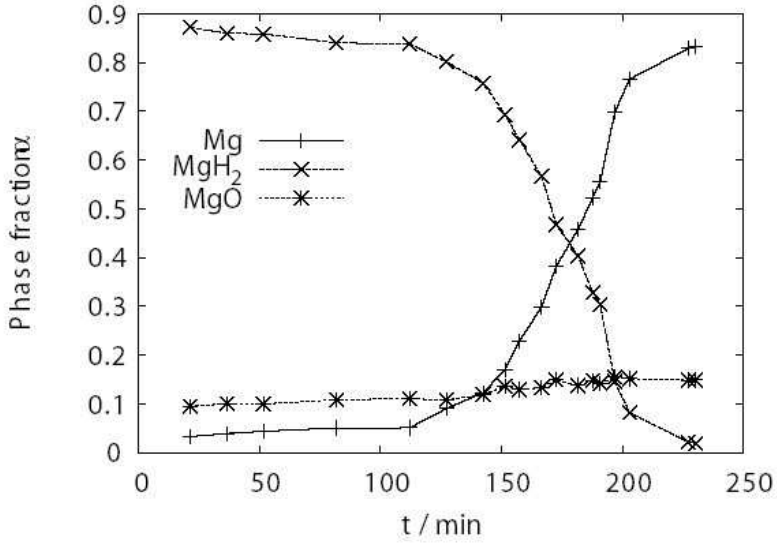

Figure 7

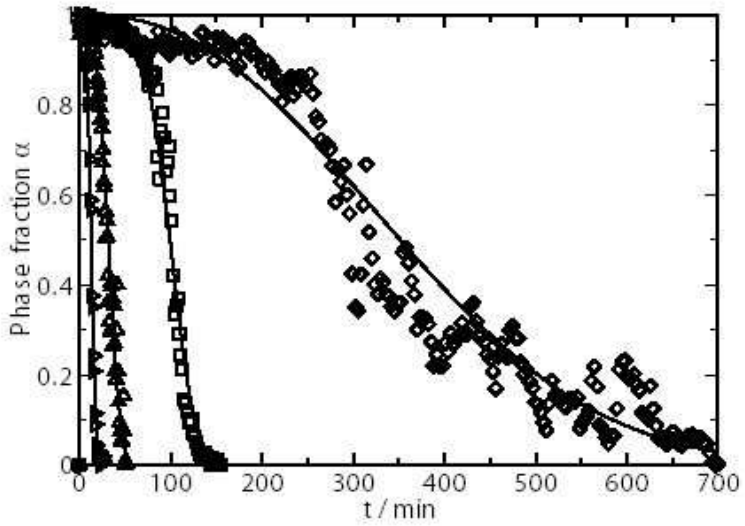

Figure 8

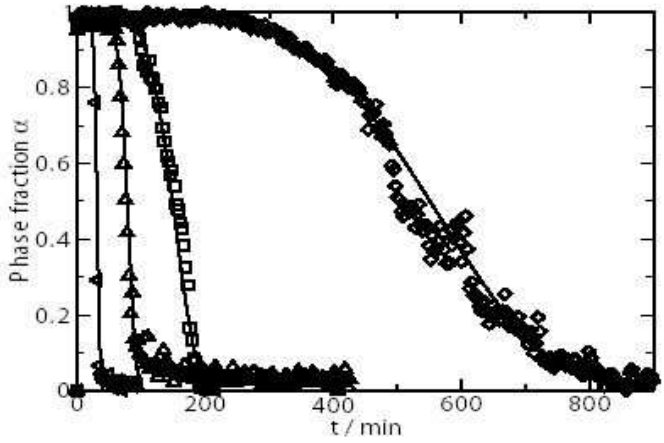

Figure 9

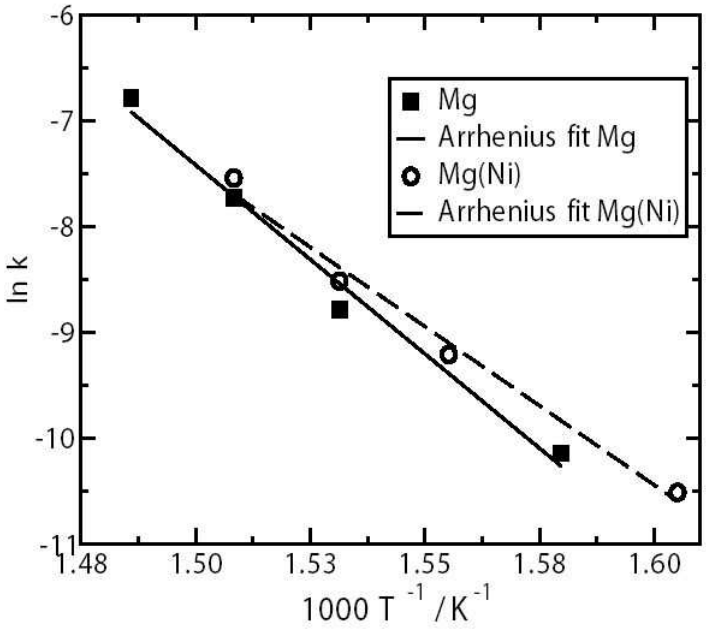

Figure 10

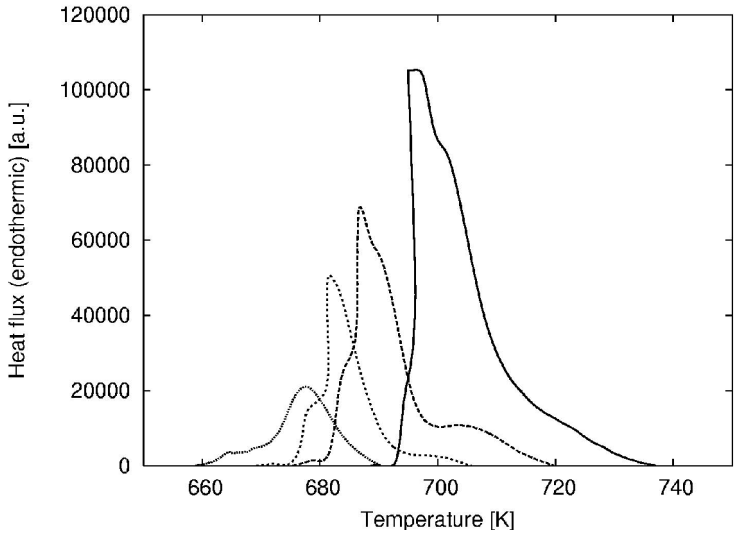

Figure 11

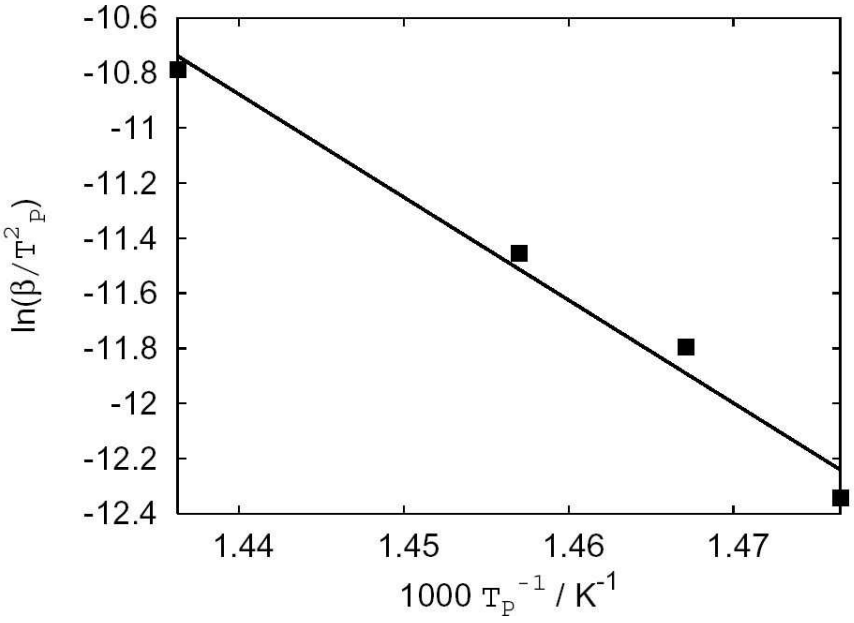

Appendix E

Paper 5

3B2v8.06a/w(Dec 5 2003).51c +model | YJSSC : 11185 | Prod.Type:COM pp.1–7(col.fig.:1) | ED:PradeepKumarR. PAGN:VG SCAN:Romio

ARTICLE IN PRESS

Available online at www.sciencedirect.com

SCIENCE DIRECT®

ELSEVIER

Journal of Solid State Chemistry ▮ (▮▮▮▮) ▮▮▮–▮▮▮

JOURNAL OF SOLID STATE CHEMISTRY

www.elsevier.com/locate/jssc

Dehydrogenation kinetics of as-received and ball-milled $LiAlH_4$

A. Andreasen[a,b,*], T. Vegge[a], A.S. Pedersen[a]

[a]*Materials Research Department, Risø National Laboratory, DK-4000 Roskilde, Denmark*

[b]*Interdisciplinary Research Center for Catalysis, Department of Chemical Engineering, Technical University of Denmark, DK-2800 Lyngby, Denmark*

Received 21 June 2005; received in revised form 14 September 2005; accepted 14 September 2005

Abstract

In this paper, we investigate the dehydrogenation kinetics of $LiAlH_4$ into Li_3AlH_6 (reaction I) and further into LiH (reaction II). We find the apparent activation energies to be ~80 and 100 kJ/mol for reactions I and II, respectively. Furthermore, we investigate the effect of ball milling on crystallite size and the dehydrogenation kinetics of both reactions I and II. We find a clear correlation between crystallite size and dehydrogenation kinetics of reaction I. On the other hand, we find the kinetics of reaction II to be independent of the crystallite size. This indicates that reaction I is limited by a mass transfer process, while reaction II is limited by the intrinsic kinetics.

Keywords: Hydrogen storage materials; Ball milling; X-ray diffraction; Lithium tetrahydroaluminate; Trilithium hexahydroaluminate; Gravimetry; Dehydrogenation kinetics

1. Introduction

The energy infrastructure is facing serious challenges in the future, due to limited supply of oil, increasing CO_2 emissions, and an expansive energy demand in the growing Asian economies.

Hydrogen is a potential major alternative energy carrier, although a smooth transition to a hydrogen-based society requires a solution to several technical problems; especially the need for a proper hydrogen storage medium for the transport sector is a great challenge [1,2].

Until recently, complex hydrides such as $NaAlH_4$ and $LiAlH_4$, with a theoretical capacity of 7.3 and 10.6 wt% H_2, respectively, have not been considered as potential solid state hydrogen storage media due to their irreversible dehydrogenation and slow kinetics. This perception did not change until the 1997 discovery of Ti-catalysed reversible solid state hydrogen storage in $NaAlH_4$ by Bogdanović and Schwickardi [3] (although reversibility was already demonstrated in 1974 by Dymova et al. for reactions in the melt [4]). Since then, $NaAlH_4$ has received massive attention focusing on improved doping procedures, screening of catalytic additives, maximizing the reversible capacity, and on obtaining a comprehension of the catalytic effect of Ti (see Refs. [5–10] and references therein).

As a hydrogen storage medium $LiAlH_4$ has not received the same attention as $NaAlH_4$, although several studies, both theoretical and experimental, have revealed important details about its thermal decomposition behaviour, thermodynamic stability, crystal structure, and the effect of ball milling and catalytic doping on its decomposition behaviour (see Refs. [11–31]).

Hydrogen is generally expected to desorb from $LiAlH_4$ in a three-step decomposition, I–III [14–16], although some controversy about the details of the mechanism exists [17,18].

$$LiAlH_4 \rightarrow \tfrac{1}{3}Li_3AlH_6 + \tfrac{2}{3}Al + H_2, \quad (1)$$

$$\tfrac{1}{3}Li_3AlH_6 \rightarrow LiH + \tfrac{1}{3}Al + \tfrac{1}{2}H_2, \quad (2)$$

$$LiH \rightarrow Li + \tfrac{1}{2}H_2. \quad (3)$$

Reactions I, II, and III proceed with a theoretical hydrogen release of 5.3, 2.6, and 2.6 wt%, respectively. However, due to the thermodynamic stability of LiH, i.e. high decom-

*Corresponding author. Materials Research Department, Risø National Laboratory, DK-4000 Roskilde, Denmark. Fax: +45 4677 5758.
E-mail address: andr1976@gmail.com (A. Andreasen).

0022-4596/$ - see front matter © 2005 Elsevier Inc. All rights reserved.
doi:10.1016/j.jssc.2005.09.027

position temperature, only 7.9 wt% H_2 is considered accessible for practical applications.

The kinetic parameters of reactions I and II have only been evaluated to a limited extent [13,31]. These investigations suffer either from unclear separation of parameters from reactions I and II [13] or limitations to reaction I only [31]. This serves as a main motivation for studying the dehydrogenation kinetics of both steps I and II for pure $LiAlH_4$. Furthermore, no systematic investigations of the influence of ball milling, application of different milling times, on kinetics have been reported. These investigations are essential in order to obtain a reliable reference for evaluation of the kinetic effects of doping with catalytic additives in combination with ball milling.

In this paper, we investigate the kinetics of direct dehydrogenation of solid $LiAlH_4$ by carrying out isothermal experiments below the melting point of $LiAlH_4$. In order to extract parameters for both reactions I and II a kinetic model, which takes both reactions into account is formulated, and kinetic parameters are found by fitting to experimental data. Finally, we investigate the effect of altering ball-milling times on the dehydrogenation kinetics of both reactions I and II. Using X-ray powder diffraction it is possible to obtain corresponding crystallite sizes from line broadening and relate this to the observed kinetic effect.

2. Experimental

Lithium aluminium hydride, $LiAlH_4$ (purity 95% min., typically 97%), was obtained in powder form from Alfa Aesar (Johnson Matthey). All materials handling was carried in an argon filled glove box in the presence of a drying agent.

X-ray powder diffraction (XRPD) was performed with a Bragg-Brantano STOE diffractometer (50 kV, 300 mA, Cu$K_{\alpha 12}$ radiation with $\bar{\lambda} = 1.5418$ Å). Powdered samples were pressed into 13 mm diameter pellets with a height of a few millimetres using a pressing tool placed in the glove box. While still in the glove box, a pellet was placed in a specially designed air-tight sample holder with an aluminium foil X-ray window. All observed peaks in the XRPD pattern of the as-received $LiAlH_4$ except for one could be indexed as belonging to a monoclinic unit cell ($P2_1/c$) with unit cell parameters $a = 4.83$ Å, $b = 7.83$ Å, $c = 7.92$ Å, and $\beta = 112.3°$ in agreement with previous observations of the crystal structure of $LiAlH_4/LiAlD_4$ [28,29]. The unexplained peak around $2\theta = 35°$ corresponds well with the strongest reflection of LiCl, suggesting that LiCl is present as an impurity as also suggested by Hauback et al. [16,29]. LiCl might originate from the preparation procedure [25]. We find no other impurities, e.g. hydroxides [16] or oxides [30], suggesting that these are either absent or in an X-ray amorphous state.

Ball milling was utilized with a Retsch PM 100 planetary ball mill using a Wolfram Carbide (WC) vial with a WC-coated aluminium lid sealed with a rubber O-ring. Three WC balls with a diameter of ~20 mm and a weight of ~60 g each were used for all ball-milling experiments. Typically 4–5 g of sample was ball milled giving a ball-to-sample mass ratio of 36–45:1.

Isothermal dehydrogenation of $LiAlH_4$ was studied using a Sartorius 4406 high-pressure balancing unit described in detail elsewhere [32]. In the glove box, typically 60–80 mg of sample was loaded in a stainless-steel crucible with a weight of ~800 mg. The crucible was placed in a sealed plastic bottle in order to protect it against air exposure during transportation from the glove box to the instrument. However, a short period of air exposure (<2 min.) could not be avoided when the sample was transferred from the plastic bottle. An empty stainless-steel crucible was used as a reference. Before the experiment was initiated, the system was evacuated to 10^{-1} mbar and refilled with Helium N47 purity from Air Liquide to 1 bar. This was repeated three times in order to keep the level of impurities (moisture and oxygen) at a tolerable level during the experiment. The sample was heated to the desired isothermal operating temperature at a heating rate of 10 °C/min. The gravimetric hydrogen release from the sample was determined on-line.

3. Results and discussion

3.1. Dehydrogenation kinetics of as-received $LiAlH_4$

In order to investigate the direct solid state decomposition of pure $LiAlH_4$ [15,17], isothermal experiments at different temperatures have been carried out well below the melting point of $LiAlH_4$. The results are shown in Fig. 1(A). As seen in the figure, increasing the temperature increases the rate of hydrogen release as would be expected for a thermally activated process.

Except for the lowest applied temperature, it is evident from the kink in the dehydrogenation curves at a hydrogen release of ~4.5 wt% that the decomposition of $LiAlH_4$ into LiH, Al and H_2 is indeed a two-step mechanism. The position of this transition is somewhat lower than expected from the theoretical hydrogen release. The maximally observed hydrogen release of ~6.7 wt% is also slightly lower than the theoretical limit even when correcting the observed hydrogen release with the purity of the sample. XRPD of the dehydrogenated samples (see list of reflections with assigned phases in Table 1) reveal that some Li_3AlH_6 (and possible also $LiAlH_4$) is left after dehydrogenation in agreement with observations of Andrei et al. [33]. Thus incomplete dehydrogenation of Li_3AlH_6 offers, at least partially, an explanation for this difference.

Modelling the kinetics of hydrogenation/dehydrogenation is essential in order to gain a detailed comprehension of the underlying physics and to identify rate-limiting step(s) of the overall process. This type of kinetic modelling has recently been performed in the case of $NaAlH_4$ [35–37].

In order to model the isothermal dehydrogenation curves in Fig. 1(A), a model with the ability to account

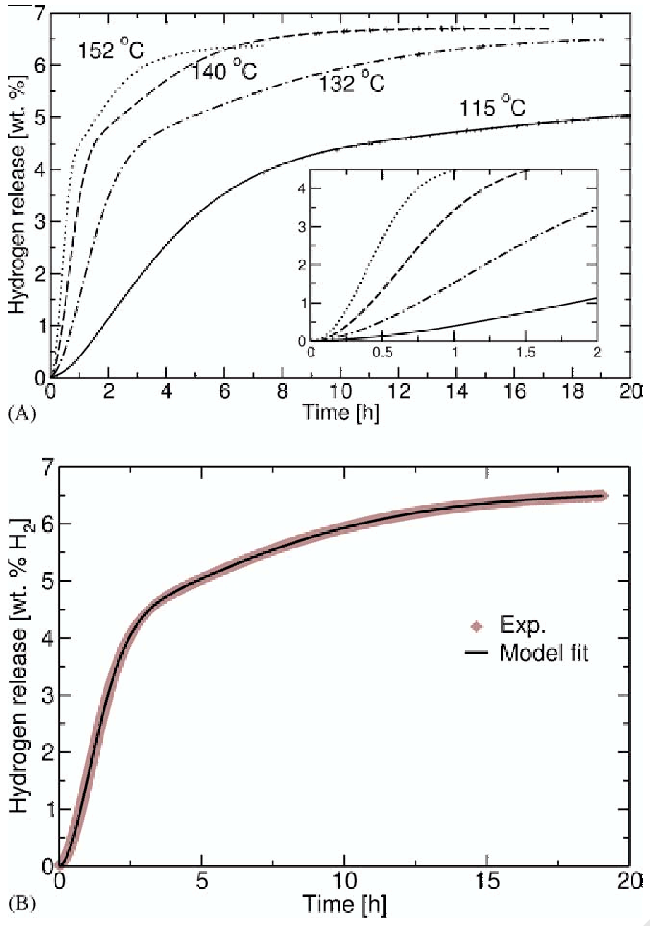

Fig. 1. (A) Isothermal dehydrogenation of as-received $LiAlH_4$ investigated in a high-pressure balance. (B) Fit of Eq. (4) to isothermal dehydrogenation data at $T = 132\,^{\circ}C$.

Table 1
Observed reflections in XRPD of a pellet pressed from the dehydrogenation product of all four as-received samples

2θ (deg)	d (Å)	I/I_{max} (%)	Phase
21.99	4.0393	1.46	Li_3AlH_6
22.55	3.9492	1.53	Li_3AlH_6
29.68	3.0071	0.96	$LiAlH_4$
30.12	2.9646	1.74	$LiAlH_4$
30.42	2.9358	1.56	$LiAlH_4$
31.70	2.8202	1.18	Li_3AlH_6
34.92	2.5673	1.47	Li_3AlH_6
38.54	2.3344	100	Al/LiH
39.97	2.2539	0.74	Li_3AlH_6
44.79	2.0219	43.93	Al/LiH

Phases of Li_3AlH_6 and $LiAlH_4$ have been assigned according to Refs. [28,34].

for both decomposition reactions should be chosen. A standard two-step kinetic expression of the following form provides a good fit to the experimental data

$$W_{tot}(t) = W_1(1 - \exp(-(k_1 t)^{\eta_1})) + W_2(1 - \exp(-(k_2 t)^{\eta_2})), \quad (4)$$

where W_{tot} is the total hydrogen release at time t, W_1 and W_2 are the release of hydrogen from reactions I and II, respectively; k_1 and k_2, and η_1 and η_2 are exponents for reactions I and II, respectively. Except for the included exponents in Eq. (4) the model is similar to the one applied by Kiyobayashi et al. in order to model dehydrogenation of $NaAlH_4$ [35]. Since only dehydrogenation is considered—and the fact that dehydrogenation is performed at constant pressure—pressure-dependent terms, as proposed by Luo and Gross [37] are ignored.

The kinetic expression is fitted to the isothermal experimental data using a Levenberg–Marquandt least-squares algorithm. A sample fit of Eq. (4) to the isothermal dehydrogenation curve at 132 °C is shown in Fig. 1(B). As seen in the figure, the model provides an excellent description of the dehydrogenation kinetics.

All extracted fitting parameters, and apparent activation energies and prefactors as determined from an Arrhenius analysis are summarized in Table 2, including χ^2 goodness-of-fit values.[1]

Early studies on the kinetics of the isothermal decomposition of $LiAlH_4$ by McCarthy et al. [13] revealed an apparent activation energy of reaction I to be ~100 kJ/mol, although it is unclear to which degree the fitted data had been influenced by reaction II. Recent studies by Blanchard et al. [31] shows a value of 102 kJ/mol for reaction I. The value of the apparent activation energy determined in this study is slightly lower (82 kJ/mol), but nevertheless in good agreement with the previous studies. McCarthy et al. [13] also reported an apparent activation energy of reaction II from constant heating rate experiments of ~100 kJ/mol which is also in good agreement with the reported value of 90 kJ/mol in this work. While the work of Blanchard et al. [31] and McCarthy et al. [13] have been limited to treating one reaction at a time, the formulation of a two-step kinetics model has allowed simultaneous extraction of kinetic parameters of both reactions I and II from a single experiment.

3.2. Kinetic effect of ball milling

In order to investigate the effect of ball-milling $LiAlH_4$ on the dehydrogenation kinetics, the as-received powder has been ball milled for different periods of time and milling intensities. These samples have been subject to both XRPD analysis and isothermal measurements of the dehydrogenation process.

XRPD patterns of all the ball milled samples are shown in Fig. 2. Generally, the reflections become broader and

[1] χ^2 goodness-of-fit calculated for each temperature by

$$\chi^2 = \frac{1}{N}\sum_{i=1}^{N}\left(\frac{(W_{obs}(i) - W_{model}(i))^2}{W_{model}(i)}\right),$$

where N is the total number of observations during an isothermal experiment, W_{obs} is the experimentally observed hydrogen release, and W_{model} is the calculated hydrogen release using Eq. (4).

Table 2
Kinetic parameters obtained from fitting isothermal measurements of the direct decomposition of as-received $LiAlH_4$

T (°C)	W_1 (wt% H_2)	W_2 (wt% H_2)	k_1 (h^{-1})	k_2 (h^{-1})	η_1 (dimensionless)	η_2 (dimensionless)	χ^2
115	4.28	1.56	0.229	0.040	1.53	1.95	0.0133
132	4.11	2.44	0.624	0.123	1.80	1.51	0.0030
140	4.25	2.44	1.191	0.235	1.99	1.71	0.0007
152	4.02	2.32	1.996	0.442	2.22	1.74	0.0302
A (h^{-1})			2.3×10^{10}	4.9×10^{10}			
E_A (kJ/mol)			82 ± 4	90 ± 4			

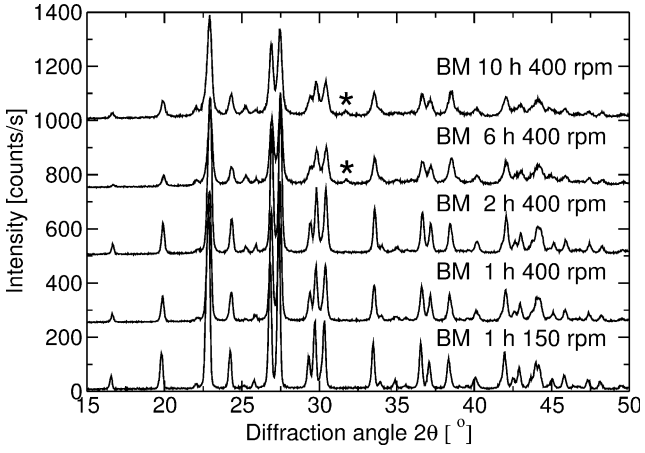

Fig. 2. XRPD of as-received $LiAlH_4$, $LiAlH_4$ ball milled for 1 h at 150 rpm, and $LiAlH_4$ ball milled for 1 h at 400 rpm.

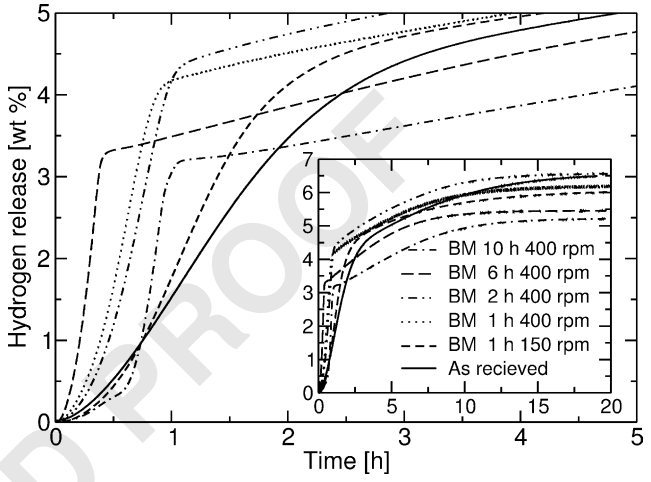

Fig. 3. Isothermal dehydrogenation curves for ball-milled samples. The isothermal temperature is ~130 °C. Dehydrogenation curve for un-milled as-received $LiAlH_4$ at 132 °C is included for comparison.

lose intensity as a function of milling time/intensity suggesting that the average coherence length (crystallite size) is reduced upon milling. After 6 h of milling an additional reflection (marked with an asterisk) appears around $2\theta = 31.7°$. This feature could originate from either the (2 2 0) reflection of monoclinic [34] Li_3AlH_6 or the (2 0 −1) reflection of rhombohedral Li_3AlH_6 [20], suggesting a partial decomposition of $LiAlH_4$. In fact, after 2 h of milling, the sample changed colour from white/greyish to light grey indicating that a solid state reaction had taken place. On the other hand, apparently no crystalline metallic aluminium is formed suggesting that if any formation of Li_3AlH_6 has taken place the resulting aluminium is in an X-ray amorphous phase. Partial decomposition of $LiAlH_4$ into Li_3AlH_6 can be explained in terms of a higher thermodynamic stability of Li_3AlH_6 compared to $LiAlH_4$ [11,15,19–22]. Although the ball-milling vial used in this work was carefully cleaned, the presence of small amounts of impurities that may act as a catalyst [26] cannot be completely ruled out. However, we consider this as unlikely. On the other hand, we noticed that the vial heated up slightly during milling, most pronounced for the longer milling times. Thus, the potential decomposition of $LiAlH_4$ may be thermally mediated.

The effect of ball milling on the dehydrogenation kinetics is visualized by isothermal dehydrogenation curves for all ball-milled samples in Fig. 3. It was intended to apply the same isothermal temperature to all dehydrogenation experiments for the ball-milled samples. Though, in practice, an inter-sample temperature variance of a few degrees around 130 °C was observed, which is expected to be within experimental uncertainty. The dehydrogenation curve for as-received $LiAlH_4$ at 132 °C is included in Fig. 3 as a reference.

From the dehydrogenation curves in Fig. 3 it is observed that ball milling effectively leads to faster kinetics for reaction I (first and steepest part of the curves up to 3–4.5 wt%), while reaction II seems to be more insensitive to the ball-milling. Applying longer ball milling times, the smooth transition between reactions I and II as observed in the un-milled sample become more abrupt. The initial rate of dehydrogenation for the sample ball milled for 10 h seems to deviate somewhat from the others. This is due to the fact that dehydrogenation initiated during the heating period. It is also observed from Fig. 3 that longer ball-milling times results in reduced hydrogen release mainly from $LiAlH_4$.

In order to quantify the effect of ball milling on the dehydrogenation kinetics of $LiAlH_4$, kinetic parameters are extracted from the dehydrogenation curves by fitting

Table 3
Kinetic parameters obtained from fitting isothermal measurements of the direct decomposition of ball-milled $LiAlH_4$

Time (h)	Intensity (rpm)	W_1 (wt% H_2)	W_2 (wt% H_2)	k_1 (h^{-1})	k_2 (h^{-1})	η_1 (dimensionless)	η_2 (dimensionless)	χ^2
1	150	3.85	2.17	0.751	0.180	2.48	1.18	0.0002
1	400	4.12	2.07	1.567	0.168	2.78	1.41	0.0047
2	400	3.57	3.26	1.305	0.190	3.66	0.80	0.0020
6	400	3.39	2.04	3.272	0.216	2.95	1.60	0.0095
10	400	2.81	1.97	3.817	0.163	2.26	1.63	0.0113

Eq. (4) to the experimental dehydrogenation curves of the ball-milled samples; the results are summarized in Table 3. In order to fit the dehydrogenation curve of the sample ball milled for 10 h it was necessary to exclude the first part of the curve corresponding to the non-isothermal hydrogen release from the fitting procedure. As seen from the fitted parameters in Table 3 the faster kinetics of reaction I seen in Fig. 3 is confirmed quantitatively. It is interesting to see that ball milling has virtually no effect on the rate constant of reaction II.

From Table 3 it is clearly observed that the parameter W_1 decreases as a function of milling time, especially for the longest periods of milling. This suggests some partial decomposition of $LiAlH_4$ during milling as discussed previously, and also in agreement with Fig. 3. This requires a careful application of the kinetic model. However, we find no reasons to believe that the fitting results are biased by the initial presence of Li_3AlH_6 in the ball-milled samples. First, the decomposition of Li_3AlH_6 is slow compared to the decomposition of $LiAlH_4$ as visualized by both Figs. 1(A) and 3. This is even more pronounced for the samples ball milled for the longest times. According to Fig. 3, the dehydrogenation of $LiAlH_4$ becomes so fast for the longest periods of milling, that an induction period in the decomposition of Li_3AlH_6 is revealed. Thus for the samples containing Li_3AlH_6 from the beginning, effectively no decomposition of Li_3AlH_6 takes place before all $LiAlH_4$ is completely transformed into Li_3AlH_6. Second, the fitting parameter W_2 shown in Table 3 is more or less constant even despite the initial presence of Li_3AlH_6. This is a natural consequence of the first point and it gives confidence in the fact that the two dehydrogenation steps described by the model are treated as separate reactions without any intermixing of kinetic parameters, i.e. the kinetic parameters of step I are independent of the kinetic parameters of step II and vice versa.

3.3. Diffusion limited kinetics?

In order to investigate a possible correlation between crystallite size and rate constants we have extracted crystallite sizes of the ball-milled samples before dehydrogenation including the as-received sample by applying the Scherrer equation

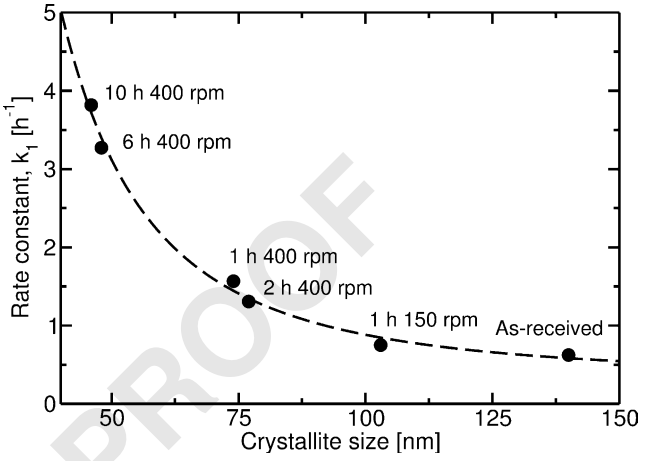

Fig. 4. Rate constants for reaction I as a function of crystallite size obtained from XRPD line broadening.

$$\beta = \frac{\lambda}{B\cos\theta}, \quad (5)$$

where β is the crystallite size, λ is the X-ray wavelength and B is the FWHM (corrected for instrumental broadening, which is assumed to be 0.10°). In order to get a reliable picture of the average crystallite size instead of an average coherence lengths in certain crystallographic directions, the average line broadening of several reflections up to 35° in 2θ have been used.

Fig. 4 shows the rate constants as a function of crystallite size. Fitting the data to a power-law yields an excellent fit (dashed line) with an $1/\beta^{2.3}$ dependence. The strong dependence of k_1 on crystallite size may suggest a mass transfer process to be limiting the kinetics, e.g. long-range atomic diffusion of Al as proposed by Kiyobayashi et al. [35] and Sandrock et al. [7]. The exact order of the exponent can be used to obtain detailed physical information about the underlying rate-limiting process(es).

In the Nabarro–Herring model [38,39], a $1/\beta^2$ relation corresponds to a process controlled by lattice (intergranular) diffusion as observed for e.g. hydrogen diffusion in $Co_{90}Zr_{10}$ [40], whereas a process controlled by grain boundary diffusion displays a $1/\beta^3$ relation according to Coble [41]; as observed for e.g. hydrogen enhanced diffusional creep in Pd [42]. Considering Fig. 4 displays a $1/\beta^{\sim 2}$ relation, reaction I is likely limited by a lattice diffusional process, although grain boundary diffusion cannot be excluded.

The fact that k_2 is more or less insensitive to the large variations in crystallite size indicates that reaction II, in contrast to reaction I, is not limited by mass transfer. Instead, the intrinsic kinetics seems to be limiting at the relatively low temperature applied. Previous DTA results [26] show that the kinetics of reaction II at elevated temperatures is indeed improved by ball milling as seen by a lowering of the decomposition temperature from ~250 to 225 °C after ball milling for only 10 min. This suggests that at the elevated temperatures in the DTA experiment, the intrinsic kinetics is improved sufficiently in order *not* to be rate limiting for the overall kinetics. Instead, the crystallite size seems to become important. However, for practical applications the temperature cannot be increased above 200 °C in order to obtain improved kinetics. Thus, ball milling alone is not sufficient to improve the kinetics of reaction II. This example very clearly illustrates the need for a suitable catalytic additive, not only to the make reaction I+II reversible [21] but also to improve the kinetics—especially of reaction II.

3.4. Influence on oxygen contamination on kinetics

Although no oxygen contamination is observed in any of the XRPD results shown in this study, it seems unquestionable that the samples contain a certain amount of oxides. This is supported by the studies of Andrei et al. [30] in which aluminium oxide was detected by EELS, even though the samples have been carefully transferred from the glove box to the instrument in a special vacuum transfer device including a removable glove bag mounted on the instrument.

The results of Andrei et al. [30] also indicated that the found aluminium oxide forms a thin layer on the particles. Hence, dehydrogenation may potentially be limited by hydrogen diffusion through the surface oxide. Although, we find this to be highly unlikely. Mainly, because even for the ball-milled samples the main weight fraction of samples belong to particles of several microns (as found by additional SEM experiments) making the determined crystallite sizes a "bulk" quantity. Thus, if diffusion though the surface oxide was rate limiting, one would not expect such a strong correlation between rate and crystallite size. Furthermore, the similarity of apparent activation energies of both reactions I and II with previous studies [13,31] despite differences in sample treatment seems to support this hypothesis.

4. Conclusion

We have investigated the dehydrogenation kinetics of as-received and ball-milled $LiAlH_4$. Isothermal experiments reveal apparent activation energies of 82 and 90 kJ/mol for dehydrogenation of $LiAlH_4$ to Li_3AlH_6 (reaction I) and the subsequent dehydrogenation of Li_3AlH_6 to LiH (reaction II), respectively.

Investigations of ball-milling $LiAlH_4$ for different periods of time and subsequent kinetic investigations at isothermal conditions at ~130 °C clearly show improved kinetics of the dehydrogenation reaction I as a function of milling time, whereas reaction II seems more or less insensitive to the ball-milling process. Detailed kinetic fitting allowing extraction of rate constants for both reactions I and II shows a clear correlation between the rate constant of reaction I and crystallite size determined from XRPD line broadening with higher rate constant corresponding to smaller crystallite sizes (longer ball-milling times). In contrast, the rate constant of reaction II is more or less unchanged despite the drastic reduction in crystallite size of $LiAlH_4$ going from 140 to 46 nm. This suggests reaction I is limited by mass transfer, whereas reaction II is limited by the intrinsic kinetics. Thus a suitable catalyst is needed in order to improve the kinetics, not only for the reversibility of reactions I and II, but certainly also the kinetics of reaction II at temperatures suitable for practical applications.

Acknowledgements

This work has received financial support from The Danish Technical Research Council through the Center of Excellence *Towards a hydrogen-based society*.

References

[1] L. Schlapbach, A. Züttel, Nature 414 (2001) 353–358.
[2] Basic research needs for the hydrogen economy, Technical Report, Argonne National Laboratory, Argonne, IL 60439, USA, 2003.
[3] B. Bogdanović, M. Schwickardi, J. Alloys Compd. 253–254 (1997) 1–9.
[4] T.N. Dymova, Y.M. Dergachev, V.A. Sokolov, N.A. Grechanaya, Dokl. Akad. Nauk. SSSR 215 (1974) 1369–1372.
[5] D.L. Anton, J. Alloys Compd. 356 (2003) 400–404.
[6] K.J. Gross, E.H. Majzoub, S.W. Spangler, J. Alloys Compd. 356–357 (2003) 423–428.
[7] G. Sandrock, K. Gross, G. Thomas, C. Jensen, D. Meeker, S. Takara, J. Alloys Compd. 330–332 (2002) 686–701.
[8] A. Leon, O. Kirchner, J. Rothe, M. Fichtner, J. Phys. Chem. B 108 (42) (2004) 16372–16376.
[9] M. Felderhoff, K. Klementiev, W. Grunert, B. Spliethoff, B. Tesche, J.M.B. von Colbe, B. Bogdanović, M. Hartel, A. Pommerin, F. Schuth, C. Weidenthaler, Phys. Chem. Chem. Phys. 6 (17) (2004) 4369–4374.
[10] H.W. Brinks, C.M. Jensen, S.S. Srinivasan, B.C. Hauback, D. Blanchard, K. Murphy, J. Alloys Compd. 376 (2004) 215–221.
[11] P. Claudy, B. Bonnetot, J.M. Létoffé, G. Turck, Thermochim. Acta 27 (1978) 213–221.
[12] J. Block, A.P. Gray, Inorg. Chem. 4 (1965) 304–305.
[13] M. McCarthy Jr., J.N. Maycook, V.R. Pai Verneker, J. Phys. Chem. 72 (1968) 4009–4014.
[14] J.A. Dilts, E.C. Ashby, Inorg. Chem. 11 (6) (1972) 1230–1236.
[15] T.N. Dymova, D.P. Aleksandrov, V.N. Konoplev, T.A. Silina, A.S. Sizareva, Russ. J. Coord. Chem. 20 (4) (1994) 279–285.
[16] D. Blanchard, H.W. Brinks, B.C. Hauback, P. Norby, Mater. Sci. Eng. B 108 (2004) 54–59.
[17] J.W. Wiench, V.P. Balema, V.K. Pecharsky, M. Pruski, J. Solid State Chem. 177 (2004) 648–653.

[18] V.P. Balema, L. Balema, Phys. Chem. Chem. Phys. 7 (6) (2005) 1310–1314.
[19] M.B. Smith, G.E. Bass Jr., J. Chem. Eng. Data 8 (3) (1963) 342–346.
[20] O.M. Løvvik, S.M. Opalka, H.W. Brinks, B.C. Hauback, Phys. Rev. B 69 (2004) 134117.
[21] J. Chen, N. Kuriyama, Q. Xu, H.T. Takeshita, T. Sakai, J. Phys. Chem. B 105 (2001) 11214–11220.
[22] S.C. Chung, H. Morioka, J. Alloys Compd. 372 (2004) 92–96.
[23] V.P. Balema, K.W. Dennis, V.K. Pecharsky, Chem. Comm. (17) (2000) 1665–1666.
[24] L. Zaluski, A. Zaluska, J.O. Ström-Olsen, J. Alloys Compd. 290 (1999) 71–78.
[25] E. Wiberg, E. Amberger, Hydrides of the Elements of Main Groups I–IV, Elsevier, Amsterdam, 1971.
[26] V.P. Balema, V.K. Pecharsky, K.W. Dennis, J. Alloys Compd. 313 (2000) 69–74.
[27] V.P. Balema, J.W. Wiench, K.W. Dennis, M. Pruski, V.K. Pecharsky, J. Alloys Compd. 329 (2001) 108–114.
[28] N. Sklar, B. Post, Inorg. Chem. 6 (1967) 669.
[29] B.C. Hauback, H. Brinks, H.W. Fjellvåg, J. Alloys. Compd. 346 (2002) 184–189.
[30] C.M. Andrei, J.C. Walmsley, H.W. Brinks, R. Holmestad, B.C. Blanchard, D. Hauback, G.A. Botton, J. Phys. Chem. B 109 (2004) 4350–4356.
[31] D. Blanchard, H.W. Brinks, B.C. Hauback, P. Norby, J. Muller, J. Alloys Compd. (2005) doi:10.1016/j.jallcom.2005.01.126.
[32] A.S. Pedersen, J. Kjøller, B. Larsen, B. Vigeholm, Int. J. Hydrogen Energy 8 (3) (1983) 205–211.
[33] C.M. Andrei, J. Walmsley, D. Blanchard, H.W. Brinks, R. Holmestad, B.C. Hauback, J. Alloys. Compd. 395 (2005) 307–312.
[34] J. Mayet, J. Tranchan, Bull. Soc. Chim. Fr. (2) (1973) 510.
[35] T. Kiyobayashi, S.S. Srinivasan, D. Sun, C.M. Jensen, J. Phys. Chem. A 107 (39) (2003) 7671–7674.
[36] R.T. Walters, J.H. Scogin, J. Alloys Compd. 379 (2004) 135–142.
[37] W. Luo, K.J. Gross, J. Alloys Compd. 385 (2004) 224–231.
[38] C. Herring, J. Appl. Phys. 21 (1950) 437–445.
[39] F.R.N. Nabarro, H.L. de Villiers, The Physics of Creep, Taylor & Francis, 1995.
[40] M. Hirsher, J. Mössinger, H. Kronmüller, NanoStructured Mater. 6 (1995) 635–638.
[41] R.L. Coble, J. Appl. Phys. 34 (1963) 1679–1682.
[42] Z.R. Xu, R.B. McLellan, Acta Mater. 46 (1998) 4543–4547.

Appendix F

Paper 6

Effect of Ti-doping on the dehydrogenation kinetic parameters of lithium aluminum hydride

Anders Andreasen [a,b,1,*]

[a] *Materials Research Department, Ris National Laboratory, DK-4000 Roskilde, Denmark*

[b] *Interdisciplinary Research Center for Catalysis, Department of Chemical Engineering, Technical University of Denmark, DK-2800 Lyngby, Denmark*

Abstract

The effect of Ti-doping on the dehydrogenation kinetics of lithium aluminum hydride has been investigated in this paper. For the decomposition of lithium aluminum hydride into trilithium hexahydridoaluminate apparent activation energies of 81 and 89 kJ/mol are found for the un-doped and Ti-doped sample, respectively. For the decomposition of trilithium hexahydridoaluminate into lithium hydride apparent activation energies of 108 and 103 kJ/mol are found. The differences in apparent activation energies between the un-doped and the Ti-doped sample are within experimental uncertainty, suggesting that the effect of Ti-doping on the kinetic parameters of dehydrogenation of lithium aluminum hydride, is mainly a prefactor effect.

Key words: Hydrogen storage materials (A), High energy ball milling (B), X-ray diffraction (C), Thermal analysis (E)

* Corresponding author. E-mail: andr1976@gmail.com (A. Andreasen).

[1] Present address: MAN B&W Diesel A/S, Teglholmsgade 41, DK-2450 Copenhagen SV, Denmark.

1 Introduction

Since the discovery of reversible solid state hydrogen storage in $NaAlH_4$ [1], the alanates and borohydrides, in general, have been subject to an intense research effort. Until present date, main focus has been on $NaAlH_4$ although it does not fully meet the DOE targets for gravimetric hydrogen storage density and thermodynamics. $LiAlH_4$, on the other hand, has a higher gravimetric hydrogen density and thermodynamics allow hydrogen desorption at 1 bar even below 100 °C, but it has not been investigated as thoroughly as $NaAlH_4$.

Hydrogen desorbs from $LiAlH_4$ in a three step decomposition, R1-R3 [2–4]

$$LiAlH_4 \rightarrow \frac{1}{3}Li_3AlH_6 + \frac{2}{3}Al + H_2 \quad \text{(R1)}$$

$$\frac{1}{3}Li_3AlH_6 \rightarrow LiH + \frac{1}{3}Al + \frac{1}{2}H_2 \quad \text{(R2)}$$

$$LiH + Al \rightarrow LiAl + \frac{1}{2}H_2 \quad \text{(R3)}$$

R1, R2, and R3 proceeds with a theoretical hydrogen release of 5.3 wt. %, 2.6 wt. %, and 2.6 wt. %, respectively.

In thermal analysis, R1 occurs around 112-220 °C [5–7] and is usually initiated by the melting of $LiAlH_4$ (endothermic), unless very low heating rates are applied, which is subsequently transformed into solid Li_3AlH_6 and Al during release of hydrogen gas (exothermic). R2 takes place around 127-260 °C (endothermic) [3,4]. R3 (endothermic) proceeds at elevated temperatures around 350-400 °C [4].

Both ball milling and doping with VCl_3, $TiCl_3$, or $TiCl_3{\cdot}1/3AlCl_3$ results in a lowering of the decomposition temperature of both R1 and R2 [6,10,4,5]. Pure $LiAlH_4$ does not decompose during ball milling at ambient temperatures [6], whereas $LiAlH_4$ doped with catalytic additives rapidly decomposes during milling [4,6,11,12]. Slow

decomposition after doping has even been monitored during storage under ambient conditions [13].

The kinetic parameters of R1 and R2 in terms of apparent activation energies and prefactors, including the influence of catalytic doping, have only been evaluated to a limited extent [5,14,15]. Further, no solid conclusions about the influence of doping on the kinetic parameters can be drawn due to contradicting results [5,15]. This serves as a main motivation for studying the influence of Ti-doping on the dehydrogenation kinetics of both R1 and R2.

2 Experimental

Lithium aluminum hydride, $LiAlH_4$ (purity 95% min., typically 97%), was obtained in powder form. Doping of $LiAlH_4$ was carried out by ball milling with 2 mole % $TiCl_3{\cdot}1/3AlCl_3$ (purity 76–78% $TiCl_3$). All chemicals were purchased from Alfa Aesar (Johnson Matthey). All materials handling was carried out in the presence of a drying agent within an argon filled glove box.

Ball milling was utilized with a Retsch PM 100 planetary ball mill using a Wolfram Carbide (WC) vial with a WC coated aluminum lid sealed with a rubber O-ring. 3 WC balls with a diameter of approx. 20 mm and a weight of approx. 60 g each were used for all ball milling experiments. Typically 4-5 gram of sample was ball milled giving a ball-to-sample mass ratio of 36–45:1.

X-ray powder diffraction (XRPD) was performed with a Bragg-Brantano STOE diffractometer (50 kV, 300 mA, Cu $K_{\alpha 12}$ radiation with $\bar{\lambda}$ = 1.5418 Å). Powdered samples were pressed into 13 mm diameter pellets with a hight of a few mm using a pressing tool placed in the glove box. While still in the glove box, a pellet was

placed in a specially designed air tight sample holder with an aluminum foil X-ray window. The holder was assembled and transported to the diffractometer for subsequent XRPD analysis.

A Seiko DSC 120 U instrument was used for differential scanning calorimetry (DSC) experiments. Typically 3-7 mg of sample was loaded in an alumina crucible in the glove box. The crucible was placed in a sealed plastic bottle in order to protect it against air exposure during transportation from the glove box to the DSC instrument. However, a few seconds of air exposure could not be avoided when the sample was transfered from the plastic bottle to the DSC apparatus. An empty crucible was used as a reference. The sample was heated from room temperature to 300 °C under an argon atmosphere with a flow of approx. 850 ml/min applying different heating rates.

3 Results and Discussion

3.1 Initial materials characterization

Figure 1 shows the XRPD pattern of the as-received $LiAlH_4$. All observed peaks except one (marked with an asterisk) can by indexed as belonging to a monoclinic unit cell ($P2_1/c$) with unit cell parameters $a = 4.83$ Å, $b = 7.83$ Å, $c = 7.92$ Å, and $\beta = 112.3\,^\circ$ in agreement with previous observations of the crystal structure of $LiAlH_4$/$LiAlD_4$ [16]. The unexplained peak around $2\theta = 35\,^\circ$ corresponds well with the strongest reflection of LiCl, suggesting that LiCl is present as an impurity as also suggested by Hauback *et al.* [4,16]. LiCl might originate from the preparation procedure [9]. No other impurities e.g. hydroxides [4] or oxides [17] are found, suggesting that these are either absent or in an X-ray amorphous state.

3.2 Dehydrogenation kinetics of as-received $LiAlH_4$

The as-received $LiAlH_4$ powder has been investigated by DSC applying different heating rates cf. Figure 2. DSC traces shows the following features: an exothermic peak at 150 °C, an endothermic peak around 170 °C, an exothermic peak at 178-198 °C, and an endothermic peak around 227-247 °C.

The first exotherm has previously been assigned to the interaction of $LiAlH_4$ with surface hydroxyl impurities [3], and the first endotherm corresponds to the melting of $LiAlH_4$ [2,3]

$$\mathrm{LiAlH_4(s)} \rightarrow \mathrm{LiAlH_4(l)} \tag{1}$$

The position of the melting point of $LiAlH_4$ is rather insensitive to the choice of heating rate. The melting of $LiAlH_4$ is immediately followed by the second exotherm corresponding to the decomposition of liquid $LiAlH_4$ [2,3]

$$\mathrm{LiAlH_4(l)} \rightarrow \frac{1}{3}\mathrm{Li_3AlH_6(s)} + \frac{2}{3}\mathrm{Al(s)} + \mathrm{H_2(g)} \tag{2}$$

The second endotherm corresponds to the decomposition of Li_3AlH_6 as described by R2 [2,3,18,6]

By performing a Kissinger analysis [19], i.e. an analysis of the sensitivity of the peak positions, in terms of T_m the temperature of the peak maximum, to the applied heating rate, β, the apparent activation energy, E_A, can be obtained from the following equation

$$\frac{d\ln\left(\frac{\beta}{T_m^2}\right)}{d\left(\frac{1}{T_m}\right)} = -\frac{E_A}{R} \tag{3}$$

Thus, E_A can be obtained as the slope in a plot of $\ln\left(\frac{\beta}{T_m^2}\right)$ vs. $\frac{1}{T_m}$. A Kissinger

analysis is applied to the 2. exotherm (R1) and the 2. endotherm (R2) cf. Figure 3. From the Kissinger analysis the apparent activation energy for decomposition of $LiAlH_4$ into Li_3AlH_6, Al and H_2 (R1) is found to be 81±4 kJ/mol. The apparent activation energy for decomposition of Li_3AlH_6 into LiH, Al and H_2 (R2) is found to be 108±8 kJ/mol.

3.3 Catalytic doping and stability of $LiAlH_4$

Before ball milling the the red/purple $TiCl_3 \cdot 1/3AlCl_3$ was gentle mixed with the white/grayish $LiAlH_4$ in the milling vial resulting in a reddish powder. The color remained after ball milling for 1 min at 100 rpm, however, the next day the reddish color had disappeared and the powder appeared very much like the un-doped starting $LiAlH_4$ indicating that a reduction of Ti^{3+} in $TiCl_3$ had taken place. A possible reduction mechanism is outlined below [4]

$$\begin{aligned} 49\mathrm{LiAlH_4} + \mathrm{TiCl_3} \cdot 1/3\mathrm{AlCl_3} \rightarrow \\ 46\mathrm{LiAlH_4} + \mathrm{Ti} + 3\mathrm{Al} + 3\mathrm{LiCl} + 1/3\mathrm{AlCl_3} + 6\mathrm{H_2} \end{aligned} \quad (4)$$

The reduced Ti species may possibly be distributed as metallic Ti across the surface of the powdered particles [17] or present as a Ti_xAl_y alloy as proposed by Balema *et al.* for $TiCl_4$ doped $LiAlH_4$ [12] and as also proposed for $NaAlH_4$ [20–22]. The fact that the color of the sample ball milled for 1 min at 100 rpm did not change i.e. no darkening due to finely dispersed Ti and Al particles, may indicate that Ti is incorporated into the $LiAlH_4$ as suggested by Fichtner *et al.* [23]. However, this work is not conclusive about the chemical state of Ti $LiAlH_4$. The sample ball milled for 5 min at 400 rpm displayed a grey colour indicating a significant decomposition of $LiAlH_4$.

Figure 4 shows XRPD patterns of 2 mole % $TiCl_3$·1/3$AlCl_3$ doped samples ball

milled for 1 min at 100 rpm and 5 min at 400 rpm. The sample ball milled for the shortest time and lowest speed shows no indication of any decomposition during the doping procedure. The diffraction pattern closely resembles that of the pure $LiAlH_4$ shown in figure 1 with no signs of metallic Al/LiH in the diffraction pattern. Increasing the milling intensity leads to an almost complete decompostion of $LiAlH_4$ into Li_3AlH_6 cf. Figure 4. This clearly demonstrates the effectiveness of $TiCl_3 \cdot 1/3AlCl_3$ as a doping material and the fact that $LiAlH_4$ is thermodynamically unstable at ambient conditions (although kinetically stable in the absence of a catalyst). This is in qualitative agreement with previous observations [3,4,6].

3.4 Dehydrogenation kinetics of Ti-doped samples

Figure 5 shows DSC experiments performed with the samples ball milled for 1 min at 100 rpm with different applied heating rates. The DSC traces mainly consists of two endotherms, one with maximum around 150 °C and the other with maximum at approx. 200 °C. The first endotherm can be assigned to the dehydrogenation of solid $LiAlH_4$ into Li_3AlH_6 according to R1. Clearly the catalytic doping procedure has lowered the decomposition temperature of $LiAlH_4$ below its melting point in agreement with the findings reported in ref. [4,5]. In this context, it should be mentioned that the melting of $LiAlH_4$ prior to decomposition can also be avoided without doping by applying either isothermal conditions [24] or very low heating rates [7]. However, this is of course only due to a change in reaction conditions and not due to any kinetic effects.

The small feature between the two dominating endothermic peaks, consisting of an endothermic and an exothermic peak, can be attributed to the melting of unreacted $LiAlH_4$ and subsequent decomposition into Li_3AlH_6. The second of the two dominating endothermic peaks corresponds to the decomposition of Li_3AlH_6 into LiH

according to R2. The decomposition temperature of Li_3AlH_6 has also been lowered significantly compared to the pure $LiAlH_4$. To further investigate the effect of Ti-doping on the dehydrogenation kinetics of $LiAlH_4$ a Kissinger analysis, as outlined previously for the un-doped sample, is performed on the data shown in Figure 5. Figure 6 shows the resulting Kissinger analysis and the analysis reveals apparent activation energies of 89±9 kJ/mol and 103±1 kJ/mol for R1 and R2, respectively. The found apparent activation energies are very close to those for the un-doped sample (81±4 kJ/mol and 108±8 kJ/mol).

3.5 Effect of Ti-doping on the kinetic parameters

Reported values of apparent activation energies for dehydrogenation of Ti-doped $NaAlH_4$ and Na_3AlH_6 are found to be in the range of 73-100 and 97-100 kJ/mol, respectively [25–28] (with only a recent study indicating a significant higher activation energy for Na_3AlH_6 decomposition [29]). This is similar to the reported values for R1 and R2 of the un-doped samples of $LiAlH_4$ in this study. The apparent activation energies for dehydrogenation of un-doped $NaAlH_4$ and Na_3AlH_6 is approx. 120 kJ/mol for both reactions [27]. Thus, apparently a lowering of the apparent activation energies of R1 and R2 in $NaAlH_4$ is a consequence of Ti-doping.

Early studies on the kinetics of the isothermal decomposition of un-doped $LiAlH_4$ by McCarthy *et al.* [14] revealed an apparent activation energy of R1 to be approx. 100 kJ/mol, although it is unclear to which degree the fitted data had been influenced by R2. Recent studies by Blanchard *et al.* [15] shows a value of 102 kJ/mol for R1. McCarthy *et al.* [14] also reported an apparent activation energy of R2 from constant heating rate experiments of approx. 100 kJ/mol. The apparent activation energies found in this work seems to be in good agreement with both the studies of McCarthy *et al.* [14] and Blanchard *et al.* [15].

In addition, Blanchard *et al.* [15] also studied the influence of doping with catalytic additives on the apparent activation energy of R1. They found a reduction of approx. 5-10 kJ/mol upon doping with either $TiCl_3$·1/3$AlCl_3$ or VCl_3. Chen *et al.* [5] have investigated the dehydrogenation kinetics of $TiCl_3 \cdot 1/3AlCl_3$ doped $LiAlH_4$ and they found apparent activation energies of 43 kJ/mol and 55 kJ/mol for R1 and R2, respectively. The low values of apparent activation energies reported by Chen *et al.* are in contradiction to the ones reported in this study for Ti-doped $LiAlH_4$ and also in contradiction to the results of Blanchard *et al.* [15].

To summarize, in this study no significant effect on the apparent activation energies are observed as a consequence of Ti-doping, although a minor change cannot be ruled out due to an uncertainty of 5-10 kJ/mol in the present experiments. This suggests that *a)* The effect of Ti-doping is different in $LiAlH_4$ compared to $NaAlH_4$, and *b)* since the dehydrogenation temperatures shift downwards in the DSC experiments upon doping this must be accounted for mainly in terms of an increase in the prefactor, since the activation energies are unaffected by the doping.

In order to get a rough estimate of the increase in prefactor, ν, upon doping the Redhead equation is used (assuming 1. order desorption)

$$\frac{E_A}{RT_m} = \left(\frac{\nu}{\beta}\right) \exp\left(-\frac{E_A}{RT_m}\right) \tag{5}$$

This equation can be used to solve for ν for a given set of parameters of β, E_A and T_m. According to Figures 2 and 5 both R1 and R2 is lowered by approx. 40 °C upon doping. Plugging in the numbers of β, E_A and T_m in the above equation, one finds the prefactor to be increased approx. by one order of magnitude for both R1 and R2 after doping with Ti.

4 Conclusion

In this paper the effect on Ti-doping on the dehydrogenation kinetics of lithium aluminum hydride has been investigated. The decomposition of lithium aluminum hydride into trilithium hexahydridoaluminate (R1) has an apparent activation energies of approx. 85 kJ/mol and is insensitive to Ti-doping. The decomposition of trilithium hexahydridoaluminate into lithium hydride (R2) has apparent activation energies of 105 kJ/mol and is also insensitive to the doping. These results suggest that the effect of Ti-doping on the kinetic parameters of dehydrogenation of lithium aluminum hydride is mainly a prefactor effect. A possible explanation to this phenomenon could be that the addition of $TiCl_3$ increases the number of nucleation sites by introducing defects or vacancies e.g. by withdrawal of Li atoms from the $LiAlH_4$ lattice during the reduction of $TiCl_3$ to either metallic Ti on the surface or Ti incorporated into the lattice.

Acknowledgment

This work has received financial support from the The Danish Technical Research Council through the Center of Excellence *Towards a hydrogen based society*.

References

[1] B. Bogdanović, M. Schwickardi, J. Alloys Comps. 253-254 (1997) 1–9.

[2] J. A. Dilts, E. C. Ashby, Inorg. Chem. 11(6) (1972) 1230–1236.

[3] T. N. Dymova, D. P. Aleksandrov, V. N. Konoplev, T. A. Silina, A. S. Sizareva, Russ. J. Coord. Chem. 20 (4) (1994) 279–285.

[4] D. Blanchard, H. W. Brinks, B. C. Hauback, P. Norby, Mater. Sci. Eng. B. 108 (2004) 54–59.

[5] J. Chen, N. Kuriyama, Q. Xu, H. T. Takeshita, T. Sakai, J. Phys. Chem. B. 105 (2001) 11214–11220.

[6] V. P. Balema, V. K. Pecharsky, K. W. Dennis, J. Alloys Comps. 313 (2000) 69–74.

[7] H. W. Brinks, B. C. Hauback, P. Norby and H. Fjellvåg, J. Alloys Compds. 351 (2003) 222–227.

[8] J. K. Kang, J. Y. Lee, R. P. Muller, W. A. Goddard III, J. Chem. Phys. 121 (21) (2004) 10623–10633.

[9] E. Wiberg, E. Amberger, Hydrides of the elements of main groups I-IV, Elsevier publishing company, Amsterdam, 1971.

[10] M. D. Resan, M. Hampton, J. K. Lomness, D. K. Slattery, Int. J. Hydrogen Energy. DOI:10.1016/j.ijhydene.2004.12.008.

[11] V. P. Balema, K. W. Dennis, V. K. Pecharsky, Chem. Comm. (17) (2000) 1665–1666.

[12] V. P. Balema, J. W. Wiench, K. W. Dennis, M. Pruski, V. K. Pecharsky, J. Alloys Comps. 329 (2001) 108–114.

[13] H. W. Brinks, A. Fossdal, J. E. Fonneløp, B. C. Hauback, J. Alloys Comps. 397 (2005) 291–295.

[14] M. McCarthy Jr., J. N. Maycook, V. R. P. Verneker, J. Phys. Chem. 72 (1968) 4009–4014.

[15] D. Blanchard, H. W. Brinks, B. C. Hauback, P. Norby, J. Muller, J. Alloys Comps. DOI:10.1016/j.jallcom.2005.01.126.

[16] B. C. Hauback, H. Brinks, H. W. Fjellvåg, J. Alloys. Comps. 346 (2002) 184–189.

[17] C. M. Andrei, J. C. Walmsley, H. W. Brinks, R. Holmestad, B. C. Blanchard, D. Hauback, G. A. Botton, J. Phys. Chem. B. In press.

[18] L. Zaluski, A. Zaluska, J. O. Ström-Olsen, J. Alloys Comps. 290 (1999) 71–78.

[19] H. Kissinger, Anal. Chem. 29 (11) (1957) 1702–1706.

[20] H. W. Brinks, C. M. Jensen, S. S. Srinivasan, B. C. Hauback, D. Blanchard, K. Murphy, J. Alloys Comps. 376 (2004) 215–221.

[21] B. Bogdanović, M. Felderhoff, M. Germann, M. Härtel, A. Pommerin, F. Schüth, C. Weidenthaler, B. Zibrowius, J. Alloys and Comps. 350 (2003) 246–255.

[22] E. H. Majzoub, K. J. Gross, J. Alloys and Comps. 356-357 (2003) 363–367.

[23] M. Fichtner, P. Canton, O. Kircher, A. Léon, J. Alloys Comps. *In press* (2005). DOI:10.1016/j.jallcom.2004.12.178

[24] A. Andreasen, T. Vegge, A. S. Pedersen, J. Solid State Chem. *Accepted* (2005), DOI:10.1016/j.jssc.2005.09.027

[25] G. Sandrock, K. Gross, G. Thomas, C. Jensen, D. Meeker, S. Takara, J. Alloys Comps. 330-332 (2002) 686–701.

[26] W. Luo, K. J. Gross, J. Alloys Comps. 385 (2004) 224–231.

[27] G. Sandrock, K. J. Gross, G. Thomas, J. Alloys Comps. 339 (2002) 299–308.

[28] T. Kiyobayashi, S. S. Srinivasan, D. Sun, C. M. Jensen, J. Phys. Chem. A. 107 (39) (2003) 7671 –7674.

[29] O. Kircher, M. Fichtner, J. Alloys Comps. *In press* (2005). DOI:doi:10.1016/j.jallcom.2004.11.121

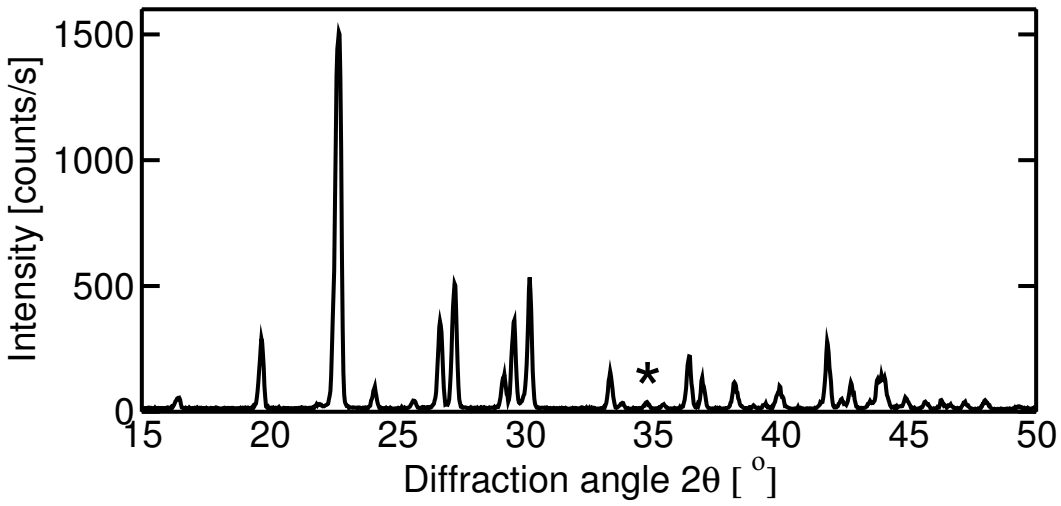

Fig. 1. XRPD pattern of as-received $LiAlH_4$.

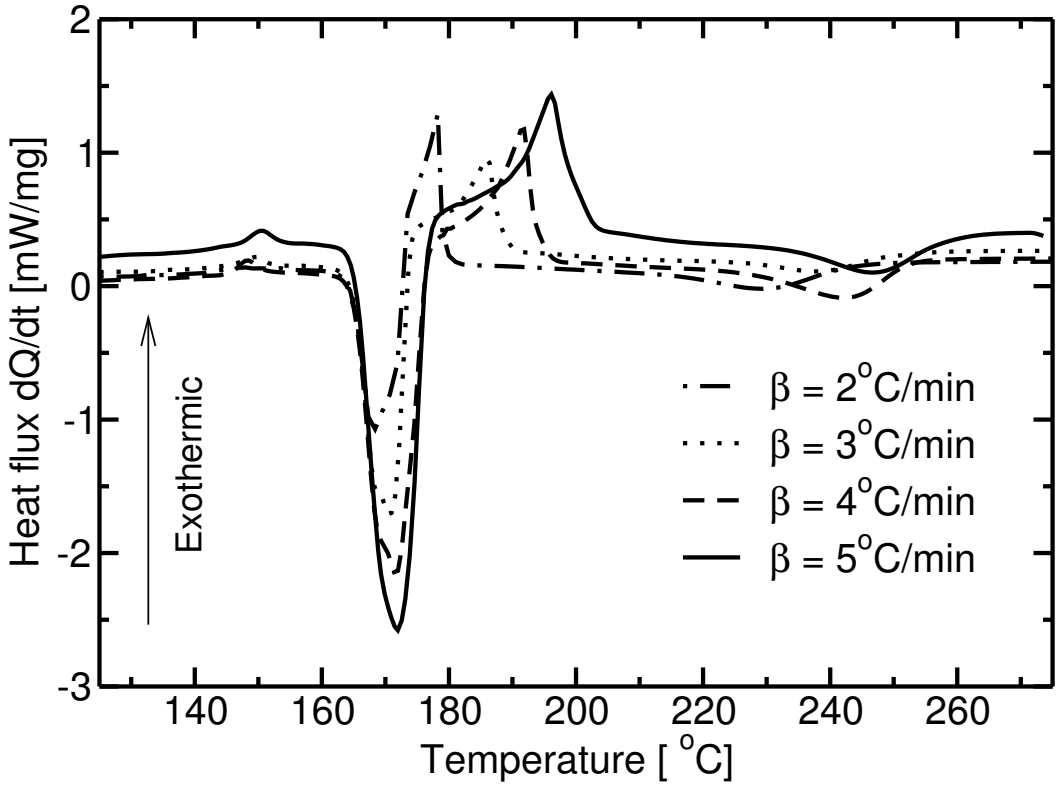

Fig. 2. Dehydrogenation of as-received $LiAlH_4$ investigated by DSC.

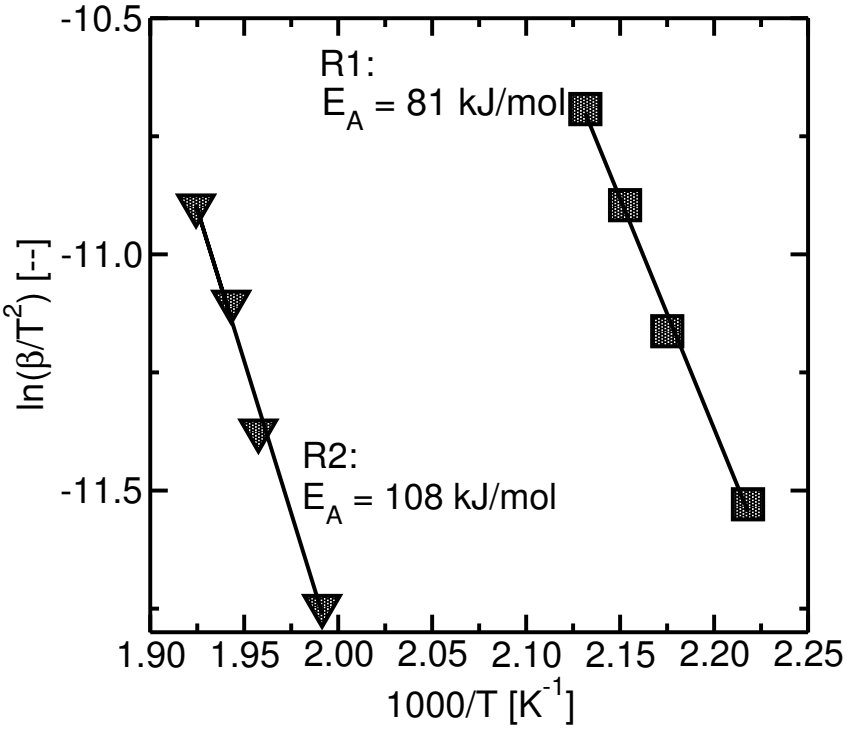

Fig. 3. Kissinger plot for dehydrogenation of as-received $LiAlH_4$.

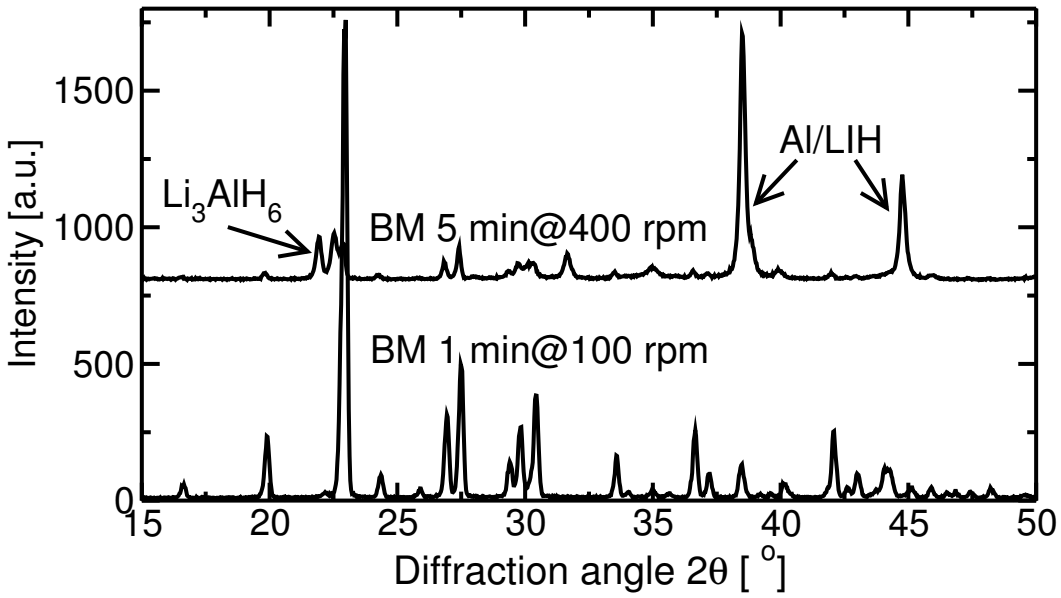

Fig. 4. XRPD of $LiAlH_4$ doped with 2 mole % $TiCl_3 \cdot 1/3AlCl_3$ ball milled for 1 min at 100 rpm and 5 min at 400 rpm, respectively.

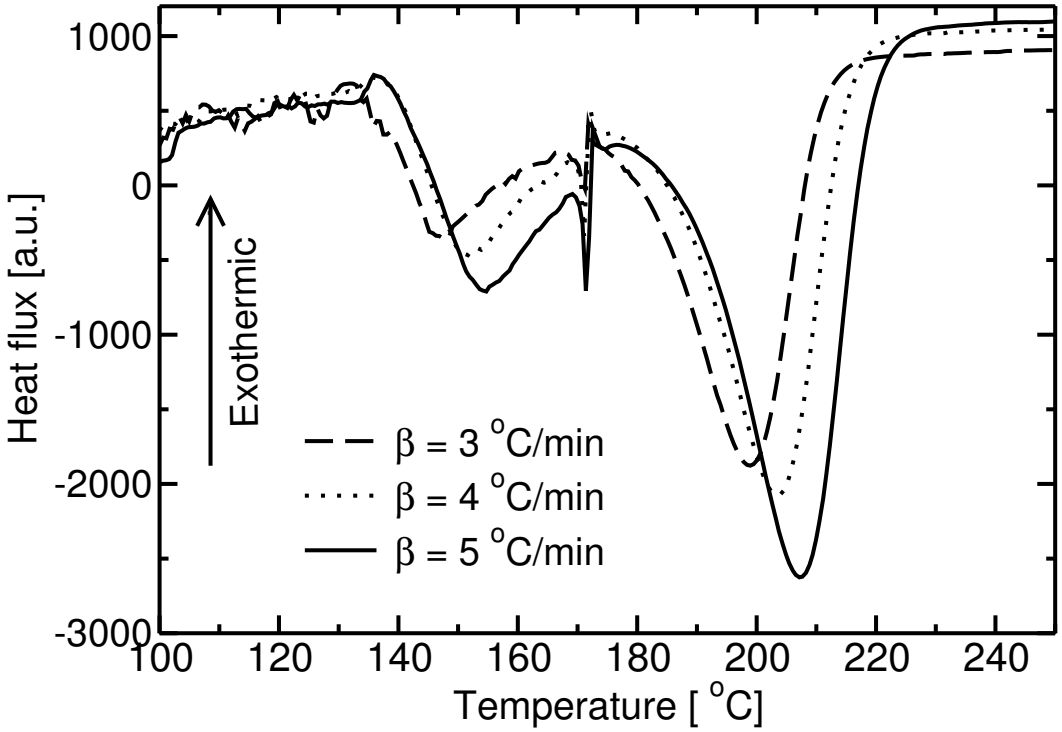

Fig. 5. DSC for $LiAlH_4$ doped with 2 mole % $TiCl_3 \cdot 1/3AlCl_3$ ball milled for 1 min at 100 rpm at different apllied heating rates.

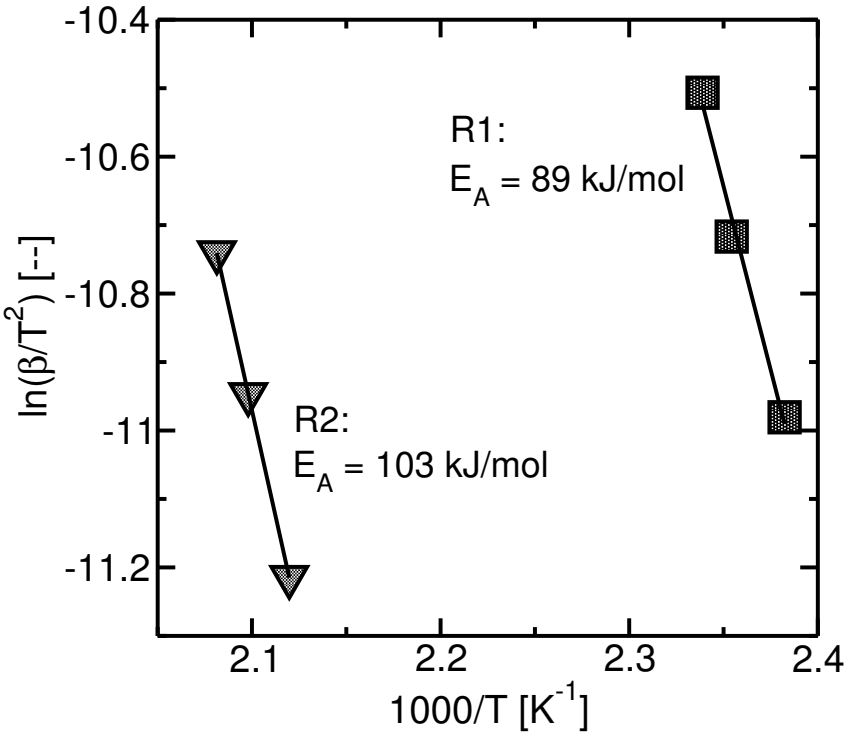

Fig. 6. Kisinger analysis for $LiAlH_4$ doped with 2 mole % $TiCl_3 \cdot 1/3AlCl_3$ ball milled for 1 min at 100 rpm.

Appendix G

Paper 7

Available online at www.sciencedirect.com
SCIENCE DIRECT®
Progress in Surface Science 77 (2004) 71–137
Progress in SURFACE SCIENCE
www.elsevier.com/locate/progsurf

Review

Analysis of simple kinetic models in heterogeneous catalysis

H. Lynggaard [a], A. Andreasen [b], C. Stegelmann [a], P. Stoltze [b,*]

[a] *Department of Chemistry and Applied Engineering Science, Aalborg University, Niels Bohrs Vej 8, DK-6700 Esbjerg, Denmark*
[b] *Department of Materials Research, Risø National Laboratory, Frederiksborgvej 399, DK-4000 Roskilde, Denmark*

Abstract

After a brief review of the theory of mechanisms and kinetics of catalytic reactions, we formulate a number of mechanisms for the hypothetical reaction $A_2 + 2B \rightarrow 2AB$ and derive analytic expressions for rate of reaction, activation enthalpy, and reaction orders.

After a discussion of a number of pitfalls in the analysis of measured kinetic data, we use the models with a range of realistic parameters to analyze degree of rate control, reaction orders, Arrhenius plots, the origin of volcano curves, and the origin compensation effects.

Abrupt changes in slope in the Arrhenius plot are traditionally interpreted as the signature of a change in rate limiting step or the onset of diffusion phenomena. One of the main results of our analysis is that simple mechanisms with realistic parameters display such signatures without a change in rate limiting step and in the absence of transport phenomena.

Finally, we extend our analysis to more complex reaction mechanisms by analysis of a number of important industrial reactions.

Keywords: Heterogeneous catalysis; Apparent activation energy; Arrhenius relationship; Micro-kinetic modeling; Compensation effect; Volcano curves; Ammonia synthesis; Ethylene epoxidation; Formaldehyde synthesis

* Corresponding author. Tel.: +45 79 12 7663 (Office); fax: +45 75 45 3643 (Department).
E-mail address: stoltze@aue.auc.dk (P. Stoltze).

0079-6816/$ - see front matter © 2004 Elsevier Ltd. All rights reserved.
doi:10.1016/j.progsurf.2004.09.001

Contents

1. Introduction

The study of kinetics in heterogeneous catalysis is very important in design of chemical reactors and in the study of mechanistic details. Traditional kinetic studies involves macro-kinetics where the catalyst activity is treated as a function of easily measured macroscopic quantities e.g. gas composition, pressure, and temperature. Macro-kinetics is very useful for different applications e.g. reactor design, quality control in catalyst production, catalyst selection, and studies of sintering and poisoning. Moreover, there are limits to the information that can be determined from experimental data by fitting empirical rate expressions. Very different kinetic expressions may fit data equally well, making it impossible to discriminate between different reaction mechanisms. Further it is dangerous to extrapolate macro-kinetic expressions, as differences between the real and the assumed mechanism may invalidate the expression outside the range of conditions the parameters are fitted to.

Another approach is micro-kinetic modeling [1–11] where the kinetics of the elementary reactions making up the reaction mechanism is mapped. The mapping between mechanism and macro-kinetics is unidirectional as macro-kinetics can be directly obtained from micro-kinetics, while the opposite is generally not the case. While a reaction mechanisms cannot be established from macro-kinetics alone, different in situ techniques may be used to establish a reaction mechanism by identifying key reaction intermediates. This is the reason why research in chemical kinetics in addition to the measurement of reaction rates also involves the study of reaction intermediates by computation, spectroscopy, isotopic labeling, etc. Once reliable data for key intermediates become available these data constraints the reaction mechanisms and thereby the predicted macroscopic kinetics. This approach enables us to discriminate between different reaction mechanism.

For a number of reactions in heterogeneous catalysis it is found experimentally that reaction orders and activation enthalpies varies with the reaction conditions [4,5,12–14]. Intuitively one might expect this to be caused by a complex reaction mechanism, e.g. a change in rate limiting step or reaction pathway, this expectation is, however, not necessarily correct. Kinetics in heterogeneous catalysis is highly non-linear due to different stoichiometry, vastly different rates among elementary steps, competition for active sites among intermediates, and non-linearity of rate constants in temperature. This means that even simple reaction mechanisms may lead to complicated macro-kinetics which display variable reaction orders and activation enthalpies.

After a brief review of the theory of mechanisms and kinetics for catalytic reactions we formulate a number of mechanisms for the hypothetical reaction $A_2 + 2B \rightleftharpoons 2AB$ and derive analytic expressions for rate of reaction, activation enthalpy, and reaction orders. For simplicity we have excluded selectivity issues and multiple overall reactions paths. We have chosen physical realistic parameters for the mechanisms. The quasi-equilibrium approximation is not generally valid and we examine its validity for the mechanisms and parameters we consider. We demonstrate by computations that simple reaction mechanisms may display varia-

tions in reaction orders and activation enthalpies. We give a brief overview of possible explanations for volcano curves from a kinetic point of view. Furthermore, our analysis suggests a simple and consistent explanation for the compensation effect. In the final section we compare our results with real reaction systems to emphasize the practical importance of our results.

2. Setting the scene

In this section we will give a brief exposition of the kinetics of catalytic reactions at solid surfaces. The competition for adsorption sites makes surface reactions more complicated than reactions in solution or in the gas phase, and surface reaction mechanisms with a few steps can have complicated kinetics. All the presented formalism is subject to the following reasonable assumptions:

- Reactions have Langmuir–Hinshelwood mechanisms.
- Elementary reactions are microscopically reversible.
- All sites are identical and the number of sites is constant under all reaction conditions.
- Each intermediate covers one site and no interactions exist between intermediates.

2.1. Reaction mechanism

The overall behavior of a reaction is determined by the underlying mechanism, consisting of a sequence of elementary steps. An elementary step is the most detailed, sensible description of a step.

For the reaction $A_2 + 2B \rightleftharpoons 2AB$ a mechanism may look like this

$$A_2 + 2* \rightleftharpoons 2A* \quad \text{(Step 1)}$$

$$B + * \rightleftharpoons B* \quad \text{(Step 2)}$$

$$A* + B* \rightleftharpoons AB* + * \quad \text{(Step 3)}$$

$$AB* \rightleftharpoons AB + * \quad \text{(Step 4)}$$

where $*$ is a surface site and $X*$ is a reaction intermediate on the surface. This mechanism is from now on called mechanism 0, and is used as an example in the remaining of this section.

The question if a step in a reaction is an elementary step obviously depend on how detailed the available information is. In mechanism 0 the first step could e.g. be split into the following two elementary steps:

$$A_2 + * \rightleftharpoons A_2* \quad \text{(Step 1a)}$$

$$A_2* + * \rightleftharpoons 2A* \quad \text{(Step 1b)}$$

A step, which consists of a sequence of two or more elementary steps is called a composite step.

To analyze reaction mechanism it is an advantage to define the stoichiometric number γ_r for each step which reflects how many turnovers step r has when the overall reaction proceeds once. This stoichiometric number can only be defined for mechanism without parallel steps. An investigation of mechanism 0 shows that steps 2–4 must proceed twice every time the overall reaction proceeds once. This mean that $\gamma_r = 2$ for these steps, whereas step 1 only proceed once which gives $\gamma_r = 1$ for this step.

The stoichiometric coefficients ν_{ri} for species i in step r is defined as the number of molecules produced in the step. For step 1 in mechanism 0 the stoichiometric coefficient for A_2 will be $\nu_{1A_2} = -1$ since one molecule is used, with respect to $A*$ and $*$ two molecules are produced and used, respectively, which leads to $\nu_{1A*} = 2$ and $\nu_{1*} = -2$.

For mechanism 0 the overall stoichiometric matrix [2,15,16] can be written as

Step	ν_{rA_2}	ν_{rB}	ν_{rAB}	ν_{rA*}	ν_{rB*}	ν_{rAB*}	ν_{r*}	γ_r
1	−1	0	0	2	0	0	−2	1
2	0	−1	0	0	1	0	−1	2
3	0	0	0	−1	−1	1	1	2
4	0	0	1	0	0	−1	1	2
Overall	−1	−2	2	0	0	0	0	

2.1.1. Equilibrium expressions

The equilibrium of the overall reaction can be written as

$$K_g = \frac{\left(\frac{p_{AB}}{p^{\ominus}}\right)^2}{\left(\frac{p_{A_2}}{p^{\ominus}}\right)\left(\frac{p_B}{p^{\ominus}}\right)^2} \tag{1}$$

where K_g is a equilibrium constant of the net reaction, p_X is the partial pressure of X, and $p^{\ominus}$ is the thermodynamic reference pressure. In a similar manner the equilibrium of each step can be defined

$$K_1 = \frac{\theta_{A*}^2}{\frac{p_{A_2}}{p^{\ominus}}\theta_*^2} \tag{2}$$

$$K_2 = \frac{\theta_{B*}}{\frac{p_B}{p^{\ominus}}\theta_*} \tag{3}$$

$$K_3 = \frac{\theta_{AB*}\theta_*}{\theta_{A*}\theta_{B*}} \tag{4}$$

$$K_4 = \frac{\frac{p_{AB}}{p^{\ominus}}\theta_*}{\theta_{AB*}} \tag{5}$$

where K_i is the equilibrium constant for step i, and θ_i is the coverage of species i. All coverages must sum up to one

$$1 = \theta_* + \theta_{A*} + \theta_{B*} + \theta_{AB*} \tag{6}$$

It can be seen from the equilibrium equations that each species is raised to the power of their stoichiometric coefficient in the overall reaction. Furthermore, dividing with the reference pressure and using coverages ensures that the equilibrium constants are dimensionless. This is in agreement with the Van't Hoff equation

$$K_i = \exp\left(-\frac{\Delta G_i^{\ominus}}{RT}\right) = \exp\left(\frac{\Delta S_i^{\ominus}}{R}\right)\exp\left(-\frac{\Delta H_i^{\ominus}}{RT}\right) \tag{7}$$

where $\Delta G_i^{\ominus}$, $\Delta S_i^{\ominus}$ and $\Delta H_i^{\ominus}$ are the standard Gibbs free energy, the standard entropy, and the standard enthalpy respectively for reaction step i.

The approach to equilibrium for an elementary step can be expressed by β

$$\beta_1 = \frac{\theta_{A*}^2}{K_1\frac{p_{A_2}}{p^{\ominus}}\theta_*^2} \tag{8}$$

$$\beta_2 = \frac{\theta_{B*}}{K_2\frac{p_B}{p^{\ominus}}\theta_*} \tag{9}$$

$$\beta_3 = \frac{\theta_{AB*}\theta_*}{K_3\theta_{A*}\theta_{B*}} \tag{10}$$

$$\beta_4 = \frac{\frac{p_{AB}}{p^{\ominus}}\theta_*}{K_4\theta_{AB*}} \tag{11}$$

Likewise for the overall reaction

$$\beta_g = \frac{1}{K_g}\frac{\left(\frac{p_{AB}}{p^{\ominus}}\right)^2}{\left(\frac{p_{A_2}}{p^{\ominus}}\right)\left(\frac{p_B}{p^{\ominus}}\right)^2} \tag{12}$$

The approach to equilibrium for the overall reaction has to be defined with respect to the same overall reaction as the stoichiometric number, we will give a brief explanation for this later.

2.1.2. Reaction rate

The rate of a step is calculated as a turnover frequency i.e. as a number of molecules produced per site per second. For elementary steps the rates can be written as

$$r_1 = k_{1+}\frac{p_{A_2}}{p^{\ominus}}\theta_*^2 - k_{1-}\theta_{A*}^2 \tag{13}$$

$$r_2 = k_{2+}\frac{p_B}{p^{\ominus}}\theta_* - k_{2-}\theta_{B*} \tag{14}$$

$$r_3 = k_{3+}\theta_{B*}\theta_{A*} - k_{3-}\theta_{AB}\theta_* \tag{15}$$

$$r_4 = k_{4+}\theta_{AB*} - k_{4-}\frac{p_{AB}}{p^{\ominus}}\theta_* \tag{16}$$

where r_i is the rate of step i, k_{i+} and k_{i-} is rate constant of step i in the forward and backward direction, respectively. At equilibrium $r = 0$, which means that the rate expression can be rearranged e.g. Eq. (13) becomes

$$\frac{k_{1+}}{k_{1-}} = \frac{\theta_{A*}^2}{\frac{p_{A_2}}{p^{\ominus}}\theta_*^2} \tag{17}$$

The right-hand side of this equation is equal to the right-hand side of Eq. (2) i.e.

$$K_1 = \frac{k_{1+}}{k_{1-}} \tag{18}$$

As the rate and equilibrium constants are independent of composition, this relation must hold universally. This means that the rate of step 1 can be expressed as

$$r_1 = k_{1+}\frac{p_{A_2}}{p^{\ominus}}(1-\beta_1)\theta_*^2 \tag{19}$$

2.1.3. Rate constant

The rate constants, k_r are only constant in the sense that they are independent of pressure and composition. However, they have a strong temperature dependency and for elementary reactions the rate constant will have an Arrhenius form

$$k_r = A_r\exp\left(-\frac{H_r^{\ddagger}}{RT}\right) \tag{20}$$

where A_r is the preexponential factor and $H_r^{\ddagger}$ is the activation enthalpy for step r.

The activation enthalpy can be calculated from k as

$$H_r^{\ddagger} = RT^2\frac{d\ln k_r}{dT} \tag{21}$$

The activation enthalpies and the enthalpy of reaction are related by

$$H_{r-}^{\ddagger} = \Delta H_r + H_{r+}^{\ddagger} \tag{22}$$

2.2. Rate approximations

The full solution of the reaction system is given by Eqs. (13)–(16), and the rate can be computed by evaluating these expressions. However, the equations will often lead to a numerical nightmare, and a number of approximations can be used in order to simplify the solution.

2.2.1. The steady-state approximation (SSA)

Under steady-state conditions there can be no accumulation of intermediates

$$\frac{\mathrm{d}\theta_i}{\mathrm{d}t} = 0 \tag{23}$$

With respect to mechanism 0 we can see that two A* are formed in step 1 and one A* is used in step 3 which means that $r_1 = 2r_3$. If the same analysis is made with respect to B* and AB* we get $r_2 = r_3$ and $r_3 = r_4$, respectively. This means that Eqs. (13)–(16) has to be solved with the restriction that $r_1 = 2r_2 = 2r_3 = 2r_4$. At steady state this is the exact solution, and the advantage is that the equations are easier to solve than the full solution. Furthermore, no assumption is made with regard to the magnitude of the coverages or to the relative rates of the steps. Some disadvantages are that all information on the transient behavior is eliminated and that the equations may still be difficult to solve and analyze.

2.2.2. The quasi-equilibrium approximation (QEA)

If one of the steps is much slower than all other steps, the fast steps can be approximated by equilibrium expressions while the slow step is assigned a rate. This slow step is termed the rate limiting step.

To give an example of how a QEA is used a rate expression for mechanism 0 with step 3 as rate limiting step is derived. Steps 1, 2 and 4 are approximated as equilibria

$$\theta_{\mathrm{A}*} = K_1^{\frac{1}{2}} \left(\frac{p_{\mathrm{A}_2}}{p^{\ominus}}\right)^{\frac{1}{2}} \theta_* \tag{24}$$

$$\theta_{\mathrm{B}*} = K_2 \frac{p_{\mathrm{B}}}{p^{\ominus}} \theta_* \tag{25}$$

$$\theta_{\mathrm{AB}*} = \frac{1}{K_4} \frac{p_{\mathrm{AB}}}{p^{\ominus}} \theta_* \tag{26}$$

When Eqs. (24)–(26) are substituted into Eq. (6), we find

$$\theta_* = \frac{1}{1 + K_1^{\frac{1}{2}} \left(\frac{p_{\mathrm{A}_2}}{p^{\ominus}}\right)^{\frac{1}{2}} + K_2 \frac{p_{\mathrm{B}}}{p^{\ominus}} + \frac{1}{K_4} \frac{p_{\mathrm{AB}}}{p^{\ominus}}} \tag{27}$$

This equation can be solved and the result is used in Eqs. (24)–(26) to find all coverages. The rate of the slow step is given by

$$r_3 = k_3 \theta_{\mathrm{A}*} \theta_{\mathrm{B}*} - \frac{k_3}{K_3} \theta_{\mathrm{AB}*} \theta_* \tag{28}$$

$$= k_3 K_1^{\frac{1}{2}} K_2 \left(\left(\frac{p_{\mathrm{A}_2}}{p^{\ominus}}\right)^{\frac{1}{2}} \frac{p_{\mathrm{B}}}{p^{\ominus}} - \frac{1}{K_g} \frac{p_{\mathrm{AB}}}{p^{\ominus}} \right) \theta_*^2 \tag{29}$$

where $K_g = K_1^{\frac{1}{2}} K_2 K_3 K_4$ is the overall equilibrium constant.

Using β_g this can be rewritten as

$$r = k_3 K_1^{\frac{1}{2}} K_2 \left(\frac{p_{\mathrm{A}_2}}{p^{\ominus}}\right)^{\frac{1}{2}} \frac{p_{\mathrm{B}}}{p^{\ominus}} \left(1 - \beta_g^{\frac{1}{2}}\right) \theta_*^2 \tag{30}$$

This short hand notation for rate expression we call "the reduced rate expression". As it can be seen β_g is raised to the power of $\frac{1}{2}$. At closer inspection it turns out that the numerator is the stoichiometric number γ_r of the rate limiting step. The reason why the rate has this dependence on β_g, is that the rate must be independent of how the net reaction is defined. This shows why β_g and γ_r has to be defined with respect to the same overall reaction otherwise the rate would depend on how we defined the net reaction. It can be shown that QEA expressions generally has this dependence on the stoichiometric number.

The great advantage of QEA is that it provides a significant simplification and that analytical solution becomes feasible for coverages, rates, reaction orders, apparent activation enthalpies, etc. A disadvantage is that the approximation cannot be used if more than one step is rate limiting.

2.2.3. Hybrid steady state approximation (HSSA)

In some cases it can be an advantage to make a hybrid between the SSA and the QEA [4,17,18] As an example, we will derive the solution for mechanism 0 when both steps 1 and 3 are slow. Steps 2 and 4 are treated as equilibria

$$\theta_{\mathrm{B}*} = K_2 \frac{p_{\mathrm{B}}}{p^{\ominus}} \theta_* \tag{31}$$

$$\theta_{\mathrm{AB}*} = \frac{1}{K_4} \frac{p_{\mathrm{AB}}}{p^{\ominus}} \theta_* \tag{32}$$

The steady-state approximation is used for A* i.e. $r_1 = 2r_3$

$$k_1 \frac{p_{\mathrm{A}_2}}{p^{\ominus}} \theta_*^2 - \frac{k_1}{K_1} \theta_{\mathrm{A}*}^2 = 2k_3 \theta_{\mathrm{A}*} \theta_{\mathrm{B}*} - 2\frac{k_3}{K_3} \theta_{\mathrm{AB}*} \theta_* \tag{33}$$

This equation is then used together with Eqs. (31) and (32) in Eq. (6). This results in a second-order polynomial in $\theta_{\mathrm{A}*}$ and can be solved as such. The resulting value for $\theta_{\mathrm{A}*}$ is then used to calculate θ_*, $\theta_{\mathrm{B}*}$, $\theta_{\mathrm{AB}*}$, and r.

The advantage of this approach is that the rate can be solved easily, and that a change in rate limiting step can be described. However, a detailed analysis of the model is quite complicated.

2.3. Analytic tools for rate expressions

When experimental data are evaluated the results are conventionally expressed in terms of e.g. activation enthalpy and reaction orders. So if we want to compare a rate expression with experimental data we need to have some analytic tools that can determine these parameters from rate expressions.

2.3.1. Apparent activation enthalpy

For an elementary reaction the activation enthalpy is the energy barrier the system must cross during the reaction. This activation enthalpy may be determined from experimental data by an Arrhenius plot, i.e. a plot of $\ln k$ vs. $1/T$.

For a composite reaction one can obviously also plot measured data in an Arrhenius plot and in most cases an activation enthalpy may, formally, be determined from this plot.

In the simplest case a composite reaction can be described by the QEA. From this we can determine the apparent activation enthalpy analytically as

$$H^{\ddagger}_{\mathrm{app}} = RT^2 \frac{\mathrm{d}\ln r_+}{\mathrm{d}T} \tag{34}$$

and the apparent prefactor can be found as

$$\ln A = \ln r_+ + \frac{H^{\ddagger}_{\mathrm{app}}}{RT} \tag{35}$$

For the QEA derived in Section 2.2.2 the forward rate is

$$r_+ = k_3 K_2 K_1^{\frac{1}{2}} \left(\frac{p_{\mathrm{A}_2}}{p^{\ominus}}\right)^{\frac{1}{2}} \frac{p_{\mathrm{B}}}{p^{\ominus}} \theta_*^2 \tag{36}$$

By straightforward calculation we find

$$H^{\ddagger}_{\mathrm{app}} = RT^2 \left(\frac{\mathrm{d}\ln(k_3)}{\mathrm{d}T} + \frac{\mathrm{d}\ln(K_2)}{\mathrm{d}T} + \cdots + \frac{\mathrm{d}\ln(\theta_*^2)}{\mathrm{d}T}\right) \tag{37}$$

Since rate constants and equilibrium constants can be described by Arrhenius and Van't Hoff expressions, respectively, the first part can be evaluated

$$H^{\ddagger}_{\mathrm{app}} = H^{\ddagger}_3 + 0.5\Delta H_1 + \Delta H_2 + RT^2 \frac{\mathrm{d}\ln(\theta_*^2)}{\mathrm{d}T} \tag{38}$$

This means that the only part left to evaluate is the coverage dependency

$$RT^2 \frac{\mathrm{d}\ln(\theta_*^2)}{\mathrm{d}T} = 2RT^2 \frac{\mathrm{d}}{\mathrm{d}T} \ln\left(\frac{1}{1 + K_1^{\frac{1}{2}}\left(\frac{p_{\mathrm{A}_2}}{p^{\ominus}}\right)^{\frac{1}{2}} + K_2 \frac{p_{\mathrm{B}}}{p^{\ominus}} + \frac{1}{K_4}\frac{p_{\mathrm{AB}}}{p^{\ominus}}}\right) \tag{39}$$

$$= -2RT^2\theta_* \frac{\mathrm{d}}{\mathrm{d}T}\left(1 + K_1^{\frac{1}{2}}\left(\frac{p_{\mathrm{A}_2}}{p^{\ominus}}\right)^{\frac{1}{2}} + K_2 \frac{p_{\mathrm{B}}}{p^{\ominus}} + \frac{1}{K_4}\frac{p_{\mathrm{AB}}}{p^{\ominus}}\right) \tag{40}$$

By straightforward calculation the result can be found

$$H^{\ddagger}_{\mathrm{app}} = H^{\ddagger}_3 + 0.5\Delta H_1 + \Delta H_2 - \Delta H_1\theta_{\mathrm{A}*} - 2\Delta H_2\theta_{\mathrm{B}*} + 2\Delta H_4\theta_{\mathrm{AB}*} \tag{41}$$

2.3.2. Reaction orders

The reaction orders are defined from a power law type of expression. For mechanism 0 this would be

$$r_+ = k_{\mathrm{app}} \left(\frac{p_{\mathrm{A}_2}}{p^{\ominus}}\right)^{\alpha_{\mathrm{A}_2}} \left(\frac{p_{\mathrm{B}}}{p^{\ominus}}\right)^{\alpha_{\mathrm{B}}} \left(\frac{p_{\mathrm{AB}}}{p^{\ominus}}\right)^{\alpha_{\mathrm{AB}}} \tag{42}$$

where α_i is the reaction order of species i and k_{app} is an apparent rate constant.

For elementary reactions the reaction orders are evidently integers. For composite reactions the reaction orders may be found by fitting measured data, and are frequently found to be non-integer.

From an analytical expression for r_+, the reaction orders may be calculated as

$$\alpha_i = \frac{\partial \ln(r_+)}{\partial \ln\left(\frac{p_i}{p^{\ominus}}\right)} \tag{43}$$

We use the QEA rate expression derived in Section 2.2.2 to find the reaction order in A_2

$$\alpha_{\mathrm{A}_2} = \frac{\partial \ln\left(k_3 K_2 K_1^{\frac{1}{2}} \left(\frac{p_{\mathrm{A}_2}}{p^{\ominus}}\right)^{\frac{1}{2}} \frac{p_{\mathrm{B}}}{p^{\ominus}} \theta_*^2\right)}{\partial \ln\left(\frac{p_{\mathrm{A}_2}}{p^{\ominus}}\right)} \tag{44}$$

$$= \frac{1}{2} + \frac{\partial \ln\left(\theta_*^2\right)}{\partial \ln\left(\frac{p_{\mathrm{A}_2}}{p^{\ominus}}\right)} \tag{45}$$

$$= \frac{1}{2} - 2\frac{p_{\mathrm{A}_2}}{p^{\ominus}}\theta_* \frac{\partial\left(1 + K_1^{\frac{1}{2}}\left(\frac{p_{\mathrm{A}_2}}{p^{\ominus}}\right)^{\frac{1}{2}} + K_2\frac{p_{\mathrm{B}}}{p^{\ominus}} + \frac{1}{K_4}\frac{p_{\mathrm{AB}}}{p^{\ominus}}\right)}{\partial\left(\frac{p_{\mathrm{A}_2}}{p^{\ominus}}\right)} \tag{46}$$

The result is

$$\alpha_{\mathrm{A}_2} = \frac{1}{2} - \theta_{\mathrm{A}*} \tag{47}$$

2.3.3. Degree of rate control

At steady state there is no net production of any intermediates. This forces all steps to have the same value of r_i/γ_i, where r_i is the net rate for step i and γ_i is the stoichiometric number for step i. The stoichiometry forces all steps to proceed with net rates that are closely related, and it may seem misleading to talk about *fast* and *slow* steps. However, only the net rates are closely related. Some steps have high rates both in the forward and backward direction and these steps are near equilibrium. Other steps have negligible forward and backward rates. The rate of the net reaction is controlled by the latter steps. To investigate which steps are determining the rate, the degree of rate control ($X_{\mathrm{RC},i}$) [7] of step i for the overall rate is introduced as

$$X_{\mathrm{RC},i} = \frac{k_i}{r}\frac{\partial r}{\partial k_i} = \frac{\partial \ln(r)}{\partial \ln(k_i)} \quad \text{for constant } K_i \tag{48}$$

The larger numeric value of $X_{RC,i}$ the larger degree of rate control does step i exhibit on the overall rate. Furthermore, the sum of all $X_{RC,i}$ is 1. Rate limiting steps have $X_{RC,i} > 0$, quasi-equilibrated steps have $X_{RC,i} \sim 0$ and inhibiting steps have $X_{RC,i} < 0$. For a mechanism with a single, rate limiting step, the rate limiting step will have $X_{RC,i} \sim 1$ while all other steps have $X_{RC,i} \sim 0$.

2.4. Reactors

The rate of a reaction may be determined in a flow reactor. The composition of the gas gradually changes as the gas flows through the reactor. Rate measurements are frequently made in a reactor, which approximates the ideal isothermal plug-flow reactor and the discussion below will be based on that reactor. Other types of reactors may be used in rate measurements, but we will not pursue this topic further here.

2.4.1. Differential reactor

The change of concentration in a differential reactor is so small that the rate may be regarded constant

$$r = \frac{F(y_{ej} - y_{ij})}{\nu_j m a \delta} \tag{49}$$

where F is the flow [mol s^{-1}], y_{ij} and y_{ej} is the inlet and outlet mole fraction for gas j, ν_j is the stoichiometric coefficient for gas j in the net reaction, m is the mass of the catalyst [kg], a is the specific area [m^2/kg], and δ is the density of sites for the catalyst [mol/m^2] The rate of the overall reaction may be calculated from concentrations of any of the reactants or products.

The advantage of the differential reactor is that the analysis of the results are straightforward. Unfortunately it can only be used at low conversions resulting in a limited applicability.

2.4.2. Integral reactor

In an integral reactor a significant conversion takes place and the reaction rate varies through the reactor. Therefore the conversion is calculated by integration of the rate through the reactor.

We use the definition of r from Eq. (49) and consider a small slice of mass dm during the time from t to $t + \mathrm{d}t$. The mass balances for this slice are

Gas	In	+	Produced	=	Out
1	$Fy_1\,\mathrm{d}t$	+	$r\nu_1 a\delta\,\mathrm{d}m\,\mathrm{d}t$	=	$(F+\mathrm{d}F)(y_1+\mathrm{d}y_1)\mathrm{d}t$
...	...	+	...	=	...
n	$Fy_n\,\mathrm{d}t$	+	$r\nu_n a\delta\,\mathrm{d}m\,\mathrm{d}t$	=	$(F+\mathrm{d}F)(y_n+\mathrm{d}y_n)\mathrm{d}t$
sum	$F\,\mathrm{d}t$	+	$r\sum_i \nu_i a\delta\,\mathrm{d}m\,\mathrm{d}t$	=	$(F+\mathrm{d}F)\mathrm{d}t$

The solutions are

$$\begin{aligned}
\frac{\mathrm{d}F}{\mathrm{d}m} &= r\sum_i \nu_i a\delta \\
\frac{\mathrm{d}y_1}{\mathrm{d}m} &= r\frac{\nu_1 - y_1\sum_i \nu_i}{F}a\delta \\
\ldots &= \ldots \\
\frac{\mathrm{d}y_n}{\mathrm{d}m} &= r\frac{\nu_n - y_n\sum_i \nu_i}{F}a\delta
\end{aligned} \tag{50}$$

We can thus calculate the flow, composition, coverages and rate at all positions in the reactor by integration of these equations starting from the flow and composition at the inlet. However, even if we may only be interested in the outlet concentration for one of the gases, the differential equations are coupled and integration can only be performed for the full system of equations.

The advantage of the integral reactor is that there are no restrictions on the change in concentration from inlet to outlet. However, the analysis of the data is rather laborious.

3. Kinetic models

In this section we propose a number of symbolic reaction mechanism for which different kinetic models are derived. All the kinetic models are based on the overall gas phase reaction

$$A_2 + 2B \rightleftharpoons 2AB \tag{51}$$

and the approach to equilibrium is given by Eq. (12).

The presented kinetic models are used in computer simulations to investigate the validity of the QEA compared to SSA and HSSA; variations in apparent activation enthalpies; variations in reaction orders; volcano curves; and compensation effect. The mechanisms and models have been chosen in such a manner that they cover a wide range of possibilities to ensure that the conclusions drawn in this manuscript are general. For all QEA models analytical reaction orders and apparent activation enthalpies are derived. Details of each kinetic model such as rate expressions, coverages, apparent activation enthalpy, reaction orders, etc. are summarized in Appendix A.

3.1. Mechanism 1

Model 1 is a mechanism which has been used in the literature [19] to analyze reactions where the dissociation of a reactant is rate limiting.

$$A_2 + 2* \rightleftharpoons 2A* \quad \text{(Step 1)}$$

$$A* + B \rightleftharpoons AB + * \quad \text{(Step 2)}$$

On the basis of this mechanism we have made three different kinetic models with different rate limiting steps

Model name	Rate limiting steps	Model type
Model 1a	Step 1: Direct dissociation	QEA
Model 1b	Step 2: Adsorbate-gas reaction	QEA
Model 1c	Steps 1 and 2	SSA

The reduced rate expressions for models 1a and 1b are

$$r_{1a} = k_1 \frac{p_{A_2}}{p^{\ominus}} (1-\beta)\theta_*^2 \tag{52}$$

$$r_{1b} = k_2 K_1^{\frac{1}{2}} \frac{p_{A_2}^{\frac{1}{2}}}{p^{\ominus}} \frac{p_B}{p^{\ominus}} \left(1-\beta^{\frac{1}{2}}\right)\theta_* \tag{53}$$

By comparing these expressions it is obvious that model 1a has a stronger dependence on the number of free sites. This is caused by differences in the number of sites used in the rate limiting step, two sites in 1a and one site in 1b. As mentioned in Section 2 the rate dependence on β is determined by the stoichiometric number of the slow step.

Model 1c is a SSA model and is remarkable in the sense that it has an easy computable analytical solution. This is unusual for SSA models and can be explained by the unusual low number of steps and the simple site balance in mechanism 1.

3.2. Mechanism 2

Mechanism 2 is the mechanism used as an example in Section 2.

$$A_2 + 2* \rightleftharpoons 2A* \quad \text{(Step 1)}$$
$$B + * \rightleftharpoons B* \quad \text{(Step 2)}$$
$$A* + B* \rightleftharpoons AB** + * \quad \text{(Step 3)}$$
$$AB* \rightleftharpoons AB + * \quad \text{(Step 4)}$$

The models based on this mechanism are

Model name	Rate limiting steps	Model type
Model 2a	Step 1: Direct dissociation	QEA
Model 2b	Step 3: Surface reaction	QEA
Model 2c	Step 4: Desorption	QEA
Model 2d	Steps 1 and 3	HSSA

The reduced rate expression for the first three models are

$$r_{2a} = k_1 \frac{p_{A_2}}{p^{\ominus}} (1-\beta)\theta_*^2 \tag{54}$$

$$r_{2b} = k_3 K_1^{\frac{1}{2}} K_2 \frac{p_{A_2}^{\frac{1}{2}}}{p^{\ominus}} \frac{p_B}{p^{\ominus}} \left(1-\beta^{\frac{1}{2}}\right)\theta_*^2 \tag{55}$$

$$r_{2c} = k_4 K_1^{\frac{1}{2}} K_2 K_3 \frac{p_{A_2}^{\frac{1}{2}}}{p^{\ominus}} \frac{p_B}{p^{\ominus}} \left(1-\beta^{\frac{1}{2}}\right)\theta_* \tag{56}$$

Model 2a is similar to model 1a as both models have dissociation of A_2 as rate limiting. The main difference between these models is that 2a contains more adsorbates than 1a, and in the limit where θ_{B*} and θ_{AB*} goes to zero, the expressions will give the same result. This means that the last three steps can be lumped together in that limit without changing the kinetics.

Model 2b is similar to model 1b, except that steps 2, 3 and 4 in model 2b is lumped into a single step (step 2) in model 1b. This has important consequences as two active sites are required in the rate limiting step in model 2b compared to one for model 1b. Even in the limit where θ_{B*} and θ_{AB*} go to zero, model 2b still differs from model 1b. This shows that fundamentally kinetic differences exist between surface reactions and adsorbate-gas reactions, and that lumping steps into a single composite step may change the kinetics of the reaction significantly.

3.3. Mechanism 3

This mechanism is a further development of the previous mechanism adding a precursor to the dissociation of A_2

$$A_2 + * \rightleftharpoons A_2* \quad \text{(Step 1)}$$
$$A_2* + * \rightleftharpoons 2A* \quad \text{(Step 2)}$$
$$B + * \rightleftharpoons B* \quad \text{(Step 3)}$$
$$A* + B* \rightleftharpoons AB** + * \quad \text{(Step 4)}$$
$$AB* \rightleftharpoons AB + * \quad \text{(Step 5)}$$

The kinetic models based on this mechanism are

Model name	Rate limiting steps	Model type
Model 3a	Step 2: Surface dissociation	QEA
Model 3b	Step 3: Adsorption	QEA
Model 3c	Step 5: Desorption	QEA
Model 3d	Steps 3 and 5	HSSA

The reduced rate expression for model 3a and 3c are

$$r_{3a} = k_2 K_1 \frac{p_{A_2}}{p^{\ominus}} (1-\beta)\theta_*^2$$
$$r_{3c} = k_5 K_1^{\frac{1}{2}} K_2 \frac{1}{2} K_3 K_4 \frac{p_{A_2}^{\frac{1}{2}}}{p^{\ominus}} \frac{p_B}{p^{\ominus}} \left(1-\beta^{\frac{1}{2}}\right)\theta_* \quad (57)$$

The major difference between r_{3a} and the equivalent rate expressions for mechanism 1 and 2 (r_{2a} and r_{1a}) is that the forward rate in model 3a depends on the stability of A_2*. This will have essentially no implication for the rate if the coverage of θ_{A_2*} is low.

3.4. Model parameters

Although the models are hypothetical, physically reasonable parameters are required in the computer simulations to ensure that our conclusions are valid. Enthalpies and entropies of the various species are chosen in such manner that, adsorptions are exothermic and accompanied by a decrease in entropy. Furthermore, the surface reaction is chosen to be exothermic with a decrease in entropy. The chosen thermodynamic parameters used in this manuscript for the kinetic models are given in Table 1 unless stated otherwise in the text.

Transition State Theory (TST) predicts a prefactor of about 10^{13} s^{-1} for first-order reactions, while experimental prefactors for surface reactions vary from 10^{10}–10^{16} s^{-1} [20]. Prefactors have generally been chosen in that interval. Activation enthalpies are given values in the range 70–95 kJ/mol. The chosen parameters can be seen in Table 2.

3.5. Summary

In this section we have presented a number of kinetic models representing a wide range of possible reaction mechanisms for the reaction $A_2 + 2B \rightleftharpoons 2AB$. These models will be investigated further by computer simulations in the remaining of this manuscript.

Table 1
Parameters for the models

Species	S_i [J/(mol K)]	H_i [J/mol]
A_2	210	6000
A_2*	160	−5000
A*	30	−42,000
B	250	63,000
B*	195	25,000
AB	275	−30,000
AB*	210	−80,000

H_i and S_i is the enthalpy and entropy, respectively, of species i.

Table 2
Arrhenius parameters for the models

Step	A_i [s^{-1}]	$H_i^{\ddagger}$ [kJ/(mol K)]
Mechanism 1		
1	5×10^{10}	80
2	5×10^{11}	95
Mechanism 2		
1	1×10^{11}	80
3	5×10^{11}	95
4	5×10^{11}	95
Mechanism 3		
2	5×10^{10}	80
3	5×10^{10}	70
5	5×10^{13}	90

A_i and $H_i^{\ddagger}$ is the prefactor and activation enthalpy of step i, respectively.

In all the examined models the net rate depend on β through $(1-\beta)$ or $(1-\beta^{\frac{1}{2}})$. However, a detailed analysis is required in each case to determine which of the factors the net rate depends on. This is a serious complication in the determination of the apparent activation enthalpy from experimental data, Section 6.4.2.

Comparing rate expressions for mechanisms 1–3 we have observed that simplifying mechanisms by lumping elementary steps is problematic. In some cases, the simplified mechanism will have the same kinetics as the original mechanism in the appropriate limits. In other cases the simplified mechanism has different kinetics than the original mechanism in all cases. A detailed analysis of this problem is beyond the scope of the manuscript and it will not be examined further.

4. Analysis of the quasi-equilibrium approximation

In Section 2 we derived kinetic models using the QEA, SSA, and HSSA. It is clear from these derivations that it is much simpler to derive and analyze QEA models than SSA and HSSA models. However, in each case it must be established if the QEA is a valid approximation. In this section we compare the results of two QEA models 2a and 2b with their equivalent HSSA solution model 2d.

4.1. Validity

To proceed we define a measure, q_i, of how much a QEA model deviates from the HSSA model:

$$q_i = \frac{r_{QEA_i}}{r_{HSSA}} \quad (58)$$

where r is the net rate for model i.

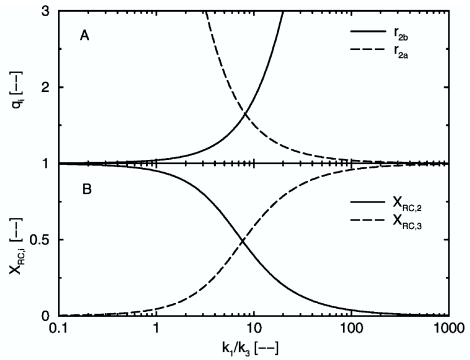

Fig. 1. Variation of q_{ij} calculated for model 2d (A) and degree of rate control (B) as function of the ratio between the two rate constants. $T = 500\,\mathrm{K}$, $p_B = p_{A_2} = 5\,\mathrm{kPa}$ and $p_{AB} = 20\,\mathrm{kPa}$.

In Fig. 1, q_i and the degree of rate control ($X_{RC,i}$) are plotted as function of the ratio between the rate constants of the two slow steps in model 2d. It is obvious that the QEA and HSSA models gives identical results when one of the slow steps is rate limiting. Furthermore, the figure shows that if the degree of rate control of a step is less than ≈0.05 the results derived from QEA will not deviate by more than ≈5% from the results obtained from HSSA. Equilibrating fast steps is therefore a valid approximation if there is a substantial difference in the rates of the steps.

It is clear from the figure that the shift in rate limiting step does not take place when $k_1 > k_3$ but when $k_1 > 8k_3$. This means that the identity of the rate limiting step cannot be determined from the numeric values of rate constants. This implies that the degree of rate control has to be calculated in order to establish which steps are rate limiting.

4.2. Dependence on reaction conditions

Extensive variations in reaction conditions may lead to a change in the rate limiting step. In Fig. 2 the degree of rate control for model 2d as a function of A_2 pressure can be seen.

A wide pressure range is used in the figure in order to establish regions where step 1 or step 3 is rate controlling. The degrees of rate control add up to one in the whole pressure range. The degree of rate control for step 1 becomes slightly negative at high A_2 pressure as this step becomes rate inhibiting. Under normal conditions the pressure can hardly be varied over such a wide range and it is likely that either step 1 or step 3 or both of them are rate controlling at all feasible conditions.

In Fig. 3 the degree of rate control of model 2d is plotted with respect to temperature. Intuitively one might expect that at higher temperatures, it should be easier for the system to overcome high activation barriers and that changes in rate limiting steps should go from low activation enthalpy at low temperature to high activation

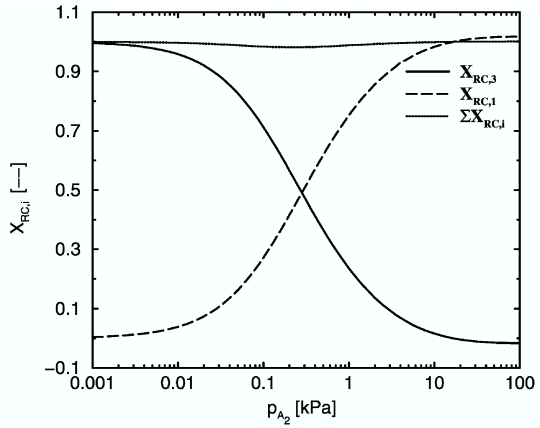

Fig. 2. The degree of rate control of step 1 and 3 for model 2d vs. A_2 pressure. $T = 500\,\mathrm{K}$ and $p_B = 10\,\mathrm{kPa}$.

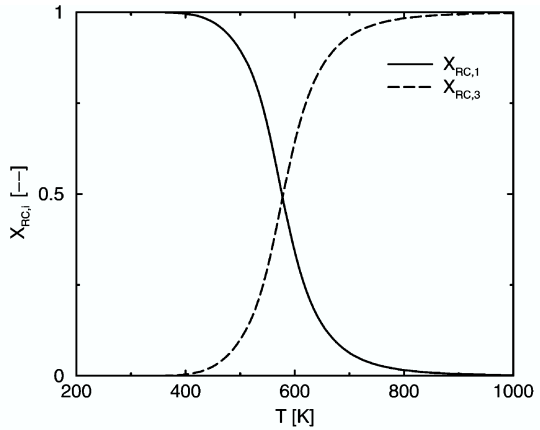

Fig. 3. The degree of rate control of step 1 and 3 for model 2d vs. temperature. $p_{A_2} = p_B = 10\,\mathrm{kPa}$ and $p_{AB} = 1\,\mathrm{kPa}$.

enthalpy at high temperature. But if we compare the Arrhenius parameters in Table 2 with the results in Fig. 3 we see that that this expectation is wrong. Step 1 has the highest activation enthalpy and is rate limiting at low temperatures whereas step 3 has the lowest activation enthalpy and is rate limiting at high temperatures. This is due to a low stability of A* which makes the dissociation of A_2* rate limiting

at low temperatures. At high temperatures the coverage of both A* and B* become low with the result that step 3 becomes rate limiting.

4.3. Summary

The analysis in this section demonstrates how the degree of rate control can be applied as a quantitative measure of the validity of using a QEA analysis.

The analysis shows that for reactions with one overall reaction the quasi-equilibrium approximation will be valid in most cases. Furthermore, the analysis outlines what it will require to observe a change in rate limiting step: Two steps x and y are required to be much slower that all other steps. Further, at on set of conditions $\gamma_x r_x \ll \gamma_y r_y$, while at another set of conditions $\gamma_x r_x \gg \gamma_y r_y$. These requirements are so tricky that observing a change in rate limiting step is highly unlikely, unless both reaction and reaction conditions have been artificially selected.

5. Reaction orders

Reaction orders are a measure of rate dependence on the partial pressures of reactants and products. Reaction orders are often used when experimental measurements are compared with models or other experimental results.

5.1. Overview

It was demonstrated in Section 2 how analytic expressions for the reaction orders may readily be derived for QEA models. In order to interpret reaction order we compare the reduced rate expressions for models 2b and 3b with their respective reaction orders. The reduced rate expressions are

$$r_{2b} = k_3 K_2 K_1^{\frac{1}{2}} \left(\frac{p_{A_2}}{p^{\ominus}}\right)^{\frac{1}{2}} \frac{p_B}{p^{\ominus}} \left(1 - \beta^{\frac{1}{2}}\right) \theta_*^2 \tag{59}$$

$$r_{3b} = k_3 \frac{p_B}{p^{\ominus}} \left(1 - \beta^{\frac{1}{2}}\right) \theta_* \tag{60}$$

The reaction orders for the models

Reaction order	Model 2b	Model 3b
α_{A_2}	$\frac{1}{2} - \theta_{A*}$	$-\theta_{A_2*} - \frac{1}{2}\theta_{A*} + \frac{1}{2}\theta_{B*}$
α_B	$1 - 2\theta_{B*}$	1
α_{AB}	$-2\theta_{AB*}$	$-\theta_{AB*} - \theta_{B*}$

From these equations it is observed that reaction orders depends on two contributions.

- A constant which is the stoichiometric coefficient for the gas in the forward rate of the rate limiting step, positive for reactants and negative for products, and zero if the gas does not participate as a reactant in the rate limiting step.
- Coverage dependent terms which reflect that increased pressure will change the number of free sites and thus the reaction rate. This contribution can be either positive or negative as an increased partial pressure can result in either higher or lower number of free sites.

5.2. Dependence on reaction conditions

It is obvious that the reaction orders may change with reaction conditions, and that the changes can be quite large. This will be analyzed for model 2b.

Fig. 4 shows the reaction orders with respect to the partial pressure of A_2. As expected θ_{A*} can be neglected at low partial pressures, but becomes more and more important as the partial pressure increases and it is the most abundant intermediate at high pressure. This results in a high reaction order in A_2 at low partial pressure and a low reaction order at high pressure. The reaction orders for B and AB are influenced by the coverage dependent terms at low A_2 pressure but these terms becomes insignificant at high pressure when A* dominates the surfaces.

Fig. 5 shows the reaction orders dependence on the temperature. As expected the coverage dependent terms are important at low temperatures where the coverages are high, whereas they can be neglected at high temperatures where the coverage of free sites is close to one. Furthermore, the reaction orders are dominated by the strongest binding intermediate AB* at low temperatures. The reaction orders have

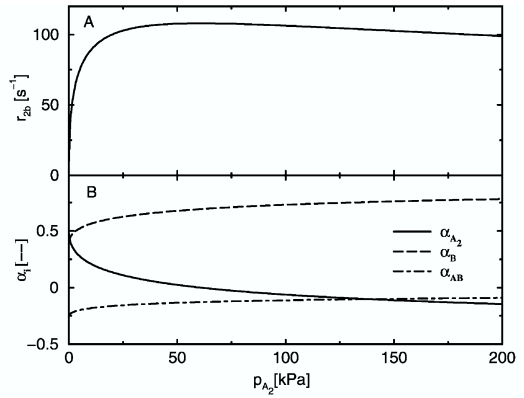

Fig. 4. Variation of reaction rate (A) and reaction order (B) calculated for model 2b as a function of A_2 pressure. $T = 550$ K, $p_B = 10$ kPa and $p_{AB} = 1$ kPa.

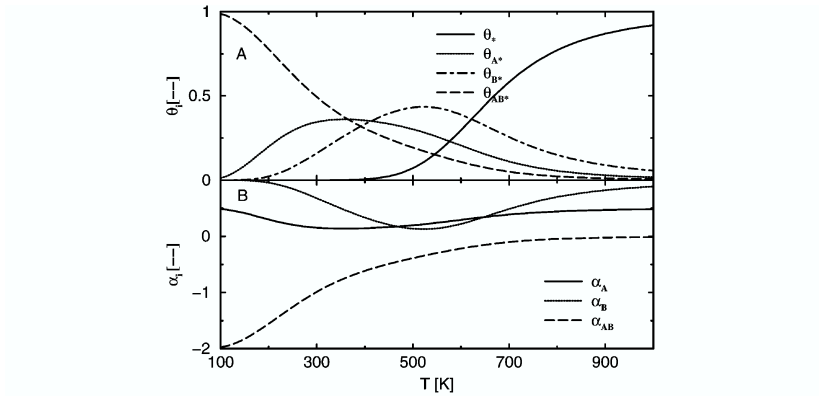

Fig. 5. Variation of coverages (A) and reaction order (B) calculated for model 2b as a function of temperature. $p = 100\,\text{kPa}$, $y_B = y_{A_2} = 0.48$ and $y_{AB} = 0.04$.

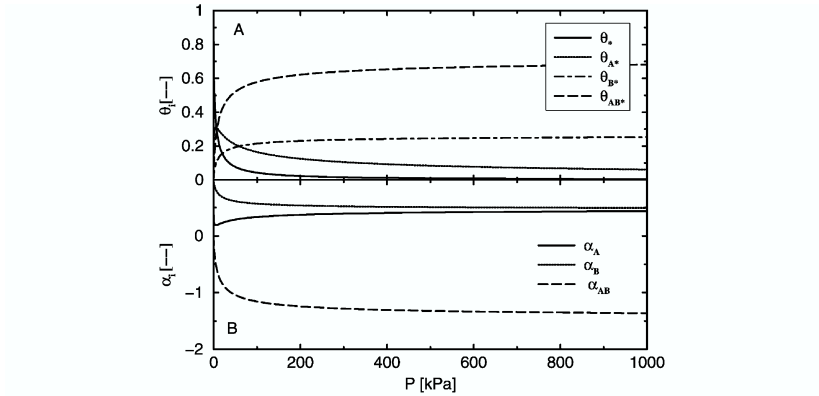

Fig. 6. Variation of coverages (A) and reaction order (B) calculated for model 2b as a function of total pressure. $T = 500\,\text{K}$, $y_B = y_{A_2} = 0.4$ and $y_{AB} = 0.2$.

a complex behavior at intermediate temperature, which is due to competition for free sites among A*, B* and AB*.

Fig. 6 shows the reaction orders as a function of total pressure. There is no contribution to the reaction orders from the coverage dependent terms at low pressures, as the coverages are essentially zero at these conditions. The coverage depended terms gain importance at higher pressures, but vary insignificantly above 100 kPa, as the coverages are almost constant above this pressure.

From the three figures it is observed that the reaction orders are almost constant over fairly large ranges of reaction conditions. This means that if the reaction orders are measured in different ranges of reaction conditions, they may seem fairly constant for each range but may have different numerical values. This may explain why different research groups can measure different reaction orders for the same reaction.

5.3. Summary

In this section we analyzed the reaction orders and showed that even for simple mechanism the reaction orders may vary in a complex manner with reaction conditions. This is due to the competition for sites and implies that a change in reaction order cannot be taken as an evidence for a change in reaction path.

6. Analysis of Arrhenius plots

Activation enthalpies are often used as a tool to provide information about mechanisms and the kinetics of reactions, an example is a kink in an Arrhenius plot which is often interpreted as a change in the rate limiting step. In some cases experimental activation enthalpies are used to validate micro-kinetic models or Density Functional Theory (DFT) calculations [21].

Experimentally, activation enthalpies are obtained from Arrhenius plots, and both integral and differential reactors are used for this purpose. However, as discussed in Section 2, Arrhenius expressions are only valid for elementary reactions. This raises the question: what does the experimental activation enthalpies for a composite reaction obtained by a Arrhenius plots reflect? To answer this question our kinetic models are analyzed in the following.

6.1. Interpretation of apparent activation enthalpy

It was demonstrated in Section 2 how analytic expressions for the apparent activation enthalpies can be established within the QEA. We rewrite the expression for the apparent activation enthalpy deduced for model 2b

$$H^{\ddagger} = \underbrace{H_3^{\ddagger}}_{\text{I}} + \underbrace{\tfrac{1}{2}\Delta H_1 + \Delta H_2}_{\text{II}} \underbrace{-\Delta H_1\theta_{A*} - 2\Delta H_2\theta_{B*} + 2\Delta H_4\theta_{AB*}}_{\text{III}}$$

From this equation it is observed that the apparent activation enthalpy consists of three different contributions [2,17]:

(I) The activation enthalpy of the rate limiting step representing an enthalpy barrier the molecules have to cross.

Table 3
Interpretation of the enthalpies entering the coverage dependent terms

Reaction	Enthalpy
$2A* \rightleftharpoons A_2(g) + 2*$	$-\Delta H_1$
$2B* \rightleftharpoons 2B(g) + 2*$	$-2\Delta H_2$
$2AB* \rightleftharpoons 2AB(g) + 2*$	$2\Delta H_4$

(II) The formation enthalpy of the reactants participating in the rate limiting step. This formation enthalpy is defined with respect to the gas phase and is generally negative since adsorptions generally are exothermic. This lowering in apparent activation barrier makes it easier to cross the barrier of the elementary step.

(III) Is a desorption enthalpy of intermediates on the surface times the number of sites used in the rate limiting step, representing a cost of freeing the needed number of adsorption sites. This term is generally positive and the apparent activation enthalpy increases with increasing coverage of intermediates as less free sites becomes available.

To get further insight into the background of the coverage dependent terms it is enlightening to look at what the reaction enthalpies represent, Table 3. It is clearly seen that these enthalpies represents the formation enthalpy of the intermediates with respect to the gasses.

From above it can be seen that contributions (I) and (II) adds up to an effective activation barrier, and that these two terms will be independent of reaction conditions. In contrast to this contribution (III) is dependent on the coverage of sites and may depend strongly on the reaction conditions.

Analytic expressions for apparent activation enthalpy of QEA models generally consists of these three contributions, Appendix A. For more complicated kinetic models the apparent activation enthalpy becomes more complex, this is, however, beyond the scope of this manuscript.

6.2. Temperature dependency

It has been established that the apparent activation enthalpy will vary with coverage of intermediates, and that the apparent activation enthalpy in most cases increases with coverage. This leads to the conclusion that the apparent activation enthalpy generally decreases with increasing temperature. Fig. 7 shows the apparent activation enthalpy for model 2b with respect to temperature using physically realistic parameters. There are three regions in Fig. 7:

Region 1. A low temperature region, where the coverage of adsorbates are high and fairly constant. This results in a almost constant apparent activation enthalpy i.e. a straight line in the Arrhenius plot.

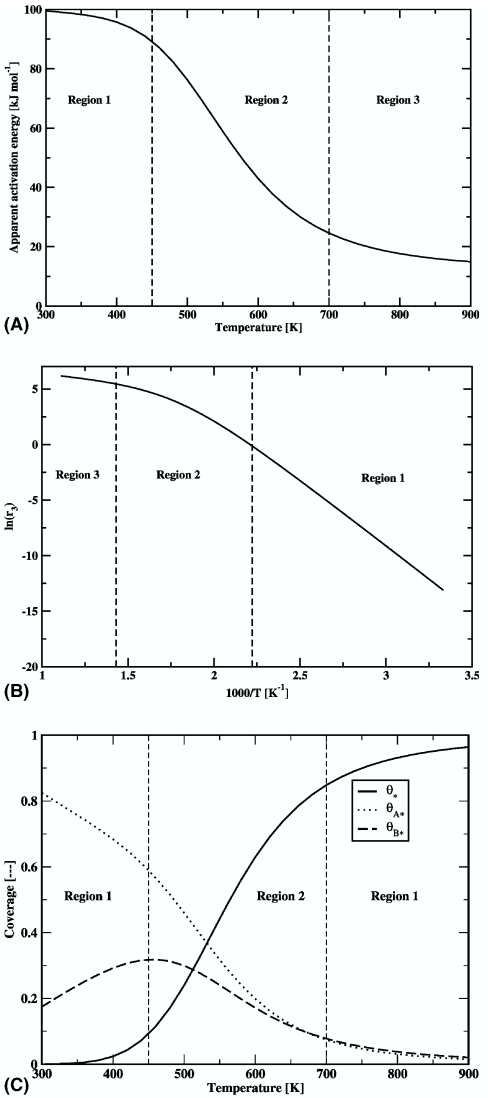

Fig. 7. Numerical results for the model 2b: (A) apparent activation enthalpy as a function of temperature; (B) Arrhenius analysis of exact activities generated and (C) coverages of intermediates as a function of temperature. $p_{A_2} = p_B = 10\,\text{kPa}$.

Region 2. A intermediate temperature region. The adsorbates are destabilized by the elevated temperature, and pronounced changes in coverages takes place throughout the region, which results in a decreasing apparent activation enthalpy, i.e. a decreasing slope in the Arrhenius plot.

Region 3. A high temperature region, where the coverage of adsorbates approach zero due to the high temperature, thus the coverage dependent term can be neglected. This results in a constant apparent activation enthalpy and a straight line in the Arrhenius plot.

If the data shown in Fig. 7B were experimental data and a detailed kinetic model had not been proposed, it would be tempting to conclude that mass transfer limitations exists in certain temperature ranges. This means that different processes could be limiting the overall rate in the different regions e.g. *Region 1*: the reaction rate, *Region 2*: pore diffusion, *Region 3*: external mass transfer. If control experiments had falsified this hypothesis it might be tempting to conclude that a change in rate limiting step takes place. And the regions could be assigned to different rate limiting elementary reactions e.g. *Region 1*: elementary reaction X, *Region 2*: elementary reactions X and Y, *Region 3*: elementary reaction *Y*.

It has been demonstrated above that it is possible to come up with three different plausible explanations for the curved Arrhenius plot in Fig. 7B. The activation enthalpy changes due to changes in the coverages, mass transfer limitations, or a change in rate limiting step. In the present case it is known that the second and third explanations are wrong, since the data was obtained from a kinetic model with only one rate limiting step and no diffusion limitations. This illustrates that caution should be taken when Arrhenius plots are analyzed.

It has been demonstrated for model 2b that the apparent activation enthalpy may have significantly different values at different temperatures. As the apparent

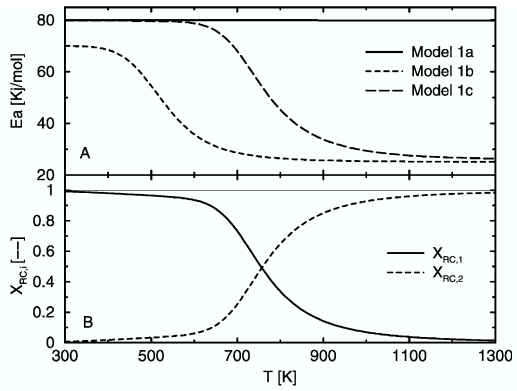

Fig. 8. (A) Apparent activation enthalpy for models 1a, 1b and 1c and (B) degree of rate control as a function of temperature for model 1c $p_{A_2} = p_B = 10$ kPa and $p_{AB} = 1$ kPa.

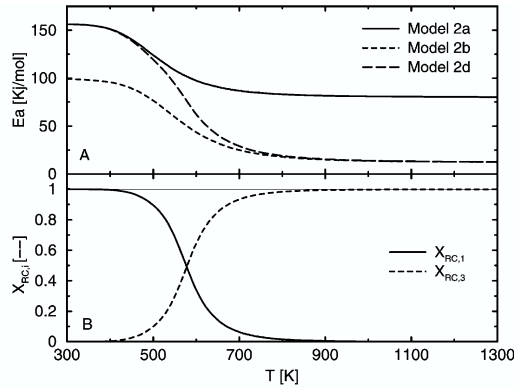

Fig. 9. (A) Apparent activation enthalpy for models 2a, 2b and 2d (B) degree of rate control as a function of temperature for model 2d $p_{A_2} = p_B = 10$ kPa and $p_{AB} = 1$ kPa.

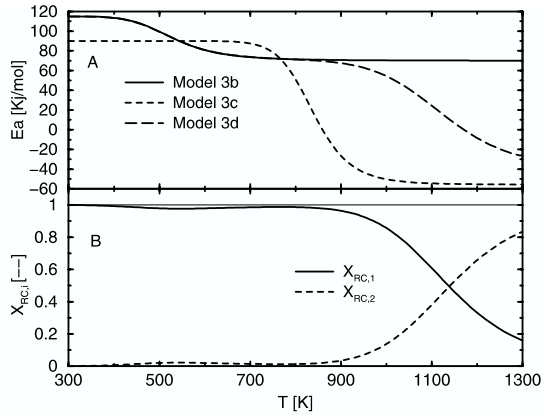

Fig. 10. (A) Apparent activation enthalpy for models 3b, 3c and 3d and (B) degree of rate control as a function of temperature for model 3d $p_{A_2} = p_B = 10$ kPa and $p_{AB} = 1$ kPa.

activation enthalpy in general depend on the coverages, we should expect a similar behavior for the other kinetic models. To demonstrate this, we have calculated the apparent activation enthalpy as a function of temperature for most of the kinetic models in Section 3, Figs. 8–10. It is observed from the figures that except for model 1a, the apparent activation enthalpies vary with temperature. Model 1a has a constant apparent activation enthalpy due to the low A* stability resulting in a negligible coverage of A*, which means that this is Region 3 under all reaction conditions.

The position of the regions depends on the model and the parameters used. For models 1c, 2d, and 3d containing two slow steps a more complex behavior of the apparent activation enthalpy is observed than for the models with only one rate limiting step. A change in rate limiting does not result in an abrupt change in apparent activation enthalpy, but a large transition region is apparent. In regions where both of the steps are rate limiting the apparent activation enthalpy lies in between the apparent activation enthalpies obtained from the corresponding QEA models. The apparent activation enthalpy in the SSA and HSSA models decreases when the rate limiting step changes, but the effect is masked by the changes in coverage and experimentally it is virtually impossible to distinguish the two phenomena.

It may be surprising that the SSA and HSSA models shifts to a low apparent activation barrier step at higher temperature. Intuitively, one could expect that a high activation enthalpy step could be climbed at higher temperature leading to a greater importance of this step and therefore a higher apparent activation enthalpy in total at high temperatures. But the rate limiting step is determined by the whole reaction mechanisms and not simply the step with the highest activation enthalpy. Further, the activation enthalpies becomes less important at high temperatures, which can be deduced from the fact that the difference between two Arrhenius expressions with high and low activation enthalpy, respectively, decreases with temperature.

6.3. Variation in pressure and composition

Due to the coverage dependency the apparent activation enthalpy will vary with pressure and composition of the reaction mixture. The pressure dependency is illustrated for model 2b in Fig. 11. As seen from the figure an increased pressure results in a shift of the earlier established regions to higher temperatures. This could be

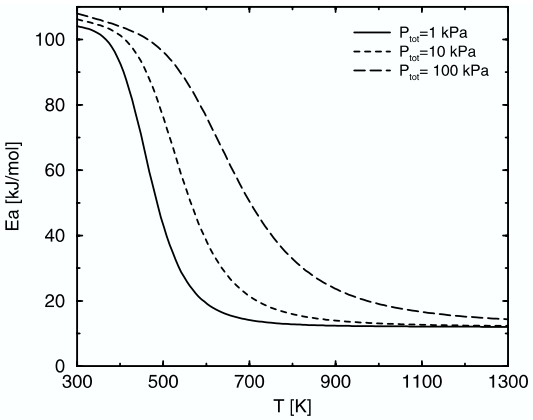

Fig. 11. Apparent activation enthalpy vs. temperature at different total pressures for model 2b. $y_{A_2} = y_{A_2} = 0.45$ and $y_{AB} = 0.1$.

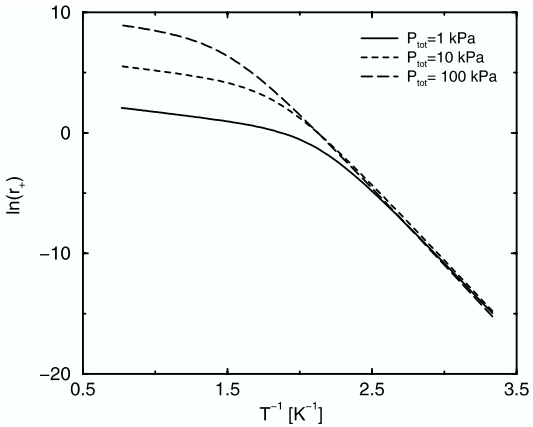

Fig. 12. Arrhenius plot of model 2b at different total pressures. $y_{A_2} = y_{A_2} = 0.45$ and $y_{AB} = 0.1$.

anticipated from the derived coverage dependence of the apparent activation enthalpy. This illustrates that it is necessary to take both pressure, composition and temperature into account when measured activation enthalpies are compared.

Fig. 12 shows that the slope in an Arrhenius plot is constant at high and low temperatures (Region 3 and 1 respectively). Furthermore, the three pressures give the same result at low temperatures whereas each pressure gives a different line at high temperature. Hence, an Arrhenius analysis will not result in a single curve but a number of almost parallel curves, one for each composition and pressure. This means that for both Regions 2 and 3 the apparent prefactor vary with reaction conditions.

To illustrate that the gas composition will influence the apparent activation enthalpy we have made simulations of the apparent activation enthalpy of model 2b with respect to conversion at different AB* stabilities, Fig. 13. This enables us to investigate how product inhibition influences the apparent activation enthalpy.

When the products are less stable than the reactants, they have only minor influence on the activation enthalpy at low conversions. This can be explained by the fact that the coverages remain almost constant. At higher conversions the apparent activation enthalpy decreases due to the consumption of reactants which forms the most stable intermediates. In contrast, when the the products are more stable than the reactants the activation enthalpy changes rapidly even at low conversions. This is due to the large relative change in product pressures leading to large variation in the coverages.

6.4. Pitfalls

The rate of a reaction cannot be measured directly but must be determined indirectly e.g. by dividing a measured conversion with the residence time. The correct

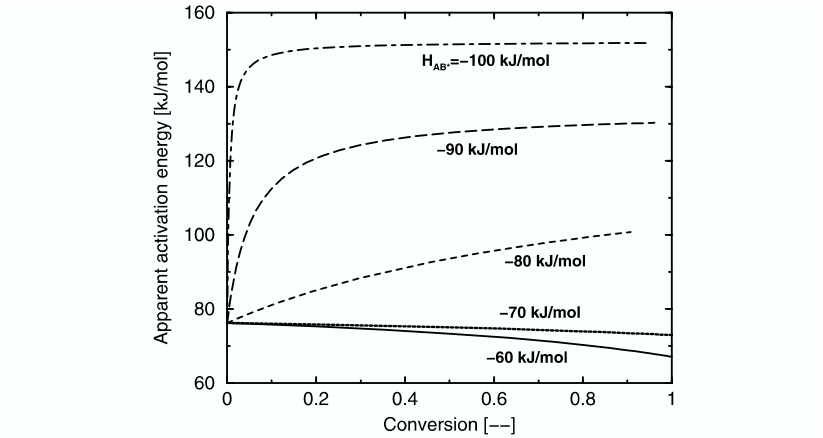

Fig. 13. Apparent activation enthalpy vs. conversion for model 2b. Different degrees of product inhibition is simulated by increasing the stability of AB*. $p_{A_2} = p_B = 10\,\text{kPa}$.

analysis of experimental data is laborious and there are rich possibilities for mistakes in the form of oversimplifications or misinterpretations.

6.4.1. Linearization problems

From the preceding analysis it is clear that the apparent activation enthalpy varies with temperature, and the question arises *Why do so many Arrhenius plots result in a straight line?* The trivial answer is that most reactions are Region 1, but there may be other explanations. The effect of temperature changes is analyzed for model 2b, Fig. 14A. The apparent activation enthalpy decreases from approximately 90 kJ/mol at

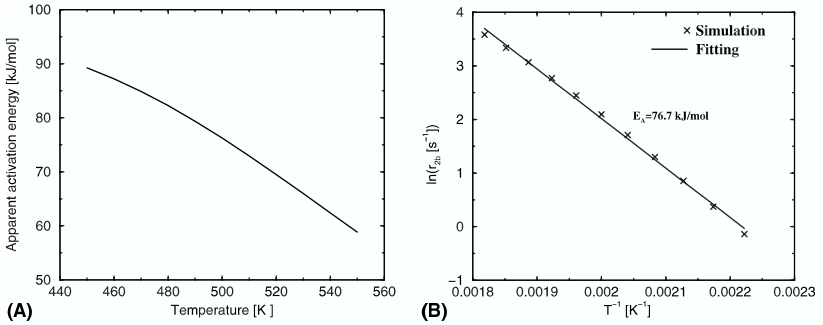

Fig. 14. Numerical results for model 2b: (A) analytic apparent activation enthalpy as a function of temperature and (B) Arrhenius analysis of the calculations. $p_{A_2} = p_B = 10\,\text{kPa}$.

450 K to approximately 60 kJ/mol at 550 K. An Arrhenius plot for this temperature range should therefore result in a curved line.

Fig. 14B shows a linear least squares fit to 11 point taken from Fig. 14A. It is obvious that the analysis results in a straight line i.e. a constant activation enthalpy of 76.7 kJ/mol. Hence, the Arrhenius plot does not capture the changes in apparent activation enthalpy. The problem is that if a straight line is expected, small deviations will be ascribed to experimental uncertainty rather than deviations from linearity.

6.4.2. Differential reactor analysis

In the previous simulations and analysis we know the reaction rate at all times from the analytic rate expressions of our kinetic models. In practical work we have to establish the rate from measurements and suitable models. To be able to measure a rate a certain conversion is necessary, but to avoid laborious calculations it might be tempting to use a differential reactor analysis under all conditions Eq. (49). There is evidently no difference between the differential rate and the exact rate at sufficiently small conversions. However, a large error is to be expected if differential reactor analysis is used at large conversions.

In the analysis of the apparent activation enthalpy the forward rate of reaction is used. But the forward rate cannot be measured directly and it might be tempting to use the net rate instead. However, this will give a different result as can be seen from a simple calculation.

$$H^{\ddagger}_{\text{app},r_j} = RT^2 \frac{\mathrm{d}\ln r_j}{\mathrm{d}T} \tag{61}$$

where

$$r_j = r_+(1 - \beta_g^{\frac{\perp}{\gamma_r}}) \tag{62}$$

after straightforward algebra we get

$$H_{\text{app},r_j} = H^{\ddagger}_{\text{app}} + 1/\gamma_r \frac{\beta^{1/\gamma_r}}{1 - \beta^{1/\gamma_r}} \Delta H \tag{63}$$

where ΔH is the enthalpy of reaction and $H^{\ddagger}_{\text{app}}$ is the apparent activation enthalpy.

The second term in the Eq. (63) is the error introduced by an Arrhenius analysis based on the total rate. Far from equilibrium ($\beta \sim 0$) the error is small, whereas error becomes infinite as equilibrium is approached ($\beta \to 1$). It is therefore clear that we need to be able to establish the forward rate from measurements of the net rate. The forward rate may be established from the following relation:

$$r_+ = \frac{r_j}{1 - \beta^{1/\gamma_r}} \tag{64}$$

Applying this equation is problematic for two reasons: (i) γ_r may be unknown and cannot be determined directly from measurements and (ii) the approach is based on the assumption that only a single step is rate limiting. Thus if two or more steps

are rate limiting the forward rate determined from Eq. (64) will have no physical meaning.

To illustrate some of the above complications the conversion in a reactor with model 2b has been calculated, and from these conversion three approximated rates have been calculated: r_j the net rate found from the differential analysis Eq. (49), $r_{\gamma=2}$ and $r_{\gamma=1}$ forward rates found by inserting r_j into Eq. (64) using two different γ values 1 (incorrect value) and 2 (correct value), Fig. 15B.

Fig. 15B shows that all the approximated rates (r_j, $r_{\gamma=2}$, $r_{\gamma=1}$) differ from the true rate at relatively small conversions, due to the products in the feed. The results clearly demonstrate that the forward rate ($r_{\gamma=1}$), calculated with a wrong stoichiometric number, will be significantly wrong if β differs from zero. Furthermore, even though the correct stoichiometric number is used the analysis breaks down at high conversions.

The main problem of using an approximated rate can be illustrated by calculating $H^{\ddagger}$ by an Arrhenius analysis

$$H^{\ddagger}_{r_i} = RT^2 \frac{\Delta \ln(r_i)}{\Delta T} \tag{65}$$

where r_i is the three approximated rates calculated at 895 K and 905 K. The results from these calculations can be seen in Fig. 15A. The calculated apparent activation enthalpies found from the correct γ is equal to the true values at low conversion but the results are wrong at high conversions. Furthermore, the activation enthalpies found from r_j and $r_{\gamma=1}$ differ ~20 kJ/mol and ~40 kJ/mol, respectively, from the true value at low conversions and the difference increases with conversion. This implies that it is of prime importance to use the forward rate and to know the correct γ value.

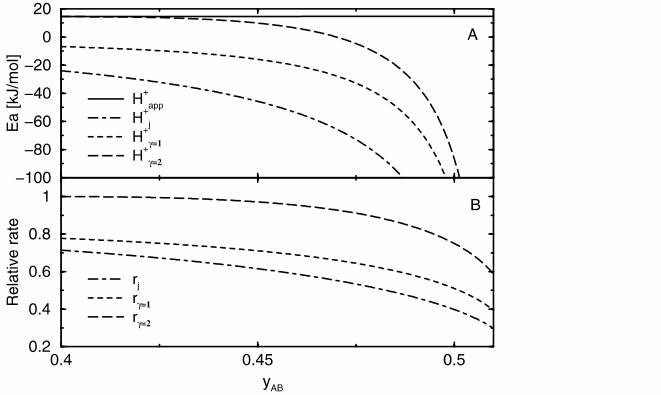

Fig. 15. Numerical results for model 2b: (A) apparent activation enthalpy and (B) rates relative to the true forward rate. Both as functions of mole fraction of AB. $\gamma = 1$ and $\gamma = 2$ refer to the assumed stoichiometric number. $y_{A_2} = 0.2$, $y_B = 0.4$, $y_{AB} = 0.4$, $p_{tot} = 10$ kPa, $T = 900$ K.

When and why the simplified analysis breaks down will depend on the reaction mechanism and how close the measurements are to equilibrium.

6.4.3. Using conversion in Arrhenius analysis

In the preceding section we saw that it is problematic to obtain a rate and activation barriers from integral reactor data without a detailed kinetic model. It may therefore be tempting to use conversions, X_i, instead of rates in the Arrhenius analysis

$$H^{\ddagger} = RT^2 \frac{\mathrm{d} \ln X}{\mathrm{d}T} \tag{66}$$

This approach has some limitations which can be seen by comparing it to the differential approach Eq. (49). First of all, neither flow nor number of sites are taken into account which limits the analysis to constant flow and loadings. If these parameters are kept constant the analysis will bare close resemblance to Arrhenius analysis of the net rate found from a differential reactor analysis.

In Fig. 16A the apparent activation enthalpy for model 2b obtained from Eq. (66) is compared to the true value. The figure may be divided into different regions: (i) below 540 K the conversion is low (Fig. 16B) and the error is small; (ii) at temperatures 540–800 K the error gradually increases, due to the increased importance of the backward rate which is not taken into account in Eq. (66) and (iii) above 800 K the approach to equilibrium becomes even more important and the error goes to infinity.

6.5. Summary

The analysis of the models shows that the apparent activation enthalpy contains coverage dependent terms. This means that even simple mechanisms may display variations in apparent activation enthalpy. Thus a kink in an Arrhenius plot cannot

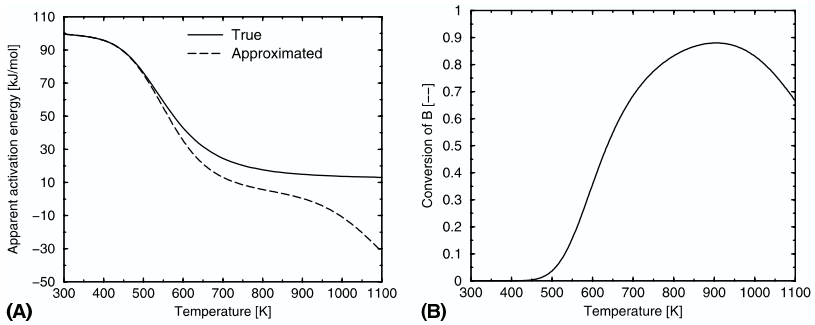

Fig. 16. Numerical results for model 2b: (A) true apparent activation enthalpy and an approximated using Eq. (66) and (B) conversion of component B at outlet. Both as functions of temperature. $p_{A_2} = p_B = 10$ kPa.

be taken as evidence for e.g. a change in reaction path or diffusion limitations. The analysis shows that three regions exist in Arrhenius plots for heterogeneous catalysis:

Region 1. A high coverage region found at low temperature where the total coverage is practically one, which leads to a constant apparent activation enthalpy under all reaction conditions.

Region 2. A mid coverage region where the total coverage is between one and zero. In this region the total coverage will vary with all reaction conditions leading to non-linearity in the Arrhenius plot.

Region 3. A low coverage region found at high temperature. In this region the apparent activation enthalpy is independent of reaction conditions since the coverage dependent terms are essentially zero. However, the apparent prefactor varies with composition and pressure, which means that variations in these conditions leads to a curve for each composition and pressure in the Arrhenius plot.

Caution should be exercised in interpretation of reported activation enthalpies and to the use of Arrhenius plots. Even if the reaction is not limited by mass transport phenomenon and the data are analyzed correctly, the apparent activation enthalpy will only agree with the activation enthalpy for the rate limiting step in one case: the rate limiting step is an adsorption and the measurements are made in Region 3. Unfortunately it is in Region 3 mass transfer phenomenon are most likely to be important. Hence it is virtually impossible to measure the activation enthalpy of the slow step by making a Arrhenius plot in heterogeneous catalysis. Instead the apparent activation enthalpy has to be interpreted by a micro-kinetic model.

In practice we are not able to measure rate constants directly in heterogeneous catalysis and it might be tempting to use macroscopic measurable values in the Arrhenius plot, e.g. the forward rate found by dividing by the approach to equilibrium, the net rate, or the conversion of a reactant. The analysis shows that each of these approaches may introduce huge errors. For the analysis of experimental data there is thus no alternative to the detailed fit of data to a suitable model for an appropriate reactor.

7. Volcano curves

For a number of reactions it has been shown that if the rate is plotted against the catalyst position in the periodic table a Volcano curve is obtained. In this section we will discuss the requirements in order to obtain a volcano curve from a kinetic point of view.

7.1. Overview

According to Sabatiers principle the best catalyst binds intermediates moderately to the surface. If the catalyst binds intermediates too weakly the reaction rate will be

low due to low coverages of reactants. If the catalyst binds intermediates to strongly the rate will be low due to high coverage of products. Therefore the optimum catalyst is a compromise in stability of intermediates.

While stability and reactivity generally show systematic trends across the transition metals, there are many complications due to structural differences, ferro magnetism, differences in bonding of chemisorbed molecules, and even different reaction pathways. A detailed analysis of the trend in reactivity across the periodic table is beyond the scope of this manuscript, instead we will analyze the detail of a specific model with respect to trends in reactivity.

If our starting point is that the optimal catalyst binds the reactants strongly without binding the products to strongly, a simple model is that the enthalpy of formation for all intermediates depend on a parameter, ϕ

$$H_i = H_{i0} + \phi(H_{i1} - H_{i0}) \tag{67}$$

such that the value for the intermediate, i, changes from H_{i0} to H_{i1} in the volcano plot.

The linear dependence of the formation enthalpy on ϕ causes the enthalpy of the reaction steps to depend on ϕ as well

$$\Delta H_i = \Delta H_{i0} + \phi(\Delta H_{i1} - \Delta H_{i0}) \tag{68}$$

The enthalpy of formation of the transition state will depend on ϕ to which in turn causes the activation enthalpy to depend on ϕ

$$H_i^{\ddagger} = H_{i0}^{\ddagger} + \phi(H_{i1}^{\ddagger} - H_{i0}^{\ddagger}) \tag{69}$$

If ϕ is eliminated in Eq. (68) and (69) we find a linear dependence between $H_i^{\ddagger}$ and ΔH_i. This is known as a *Brønsted–Evans–Polanyi* (BEP) relation. Combining this simple model with Sabatiers principle will result in a volcano curve, Fig. 17.

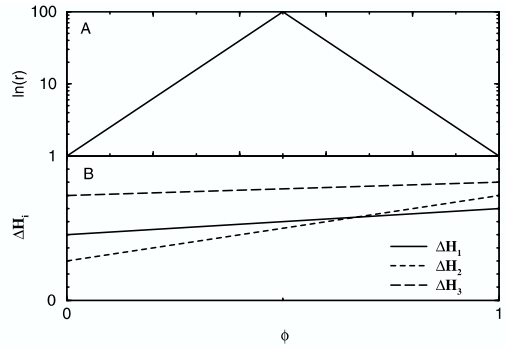

Fig. 17. Principle sketch showing rate of reaction (A) when Sabatiers principle is used on the simple model describing surface stabilities (B).

It has been shown by DFT calculations that the dissociation barrier for simple diatomic molecules e.g. O_2, CO, and N_2 is linearly dependent on the dissociative chemisorption energy. Calculations indicate that dissociation of different simple molecules may be described by the same BEP relation leading to the concept of universality in heterogeneous catalysis [22–26].

7.2. Requirements for a Volcano curve

Nørskov et al. [27] showed that the activation energy of N_2 dissociation is related to the adsorption energy of atomic nitrogen by a BEP relation. Furthermore they show that the BEP relationship combined with a QEA model results in a volcano curve when the stability of $N*$ is varied [27,25]. That a volcano curve results from this is to be expected since (i) the activation enthalpy will be large at low stabilities resulting in a zero turnover and (ii) at high stability the intermediates will cover the surface and thereby inhibit the reaction.

Using a QEA-model in the mentioned analysis can be problematic, since changing the stabilities of the adsorbates can result in a change in rate limiting step. e.g. if an adsorption is rate limiting the rate of this step will speed up when the stabilities are lowered as more sites becomes available. Surface reactions and desorption will, however, become slower as the coverages becomes lower. Thus if the stability is lowered sufficiently, surface reaction and desorptions must become slower than adsorptions, i.e. the rate limiting step will shift and the QEA will break down.

To illustrate the above points a number of simulations have been made for models 2a–2d. All of these models are investigated with respect to three different variations: (1) the stability of A* is varied, (2) the stability of all intermediates is varied (3) the stability of either a reactant or a product is varied with a simultaneous change in activation enthalpy, Table 4. The results of these simulations can be seen in Fig. 18.

From the figure it is seen that the surface reaction and the HSSA model results in a volcano curve under all assumptions. This means that these are simple explanations of the experimentally observed Volcano curves. Furthermore, it is clearly seen that the BEP relation results in a Volcano curve for all the different models. Nevertheless, since so many different models and assumptions results in Volcano curves, the existence of volcano curves cannot be taken as an evidence for the BEP relationship.

Furthermore, the ammonia synthesis is precursor meditated [1] which means that it is actually a surface reaction, and it was clearly shown in the figure that surface

Table 4
The used BEP relationships

Relation	Equation
BEP_{2a}	$H_1^{\ddagger} = 80\text{kJ/mol} + 0.4H_{A*}$
BEP_{2b}	$H_3^{\ddagger} = 95\text{kJ/mol} + 0.4H_{B*}$
BEP_{2c}	$H_4^{\ddagger} = 95\text{kJ/mol} - 0.4H_{AB*}$
BEP_{2d}	BEP_{2a} and BEP_{2b}

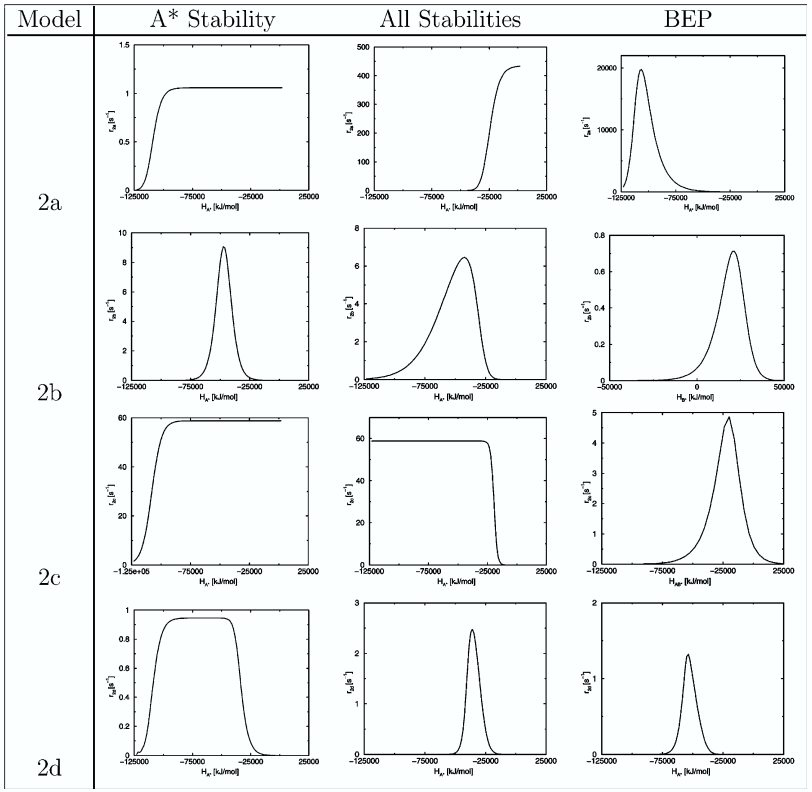

Fig. 18. Rates for models 2a–2d as function of intermediate stability and different assumptions. $T = 600\,\text{K}$ $p_{A_2} = p_B = 100\,\text{kPa}$ and $p_{AB} = 10\,\text{kPa}$.

reaction results in volcano curves if the stability of one of the reactants is varied. Hence if a QEA model with a precursor is included and the stability of this precursor is varied a Volcano curve would result.

7.3. Summary

We have analyzed a simple model where the stability of intermediates depend linearly on a parameter, and show that this model in a number of cases result in a sharp maximum in reaction rate, a volcano curve.

A linear dependence of the activation enthalpy on the stability of adsorbates, a BEP relation, always leads to a volcano curve, right-hand column of Fig. 18. However, a volcano curve may also be observed in the absence of a BEP relation second

and third row in Fig. 18. The experimental observation of a volcano curve thus cannot be taken as a evidence for the existence of a BEP relation.

8. Compensation effect

For some reaction systems in heterogeneous catalysis it has been observed that apparent activation enthalpies, $H^{\ddagger}_{app}$, measured under different conditions vary. This variation is accompanied by a change in prefactor, A_{app}, in such manner that a large apparent activation enthalpy is accompanied by a large prefactor and vice versa. This phenomenon is referred to as the *compensation effect*.

8.1. Overview

In this section we give an analysis of the compensation effect observed in heterogeneous catalysis. Plotting $H^{\ddagger}_{app}$ against $\ln A_{app}$ is denoted a *Constable* plot, sometimes the dependence will be linear according to the Cremer–Constable relation

$$\ln A_{app} = aH^{\ddagger}_{app} + b \tag{70}$$

Compensation effects have been observed in a variety of cases in heterogeneous catalysis, e.g. variations in reaction conditions (temperature, pressure and composition) [28], varying catalyst loadings, and by testing the same reaction on different metals [28,29]. Furthermore, compensation effects have been observed in several sciences: heterogeneous catalysis [19,30–35], temperature programmed desorption (TPD) [36,37], diffusion phenomenon [38], and homogeneous catalysis [39].

Although the compensation effect in heterogeneous catalysis has been known and studied since Constable [40] in 1925 observed a linear relationship between $\ln A_{app}$ and $H^{\ddagger}_{app}$ for the dehydrogenation of ethanol on different catalysts a full explanation is still lacking [30]. Different explanations have been suggested in order to explain these observations, these may roughly be divided into two different categories i.e. the compensation effect is caused by the data analysis [28,31,33,34,41,42] or by physical effects [19,28–30,43,44].

8.2. Variations in reaction conditions

Previously we have discussed that the apparent activation enthalpy varies with reaction conditions due to coverage dependent contributions, Section 6. Since the slope of a given tangent in an Arrhenius plot is $H^{\ddagger}_{app}/R$ and the intersection with the y-axis is $\ln(A_{app})$ it must be expected that both of these values change if any of them change. This is illustrated in Fig. 19. It can be seen from the figure that a large apparent activation enthalpy leads to a large apparent prefactor and vice versa. This means that an Arrhenius analysis not resulting in a straight line will lead to some sort of compensation effect. The question is then: does this effect originating from the Arrhenius analysis result in a compensation effect according to the Cremer–Constable relation?

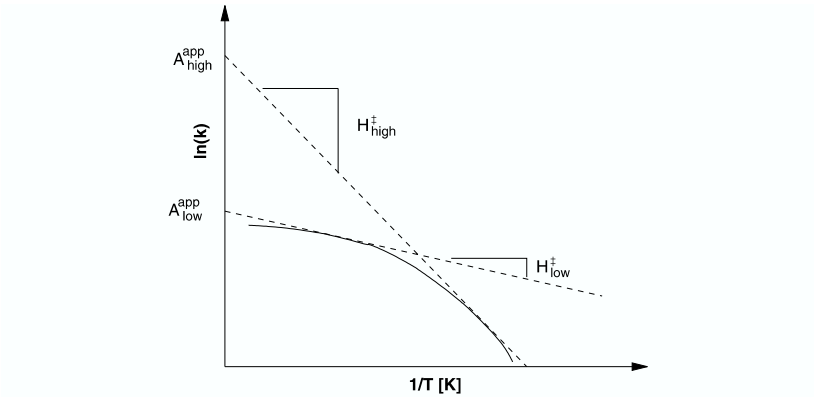

Fig. 19. Illustration of compensation effect originating from an Arrhenius analysis.

To investigate this we derive the slope in the Constable plot with respect to variations in temperature. Since the curve is deduced from an Arrhenius analysis the coordinates will be given by

$$\ln(A_{app}) = \frac{H^{\ddagger}_{app}}{RT} + \ln(r_{+}(T)) \tag{71}$$

$$H^{\ddagger}_{app} = RT^2 \frac{\partial \ln(r_{+}(T))}{\partial T} \tag{72}$$

By eliminating $H^{\ddagger}_{app}$ in $\ln(A_{app})$ the slope is given by

$$\frac{d\ln(A_{app})}{dH^{\ddagger}_{app}} = \frac{\frac{\partial \ln(A_{app})}{\partial T}}{\frac{\partial H^{\ddagger}_{app}}{\partial T}} = \frac{\frac{\partial}{\partial T}\left(T\frac{\partial \ln(r_{+}(T))}{\partial T} + \ln(r_{+}(T))\right)}{\frac{\partial}{\partial T}\left(RT^2\frac{\partial \ln(r_{+}(T))}{\partial T}\right)} \tag{73}$$

$$\frac{d\ln(A_{app})}{dH^{\ddagger}_{app}} = \frac{1}{RT} \tag{74}$$

This means that if experimental series resulting in variations in apparent activation enthalpy is based on variations in temperature alone, the slope in the resulting Constable plot will be independent of the mechanism and will only depend on temperature. To show that the analysis is valid for a rate expression we use model 2b to calculate apparent prefactors and apparent activation enthalpies as a function of temperature at three different pressures. The results can be seen in Fig. 20. A corresponding Arrhenius plot was shown earlier in Fig. 12.

Numerical differentiation of the curves shown in Fig. 20 shows that all three curves have the slope $(RT)^{-1}$ in each point. Hence, if a Constable plot is made for experiments where temperature and other reaction conditions are varied, this will re-

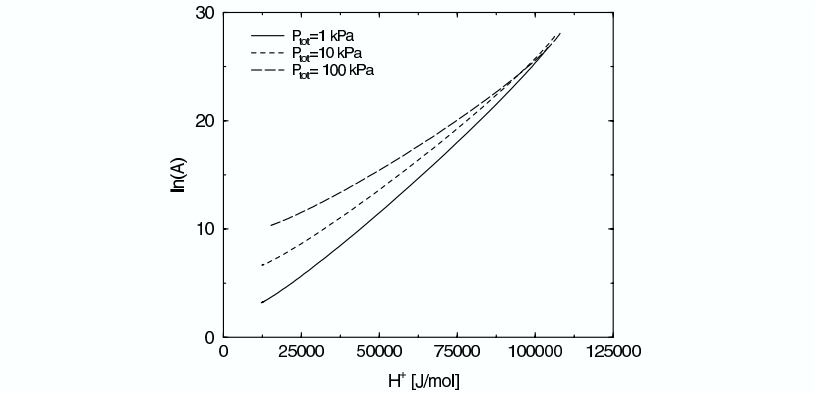

Fig. 20. Constable plot for variations in apparent prefactors and activation enthalpies due to temperature changes at different total pressures for model 2b. $y_{A_2} = y_B = 0.45$, $y_{AB} = 0.1$ and $T = 300\,K$–$1300\,K$.

sult in a number of scattered points and the average slope is expected to be close to $(RT)^{-1}$. The magnitude of this scattering will depend on the system.

If the compensation effect is found with respect to another variable than temperature this result is not directly applicable. Instead a more general explanation for the compensation effect can be found from the definition of the apparent prefactor

$$\ln(A_{app}) = H^{\ddagger}_{app}\frac{1}{RT} + \ln(r_+) \tag{75}$$

It is observed from Eq. (75) that unless r_+ varies dramatically (at least an order of magnitude) $\ln(A_{app})$ will be linearly correlated with $H^{\ddagger}_{app}$. Thus in most cases we must expect that the constable plot will have a slope of approximately $1/(RT)$.

To illustrate this we have made a Constable plot for model 2b where the pressure of one of the reactants (A_2) is varied, Fig. 21. The rate of reaction for this simulation is presented in Fig. 4A.

Fig. 21 shows obvious compensation effect according to the Cremer–Constable relation. As in the case of variations in temperature the changes in apparent activation enthalpy and prefactor is due to the coverage dependent terms. These results are in agreement with the work of Bond et al. [33,34] who show both by model calculations and experimentally that the apparent activation enthalpy and prefactor increases with increasing reactant pressure.

8.2.1. Experimental examples

To illustrate that compensation effects observed in catalysis can be explained through our analysis, we present two examples. Ribeiro et al. [45] have compiled extensive kinetic data for the ethane hydrogenolysis on Pt and for CO hydrogenation on Co.

A Constable plot of ethane hydrogenolysis is shown in Fig. 22. The data shows a clear correlation between the apparent activation enthalpy and the apparent

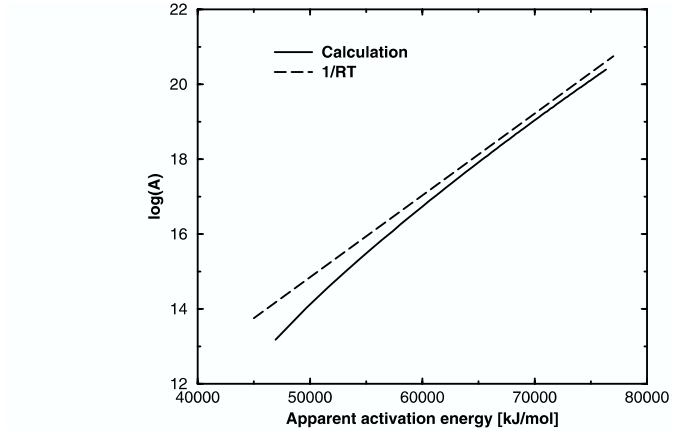

Fig. 21. Constable plot for variations in apparent prefactors and activation enthalpies due to changes in p_{A_2} for model 2b. $p_{A_2} = 0.01$–$200\,kPa$, $p_B = 10{,}000\,Pa$ and $T = 550\,K$.

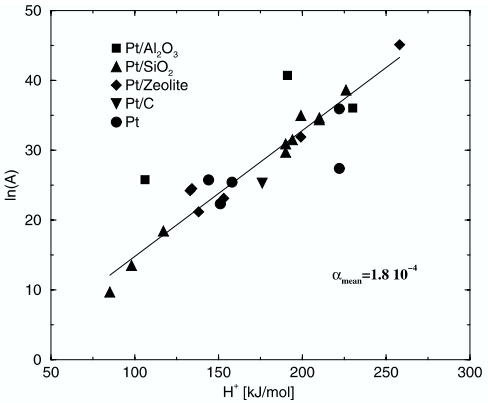

Fig. 22. Apparent prefactors as a function of apparent activation enthalpies for ethane hydrogenolysis on Pt with different supports. Loadings 0.5–10 wt.% Pt to pure Pt. Temperature = 230–400 °C and $p_{H_2} = 2$–$712\,Torr$, $p_{C_2H_3} = 1$–$190\,Torr$ [45].

prefactor, which is evidence for a compensation effect. Three of the data points seems to be outliers, and have been left out in the calculation of the average slope. The average slope $\alpha_{mean} = 1.80 \times 10^{-4}\,mol/J$ is in reasonable agreement with $1/(RT_{mean}) = 2.05 \times 10^{-4}\,mol/J$.

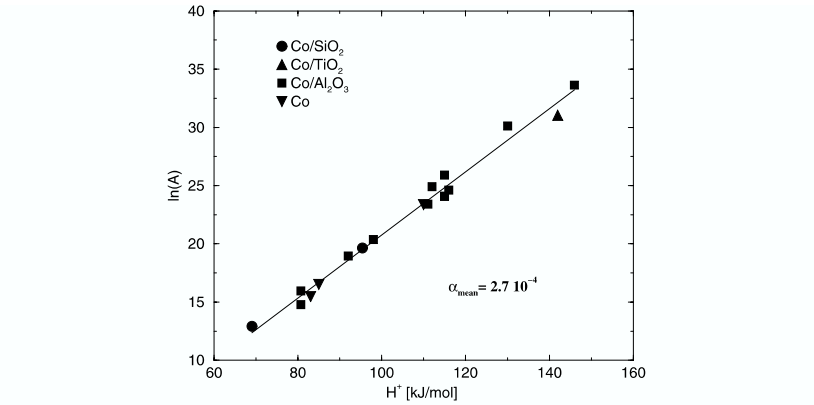

Fig. 23. Apparent prefactors as a function of apparent activation enthalpies for CO hydrogenation on Co with different supports. Loadings 3–31.4wt.% Co to pure Co. $T = 448$–548K, $p_{H_2} = 0.67$–3 ATM $p_{CO} = 0.25$–10.05 ATM [45].

For CO hydrogenation on Co only apparent activation enthalpies and turnover frequencies (TOF) are given in Ref. [45]. To calculate the apparent prefactor we use the tabulated TOF's and apparent activation enthalpies.

$$\ln(A) = \ln\left(\frac{r}{\exp\left(-\frac{H^{\ddagger}_{app}}{RT}\right)}\right) \tag{76}$$

A Constable plot of the CO hydrogenation on Co based on tabulated values of apparent activation enthalpies and calculated apparent prefactors is shown in Fig. 23. Again a clear compensation effect is illustrated, with reasonable agreement between the measured slope $\alpha_{mean} = 2.7 \times 10^{-4}$mol/J and the calculated slope $1/(RT_{mean}) = 2.4 \times 10^{-4}$mol/J.

The good agreement between the measured and the calculated slopes for both experiments corroborate our analysis and the hypothesis that compensation effects is an artifact of the data analysis.

8.3. Catalyst material

Some of the classical examples of compensation effects are the cases when the same reactions is run over different catalyst materials. Recently, Bligaard et al. [19] explained the compensation effect observed for the ammonia synthesis by a BEP relationship between activation barrier of dissociation and the enthalpy of adsorption of the dissociation products. Bligaard et al. demonstrated that the compensation effect with varying catalyst materials is general to all systems where such a BEP relationship exists when the dissociation is rate limiting. Since our analysis

shows that a BEP relationship is unnecessary to explain compensation effects with respect to reaction conditions, we will investigate if the compensation effect may be explained without the BEP relation for changing catalyst material as well.

To investigate this we find the coordinates in a Constable plot as a function of reactant stability (H_{A*}) for model 2b. The slope in the Constable plot is

$$\frac{d(\ln(A))}{d(H^{\ddagger})} = \frac{\frac{\partial(\ln(A))}{\partial(H_{A*})}}{\frac{\partial(H^{\ddagger})}{\partial(H_{A*})}} = \frac{\frac{\partial(H^{\ddagger})}{\partial(H_{A*})}\frac{1}{RT} + \frac{\partial(\ln(r))}{\partial(H_{A*})}}{\frac{\partial(H^{\ddagger})}{\partial(H_{A*})}} \tag{77}$$

This means that the slope will be $(RT)^{-1}$ if $\frac{\partial(\ln(r))}{\partial(H_{A*})} = 0$. Which corresponds to the maximum rate and optimum stability of A* in the volcano curve, Fig. 18. Intuitively, it might be expected that this was valid for high and low stability too, since r_+ is zero in these limits. This is, however, not the case which can be shown by deriving the high and low stability limits of ln(A) and $H^{\ddagger}$, from

$$H^{\ddagger} = H^{\ddagger}_3 + \frac{1}{2}\Delta H_1 + \Delta H_2 - \Delta H_1\theta_{A*} - 2\Delta H_2\theta_{B*} + 2\Delta H_4\theta_{AB*} \tag{78}$$

$$\ln(A) = \frac{H^{\ddagger}}{RT} + \ln\left(k_3K_2\left(K_1\frac{p_{A_2}}{p^{\ominus}}\right)^{\frac{1}{2}}\frac{p_B}{p^{\ominus}}\theta_*^2\right) \tag{79}$$

The high stability limit is

$$H^{\ddagger} = H^{\ddagger}_3 - \frac{1}{2}\Delta H_1 + \Delta H_2 \tag{80}$$

$$\ln(A) = \frac{-\frac{1}{2}\Delta S_1 + \Delta S_2}{R} + \ln\left(A_3\left(\frac{p_{A_2}}{p^{\ominus}}\right)^{-\frac{1}{2}}\frac{p_B}{p^{\ominus}}\right) \tag{81}$$

The low stability limit is

$$H^{\ddagger} = H^{\ddagger}_3 + \frac{1}{2}\Delta H_1 + \Delta H_2 - 2\Delta H_2\theta_{B*} + 2\Delta H_4\theta_{AB*} \tag{82}$$

$$\ln(A) = \frac{2(\Delta H_4\theta_{AB*} - \Delta H_2\theta_{B*})}{RT} + \frac{\frac{1}{2}\Delta S_1 + \Delta S_2}{R} + \ln\left(A_3\left(\frac{p_{A_2}}{p^{\ominus}}\right)^{\frac{1}{2}}\frac{p_B}{p^{\ominus}}\theta_*^2\right) \tag{83}$$

For both limits it is seen that the activation enthalpy is linearly correlated with the stability of H_{A*} whereas the prefactor is independent of the stability. This means that the slope in both of these regions is zero. This means that the Constable plot for model 2b consist of low and high stability regions with zero slope and an intermediate region with slope $(RT)^{-1}$, Fig. 24. If the above analysis is carried out for model 2a with and without the BEP relationship, Fig. 25, it is found that both high and low stability limits will be present in the case of BEP, but only the high stability limit is present without it. This different behavior can be explained by the different behavior

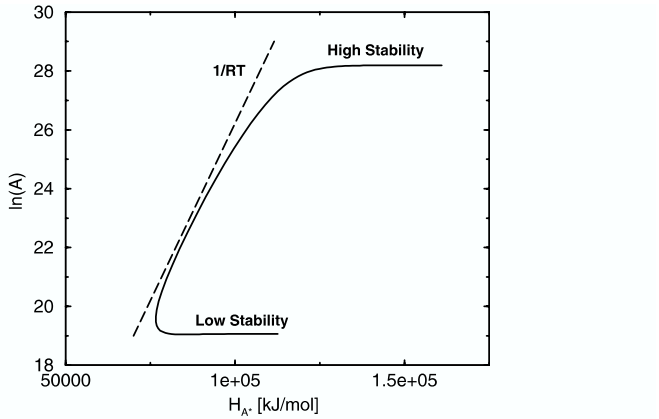

Fig. 24. Constable plot for model 2b with respect to variations in the adsorption enthalpy of reactant A_2. Calculated with model 2b. $H_{A*} = -100$–0 kJ, $p_{A_2} = p_B = 10$ kPa, $p_{AB} = 1$ kPa and $T = 500$ K.

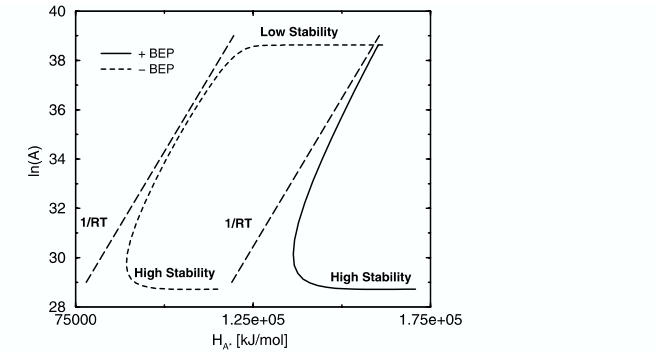

Fig. 25. Constable plot for model 2a with respect to variations in the adsorption enthalpy of reactant A_2. Calculated with model 2a with and without the BEP relation. $H_{A*} = -140$–0 kJ, $p_{A_2} = p_B = 100$ kPa, $p_{AB} = 10$ kPa and $T = 500$ K.

in reaction rates with respect to H_{A*} for the two models, Fig. 18. The model without the BEP relation goes towards a constant rate at low stability, thus the slope will be $\sim 1/RT$.

All three simulations have fairly large ranges where they show compensation effect. This demonstrates that the BEP relation is not necessary to explain the compensation effect.

8.4. Summary

In the analysis of the Constable plots it is a danger to overlook the fact that the x- and y-coordinates in this plot ultimately come from the slope and the intercept in the Arrhenius plot and are thus heavily correlated.

In this section we showed that the compensation effect will be observed when reactions show nonlinearity in the Arrhenius plot. Under Region 2 conditions we must thus always expect to find compensation effect. With respect to different catalyst materials the nonlinearity is caused by differences in binding energies and activation enthalpies, which means that a compensation effect should be quite general since these contributions are likely to vary. In both cases our analysis shows that the slope in the Constable plot will be close to $1/(RT)$, which means that it is independent of reaction mechanism and kinetics.

Compensation effects should therefore be quite general, and this offers an explanation to why the compensation effect is observed for so many different reactions.

9. Industrial reactions

Until now we have focused on models. However, the phenomena treated in this manuscript have consequences for industrial reactions too. To illustrate this we use three important industrial reactions, the ethylene epoxidation, [13,46–55] the methanol oxidation to formaldehyde [12,56–64] and the ammonia synthesis [1,6,14,65–75]. The reason why these three reactions are used is that they have been studied extensively and a fairly good understanding have been obtained.

9.1. Ethylene epoxidation

The overall reaction can be written as:

$$C_2H_4 + \frac{1}{2}O_2 \rightleftharpoons C_2H_4O \tag{84}$$

The selectivity is limited by combustion of ethylene and ethylene oxide.

$$C_2H_4 + 3O_2 \rightleftharpoons 2CO_2 + 2H_2O \tag{85}$$

$$C_2H_4O + \frac{5}{2}O_2 \rightleftharpoons 2CO_2 + 2H_2O \tag{86}$$

We recently developed a micro-kinetic model of ethylene epoxidation on Ag, Table 5, which describes both steady-state kinetics and transient surface science experiments [13,54,55]. The rate equations are solved using the steady state approximation, and it turns out that steps 2, 5, 8 and 9 are rate limiting while all the others are equilibrated. The reaction mechanism and model parameters are mainly extracted from transient UHV experiments on Ag(1 1 1), and a few parameters were fitted to steady state kinetics on Ag(1 1 1) [13].

Table 5
Reaction mechanism for the ethylene oxidation

$O_2(g) + * \rightleftharpoons O_2*$	(step 1)
$O_2* + * \rightleftharpoons 2O*$ (slow)	(step 2)
$O_2(g) + 2O* \rightleftharpoons 2O/O*$	(step 3)
$C_2H_4(g) + O* \rightleftharpoons C_2H_4/O*$	(step 4)
$C_2H_4/O* + O/O* \rightleftharpoons CH_2\ CH_2O/O* + O*$ (slow)	(step 5)
$C_2H_4O(g) + O* \rightleftharpoons C_2\ H_4O/O*$	(step 6)
$CH_2CH_2O/O* \rightleftharpoons C_2H_4O/O*$	(step 7)
$CH_2CH_2O/O* \rightleftharpoons CH_3CHO/O*$ (slow)	(step 8)
$CH_3CHO/O* \rightleftharpoons CH_3CHO(g) + O*$ (slow)	(step 9)
$CH_3CHO/O* + 6O* \rightleftharpoons 2CO_2* + 4OH* + *$	(step 10)
$C_2H_4(g) + * \rightleftharpoons C_2H_4*$	(step 11)
$2OH* \rightleftharpoons H_2O* + O*$	(step 12)
$CO_2* \rightleftharpoons CO_2(g) + *$	(step 13)
$H_2O* \rightleftharpoons H_2O(g) + *$	(step 14)

* is a Ag site, /O* is a surface oxide site, and X* and Y/O* is an adsorbed species on Ag and surface oxide, respectively.

9.1.1. Apparent activation enthalpy

In Fig. 26 the model has been used to simulate the experimental Arrhenius plots of Campbell [47] and Grant and Lambert [46]. The mechanism reproduces the activation enthalpy in both series closely, however, the predicted activities for Grant and Lamberts experiment are a bit too low.

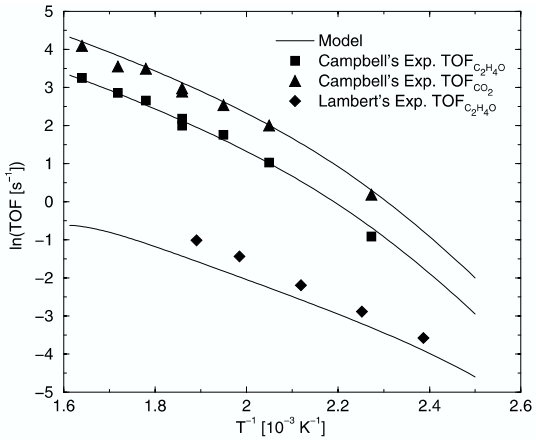

Fig. 26. Simulated and experimental Arrhenius plot of C_2H_4O and CO_2 formation on Ag(111). Campbell's experiments [47]: $p_{O_2} = 150$ Torr, $p_{C_2H_4} = 20$ Torr, Lambert's experiment [46]: $p_{O_2} = 5$ Torr, $p_{C_2H_4} = 5$ Torr. Obtained on Ag(111) and $T = 440$–620 K.

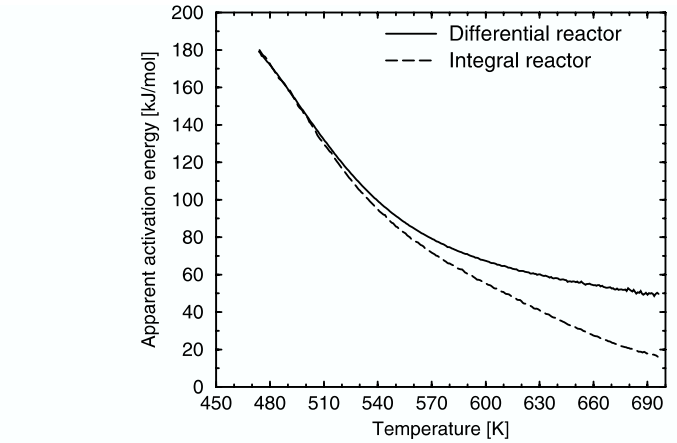

Fig. 27. Calculated apparent activation enthalpy for ethylene oxidation for a differential and a integral reactor. $p_{CO_2} = p_{O_2} = 120$ kPa and $p_{C_2H_4} = 400$ kPa.

Both simulations and experiments show a curved Arrhenius plot for Campbells experiments, but a almost straight line in Grant and Lambert's experiments. The reason for this behavior is that Campbell used moderate reactant pressures while Grant and Lambert used very low pressures. Thus Grant and Lambert conducted their measurements in Region 3, while Campbell measurements are in Region 2, Section 6.4.1. It is clear that the changing activation enthalpy in Campbell's experiments was observed because of the large temperature range applied. If the measurement at the lowest temperature was omitted this trend would not have been observed.

The dependence of the apparent activation enthalpy on temperature can be seen in Fig. 27. Ethylene oxidation is carried out at 473–573 K which means that this is an example of a reaction system which is run in *Region 2*, Section 6.2. This explains why experimentally measured values varies from 20 kJ/mol to 100 kJ/mol dependent on reaction conditions [13]. Further, most Arrhenius plots reported for this reaction system results in straight lines, this demonstrates the problems of linearization in Arrhenius analysis as discussed in Section 6.4.1.

9.1.2. Reaction orders

The reaction orders in oxygen and ethylene are known to decrease from positive to negative values with increasing oxygen and ethylene pressures, respectively, [13].

In Fig. 28A experimental and calculated turnover frequencies for ethylene oxide production are compared. It is clear that a maxima in turnover frequencies exist, which indicates that the reaction order in ethylene pressure decreases from positive to negative values with ethylene pressure. This is shown directly in Fig. 28B where

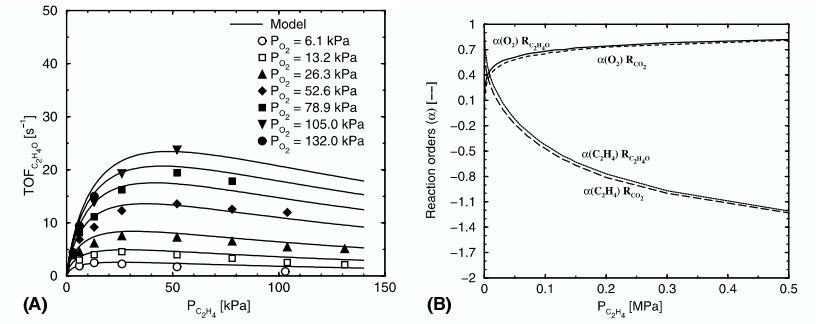

Fig. 28. (A) Experimental [76] and calculated turnover frequencies for ethylene oxide production vs. ethylene pressure at different oxygen pressures at $T = 493$ K and (B) calculated reaction orders in ethylene and oxygen pressure for the experimental series of $p_{O_2} = 52.6$ kPa.

the reaction order in ethylene and oxygen pressure is calculated for the experimental series of $p_{O_2} = 52.6$ kPa.

9.2. Methanol oxidation

The partial oxidation of methanol to formaldehyde may be written as the following overall reaction [12]:

$$2CH_3OH(g) + \frac{1}{2}O_2(g) \rightleftharpoons 2H_2CO(g) + H_2O(g) + H_2(g) \quad (87)$$

with selectivity limitations due to further oxidation of formaldehyde

$$H_2CO(g) + \frac{1}{2}O_2(g) \rightleftharpoons CO_2(g) + H_2(g) \quad (88)$$

Recently we proposed a detailed micro-kinetic model [12] of the oxidation of methanol on Ag. This model explains both UHV experiments and the kinetics at industrial reaction conditions.

The model is based on the Langmuir–Hinshelwood mechanism presented in Table 6, where steps 5 and 10 are rate limiting. All of the elementary steps have have been extracted from the UHV work of Wachs and Madix on Ag(1 1 0) [56]. The rate equations have been solved using quasi-equilibrium approximation. The parameters are mainly determined from surface science experiments on single crystals, but a few parameters have been determined from steady state kinetics [12].

9.2.1. Apparent activation enthalpies

The apparent activation enthalpy is calculated as a function of temperature for the oxidation of methanol to formaldehyde both for differential and integral reactor conditions as outlined in Section 6. The predictions of the model are compared with experimental data, Fig. 29. The experimental data are from references [77,64,78,79].

Table 6
Reaction mechanism used for methanol oxidation

$CH_3OH(g) + * \rightleftharpoons CH_3OH*$	(step 1)
$O_2(g) + * \rightleftharpoons O_2*$	(step 2)
$O_2* + * \rightleftharpoons 2O*$	(step 3)
$2CH_3OH* + O* \rightleftharpoons 2CH_3O* + H_2O*$	(step 4)
$CH_3O* + * \rightleftharpoons H_2CO* + H*$ (slow)	(step 5)
$H_2CO* \rightleftharpoons H_2CO(g) + *$	(step 6)
$2H* \rightleftharpoons H_2(g) + 2*$	(step 7)
$H_2O \rightleftharpoons H_2O(g) + *$	(step 8)
$H_2CO* + O* \rightleftharpoons H* + HCOO*$	(step 9)
$HCOO* + * \rightleftharpoons H* + CO_2*$ (slow)	(step 10)
$CO_2* \rightleftharpoons CO_2(g) + *$	(step 11)

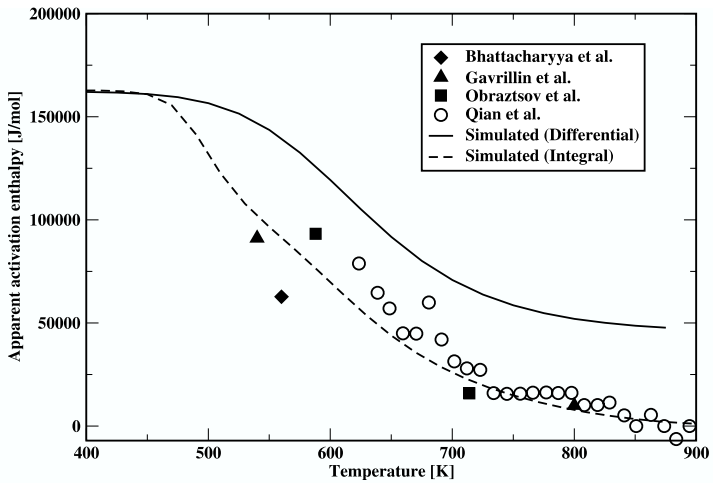

Fig. 29. Calculated apparent activation enthalpies as a function of temperature of methanol oxidation to formaldehyde compared with experimental values. Both by the differential and integral reactor formalism.

The data from Qian et al. [78] is calculated by Eq. (66) from reported methanol conversions.

Based on the temperature dependence of the observed activation enthalpies it has been proposed that two different reaction mechanism are dominating at high and low temperature [59,77]. The micro-kinetic model uses the same mechanism at all conditions and reproduces the experimental observations well, especially when the reactor is treated as an integral reactor. It is thus not necessary to assume two different reaction mechanism in order to explain the observed temperature dependence of the apparent activation enthalpy.

Table 7
Reaction mechanism used for the ammonia synthesis

$N_2(g) + * \rightleftharpoons N_2*$	(step 1)
$N_2* + * \rightleftharpoons 2N*$	(step 2)
$H_2(g) + 2* \rightleftharpoons 2H*$	(step 3)
$N* + H* \rightleftharpoons NH* + *$	(step 4)
$NH* + H* \rightleftharpoons NH_2* + *$	(step 5)
$NH_2* + H* \rightleftharpoons NH_3* + *$	(step 6)
$NH_3* \rightleftharpoons NH_3(g) + *$	(step 7)

Industrially the partial oxidation of methanol to formaldehyde is carried out at approximately 900 K and 1 bar. Under these conditions the reaction can be classified as *Region 3*, Section 6.2. However, many laboratory experiments are carried out at lower temperatures, and at these conditions the reaction is in *Region 2*.

9.3. Ammonia synthesis

The ammonia synthesis can be described by the following overall reaction

$$N_2(g) + 3H_2(g) \rightleftharpoons 2NH_3(g) \quad (89)$$

The reaction has been modeled [1] with the QEA based on the mechanism shown in Table 7 with step 2 as the rate limiting step. The mechanism and parameters are extracted [1] from UHV measurements on single crystals.

9.3.1. Apparent activation enthalpy

We have used the micro-kinetic model to calculate the apparent activation enthalpy as a function of temperature. A step is included to describe poisoning by water

$$H_2O(g) + * \rightleftharpoons O* + H_2(g) \quad (90)$$

The results, Fig. 30, show that the apparent activation enthalpy in the dry gas is independent of temperature changes. This can be explained by a high and nearly constant coverage of N* throughout the investigated temperature range, and classifies the ammonia synthesis as *Region 1*, Section 6.2. Introducing water into the reaction feed results in much higher apparent activation enthalpies at low temperature. The effect of water can be rationalized by comparing the stabilities of O*, N* and H*

Reaction	ΔG°	ΔH°
$0.5H_2 + * \rightleftharpoons H*$	−4 kJ/mol	−47 kJ/mol
$NH_3 + * \rightleftharpoons N* + 1.5H_2$	−63 kJ/mol	−65 kJ/mol
$H_2O + * \rightleftharpoons O* + H_2$	−93 kJ/mol	−117 kJ/mol

O* is more stable on the surface at low temperatures due to the more pronounced exothermic reaction.

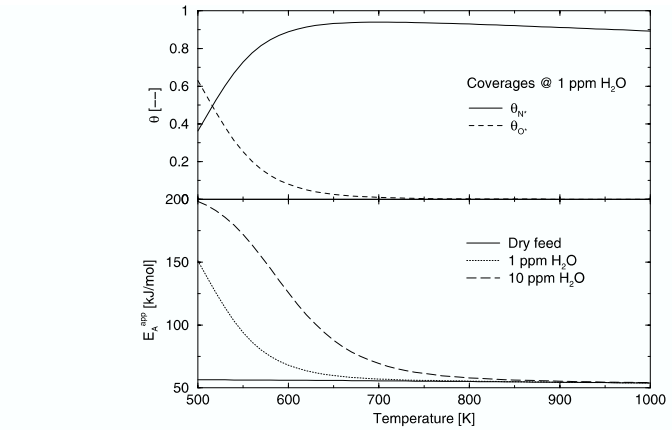

Fig. 30. Apparent activation enthalpy for ammonia synthesis on a Fe catalyst as a function of temperature. p_{tot} = 10.1 MPa, N:H:NH_3 ratio 9:27:7, with a dry feed, with 1 ppm and 10 ppm of water.

9.4. Summary

In this section we have demonstrated that the phenomenons treated in this manuscript based on model calculations e.g. changes in apparent activation enthalpy and reaction orders, respectively, with reaction conditions are directly applicable to industrial reactions. Based on the framework of regions in Arrhenius plots developed in Section 6, we classify ammonia Synthesis on Fe as a Region 1 reaction, ethylene epoxidation on Ag as a Region 2 reaction, and finally methanol to formaldehyde on Ag as a Region 3 reaction.

10. Conclusion

We have analyzed a number of kinetic models representing a wide range of possibilities for reaction mechanisms for the reaction $A_2 + 2B \rightleftharpoons 2AB$. As a first analysis we used the degree of rate control to test the validity of using a quasi-equilibrium approximation. This analysis showed that for reactions with one overall reaction the quasi-equilibrium approximation will be valid in most cases. The observation of a change in rate limiting step requires relations between rate constants and reaction conditions which are unlikely to occur by chance.

The analysis of reaction orders in Section 5 showed that even for simple reactions the reaction orders vary in a complex manner with reaction conditions. This variation is due to the competition for active sites and implies that a change in reaction

order can not be taken as an evidence for a change in reaction path or similar explanations.

In Section 6 we analyzed a number of pitfalls in the analysis of experimental data. In practice rate constants cannot be measured directly and it might be tempting to use macroscopic measurable values in the Arrhenius plot, such as by the approach to equilibrium, the net rate, or the conversion of a reactant. The analysis showed that each of these shortcuts may introduce large errors. For the analysis of experimental data there is thus no alternative to the detailed fit of data to a suitable model for an appropriate reactor.

The analysis of the models in Section 6 showed that the apparent activation enthalpy contains coverage dependent terms. This means that even simple mechanisms may display variations in apparent activation enthalpy. Thus, a kink in an Arrhenius plot can be caused by different phenomena e.g. a change in reaction path, diffusion limitations or changes in coverages. Without other experimental evidence we are not able to discriminate between these explanations.

The analysis showed that three regions exist in Arrhenius plots for heterogeneous catalysis

Region 1 is a high coverage region found at low temperature where the coverage dependent terms are almost constant leading to a practically constant apparent activation enthalpy under all reaction conditions. Ammonia synthesis on Fe is an example of a reaction operated industrially under these conditions.

Region 2 is an intermediate coverage region. In this region the total coverage will vary with the reaction conditions leading to non-linearity in the Arrhenius plot. The epoxidation of ethylene is an example of a reaction operated industrially under these conditions.

Region 3 is a low coverage region found at high temperature. In this region the apparent activation enthalpy is independent of reaction conditions since the coverage dependent terms are essentially zero. However, the apparent prefactor varies with composition and pressure, which means that a variations in these conditions leads to a curve for each composition and pressure in the Arrhenius plot. The selective oxidation of methanol to formaldehyde is operated industrially under these conditions, but most of the experimental work for the reaction is carried out under Region 2 conditions.

Caution should be exercised in the interpretation of reported activation enthalpies and to the use of Arrhenius plots. Even if the reaction is not limited by mass transfer phenomenon and the data is analyzed correctly, the apparent activation enthalpy will only agree with the activation enthalpy of the rate limiting step in one case: the rate limiting step is an adsorption and the measurements are made in Region 3. Unfortunately it is in Region 3 that mass transfer phenomena are most likely to be important.

Comparing rate expressions for mechanisms 1–3 we have observed that simplifying mechanisms by lumping elementary steps is problematic. In some cases, the simplified mechanism will have the same kinetics as the original mechanism in the appropriate limits. In other cases, the simplified mechanism has different kinetics than the original mechanism in all cases. This shows that caution should be taken when mechanism are simplified and that it has to be checked if the simplified mechanism has the correct boundaries.

We have analyzed a simple model where the stability of intermediates depend linearly on a parameter, and shown that this model in a number of cases result in a sharp maximum in reaction rate, a volcano curve. A linear dependence of the activation enthalpy on the stability of adsorbates, a BEP relation, always leads to a volcano curve. However a volcano curve may also be observed in the absence of a BEP relation. The experimental observation of a volcano curve can thus not be taken as a evidence for the existence of a BEP relation.

In Section 8 we showed that compensation effect will be observed when reactions show nonlinearity in the Arrhenius plot. Under Region 2 conditions we must thus always expect to find compensation effect. With respect to different catalyst materials the nonlinearity is caused by differences in binding energies and activation enthalpies, which are likely to vary between different metals. In both cases our analysis shows that the slope in the Constable plot will be close to $1/(RT)$, which means that it is independent of reaction mechanism and kinetics, this offers an explanation to why the compensation effect is observed for so many different reactions.

The synthesis of ammonia, methanol and formaldehyde are all industrial reactions catalyzed by metals, yet all three reactions proceed in different kinetic regimes. This demonstrates that generalizations must be made with caution and care.

In conclusion our analysis of a series of possible mechanism for the reaction $A_2 + 2B \rightleftharpoons 2AB$ has illustrated that the macro-kinetics is easily deduced from the micro-kinetics, while it is generally difficult to derive information on the reaction mechanism from measured macro-kinetics. Even conventional kinetic parameters such as apparent activation enthalpy and reaction orders depend on the reaction conditions and has to be analyzed by a micro-kinetic model.

The ambiguities and pitfalls uncovered by our analysis can be traced to the complexity introduced by the competition for adsorption sites in a heterogeneous catalyzed reaction. Macroscopic measurements imply an averaging out of details at the molecular level which further increases the complexity. The only road to tenable conclusions is in our opinion to combine quantum mechanical calculations and careful experiments using a range of techniques with extensive micro-kinetic simulations. Calculations, measurements or simulations alone is unlikely to take us anywhere.

Acknowledgment

We would like to express our sincere thanks to Haldor Topsøe A/S for financial support of H. Lynggaard.

Appendix A. Kinetic models

This Appendix contains expressions for rates, coverages, apparent activation enthalpy, and reaction orders for the kinetic models presented in Section 3. The derivations of these formulas are similar to the presented examples in Section 2 and details in the derivations are therefore omitted.

A.1. Mechanism 1

Model 1 is a simple mechanism which has been used in the literature [19] to analyze reactions where the dissociation of a reactant is rate limiting

$$A_2 + 2* \rightleftharpoons 2A* \quad \text{(Step 1)}$$

$$A* + B \rightleftharpoons AB + * \quad \text{(Step 2)}$$

The stoichiometric matrix for this reaction is

Step	A_2	B	AB	A*	γ_r
1	−1	0	0	2	1
2	0	−1	1	1	2
Sum	−1	−2	2	0	

On the basis of this mechanism we have made three different kinetic models with different rate limiting steps they are:

Model name	Rate limiting steps	Model type
Model 1a	Step 1	QEA
Model 1b	Step 2	QEA
Model 1c	Steps 1 and 2	SSA

A.1.1. Model 1a

Coverages

$$\theta_{A*} = \frac{1}{K_2}\frac{p_{AB}}{p_B}\theta_* \tag{A.1}$$

$$\theta_* = \frac{1}{1 + \frac{1}{K_2}\frac{p_{AB}}{p_B}} \tag{A.2}$$

Rate expression

$$r_{1a} = k_1\frac{p_{A_2}}{p^\ominus}\theta_*^2 - \frac{k_1}{K_1}\theta_{A*}^2 \tag{A.3}$$

$$= k_1\frac{p_{A_2}}{p^\ominus}(1-\beta)\theta_*^2 \tag{A.4}$$

$$= \frac{\frac{p_{A_2}}{p^\ominus}(1-\beta)}{\left(1 + \frac{1}{K_2}\frac{p_{AB}}{p_B}\right)^2} \tag{A.5}$$

Reaction orders

$$\alpha_{A_2} = 1 \tag{A.6}$$

$$\alpha_B = 2\theta_{A*} \tag{A.7}$$

$$\alpha_{AB} = -2\theta_{A*} \tag{A.8}$$

Apparent activation enthalpy

$$H^\ddagger = H_1^\ddagger + 2\Delta H_2\theta_{A*} \tag{A.9}$$

A.1.2. Model 1b

Coverages

$$\theta_{A*} = \sqrt{K_1\frac{p_{A_2}}{p^\ominus}}\theta_* \tag{A.10}$$

$$\theta_* = \frac{1}{1 + \sqrt{K_1\frac{p_{A_2}}{p^\ominus}}} \tag{A.11}$$

Rate expression

$$r_{1b} = k_2\frac{p_B}{p^\ominus}\theta_{A*} - \frac{k_2}{K_2}\frac{p_{AB}}{p^\ominus}\theta_* \tag{A.12}$$

$$= k_2\sqrt{K_1\frac{p_{A_2}}{p^\ominus}}\frac{p_B}{p^\ominus}(1-\sqrt{\beta})\theta_* \tag{A.13}$$

$$= \frac{k_2\sqrt{K_1\frac{p_{A_2}}{p^\ominus}}\frac{p_B}{p^\ominus}(1-\sqrt{\beta})}{1 + \sqrt{K_1\frac{p_{A_2}}{p^\ominus}}} \tag{A.14}$$

Reaction orders

$$\alpha_{A_2} = \frac{1}{2} - \frac{1}{2}\theta_{A*} \tag{A.15}$$

$$\alpha_B = 1 \tag{A.16}$$

$$\alpha_{AB} = 0 \tag{A.17}$$

Apparent activation enthalpy

$$H^{\ddagger} = H_2^{\ddagger} + \frac{1}{2}\Delta H_1 - \frac{1}{2}\Delta H_1 \theta_{A*} \tag{A.18}$$

A.1.3. Model 1c

Steady-state balance

$$2r_1 = r_2 \tag{A.19}$$

$$k_1 \frac{p_{A_2}}{p^{\ominus}} \theta_*^2 - 2\frac{k_1}{K_1}\theta_{A*}^2 = k_2 \theta_{A*} \frac{p_B}{p^{\ominus}} - \frac{k_2}{K_2}\frac{p_{AB}}{p^{\ominus}}\theta_* \tag{A.20}$$

$$2k_1 \frac{p_{A_2}}{p^{\ominus}} (1-\theta_{A*})^2 - 2\frac{k_1}{K_1}\theta_{A*}^2 = k_2 \theta_{A*} \frac{p_B}{p^{\ominus}} - \frac{k_2}{K_2}\frac{p_{AB}}{p^{\ominus}}(1-\theta_{A*}) \tag{A.21}$$

Coverages

$$\theta_{A*} = \frac{-b \pm \sqrt{b^2 - 4ac}}{2a} \tag{A.22}$$

$$\theta_* = 1 - \theta_{A*} \tag{A.23}$$

where

$$a = 2k_1 \frac{p_{A_2}}{p^{\ominus}} - 2\frac{k_1}{K_1} \tag{A.24}$$

$$b = -4k_1 \frac{p_{A_2}}{p^{\ominus}} - k_2 \frac{p_B}{p^{\ominus}} - \frac{k_2}{K_2}\frac{p_{AB}}{p^{\ominus}} \tag{A.25}$$

$$c = 2k_1 \frac{p_{A_2}}{p^{\ominus}} + \frac{k_2}{K_2}\frac{p_{AB}}{p^{\ominus}} \tag{A.26}$$

Rate of reaction

$$r_{1c,step1} = k_1 \frac{p_{A_2}}{p^{\ominus}} \theta_*^2 - \frac{k_1}{K_1}\theta_{A*}^2 \tag{A.27}$$

$$r_{1c,step2} = k_2 \frac{p_B}{p^{\ominus}} \theta_{A*} - \frac{k_2}{K_2}\frac{p_{AB}}{p^{\ominus}}\theta_* \tag{A.28}$$

A.2. Mechanism 2

Mechanism 2 is a Langmuir–Hinshelwood mechanism

$$A_2 + 2* \rightleftharpoons 2A* \quad \text{(Step 1)}$$

$$B + * \rightleftharpoons B* \quad \text{(Step 2)}$$

$$A* + B* \rightleftharpoons AB* + * \quad \text{(Step 3)}$$

$$AB* \rightleftharpoons AB + * \quad \text{(Step 4)}$$

The stoichiometric matrix for this mechanism is

Step	A_2	B	AB	A*	B*	AB*	γ_r
1	−1	0	0	2	0	0	1
2	0	−1	0	0	1	0	2
3	0	0	0	−1	−1	1	2
4	0	0	1	0	0	−1	2
Sum	−1	−2	2	0	0	0	

The chosen models based on this mechanism are

Model name	Rate limiting steps	Model type
Model 2a	Step 1	QEA
Model 2b	Step 3	QEA
Model 2c	Step 4	QEA
Model 2d	Steps 1 and 3	HSSA

A.2.1. Model 2a

Coverages

$$\theta_{A*} = \frac{1}{K_2 K_3 K_4}\frac{p_{AB}}{p_B}\theta_* \tag{A.29}$$

$$\theta_{B*} = K_2 \frac{p_B}{p^{\ominus}}\theta_* \tag{A.30}$$

$$\theta_{AB*} = \frac{1}{K_4}\frac{p_{AB}}{p^{\ominus}}\theta_* \tag{A.31}$$

$$\theta_* = \frac{1}{1 + \frac{1}{K_2K_3K_4}\frac{p_{AB}}{p_B} + K_2\frac{p_B}{p^{\ominus}} + \frac{1}{K_4}\frac{p_{AB}}{p^{\ominus}}} \tag{A.32}$$

Rate expression

$$r_{2a} = k_1 \frac{p_{A_2}}{p^{\ominus}}\theta_*^2 - \frac{k_1}{K_1}\theta_{A*}^2 \tag{A.33}$$

$$= k_1 \frac{p_{A_2}}{p^{\ominus}}(1-\beta)\theta_*^2$$

$$= \frac{k_1 \frac{p_{A_2}}{p^{\ominus}}(1-\beta)}{\left(1 + \frac{1}{K_2K_3K_4}\frac{p_{AB}}{p_B} + K_2\frac{p_B}{p^{\ominus}} + \frac{1}{K_4}\frac{p_{AB}}{p^{\ominus}}\right)^2} \tag{A.34}$$

Reaction orders

$$\alpha_{A_2} = 1 \tag{A.35}$$

$$\alpha_B = 2\theta_{A*} - 2\theta_{B*} \tag{A.36}$$

$$\alpha_{AB} = -2\theta_{A*} - 2\theta_{AB*} \tag{A.37}$$

Apparent activation enthalpy

$$H^{\ddagger} = H_1^{\ddagger} + 2(\Delta H_2 + \Delta H_3 + \Delta H_4)\theta_{A*} - 2\Delta H_2\theta_{B*} + 2\Delta H_4\theta_{AB*} \tag{A.38}$$

A.2.2. Model 2b

Coverages

$$\theta_{A*} = \sqrt{K_1 \frac{p_{A_2}}{p^{\ominus}}}\theta_* \tag{A.39}$$

$$\theta_{B*} = K_2 \frac{p_B}{p^{\ominus}}\theta_* \tag{A.40}$$

$$\theta_{AB*} = \frac{1}{K_4}\frac{p_{AB}}{p^{\ominus}}\theta_* \tag{A.41}$$

$$\theta_* = \frac{1}{1 + \sqrt{K_1 \frac{p_{A_2}}{p^{\ominus}}} + K_2 \frac{p_B}{p^{\ominus}} + \frac{1}{K_4}\frac{p_{AB}}{p^{\ominus}}} \tag{A.42}$$

Rate expression

$$r_{2b} = k_3\theta_{A*}\theta_{B*} - \frac{k_3}{K_3}\theta_{AB*}\theta_* \tag{A.43}$$

$$= k_3K_2\sqrt{K_1\frac{p_{A_2}}{p^{\ominus}}\frac{p_B}{p^{\ominus}}}\left(1-\sqrt{\beta}\right)\theta_*^2 = \frac{k_3K_2\sqrt{K_1\frac{p_{A_2}}{p^{\ominus}}\frac{p_B}{p^{\ominus}}}\left(1-\sqrt{\beta}\right)}{\left(1 + \sqrt{K_1\frac{p_{A_2}}{p^{\ominus}}} + K_2\frac{p_B}{p^{\ominus}} + \frac{1}{K_4}\frac{p_{AB}}{p^{\ominus}}\right)^2} \tag{A.44}$$

Reactions orders

$$\alpha_{A_2} = \frac{1}{2} - \theta_{A*} \tag{A.45}$$

$$\alpha_B = 1 - 2\theta_{B*} \tag{A.46}$$

$$\alpha_{AB} = -2\theta_{AB*} \tag{A.47}$$

Apparent activation enthalpy

$$H^{\ddagger} = H_3^{\ddagger} + \frac{1}{2}\Delta H_1 + \Delta H_2 - \Delta H_1\theta_{A*} - 2\Delta H_2\theta_{B*} + 2\Delta H_4\theta_{AB*} \tag{A.48}$$

A.2.3. Model 2c

Coverages

$$\theta_{A*} = \sqrt{K_1\frac{p_{A_2}}{p^{\ominus}}}\theta_* \tag{A.49}$$

$$\theta_{B*} = K_2\frac{p_B}{p^{\ominus}}\theta_* \tag{A.50}$$

$$\theta_{AB*} = \sqrt{K_1}K_2K_3\sqrt{\frac{p_{A_2}}{p^{\ominus}}\frac{p_B}{p^{\ominus}}}\theta_* \tag{A.51}$$

$$\theta_* = \frac{1}{1 + \sqrt{K_1\frac{p_{A_2}}{p^{\ominus}}} + K_2\frac{p_B}{p^{\ominus}} + \sqrt{K_1}K_2K_3\sqrt{\frac{p_{A_2}}{p^{\ominus}}\frac{p_B}{p^{\ominus}}}} \tag{A.52}$$

Rate expression

$$r_{2c} = k_4\theta_{AB*} - \frac{k_4}{K_4}\frac{p_{AB}}{p^{\ominus}}\theta_* \tag{A.53}$$

$$= k_4\sqrt{K_1}K_2K_3\sqrt{\frac{p_{A_2}}{p^{\ominus}}\frac{p_B}{p^{\ominus}}}\left(1-\sqrt{\beta}\right)\theta_* = \frac{k_4\sqrt{K_1}K_2K_3\sqrt{\frac{p_{A_2}}{p^{\ominus}}\frac{p_B}{p^{\ominus}}}\left(1-\sqrt{\beta}\right)}{1 + \sqrt{K_1\frac{p_{A_2}}{p^{\ominus}}}^M + K_2\frac{p_B}{p^{\ominus}} + \sqrt{K_1}K_2K_3\sqrt{\frac{p_{A_2}}{p^{\ominus}}\frac{p_B}{p^{\ominus}}}} \tag{A.54}$$

Reaction orders

$$\alpha_{A_2} = \frac{1}{2} - \frac{1}{2}\theta_{A*} - \frac{1}{2}\theta_{AB*} \tag{A.55}$$

$$\alpha_B = 1 - \theta_{B*} - \theta_{AB*} \tag{A.56}$$

$$\alpha_{AB} = 0 \tag{A.57}$$

Apparent activation enthalpy

$$H^{\ddagger} = H_3^{\ddagger} + \frac{1}{2}\Delta H_1 + \Delta H_2 - \frac{1}{2}\Delta H_1\theta_{A*} - \Delta H_2\theta_{B*} - \left(\frac{1}{2}\Delta H_1 + \Delta H_2 + \Delta H_3\right)\theta_{AB*} \tag{A.58}$$

A.2.4. Model 2d

Steady-state balance

$$\frac{d\theta_{A*}}{dt} = 2r_1 - r_3 = 0 \Rightarrow \tag{A.59}$$

$$2k_1\frac{p_{A_2}}{p^{\ominus}}\theta_*^2 - 2\frac{k_1}{K_1}\theta_{A*}^2 = k_3\theta_{B*}\theta_{A*} - \frac{k_3}{K_3}\theta_{AB*}\theta_* \quad \text{(A.60)}$$

Coverages

$$\theta_{B*} = K_2\frac{p_B}{p^{\ominus}}\theta_* \quad \text{(A.61)}$$

$$\theta_{AB*} = \frac{1}{K_4}\frac{p_{AB}}{p^{\ominus}}\theta_* \quad \text{(A.62)}$$

$$\theta_{A*} = \frac{-b \pm \sqrt{b^2 - 4ac}}{2a}\theta_* \quad \text{(A.63)}$$

$$\theta_* = 1 - \theta_{A*} - \theta_{B*} - \theta_{AB*} \quad \text{(A.64)}$$

where

$$a = 2\frac{k_1}{K_1} \quad \text{(A.65)}$$

$$b = k_3K_2\frac{p_B}{p^{\ominus}} \quad \text{(A.66)}$$

$$c = -2k_1\frac{p_{A_2}}{p^{\ominus}} - \frac{k_3}{K_3K_4}\frac{p_{AB}}{p^{\ominus}} \quad \text{(A.67)}$$

Rate expression

$$r_{2d,step1} = k_1\frac{p_{A_2}}{p^{\ominus}}\theta_*^2 - \frac{k_1}{K_1}\theta_{A*}^2 \quad \text{(A.68)}$$

$$r_{2d,step3} = k_3\theta_{A*}\theta_{B*} - \frac{k_3}{K_3}\theta_{AB*}\theta_* \quad \text{(A.69)}$$

A.3. Mechanism 3

This mechanism is a further development of the previous mechanism adding a precursor to the dissociative adsorption of A_2.

$$A_2 + * \rightleftharpoons A_2* \quad \text{(Step 1)}$$

$$A_2* + * \rightleftharpoons 2A* \quad \text{(Step 2)}$$

$$B + * \rightleftharpoons B* \quad \text{(Step 3)}$$

$$A* + B* \rightleftharpoons AB* + * \quad \text{(Step 4)}$$

$$AB* \rightleftharpoons AB + * \quad \text{(Step 5)}$$

The stoichiometric matrix for this model is

Step	A_2	B	AB	A2*	A*	B*	AB*	γ_r
1	−1	0	0	1	0	0	0	1
2	0	0	0	−1	2	0	0	1
3	0	−1	0	0	0	1	0	2
4	0	0	0	0	−1	−1	1	2
5	0	0	1	0	0	0	−1	2
Sum	−1	−2	2	0	0	0	0	

The chosen kinetic models based on this mechanism are

Model name	Rate limiting steps	Model type
Model 3a	Step 2	QEA
Model 3b	Step 3	QEA
Model 3c	Step 5	QEA
Model 3d	Steps 3 and 5	HSSA

A.3.1. Model 3a

Coverages

$$\theta_{A_2*} = K_1\frac{p_{A_2}}{p^{\ominus}}\theta_* \quad \text{(A.70)}$$

$$\theta_{A*} = \frac{1}{K_3K_4K_5}\frac{p_{AB}}{p_B}\theta_* \quad \text{(A.71)}$$

$$\theta_{B*} = K_3\frac{p_B}{p^{\ominus}}\theta_* \quad \text{(A.72)}$$

$$\theta_{AB*} = \frac{1}{K_5}\frac{p_{AB}}{p^{\ominus}}\theta_* \quad \text{(A.73)}$$

$$\theta_* = \frac{1}{1 + K_1\frac{p_{A_2}}{p^{\ominus}} + \frac{1}{K_3K_4K_5}\frac{p_{AB}}{p_B} + K_3\frac{p_B}{p^{\ominus}} + \frac{1}{K_5}\frac{p_{AB}}{p^{\ominus}}} \quad \text{(A.74)}$$

Rate expression

$$r_{3a} = k_2\theta_{A_2*}\theta_* - \frac{k_2}{K_2}\theta_{A*}^2 \quad \text{(A.75)}$$

$$= k_2K_1\frac{p_{A_2}}{p^{\ominus}}(1-\beta)\theta_*^2$$

$$= \frac{k_2K_1\frac{p_{A_2}}{p^{\ominus}}(1-\beta)}{\left(1 + K_1\frac{p_{A_2}}{p^{\ominus}} + \frac{1}{K_3K_4K_5}\frac{p_{AB}}{p_B} + K_3\frac{p_B}{p^{\ominus}} + \frac{1}{K_5}\frac{p_{AB}}{p^{\ominus}}\right)^2} \quad \text{(A.76)}$$

Reaction orders

$$\alpha_{A_2} = 1 - 2\theta_{A_2*} \tag{A.77}$$

$$\alpha_{B} = -2\theta_{B*} + 2\theta_{A*} \tag{A.78}$$

$$\alpha_{AB} = -2\theta_{A*} - 2\theta_{AB*} \tag{A.79}$$

Apparent activation enthalpy

$$H^{\ddagger} = H_2^{\ddagger} + \Delta H_1 - 2\Delta H_1\theta_{A_2*} - 2\Delta H_3\theta_{B*} + 2(\Delta H_3 + \Delta H_4 + \Delta H_5)\theta_{A*} + 2\Delta H_5\theta_{AB*} \tag{A.80}$$

A.3.2. Model 3b

Coverages

$$\theta_{A_2*} = K_1\frac{p_{A_2}}{p^{\ominus}}\theta_* \tag{A.81}$$

$$\theta_{A*} = \sqrt{K_1K_2\frac{p_{A_2}}{p^{\ominus}}}\theta_* \tag{A.82}$$

$$\theta_{B*} = \frac{1}{\sqrt{K_1K_2}K_4K_5}\frac{p_{AB}}{\sqrt{p_{A_2}p^{\ominus}}}\theta_* \tag{A.83}$$

$$\theta_{AB*} = \frac{1}{K_5}\frac{p_{AB}}{p^{\ominus}}\theta_* \tag{A.84}$$

$$\theta_* = \frac{1}{1 + K_1\frac{p_{A_2}}{p^{\ominus}} + \sqrt{K_1K_2\frac{p_{A_2}}{p^{\ominus}}} + \frac{1}{\sqrt{K_1K_2}K_4K_5}\frac{p_{AB}}{\sqrt{p_{A_2}p^{\ominus}}} + \frac{1}{K_5}\frac{p_{AB}}{p^{\ominus}}} \tag{A.85}$$

Rate expression

$$r_{3b} = k_3\frac{p_B}{p^{\ominus}}\theta_* - \frac{k_3}{K_3}\theta_{B*}$$

$$= k_3\frac{p_B}{p^{\ominus}}(1-\sqrt{\beta})\theta_* \tag{A.86}$$

$$= \frac{k_3\frac{p_B}{p^{\ominus}}(1-\sqrt{\beta})}{1 + K_1\frac{p_{A_2}}{p^{\ominus}} + \sqrt{K_1K_2\frac{p_{A_2}}{p^{\ominus}}} + \frac{1}{\sqrt{K_1K_2}K_4K_5}\frac{p_{AB}}{\sqrt{p_{A_2}p^{\ominus}}} + \frac{1}{K_5}\frac{p_{AB}}{p^{\ominus}}} \tag{A.87}$$

Reaction orders

$$\alpha_{A_2} = -\theta_{A_2*} - \frac{1}{2}\theta_{A*} + \frac{1}{2}\theta_{B*} \tag{A.88}$$

$$\alpha_{B} = 1 \tag{A.89}$$

$$\alpha_{AB} = -\theta_{AB*} - \theta_{B*} \tag{A.90}$$

Activation enthalpy

$$H^{\ddagger} = H_3^{\ddagger} - \Delta H_1\theta_{A_2*} + \left(\frac{1}{2}\Delta H_1 + \frac{1}{2}\Delta H_2 + \Delta H_4 + \Delta H_5\right)\theta_{B*} - \frac{1}{2}(\Delta H_1 + \Delta H_2)\theta_{A*} + \Delta H_5\theta_{AB*} \tag{A.91}$$

A.3.3. Model 3c

Coverages

$$\theta_{A_2*} = K_1\frac{p_{A_2}}{p^{\ominus}}\theta_* \tag{A.92}$$

$$\theta_{A*} = \sqrt{K_1K_2\frac{p_{A_2}}{p^{\ominus}}}\theta_* \tag{A.93}$$

$$\theta_{B*} = K_3\frac{p_B}{p^{\ominus}}\theta_* \tag{A.94}$$

$$\theta_{AB*} = \sqrt{K_1K_2}K_3K_4\sqrt{\frac{p_{A_2}}{p^{\ominus}}}\frac{p_B}{p^{\ominus}}\theta_* \tag{A.95}$$

$$\theta_* = \frac{1}{1 + K_1\frac{p_{A_2}}{p^{\ominus}} + \sqrt{K_1K_2\frac{p_{A_2}}{p^{\ominus}}} + K_3\frac{p_B}{p^{\ominus}} + \sqrt{K_1K_2}K_3K_4\sqrt{\frac{p_{A_2}}{p^{\ominus}}}\frac{p_B}{p^{\ominus}}} \tag{A.96}$$

Rate expression

$$r_{3c} = k_5\theta_{AB*} - \frac{k_5}{K_5}\frac{p_{AB}}{p^{\ominus}}\theta_* \tag{A.97}$$

$$= k_5\sqrt{K_1K_2}K_3K_4\sqrt{\frac{p_{A_2}}{p^{\ominus}}}\frac{p_B}{p^{\ominus}}(1-\sqrt{\beta})\theta_*$$

$$= \frac{k_5\sqrt{K_1K_2}K_3K_4\sqrt{\frac{p_{A_2}}{p^{\ominus}}}\frac{p_B}{p^{\ominus}}(1-\sqrt{\beta})}{1 + K_1\frac{p_{A_2}}{p^{\ominus}} + \sqrt{K_1K_2\frac{p_{A_2}}{p^{\ominus}}} + K_3\frac{p_B}{p^{\ominus}} + \sqrt{K_1K_2}K_3K_4\sqrt{\frac{p_{A_2}}{p^{\ominus}}}\frac{p_B}{p^{\ominus}}} \tag{A.98}$$

Reaction orders

$$\alpha_{A_2} = \frac{1}{2} - \theta_{A_2*} - \frac{1}{2}\theta_{A*} \tag{A.99}$$

$$\alpha_{B} = 1 - \theta_{B*} - \theta_{AB*} \tag{A.100}$$

$$\alpha_{AB} = 0 \tag{A.101}$$

Apparent activation enthalpy

$$H^{\ddagger} = H_5^{\ddagger} + \frac{1}{2}\Delta H_1 + \frac{1}{2}\Delta H_2 + \Delta H_3 + \Delta H_4 - \Delta H_1\theta_{A_2*} - \Delta H_3\theta_{B*} - \frac{1}{2}(\Delta H_1 + \Delta H_2)\theta_{A*} - \left(\frac{1}{2}\Delta H_1 + \frac{1}{2}\Delta H_2 + \Delta H_3 + \Delta H_4\right)\theta_{AB*} \quad \text{(A.102)}$$

A.3.4. Model 3d

Steady-state balance

$$r_3 = r_5 \quad \text{(A.103)}$$

$$k_3\frac{p_B}{p^{\ominus}}\theta_* - \frac{k_3}{K_3}\theta_{B*} = k_5\theta_{AB} - \frac{k_5}{K_5}\frac{p_{AB}}{p^{\ominus}}\theta_* \quad \text{(A.104)}$$

Coverages

$$\theta_{A_2*} = K_1\frac{p_{A_2}}{p^{\ominus}}\theta_* \quad \text{(A.105)}$$

$$\theta_{A*} = \sqrt{K_1K_2\frac{p_{A_2}}{p^{\ominus}}}\theta_* \quad \text{(A.106)}$$

$$\theta_{B*} = \frac{1}{\sqrt{K_1K_2}K_4}\sqrt{\frac{p^{\ominus}}{p_{A_2}}}\theta_{AB*} \quad \text{(A.107)}$$

$$\theta_{AB*} = \frac{k_3\frac{p_B}{p^{\ominus}} + \frac{k_5}{K_5}\frac{p_{AB}}{p^{\ominus}}}{\frac{k_3}{\sqrt{K_1K_2}K_3K_4}\sqrt{\frac{p^{\ominus}}{p_{A_2}}} + k_5}\theta_* \quad \text{(A.108)}$$

$$\frac{1}{\theta_*} = 1 + K_1\frac{p_{A_2}}{p^{\ominus}} + \sqrt{K_1K_2\frac{p_{A_2}}{p^{\ominus}}} + \frac{k_3\frac{p_B}{p^{\ominus}} + \frac{k_5}{K_5}\frac{p_{AB}}{p^{\ominus}}}{\frac{k_3}{\sqrt{K_1K_2}K_3K_4}\sqrt{\frac{p^{\ominus}}{p_{A_2}}} + k_5} + \frac{1}{\sqrt{K_1K_2}K_4}\sqrt{\frac{p^{\ominus}}{p_{A_2}}}\left(\frac{k_3\frac{p_B}{p^{\ominus}} + \frac{k_5}{K_5}\frac{p_{AB}}{p^{\ominus}}}{\frac{k_3}{\sqrt{K_1K_2}K_3K_4}\sqrt{\frac{p^{\ominus}}{p_{A_2}}} + k_5}\right) \quad \text{(A.109)}$$

Rate expression

$$r_{3d,Step\ 3} = k_3\frac{p_B}{p^{\ominus}}\theta_* - \frac{k_3}{K_3}\theta_{B*} \quad \text{(A.110)}$$

$$r_{3d,Step\ 5} = k_5\theta_{AB} - \frac{k_5}{K_5}\frac{p_{AB}}{p^{\ominus}}\theta_* \quad \text{(A.111)}$$

References

[1] P. Stoltze, Phys. Scr. 36 (1987) 824.
[2] P. Stoltze, Prog. Surf. Sci. 65 (2000) 65.
[3] R.D. Cortright, J.A. Dumesic, Adv. Catal. 46 (2001) 161.
[4] T. Askgaard, J.K. Nørskov, C.V. Ovesen, P. Stoltze, J. Catal. 156 (1995) 229.
[5] C.V. Ovesen, B.S. Clausen, B.S. Hammershøi, G. Steffensen, T. Askgaard, I. Chorkendorff, J.K. Nørskov, P.B. Rasmussen, P. Stoltze, P. Taylor, J. Catal. 158 (1996) 170.
[6] J.A. Dumesic, D.A. Rudd, L.M. Aparicio, J.E. Rekoske, A.A. Treviño, The Microkinetics of Heterogeneous Catalysis, ACS, 1993.
[7] C.T. Campbell, Top. Catal. 1 (1994) 353.
[8] S.H. Oh, G.B. Fischer, J.E. Carpenter, D.W. Goodman, J. Catal. 100 (1986) 360.
[9] V.B. Zdanov, B. Kasermo, Surf. Sci. Rep. 20 (1986) 111.
[10] N. Waletzko, L.D. Schmidt, AIChE J. 34 (1988) 1146.
[11] D.A. Hickman, L.D. Schmidt, AIChE J. 39 (1993) 1164.
[12] A. Andreasen, H. Lynggaard, C. Stegelmann, P. Stoltze, Surf. Sci. 544 (1) (2003) 5.
[13] C. Stegelmann, N.C. Schiødt, C.T. Campbell, P. Stoltze, J. Catal. 221 (1–3) (2004) 630.
[14] P. Stoltze, J.K. Nørskov, Phys. Rev. Lett. 55 (1985) 2502.
[15] R. Aris, Elementary Chemical Reactor Analysis, Butterworths, London, 1989.
[16] G. Yaglonskii, V. Bykov, A. Gorban, V. Elokin, Kinetic models of catalytic reactors, in: R.G. Compton (Ed.), Comprehensive Chemical Kinetics, vol. 32, Elsevier, Amsterdam, 1991.
[17] C.V. Ovesen, B.S. Clausen, J. Schiøtz, P. Stoltze, H. Topsøe, J.K. Nørskov, J. Catal. 168 (1997) 7133.
[18] H. Topsøe, C.V. Ovesen, B.S. Clausen, N.-Y. Topsøe, Stud. Surf. Sci. Catal. 109 (1997) 121.
[19] T. Bligaard, K. Honkala, A. Logadottir, J.K. Nørskov, S. Dahl, C.J.H. Jacobsen, J. Phys. Chem. B. 107 (2003) 9325.
[20] R.I. Masel, Principles of Adsorption and Reaction on Solid Surfaces, John Wiley and Sons, New York, 1996.
[21] S. Linic, M.A. Barteau, J. Catal. 125 (2003) 200.
[22] M.A. Barteau, Catal. Lett. 8 (1991) 175.
[23] A.J. Gellman, Q. Dai, J. Am. Chem Soc. 115 (1993) 714.
[24] V. Pallasana, M. Neurock, J. Catal. 191 (2001) 301.
[25] A. Logadottir, T.H. Rod, J.K. Nørskov, B. Hammer, S. Dahl, C.J.H. Jacobsen, J. Catal. 197 (2001) 229.
[26] Z.P. Liu, P. Hu, J. Chem. Phys. 114 (2001) 8244.
[27] J.K. Nørskov, T. Bligaard, A. Logadottir, S. Bahn, L.B. Hansen, M. Bollinger, H. Bengaard, B. Hammer, Z. Sljivancanin, M. Mavrikakis, Y. Xu, S. Dahl, C.J.H. Jacobsen, J. Catal. 209 (2002) 275.
[28] G.C. Bond, M.A. Keane, H. Kral, J.A. Lercher, Catal. Rev. Sci. Eng. 42 (2000) 319.
[29] A.K. Galwey, Adv. Catal 26 (1977) 247.
[30] G.A. Somorjai, Introduction to Surface Chemistry and Catalysis, John Wiley and Sons, New York, 1994.
[31] A. Wootsch, Z. Páal, J. Catal. 205 (2002) 86.
[32] H. Kral, Chem. Eng. Technol. 11 (1988) 113.
[33] G.C. Bond, Catal. Today 49 (1999) 41.
[34] G.C. Bond, A.D. Hooper, J.C. Slaa, A.O. Taylor, J. Catal. 163 (1996) 319.
[35] J. Guilherme, R. Poço, H. Furlan, R. Giudici, J. Phys. Chem. B 106 (2002) 4873.
[36] J.B. Miller, H.R. Siddiqui, S.M. Gates, J.N. Russell Jr., J.T. Yates Jr., J.C. Tully, M.J. Cardillo, J. Chem. Phys. 87 (1987) 6725.
[37] D.L.S. Nieskens, A.P. van Bravel, J.W. Niemantsverdriet, Surf. Sci. 546 (2003) 159.
[38] J.V. Barth, H. Brune, B. Fischer, J. Weckesser, K. Kern, Phys. Rev. Lett. 84 (2000) 1732.
[39] G.V. Loukova, A.I. Mikhailov, A.E. Shilov, Kinet. Catal. 43 (2002) 746.
[40] F.H. Constable, Proc. R. Soc. London A 108 (1925) 355.

Mission

To promote an innovative and environmentally sustainable technological development within the areas of energy, industrial technology and bioproduction through research, innovation and advisory services.

Vision

Risø's research **shall extend the boundaries** for the understanding of nature's processes and interactions right down to the molecular nanoscale.

The results obtained shall **set new trends** for the development of sustainable technologies within the fields of energy, industrial technology and biotechnology.

The efforts made **shall benefit** Danish society and lead to the development of new multi-billion industries.